

Ministry of Education and Science of the Russian Federation
Saint Petersburg National Research University of Information
Technologies, Mechanics, and Optics

NANOSYSTEMS:
PHYSICS, CHEMISTRY, MATHEMATICS

2022, volume 13(2)

Наносистемы: физика, химия, математика

2022, том 13, № 2



NANOSYSTEMS:

PHYSICS, CHEMISTRY, MATHEMATICS

ADVISORY BOARD MEMBERS

Chairman: V.N. Vasiliev (*St. Petersburg, Russia*),
V.M. Buznik (*Moscow, Russia*); V.M. Ievlev (*Voronezh, Russia*), P.S. Kop'ev (*St. Petersburg, Russia*), N.F. Morozov (*St. Petersburg, Russia*), V.N. Parmon (*Novosibirsk, Russia*),
A.I. Rusanov (*St. Petersburg, Russia*),

EDITORIAL BOARD

Editor-in-Chief: I.Yu. Popov (*St. Petersburg, Russia*)

Section Co-Editors:

Physics – V.M. Uzdin (*St. Petersburg, Russia*),
Material science – V.V. Gusarov (*St. Petersburg, Russia*),
Chemistry – V.K. Ivanov (*Moscow, Russia*),
Mathematics – I.Yu. Popov (*St. Petersburg, Russia*).

Editorial Board Members:

V.M. Adamyan (*Odessa, Ukraine*); O.V. Al'myasheva (*St. Petersburg, Russia*);
A.P. Alodjants (*Vladimir, Russia*); S. Bechta (*Stockholm, Sweden*); J. Behrndt (*Graz, Austria*);
M.B. Belonenko (*Volgograd, Russia*); A. Chatterjee (*Hyderabad, India*); A.V. Chizhov
(*Dubna, Russia*); A.N. Enyashin (*Ekaterinburg, Russia*), P.P. Fedorov (*Moscow, Russia*);
E.A. Gudilin (*Moscow, Russia*); H. Jónsson (*Reykjavik, Iceland*); A.A. Kiselev (*Durham, USA*);
Yu.S. Kivshar (*Canberra, Australia*); S.A. Kozlov (*St. Petersburg, Russia*);
P.A. Kurasov (*Stockholm, Sweden*); A.V. Lukashin (*Moscow, Russia*); I.V. Melikhov
(*Moscow, Russia*); G.P. Miroshnichenko (*St. Petersburg, Russia*); I.Ya. Mittova (*Voronezh, Russia*);
Nguyen Anh Tien (*Ho Chi Minh, Vietnam*); V.V. Pankov (*Minsk, Belarus*);
K. Pankrashkin (*Orsay, France*); A.V. Ragulya (*Kiev, Ukraine*); V. Rajendran (*Tamil Nadu, India*);
A.A. Rempel (*Ekaterinburg, Russia*); V.Ya. Rudyak (*Novosibirsk, Russia*);
H.M. Sedighi (*Ahvaz, Iran*); D Shoikhet (*Karmiel, Israel*); P Stovicek (*Prague, Czech Republic*);
V.M. Talanov (*Novocherkassk, Russia*); A.Ya. Vul' (*St. Petersburg, Russia*);
A.V. Yakimansky (*St. Petersburg, Russia*), V.A. Zagrebnoy (*Marseille, France*).

Editors:

I.V. Blinova; A.I. Popov; A.I. Trifanov; E.S. Trifanova (*St. Petersburg, Russia*),
R. Simoneaux (*Philadelphia, Pennsylvania, USA*).

Address: ITMO University, Kronverkskiy pr., 49, St. Petersburg 197101, Russia.

Phone: +7(812)607-02-54, **Journal site:** <http://nanojournal.ifmo.ru/>,

E-mail: nanojournal.ifmo@gmail.com

AIM AND SCOPE

The scope of the journal includes all areas of nano-sciences. Papers devoted to basic problems of physics, chemistry, material science and mathematics inspired by nanosystems investigations are welcomed. Both theoretical and experimental works concerning the properties and behavior of nanosystems, problems of its creation and application, mathematical methods of nanosystem studies are considered.

The journal publishes scientific reviews (up to 30 journal pages), research papers (up to 15 pages) and letters (up to 5 pages). All manuscripts are peer-reviewed. Authors are informed about the referee opinion and the Editorial decision.

CONTENT

MATHEMATICS

T.K. Yuldashev

- Periodic solutions for an impulsive system of nonlinear differential equations with maxima** 135

PHYSICS

Yu.V. Dvuzhilova, N.G. Glazkova, I.S. Dvuzhilov,
I.V. Zaporotskova, M.B. Belonenko

- Three-dimensional extremely short optical pulses in a photonic crystal with a superlattice** 142

A.E. Atamuratov, B.O. Jabbarova, M.M. Khalilloev,
A. Yusupov, K. Sivasankaran, J.C. Chedjou

- Impact of the channel shape, back oxide and gate oxide layers on self-heating in nanoscale JL FINFET** 148

A.S. Bagmutov, H. Najar, I.F. Melikhov, I.Y. Popov

- On the discrete spectrum of a quantum waveguide with Neumann windows in presence of exterior field** 156

CHEMISTRY AND MATERIAL SCIENCE

O.V. Almjasheva, V.I. Popkov, O.V. Proskurina, V.V. Gusarov

- Phase formation under conditions of self-organization of particle growth restrictions in the reaction system** 164

Muhammad Irfan Asghar, Muhammad Kashif Shahid, Muhammad Haq Nawaz, Muhammad Idrees, Muhammad Asif, Ahsan Ali,

- Synthesis, characterization and electrical properties of the nanosized perovskite LaFeO₃** 181

S. Kuznetsova, O. Khalipova, Yu-Wen Chen, V. Kozik

- The joint effect of doping with tin(IV) and heat treatment on the transparency and conductivity of films based on titanium dioxide as photoelectrodes of sensitized solar cells** 192

A.L. Popov, I.V. Savintseva, A.M. Ermakov, N.R. Popova,
D.D. Kolmanovich, N.N. Chukavin, A.F. Stolyarov,

- A.B. Shcherbakov, O.S. Ivanova, V.K. Ivanov
Synthesis and analysis of cerium-containing carbon quantum dots for bioimaging *in vitro* 204

Yu.A. Avdeeva, I.V. Luzhkova, A.N. Ermakov Mechanism of formation of nanocrystalline particles with core-shell structure based on titanium oxynitrides with nickel in the process of plasma-chemical synthesis of TiNi in a low-temperature nitrogen plasma	212
R.S. Dubey, S. Saravanan Impact of distributed Bragg's reflectors and nanogratings in thin film silicon solar cells	220
Information for authors	227

Periodic solutions for an impulsive system of nonlinear differential equations with maxima

T. K. Yuldashev

National University of Uzbekistan, University street, 4, NUUZ, Tashkent, 100174, Uzbekistan

tursun.k.yuldashev@gmail.com

Corresponding author: T. K. Yuldashev, tursun.k.yuldashev@gmail.com

ABSTRACT In this paper, a periodical boundary value problem for a first order system of ordinary differential equations with impulsive effects and maxima is investigated. We define a nonlinear functional-integral system, the set of periodic solutions of which coincides with the set of periodic solutions of the given problem. In the proof of the existence and uniqueness of the periodic solution of the obtained system, the method of compressing mapping is used.

KEYWORDS impulsive differential equations, periodical boundary value condition, successive approximations, existence and uniqueness of periodic solution.

FOR CITATION Yuldashev T. K. Periodic solutions for an impulsive system of nonlinear differential equations with maxima. *Nanosystems: Phys. Chem. Math.*, 2022, **13** (2), 135–141.

1. Introduction

The dynamics of evolving processes is often subjected to abrupt changes such as shocks, harvesting, and natural disasters. Often these short-term perturbations are treated as having acted instantaneously or in the form of impulses. Mathematically, this leads to an impulsive dynamical system. So, differential equations, the solutions of which are functions with first kind “discontinuities” at fixed or non-fixed times, have applications in biological, chemical and physical sciences, ecology, biotechnology, industrial robotic, pharmacokinetics, optimal control, etc. [1–5]. In particular, such kind of problems appear in biophysics at micro- and nano-scales [6–10]. Such differential equations with “discontinuities” at fixed or non-fixed times are called differential equations with impulsive effects. A lot of publications of studying on differential equations with impulsive effects, describing many natural and technical processes, are appearing [11–21].

As is known, in recent years the interest in the study of differential equations with periodical boundary conditions has increased. In the works [22–26] periodic solutions of the differential equations with impulsive effects are studied. In [27] the problems of bifurcation of positive periodic solutions of first-order impulsive differential equations are studied. In [28] the problems of stability of periodic impulsive systems are studied.

In this paper, in contrast to works [22–26], we study a periodical boundary value problem for a system of first order differential equations with impulsive effects and “maxima”. The questions of the existence and uniqueness of the solution to the periodical boundary value problem are studied. In addition, the technique used in our work is constructive (see [5]) and allows the practical calculation of periodic solutions of nonlinear dynamical systems with deviations, including those with maxima.

2. Problem statement

On the interval $[0, T]$ for $t \neq t_i$, $i = 1, 2, \dots, p$ we consider the questions of existence and constructive methods of finding the periodic solutions of the system of nonlinear ordinary first order differential equations with impulsive effects and maxima

$$x'(t) = f(t, x(t), \max \{x(\tau) \mid \tau \in [t-h, t]\}), \quad 0 < h = \text{const.} \quad (1)$$

We study equation (1) with periodic condition

$$\begin{cases} x(t) = \varphi(t), & t \in [-h, 0], \\ x(0) = x(T) \end{cases} \quad (2)$$

and nonlinear impulsive effect

$$x(t_i^+) - x(t_i^-) = F_i(x(t_i)), \quad i = 1, 2, \dots, p, \quad (3)$$

where $0 < \bar{t} < T$, $\bar{t} \neq t_i$, $i = 1, 2, \dots, p$, $0 = t_0 < t_1 < \dots < t_p < t_{p+1} = T$, $x, y \in X$, X is a closed bounded domain in the space \mathbb{R}^n , ∂X is its border, $f \in \mathbb{R}^n$, $x(t_i^+) = \lim_{\nu \rightarrow 0^+} x(t_i + \nu)$, $x(t_i^-) = \lim_{\nu \rightarrow 0^-} x(t_i - \nu)$ are right-hand

side and left-hand side limits of function $x(t)$ at the point $t = t_i$, respectively. The function f is T -periodic, $F_i = F_{i+p}$, $t_{i+p} = t_i + T$.

$C([0, T], \mathbb{R}^n)$ is the notation of the Banach space, which consists of continuous vector functions $x(t)$, defined on the segment $[0, T]$, with values in \mathbb{R}^n and with the norm

$$\|x(t)\| = \sqrt{\sum_{j=1}^n \max_{0 \leq t \leq T} |x_j(t)|}.$$

$PC([0, T], \mathbb{R}^n)$ is the notation of the linear vector space

$$PC([0, T], \mathbb{R}^n) = \{x : [0, T] \rightarrow \mathbb{R}^n; x(t) \in C((t_i, t_{i+1}], \mathbb{R}^n), i = 1, \dots, p\},$$

where $x(t_i^+)$ and $x(t_i^-)$ ($i = 0, 1, \dots, p$) exist and are bounded; $x(t_i^-) = x(t_i)$. Note, that the linear vector space $PC([0, T], \mathbb{R}^n)$ is Banach space with the following norm

$$\|x(t)\|_{PC} = \max \left\{ \|x\|_{C((t_i, t_{i+1}])}, i = 1, 2, \dots, p \right\}.$$

Formulation of problem. To find the T -periodic function $x(t) \in PC([0, T], \mathbb{R}^n)$, which for all $t \in [0, T]$, $t \neq t_i$, $i = 1, 2, \dots, p$ satisfies the system of differential equation (1), periodic condition (2) and for $t = t_i$, $i = 1, 2, \dots, p$, $0 < t_1 < t_2 < \dots < t_p < T$ satisfies the nonlinear limit condition (3) and goes through x_0 at $t = 0$.

3. Reduction to an functional-integral equation

Let the function $x(t) \in PC([0, T], \mathbb{R}^n)$ is a solution of the periodic boundary value problem (1)–(3). Then by integration of the equation (1) on the intervals: $(0, t_1]$, $(t_1, t_2]$, \dots , $(t_p, t_{p+1}]$, we obtain:

$$\begin{aligned} \int_0^{t_1} f(s, x, y) ds &= \int_0^{t_1} x'(s) ds = x(t_1^-) - x(0^+), \quad t \in (0, t_1], \\ \int_{t_1}^{t_2} f(s, x, y) ds &= \int_{t_1}^{t_2} x'(s) ds = x(t_2^-) - x(t_1^+), \quad t \in (t_1, t_2], \\ &\dots\dots\dots \\ \int_{t_p}^{t_{p+1}} f(s, x, y) ds &= \int_{t_p}^{t_{p+1}} x'(s) ds = x(t_{p+1}^-) - x(t_p^+), \quad t \in (t_p, t_{p+1}], \end{aligned}$$

where $f(s, x, y) = f(t, x(t), \max \{x(\tau) | \tau \in [t - h, t]\})$.

Hence, taking $x(0^+) = x(0)$, $x(t_{k+1}^-) = x(t)$ into account, on the interval $(0, T]$ we have

$$\begin{aligned} \int_0^t f(s, x, y) ds &= [x(t_1) - x(0^+)] + [x(t_2) - x(t_1^+)] + \dots + [x(t) - x(t_p^+)] = \\ &= -x(0) - [x(t_1^+) - x(t_1)] - [x(t_2^+) - x(t_2)] - \dots - [x(t_p^+) - x(t_p)] + x(t). \end{aligned}$$

Taking into account the condition (3), the last equality we rewrite as

$$x(t) = x(0) + \int_0^t f(s, x, y) ds + \sum_{0 < t_i < t} F_i(x(t_i)). \tag{4}$$

We subordinate the function $x(t) \in PC([0, T], \mathbb{R}^n)$ in (4) to satisfy the periodic condition (2):

$$x(T) = x(0) + \int_0^T f(s, x, y) ds + \sum_{0 < t_i < T} F_i(x(t_i)).$$

Hence, taking the condition (2) into account, we obtain:

$$\int_0^T f(s, x, y) ds + \sum_{0 < t_i < T} F_i(x(t_i)) = 0.$$

Consequently, the differential equation (1) one can write as

$$x'(t) = f(t, x(t), \max \{x(\tau) \mid \tau \in [t - h, t]\}) - \frac{1}{T} \int_0^T f(t, x(t), \max \{x(\tau) \mid \tau \in [t - h, t]\}) dt - \frac{1}{T} \sum_{i=1}^p F_i(x(t_i)). \quad (5)$$

Then by integration of the equation (5) on the intervals: $(0, t_1], (t_1, t_2], \dots, (t_p, t_{p+1}]$, instead (4) we obtain the following equation:

$$x(t) = x_0 + \int_0^t \left[f(s, x(s), \max \{x(\tau) \mid \tau \in [s - h, s]\}) - \frac{1}{T} \int_0^T f(\theta, x(\theta), \max \{x(\tau) \mid \tau \in [\theta - h, \theta]\}) d\theta - \frac{1}{T} \sum_{i=1}^p F_i(x(t_i)) \right] ds + \sum_{0 < t_i < t} F_i(x(t_i)). \quad (6)$$

Lemma 1. For solution of equation (6) one has the following estimate

$$\|x(t) - x_0\|_{PC} \leq M \left(\frac{T}{2} + 2p \right), \quad (7)$$

where $M = \max \left\{ \|f(t, x(t), y(t))\|; \max_{1 \leq i \leq p} \|F_i(t, x(t))\| \right\}$.

Proof. We rewrite the equation (6) as

$$\begin{aligned} x(t) - x_0 &= \int_0^t \left[f(s, x(s), y(s)) - \frac{1}{T} \int_0^T f(\theta, x(\theta), y(\theta)) d\theta - \frac{1}{T} \sum_{i=1}^p F_i(x(t_i)) \right] ds + \sum_{0 < t_i < t} F_i(x(t_i)) = \\ &= \int_0^t f(s, x(s), y(s)) ds - \frac{t}{T} \int_0^t f(s, x(s), y(s)) ds - \frac{t}{T} \int_t^T f(s, x(s), y(s)) ds - \frac{t}{T} \sum_{i=1}^p F_i(x(t_i)) + \sum_{0 < t_i < t} F_i(x(t_i)). \end{aligned}$$

Hence, implies that there is true the following estimate

$$\|x(t) - x_0\|_{PC} \leq \alpha(t) \cdot \|f(t, x(t), y(t))\| + 2p \cdot \max_{1 \leq i \leq p} \|F_i(t, x(t))\|, \quad (8)$$

where $\alpha(t) = 2t \left(1 - \frac{t}{T} \right)$. It is easy to check that from (8) follows (7). Lemma 1 is proved.

Remark. T -periodic solution $x_{\varphi(t)} = \psi(t)$ of the system (1) with initial value function $\varphi(t)$ on the initial set $[-h, 0]$ is defined by the initial value function $\varphi(t)$, which is periodical continuation of the solution $\psi(t)$ into initial set $[-h, 0]$.

Lemma 2. For the difference of two functions with maxima there holds the following estimate

$$\| \max \{x(\tau) \mid \tau \in [t - h, t]\} - \max \{y(\tau) \mid \tau \in [t - h, t]\} \| \leq \|x(t) - y(t)\| + 2h \left\| \frac{\partial}{\partial t} [x(t) - y(t)] \right\|. \quad (9)$$

Proof. We use obvious true relations

$$\begin{aligned} \max \{x(\tau) \mid \tau \in [t - h, t]\} &= \max \{[x(\tau) - y(\tau) + y(\tau)] \mid \tau \in [t - h, t]\} \leq \\ &\leq \max \{[x(\tau) - y(\tau)] \mid \tau \in [t - h, t]\} + \max \{y(\tau) \mid \tau \in [t - h, t]\}. \end{aligned}$$

Hence, we obtain

$$\max \{x(\tau) \mid \tau \in [t - h, t]\} - \max \{y(\tau) \mid \tau \in [t - h, t]\} \leq \max \{[x(\tau) - y(\tau)] \mid \tau \in [t - h, t]\}. \quad (10)$$

We denote by t_1 and t_2 the points of $[t - h, t]$, on which the maximums of the functions $x(t)$ and $y(t)$ are reached:

$$\begin{aligned} \max \{x(\tau) \mid \tau \in [t - h, t]\} &= x(t_1), \quad \max \{y(\tau) \mid \tau \in [t - h, t]\} = y(t_1), \\ \max \{[x(\tau) - y(\tau)] \mid \tau \in [t - h, t]\} &= x(t_2) - y(t_2). \end{aligned}$$

Then, taking (10) and last equalities, we have

$$\begin{aligned} \| \max \{x(\tau) \mid \tau \in [t - h, t]\} - \max \{y(\tau) \mid \tau \in [t - h, t]\} - x(t) + y(t) \| &\leq \\ &\leq \| [x(t) - y(t)] - [x(t_1) - y(t_1)] \| + \| [x(t_2) - y(t_2)] - [x(t_1) - y(t_1)] \|. \end{aligned} \quad (11)$$

From another side, it is obvious that, there holds the estimate

$$\| [x(\bar{t}) - y(\bar{t})] - [x(\bar{\bar{t}}) - y(\bar{\bar{t}})] \| \leq h \left\| \frac{d}{dt} [x(t^*) - y(t^*)] \right\| \leq h \left\| \frac{d}{dt} [x(t) - y(t)] \right\|, \quad (12)$$

where $\bar{t}, \bar{t} \in [t-h, t]$, $t^* \in (\bar{t}, \bar{t})$. From the estimates (11) and (12) we come to the following estimate:

$$\| \max \{x(\tau) \mid \tau \in [t-h, t]\} - \max \{y(\tau) \mid \tau \in [t-h, t]\} - x(t) + y(t) \| \leq 2h \left\| \frac{d}{dt}[x(t) - y(t)] \right\|.$$

Therefore, it is easy to check that there holds the inequality (9) and we complete the proof of the Lemma 2.

By the BD we denote the Banach space of functions on the interval $[0, T]$ with the norm

$$\|x(t)\|_{BD} \leq \|x(t)\|_{PC} + h \|x'(t)\|_{PC}.$$

Theorem 1. Assume that for all $t \in [0, T]$, $t \neq t_i$, $i = 1, 2, \dots, p$ are fulfilled the following conditions:

1. $\max \left\{ \|f(t, x(t), y(t))\|; \max_{1 \leq i \leq p} \|F_i(t, x(t))\| \right\} = M < \infty$;
2. $\|f(t, x_1, y_1) - f(t, x_2, y_2)\| \leq L_1 (\|x_1 - x_2\| + \|y_1 - y_2\|)$;
3. $\|F_i(x_1) - F_i(x_2)\| \leq L_2 \|x_1 - x_2\|$;
4. The radius of the inscribed ball in X is greater than $M \left(\frac{T}{2} + 2p \right)$;
5. $2L_1 \left(\frac{T}{2} + h \right) + L_2 p \left(2 + \frac{h}{T} \right) < 1$.

If the system (1) has a periodic solution for all $t \in [0, T]$, $t \neq t_i$, $i = 1, 2, \dots, p$, then this solution can be founded by the system of nonlinear functional-integral equations

$$\begin{aligned} x(t, x_0) = & x_0 + \int_0^t \left[f(s, x(s, x_0), \max \{x(\tau, x_0) \mid \tau \in [s-h, s]\}) - \right. \\ & \left. - \frac{1}{T} \int_0^T f(\theta, x(\theta, x_0), \max \{x(\tau, x_0) \mid \tau \in [\theta-h, \theta]\}) d\theta - \frac{1}{T} \sum_{i=1}^p F_i(x(t_i, x_0)) \right] ds + \sum_{0 < t_i < t} F_i(x(t_i, x_0)). \end{aligned} \quad (13)$$

Proof. We will show that the right-hand side of the system of equations (13) as an operator maps a ball with radius $M \cdot \left(\frac{T}{2} + 2p \right)$ into itself and is a contraction operator. So, according to the lemma 1, from (7) we have

$$\|x(t, x_0) - x_0\|_{PC} \leq M \left(\frac{T}{2} + 2p \right). \quad (14)$$

From the equation (5) we obtain

$$\|x'(t, x_0)\|_{PC} \leq M \left(2 + \frac{p}{T} \right). \quad (15)$$

We consider a difference $x(t, x_0) - \vartheta(t, x_0)$, where functions $x(t, x_0)$ and $\vartheta(t, x_0)$ satisfy the system of equations (13). By the conditions of the theorem, from (13) we have

$$\begin{aligned} \|x(t, x_0) - \vartheta(t, x_0)\| & \leq L_1 \int_0^t \left\{ \|x(s, x_0) - \vartheta(s, x_0)\| + \right. \\ & + \left\| \max \{x(\tau, x_0) \mid \tau \in [s-h, s]\} - \max \{\vartheta(\tau, x_0) \mid \tau \in [s-h, s]\} \right\| + \frac{1}{T} \int_0^T \left[\|x(\theta, x_0) - \vartheta(\theta, x_0)\| + \right. \\ & \left. + \left\| \max \{x(\tau, x_0) \mid \tau \in [\theta-h, \theta]\} - \max \{\vartheta(\tau, x_0) \mid \tau \in [\theta-h, \theta]\} \right\| \right] d\theta \Big] ds + \\ & + \sum_{i=1}^p L_2 \|x(t_i, x_0) - \vartheta(t_i, x_0)\| + \sum_{0 < t_i < t} L_2 \|x(t_i, x_0) - \vartheta(t_i, x_0)\| \leq \\ & \leq 2\alpha(t)L_1 \left[\|x(t, x_0) - \vartheta(t, x_0)\|_{PC} + h \|x'(t, x_0) - \vartheta'(t, x_0)\|_{PC} \right] + 2pL_2 \|x(t, x_0) - \vartheta(t, x_0)\|_{PC} \leq \\ & \leq 2 \left(L_1 \frac{T}{2} + pL_2 \right) \|x(t, x_0) - \vartheta(t, x_0)\|_{PC} + L_1 T h \|x'(t, x_0) - \vartheta'(t, x_0)\|_{PC}. \end{aligned} \quad (16)$$

Similarly, by the assumptions of the theorem 1, from (5) we have

$$\|x'(t, x_0) - \vartheta'(t, x_0)\|_{PC} \leq \left(2L_1 + L_2 \frac{p}{T} \right) \|x(t, x_0) - \vartheta(t, x_0)\|_{PC} + 2L_1 h \|x'(t, x_0) - \vartheta'(t, x_0)\|_{PC}. \quad (17)$$

Multiplying both sides of (17) to h and the result adding to (16), we obtain

$$\|x(t, x_0) - \vartheta(t, x_0)\|_{BD} \leq \rho \cdot \|x(t, x_0) - \vartheta(t, x_0)\|_{BD}, \quad \rho = 2L_1 \left(\frac{T}{2} + h \right) + L_2 p \left(2 + \frac{h}{T} \right). \quad (18)$$

According to the last condition of the theorem 1, $\rho < 1$. So, from the estimate (18) we deduce that the operator on right-hand side of (13) is compressing. From the estimates (14), (15) and (18) implies that there exists unique fixed point $x(t, x_0) \in BD$. The theorem 1 is proved.

From the estimate (18) it is easy to obtain that for $x_0, \bar{x}_0 \in X$ holds

$$\|x(t, x_0) - x(t, \bar{x}_0)\|_{BD} \leq \frac{|x_0 - \bar{x}_0|}{1 - \rho}.$$

We note that the theorem 1 one can proof by the method of successive approximations, defining iteration process as

$$\begin{aligned} x_0(t, x_0) = x_0, \quad x_{k+1}(t, x_0) = x_0 + \int_0^t & \left[f(s, x_k(s, x_0), \max \{x_k(\tau, x_0) \mid \tau \in [s - h, s]\}) - \right. \\ & \left. - \frac{1}{T} \int_0^T f(\theta, x_k(\theta, x_0), \max \{x_k(\tau, x_0) \mid \tau \in [\theta - h, \theta]\}) d\theta - \frac{1}{T} \sum_{i=1}^p F_i(x_k(t_i, x_0)) \right] ds + \\ & + \sum_{0 < t_i < t} F_i(x_k(t_i, x_0)). \end{aligned} \quad (19)$$

Now we will show the existence of periodic solutions of the system of impulsive differential equations (1). We introduce designations:

$$\Delta(x_0) = \frac{1}{T} \int_0^T f(t, x_\infty(t, x_0), \max \{x_\infty(\tau, x_0) \mid \tau \in [t - h, t]\}) dt + \frac{1}{T} \sum_{i=1}^p F_i(x_\infty(t_i, x_0)), \quad (20)$$

$$\Delta_k(x_0) = \frac{1}{T} \int_0^T f(t, x_k(t, x_0), \max \{x_k(\tau, x_0) \mid \tau \in [t - h, t]\}) dt + \frac{1}{T} \sum_{i=1}^p F_i(x_k(t_i, x_0)), \quad (21)$$

where $x(t, x_0) = \lim_{k \rightarrow \infty} x_k(t, x_0) = x_\infty(t, x_0)$ is solution of the nonlinear system (13). Therefore, $x_\infty(t, x_0)$ is the solution of the system of impulsive differential equations (1) for $\Delta(x_0) = 0$ going through x_0 at $t = 0$. Consequently, the questions of existence of solution of the system of impulsive differential equations (1) we reduce to the questions of existence of zeros of function $\Delta(x_0)$ and we solve this problem, finding zeros of the function $\Delta_k(x_0)$.

Theorem 2. Assume that

1. All conditions of the theorem 1 are fulfilled;
2. There is a natural number k such that the function $\Delta_k(x_0)$ has an isolated singular point $\Delta_k(x_0) = 0$, index of which is nonzero;
3. There is a closed convex region $X_0 \subset X$, containing a single singular point such that on the its border ∂X_0 is fulfilled estimate

$$\inf_{x \in \partial X_0} \|\Delta_k(x)\| \geq \frac{M \rho^{k+1}}{1 - \rho}. \quad (22)$$

Then the system of impulsive differential equations (1) has a periodic solution for all $t \in [0, T]$, $t \neq t_i$, $i = 1, 2, \dots, p$ that $x(0) \in X_0$.

Proof. Let us consider families of everywhere continuous on ∂X vector fields

$$V(\sigma, x_0) = \Delta_k(x_0) + \sigma(\Delta(x_0) - \Delta_k(x_0)),$$

which connect the fields

$$V(0, x_0) = \Delta_k(x_0), \quad V(1, x_0) = \Delta(x_0).$$

We note that there is true the estimate

$$\|\Delta(x_0) - \Delta_k(x_0)\| \leq \frac{M \rho^{k+1}}{1 - \rho}. \quad (23)$$

Therefore, the vector field $V(\sigma, x_0)$ does not vanish anywhere on ∂X_0 . Indeed, from (22) and (23) implies that

$$\|V(\sigma, x_0)\| \geq \|\Delta_k(x_0)\| - \|\Delta(x_0) - \Delta_k(x_0)\| > 0. \quad (24)$$

The fields $\Delta_k(x_0)$ and $\Delta(x_0)$ are homotopic on ∂X and the rotations of the fields homotopic on the compact are equal. Hence, taking into account (24), we conclude that the rotation of the field $\Delta(x_0)$ on the ∂X_0 is equal to the index of the singular point x_0 of the field $\Delta_k(x_0)$ and nonzero. Consequently, the vector field $\Delta(x_0)$ on the X_0 has a singular point x_0 , for which $\Delta(x_0) = 0$. Therefore, the system of impulsive differential equations (1) has a periodic solution for all $t \in [0, T]$, $t \neq t_i$, $i = 1, 2, \dots, p$ that $x(0) \in X_0$. In addition, we note that for $x_0, \bar{x}_0 \in X$ from (20) and (21) we have

$$\|\Delta(x_0)\|_{PC} \leq M \left(1 + \frac{p}{T}\right),$$

$$\|\Delta(x_0) - \Delta(\bar{x}_0)\|_{BD} \leq \frac{|x_0 - \bar{x}_0|}{1 - \rho}.$$

Theorem is proved.

4. Conclusion

The theory of differential equations plays an important role in solving applied problems. Especially, nonlocal boundary value problems for differential equations with impulsive actions have many applications in mathematical physics, mechanics and technology, in particular in nanotechnology. In this paper, we investigated the system of first order differential equations (1) with periodical boundary value condition (2) and with nonlinear condition (3) of impulsive effects for $t = t_i$, $i = 1, 2, \dots, p$, $0 < t_1 < t_2 < \dots < t_p < T$. The nonlinear right-hand side of this equation consists of the construction of maxima. The questions of existence and uniqueness of the T -periodic solution of the boundary value problem (1)–(3) are studied. If the system (1) has a solution for all $t \in [0, T]$, $t \neq t_i$, $i = 1, 2, \dots, p$, then it is proved that this solution can be founded by the system of nonlinear functional-integral equations (13). The questions of existence of solution of the system of impulsive differential equations (1) we reduce to the questions of existence of zeros of function $\Delta(x_0)$ and we solve this problem finding zeros of the function $\Delta_k(x_0)$ in (21).

The results obtained in this work will allow us in the future to investigate another kind periodical boundary value problems for the heat equation and the wave equation with impulsive actions.

References

- [1] Benchohra M., Henderson J., Ntouyas S.K. *Impulsive differential equations and inclusions. Contemporary mathematics and its application.* Hindawi Publishing Corporation, New York, 2006.
- [2] Halanay A., Veksler D. *Qualitative theory of impulsive systems.* Mir, Moscow, 1971. 309 p. (in Russian).
- [3] Lakshmikantham V., Bainov D. D., Simeonov P. S. *Theory of impulsive differential equations.* World Scientific, Singapore, 1989. 434 p.
- [4] Perestyk N. A., Plotnikov V. A., Samoilenko A. M., Skripnik N. V. *Differential equations with impulse effect: multivalued right-hand sides with discontinuities.* DeGruyter Stud. 40, Math. Walter de Gruyter Co., Berlin, 2011.
- [5] Samoilenko A. M., Perestyk N. A. *Impulsive differential equations.* World Sci., Singapore, 1995.
- [6] Stamova I., Stamov G. *Impulsive biological models. In: Applied impulsive mathematical models.* CMS Books in Mathematics. Springer, Cham, 2016.
- [7] Catlla J., Schaeffer D. G., Witelski Th. P., Monson E. E., Lin A. L. On spiking models for synaptic activity and impulsive differential equations. *SIAM Review.* 2008, **50**(3), P 553–569.
- [8] Fedorov E. G., Popov I. Yu. Analysis of the limiting behavior of a biological neurons system with delay. *J. Phys.: Conf. Ser.*, 2021, **2086**, 012109.
- [9] Fedorov E. G., Popov I. Yu. Hopf bifurcations in a network of Fitzhugh-Nagumo biological neurons. *International Journal of Nonlinear Sciences and Numerical Simulation*, 2021.
- [10] Fedorov E. G. Properties of an oriented ring of neurons with the FitzHugh-Nagumo model. *Nanosystems: Phys. Chem. Math.*, 2021, **12**(5), P. 553–562.
- [11] Anguraj A., Arjunan M. M. Existence and uniqueness of mild and classical solutions of impulsive evolution equations. *Elect. J. of Differential Equations*, 2005, **2005**(111), 1–8.
- [12] Ashyralyev A., Sharifov Y. A. Existence and uniqueness of solutions for nonlinear impulsive differential equations with two-point and integral boundary conditions. *Advances in Difference Equations*, 2013, **2013**(173).
- [13] Ashyralyev A., Sharifov Y. A. Optimal control problems for impulsive systems with integral boundary conditions. *Elect. J. of Differential Equations*, 2013, **2013**(80), 1–11.
- [14] Bin L., Xinzhi L., Xiaoxin L. Robust global exponential stability of uncertain impulsive systems. *Acta Mathematica Scientia*, 2005, **25**(1), P. 161–169.
- [15] Mardanov M. J., Sharifov Ya. A., Habib M. H. Existence and uniqueness of solutions for first-order nonlinear differential equations with two-point and integral boundary conditions. *Electr. J. of Differential Equations*, 2014, **2014**(259), 1–8.
- [16] Sharifov Ya. A. Optimal control problem for systems with impulsive actions under nonlocal boundary conditions. *Vestnik samarskogo gosudarstvennogo tekhnicheskogo universiteta. Seria: Fiziko-matematicheskie nauki*, 2013, **33**(4), P. 34–45 (Russian).
- [17] Sharifov Ya. A. Optimal control for systems with impulsive actions under nonlocal boundary conditions. *Russian Mathematics (Izv. VUZ)*, 2013, **57**(2), P. 65–72.
- [18] Sharifov Y. A., Mammadova N. B. Optimal control problem described by impulsive differential equations with nonlocal boundary conditions. *Differential equations*, 2014, **50**(3), P. 403–411.
- [19] Sharifov Y. A. Conditions optimality in problems control with systems impulsive differential equations with nonlocal boundary conditions. *Ukrainian Math. Journ.*, 2012, **64**(6), P. 836–847.
- [20] Yuldashev T. K., Fayziev A. K. On a nonlinear impulsive differential equations with maxima. *Bull. Inst. Math.*, 2021, **4**(6), P. 42–49.
- [21] Yuldashev T. K., Fayziev A. K. On a nonlinear impulsive system of integro-differential equations with degenerate kernel and maxima. *Nanosystems: Phys. Chem. Math.*, 2022, **13**(1), P. 36–44.
- [22] Bai Ch., Yang D. Existence of solutions for second-order nonlinear impulsive differential equations with periodic boundary value conditions. *Boundary Value Problems (Hindawi Publishing Corporation)*, 2007, **2007**(41589), 1–13.
- [23] Chen J., Tisdell Ch. C., Yuan R. On the solvability of periodic boundary value problems with impulse. *J. of Math. Anal. and Appl.*, 2007, **331**, P. 902–912.
- [24] Li X., Bohner M., Wang Ch.-K. Impulsive differential equations: Periodic solutions and applications. *Automatica*, 2015, **52**, P. 173–178.
- [25] Hu Z., Han M. Periodic solutions and bifurcations of first order periodic impulsive differential equations. *International Journal of Bifurcation and Chaos*, 2009, **19**(8), P. 2515–2530.
- [26] Samoilenko A. M., Perestyuk N. A. Periodic solutions of weakly nonlinear impulsive systems. *Differentsial'nye uravneniya*, 1978, **14**(6), P. 1034–1045 (in Russian).

- [27] Ma R., Yang B., Wang Z. Bifurcation of positive periodic solutions of first-order impulsive differential equations. *Boundary Value Problems*, 2012, **2012**(83), 1–16.
- [28] Gladilina R. I., Ignatyev A. O. On the stability of periodic impulsive systems. *Math. Notes*, 2004, **76**(1), P. 41–47.

Submitted 8 March 2022; revised 26 March 2022; accepted 2 April 2022

Information about the authors:

T. K. Yuldashev – National University of Uzbekistan, University street, 4, NUUZ, Tashkent, 100174, Uzbekistan; tursun.k.yuldashev@gmail.com

Conflict of interest: the authors declare no conflict of interest.

Three-dimensional extremely short optical pulses in a phonic crystal with a superlattice

Yu. V. Dvuzhilova^a, N. G. Glazkova, I. S. Dvuzhilov, I. V. Zaporotskova, M. B. Belonenko^b

Volgograd State University, Volgograd, 400062, Russia

^advuzhilov.ilya@volsu.ru, ^bmbelonenko@yandex.ru

Corresponding author: Yu. V. Dvuzhilova, dvuzhilov.ilya@volsu.ru

PACS 42.65.Tg

ABSTRACT Based on Maxwell's equations in Coulomb calibration, which describe the dynamics of extremely short optical pulses in a photonic crystal with a three-dimensional superlattice connected by strong tunneling along one axis, a phenomenological equation was obtained in the form of the classical 2 + 1-dimensional sine-Gordon equation with variable coefficients for the case of cylindrical symmetry. The steady propagation of such pulses is established, as well as the dependence of the evolution of these pulses on the parameters of the photonic crystal.

KEYWORDS superlattice, extremely short optical pulses, photonic crystal.

ACKNOWLEDGEMENTS Yu. V. Dvuzhilova, I. S. Dvuzhilov and M. B. Belonenko thank the Ministry of Science and Higher Education of the Russian Federation for the numerical modeling and parallel computations support under the government task (0633-2020-0003).

FOR CITATION Dvuzhilova Yu.V., Glazkova N.G., Dvuzhilov I.S., Zaporotskova I.V., Belonenko M.B. Three-dimensional extremely short optical pulses in a phonic crystal with a superlattice. *Nanosystems: Phys. Chem. Math.*, 2022, **13** (2), 142–147.

1. Introduction

One of the key tasks of nonlinear optics, nanophotonics and nanoelectronics and, as a consequence, based on their latest advances in science and technology, is to reduce the size of structural elements of devices, as well as to create new materials with which it will be possible to control the parameters of optical signals, as well as create their basis is the system of transmission, processing and storage of data. One of the suitable materials are the so-called superlattices. These are structures in which, in addition to the lattice, there is an artificially created potential (with a period significantly exceeding the lattice period) acting on electrons. Thus, it is possible to control the zone spectrum. One of the simplest ways to create a superlattice is the formation of a periodic system of quantum wells in a solid, which are bound by the tunnel effect, and as a result, collectivized states of electrons with a particular law of dispersion are formed. In this case, it is possible to control the size of the mini-zone, due to changes in the distance between quantum wells [1, 2].

As a medium for the formation of a superlattice, a photonic crystal with a spatially variable refractive index can be used. The choice of a system of quantum wells with tunneling as a material for a photonic crystal is due to the non-parabolic law of electron dispersion, which in turn determines the non-linearity of the response to the influence of electromagnetic moderate strengths, starting from the values of 10^3 – 10^4 V/cm [3, 4]. It should be noted that the inhomogeneity of the photonic crystal provides an ideal medium for the propagation of extremely short optical pulses, light bullets, and other soliton – like states [5–7].

Let us pay attention to three-dimensional extremely short optical pulses, which are localized in space electric field pulses with a duration corresponding to several periods of field oscillation, and all the energy of which remains concentrated in a finite limited region of space [8, 9].

The study of the propagation of electromagnetic pulses in photonic crystals is of great theoretical and practical importance in modern nonlinear optics and nanophotonics, so the problem considered in this paper is very relevant [10].

2. Physical model and basic equations

The geometry of the problem (Fig. 1) assumes that the current, the applied electric field, and the electric field of the pulse are directed along the *OY* axis, and the pulse moves along the *OZ* axis. Quantum dots form a system of quantum wells placed in a photonic crystal. It is assumed that the tunneling between quantum wells along the *OX* and *OZ* axes is small and can be neglected. It should be noted that the paper considers pulses containing few electromagnetic field cycles (1–5), so the longitudinal size of the wave packet is only a small number of wavelengths. That is, the wave packet under consideration is a light pancake with transverse dimensions significantly exceeding the longitudinal ones.

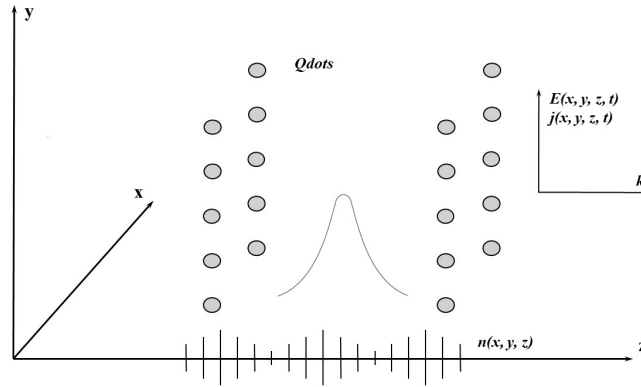


FIG. 1. Problem geometry

The Hamiltonian of a system of electrons, taking into account the geometry presented above can be represented in the form:

$$H = \sum_{jkl} t_0 a_{jkl\sigma}^+ a_{jkl\sigma} + t \left(a_{jkl\sigma}^+ a_{jkl\sigma+1} + a_{jkl\sigma+1}^+ a_{jkl\sigma} \right) \quad (1)$$

where $a_{jkl\sigma}^+$ and $a_{jkl\sigma}$ – are the electron creation and annihilation operators in the quantum well with coordinates j, k, l along the axes OX, OY , and OZ , respectively, t_0 – is the electron energy of the quantum well, t – is the tunneling integral determined by overlapping of the electron wave functions in adjacent wells.

Thanks to the Fourier transform for the operators $a_{jkl\sigma}^+$ and $a_{jkl\sigma}$, one can diagonalize the Hamiltonian H from (1) and obtain the dispersion relation for electrons in the superlattice, which is clearly shown, for example, in [3, 4, 15]:

$$\varepsilon(p) = t_0 + 2t \cdot \cos(ap), \quad (2)$$

where p – angular momentum, which is directed along the OY axis, a – the distance between adjacent quantum wells (along the OY axis).

It can be noted that a spectrum similar to (2) can be recorded under the conditions of electron-electron and electron-photon interactions, if t_0 and t are understood as the corresponding renormalized constants.

Using Maxwell's equations, using the Coulomb gauge ($E = -\partial A/c\partial t$), the equation for the vector potential of the electromagnetic field of a three-dimensional extremely short optical pulse propagating inside a photonic crystal with a superlattice, in accordance with the geometry (Fig. 1), presented above will have the form [11]:

$$\frac{\partial^2 \mathbf{A}}{\partial x^2} + \frac{\partial^2 \mathbf{A}}{\partial y^2} + \frac{\partial^2 \mathbf{A}}{\partial z^2} - \frac{n^2(x, y, z)}{c^2} \frac{\partial^2 \mathbf{A}}{\partial t^2} + \frac{4\pi}{c} \mathbf{j} = 0, \quad (3)$$

where $A = (0, A(x, y, z, t), 0)$ – vector potential of the pulse electric field, $j = (0, j(x, y, z, t), 0)$ – electric current density, $n(x, y, z)$ – spatial change in refractive index, c – speed of light.

When constructing a model for the propagation of an extremely short pulse in a photonic crystal based on a superlattice, the following approximations were used: the electric field of the substrate is not taken into account; the continuum approximation is used; the length at which the refractive index of the photonic crystal changes is much larger than the spatial size of the pulse localization region; the Coulomb gauge is used to describe the magnetic and dielectric properties of the medium.

Since the typical relaxation time for electrons can be estimated as 10^{-12} – 10^{-13} s [12]. The following approximation was used in equation (3): we neglected the term responsible for the inhomogeneity of the electron distribution function along the z axis. This is due to the general statement of the problem, in which the initial conditions along the z axis are chosen to be homogeneous, and the effects associated with the inhomogeneity of the electromagnetic field along this axis were not taken into account. In our opinion, this is justified by the introduced assumption about the homogeneity of the laser radiation wavefront.

The evolution of an ensemble of particles will be described by the classical kinetic Boltzmann equation in the relaxation time approximation:

$$\frac{\partial f}{\partial t} - \frac{q}{c} \frac{\partial A}{\partial t} \frac{\partial f}{\partial p} = \frac{F_0 - f}{\tau}, \quad (4)$$

where f – distribution function that has an implicit dependence on the coordinate; F_0 – Fermi distribution function, τ – relaxation time, q – charge, A – component of the vector potential of the electric field of the pulse.

For the current density, we use the standard expression [3]:

$$j = 2e \sum_{s=1}^m \int_{ZB} v_s(p) \cdot f(p, s) dp, \quad (5)$$

where the group velocity of electrons is introduced $v_s(p) = \frac{\partial \varepsilon_s(p)}{\partial p}$, $\varepsilon_s(p)$ – dispersion law describing the electronic properties of a system of quantum wells (equation (2)), e – electron charge. Integration is carried out over the first Brillouin zone.

Taking into account the formula for the current density (equation 5), we can obtain the generalized sine-Gordon equation [13], which describes the dynamics of an extremely short optical pulse in a photonic crystal with a superlattice:

$$\begin{aligned} \frac{\partial^2 A}{\partial x^2} + \frac{\partial^2 A}{\partial y^2} - \frac{n^2(x, y, z)}{c^2} \frac{\partial^2 A}{\partial t^2} + \frac{qb}{\pi h \tau} \sin\left(\frac{aq}{c} A\right) &= 0, \\ b &= \int_{-q_0}^{q_0} dp \cdot \cos(ap) F_0(p), \\ F_0(p) &= \frac{1}{1 + \exp\{\varepsilon(p)/k_b T\}}, \end{aligned} \quad (6)$$

where k_b – Boltzmann constant, T – temperature, q_0 – boundaries of the first Brillouin zone.

A detailed derivation of equation (6) is shown in earlier works of the authors [14, 15]. Since the effect of charge accumulation can be neglected [16], it can be assumed that the cylindrical symmetry in the field distribution is preserved. Taking into account the above, the final equation for the vector potential in a cylindrical coordinate system will take the form:

$$\begin{aligned} \frac{\partial^2 A}{\partial z^2} + \frac{1}{r} \frac{\partial}{\partial r} \left(r \frac{\partial A}{\partial r} \right) - \frac{n^2(z, r)}{c^2} \frac{\partial^2 A}{\partial t^2} + \frac{qb}{\pi h \tau} \sin\left(\frac{aq}{c} A\right) &= 0, \\ r &= \sqrt{x^2 + y^2}. \end{aligned} \quad (7)$$

The initial conditions for the vector potential correspond to the Gaussian profile of the pulse for one oscillation of the electric field and the refractive index of the medium of a photonic crystal made of CNTs are set as follows:

$$\begin{aligned} A_{t=0} &= A_0 \exp\left\{-\frac{r^2}{\gamma^2}\right\} \exp\left\{-(z - z_c)^2 / \beta^2\right\}, \\ \left. \frac{dA}{dt} \right|_{t=0} &= \frac{2vz}{\gamma^2} A_0 \exp\left\{-\frac{r^2}{\gamma^2}\right\} \exp\left\{-(z - z_c)^2 / \beta^2\right\}, \\ n(z, r) &= 1 + \alpha \cos(2\pi z / \chi). \end{aligned}$$

Here β, γ – parameters defining the pulse width of the axes z and r , respectively, A_0 – initial pulse amplitude, v – initial pulse velocity when entering the medium, z_c – start coordinate, α – refractive index modulation depth, χ – refractive index modulation period.

3. Numerical simulation results

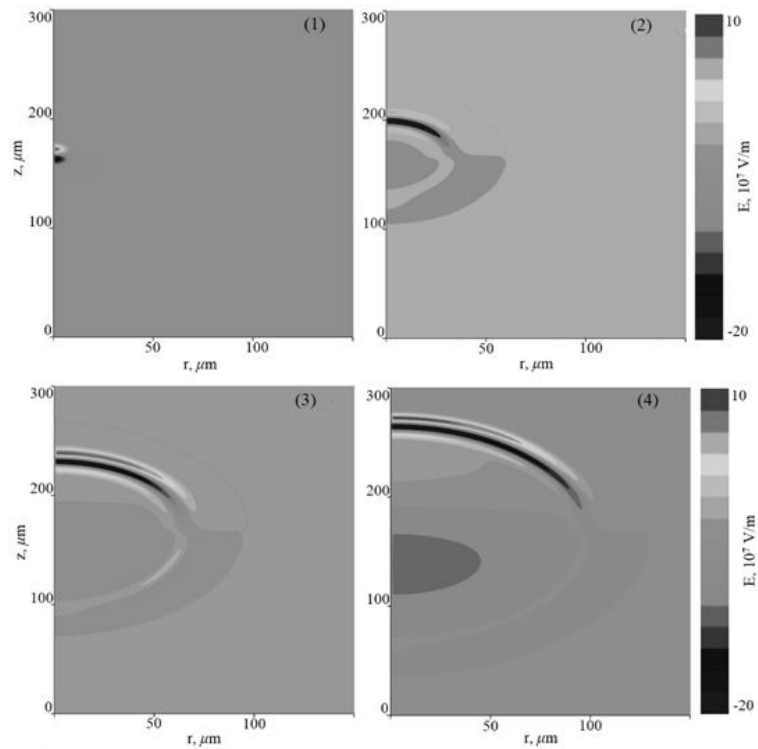
The investigated equation (7) was solved numerically using an explicit difference scheme of the “cross” type [17]. In numerical simulation of the system under study, its parameters were chosen as follows: $m = 13$, $T = 293$ K, relaxation time in the superlattice $\approx 10^{-11}$ s; pulse duration $\approx 10^{-14}$ s. The values of the parameters that determine the pulse width, as well as the initial pulse velocity upon entering the medium, were set as follows ($\beta = \gamma = \sqrt{1 - v^2}$, $v = 0.95c$).

The evolution of an electromagnetic field pulse during its propagation in a medium with a spatially variable refractive index (photonic crystal) with a superlattice, in the case of one electric field oscillation, is shown in Fig. 2.

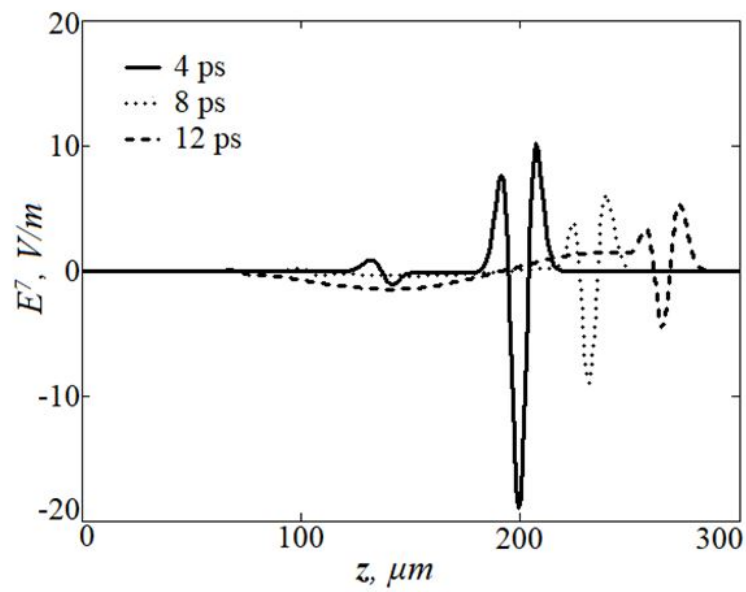
The figure presented earlier, we can conclude that the pulse energy remains localized in a limited spatial area, that the impulse spreads steadily. However, due to diffraction and dispersion effects, there is a damping effect, and a “tail” appears at the trailing edge.

The evolution of a three-dimensional extremely short optical pulse, at a time instant of 4 ps, in a photonic crystal with a superlattice, with various parameters of the photonic crystal, is shown in Fig. 3,4.

It can be seen from Fig. 3,4 that, by changing the modulation depth of the refractive index, the pulse shape changes, but its energy remains in a limited spatial region. In turn, by varying the modulation period of the refractive index, it is possible to control the change in the group velocity of the wave packet of an extremely short optical pulse. Moreover, the longer the period, the faster the impulse spreads. This is due to the fact that the processes of reflection and interference occur less frequently. Note that from a practical point of view, this result is important because it allows one to control the pulse rate by changing the parameters of the photonic crystal. At the same time, the propagation of extremely short optical pulses in a photonic crystal with a superlattice has a number of important differences from the case of a medium with a constant refractive index. Perhaps the most important difference is that pulses in such a medium have a more complex



(A)



(B)

FIG. 2. Problem geometry A) Dynamics of a three-dimensional extremely short optical pulse in a photonic crystal with a superlattice, at different times (refractive index modulation parameters: modulation depth $\alpha = 0.1$; modulation period $\chi = 2.5 \mu\text{m}$): 1) 0.2 ps, 2) 4 ps, 3) 8 ps, 4) 12 ps; B) Cuts of an extremely short optical pulse at different times (4 ps, 8 ps, 12 ps)

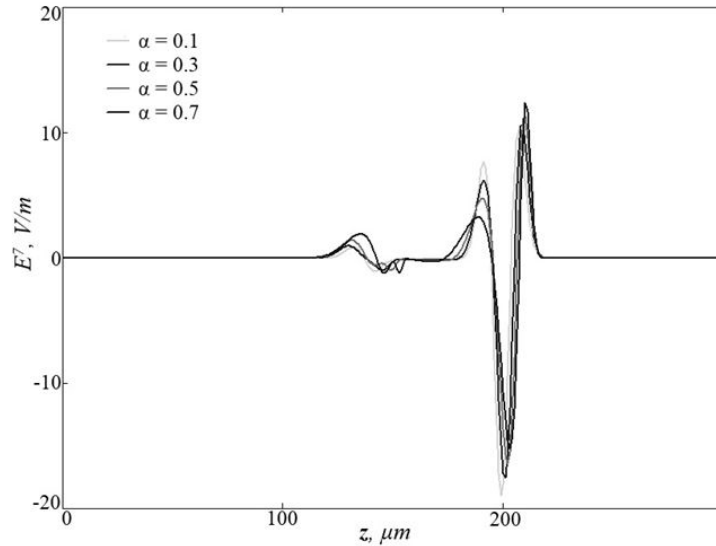


FIG. 3. Sections of a three-dimensional extremely short optical pulse in a photonic crystal made of CNTs with a superlattice, at a time instant of 4 ps, with different values of the modulation depth of the refractive index, at a fixed modulation period $\chi = 2.5 \mu\text{m}$: $\alpha = 0.1, 0.3, 0.5, 0.7$

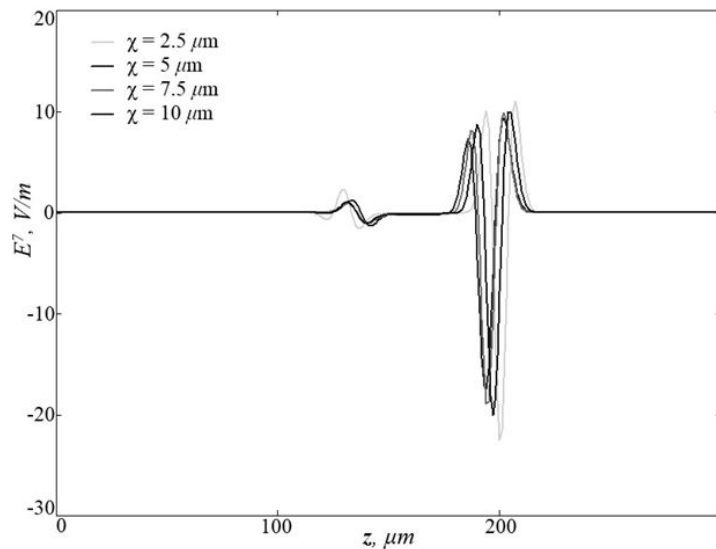


FIG. 4. The dynamics of propagation of a three-dimensional extremely short optical pulse in a photonic crystal of CNTs with a superlattice, at a time instant of 4 ps, with different values of the refractive index modulation period, at a fixed modulation depth $\alpha = 0.3$: $\chi = 2.5 \mu\text{m}, 5 \mu\text{m}, 7.5 \mu\text{m}, 10 \mu\text{m}$

transverse structure, which, in our opinion, is associated with the excitation of internal vibration modes of an extremely short pulse when interacting with an inhomogeneity of the refractive index of the medium.

The influence of the parameters of a photonic crystal on the shape and group velocity of the wave packet of an extremely short pulse has been repeatedly tested for extremely short pulses and light bullets of various initial shapes, including Gaussian, super-Gaussian, as well as on diffractionless pulses, Bessel and Airy cross sections, in the case of carbon nanotubes with a similar dispersion law for electrons [18–20].

4. Conclusions

1. A physical model was constructed that describes the dynamics of a three-dimensional extremely short optical pulse in a photonic crystal with a superlattice (a system of quantum wells that are coupled by tunneling).

2. It was found that pulses in such a medium propagate stably, keeping their energy in a limited spatial region. The shape of the pulse undergoes insignificant changes; after its passage, a “tail” is formed, due to the influence of dispersion and diffraction effects.

3. The period and depth of modulation of the refractive index affect the shape and group velocity of an extremely short optical pulse.

The results obtained in this work are important from a theoretical and practical point of view, since they can be applied to create, for example, all-optical delay lines, as well as form the basis of the elemental base of optoelectronic and nanoelectronic devices, storage devices, transmission and processing of data, which in its turn is relevant for infocommunication technologies.

References

- [1] Bass F.G., Bulgakov A.A., Tetervov A.P. *High-Frequency Properties of Semiconductors with Superlattices*. Nauka, Moscow, 1989.
- [2] Voos M. Some properties of semiconductor superlattices. *Ann. Telecommun.*, 1988, **43**(7), P. 357–364.
- [3] Belonenko M.B., Demushkina E.V., Lebedev N.G. Electromagnetic solitons in a system of carbon nanotubes. *J. Rus. Las. Res.*, 2006, **27**, P. 457.
- [4] Zhukov A.V., Bouffanais R., et. al. Two-dimensional extremely short electromagnetic pulses in a Bragg medium with carbon nanotubes. *Eur. Phys. J. D.*, 2015, **69**, P. 129.
- [5] Mekis A., Chen J.C., et. al. High Transmission through Sharp Bends in Photonic Crystal Waveguides. *Phys. Rev. Lett.*, 1996, **77**(18), P. 3787–3790.
- [6] Tokushima M., Kosaka H., Tomita A., Yamada H. Lightwave propagation through a 120 sharply bent single-line-defect photonic crystal waveguide. *Appl. Phys. Lett.*, 2000, **76**(8), P. 952–954.
- [7] Sazonov S.V., Ustinov N.V. Propagation of few-cycle pulses in a nonlinear medium and an integrable generalization of the sine-gordon equation. *Phys. Rev. A*, 2018, **98**(6), 063803(1–12).
- [8] Fibich G., Ilan B. Optical light bullets in a pure Kerr medium. *Opt. Lett.*, 2004, **29**(8), P. 887–889.
- [9] Goorjian P.M., Silberberg Y. Numerical simulations of light bullets using the full-vector time-dependent nonlinear Maxwell equations. *J. Opt. Soc. Am. B.*, 1997, **14**(11), P. 3253–3260.
- [10] Fedorov E.G., Zhukov A.V., et. al. Asymptotic dynamics of three-dimensional bipolar ultrashort electromagnetic pulses in an array of semiconductor carbon nanotubes. *Opt. Express*, 2019, **27**(20), P. 27592–27609.
- [11] Landau L.D. and Lifshitz E.M. *Field Theory* [in Russian]. Nauka, Moscow, 1988.
- [12] Grahn H.T., Klitzing K., Ploog K., et al. Electrical transport in narrow-miniband semiconductor superlattices. *Phys. Rev. B*, 1991, **43**, 12095.
- [13] Li P., Mihalache D., Malomed B.A. Optical solitons in media with focusing and defocusing saturable nonlinearity and a parity-time-symmetric external potential. *Phil. Trans. R. Soc. A.*, 2018, **376**(2124), 20170378.
- [14] Belonenko M.B., Meshcheryakova N.E. Electromagnetic solitons in a system of quantum dots taking into account the Hubbard interaction. *J. of Rus. Las. Res.*, 2008, **29**(1), P. 544–550.
- [15] Fedorov E.G., Konobeeva N.N., Belonenko M.B. Extremely short electromagnetic pulse in a superlattice taking into account field inhomogeneity along its axis. *Semiconductors*, 2014, **48**(10), P. 1348–1352.
- [16] Zhukov A.V., Bouffanais R., Fedorov E.G., Belonenko M.B. Three-dimensional electromagnetic breathers in carbon nanotubes with the field inhomogeneity along their axes. *J. Appl. Phys.*, 2013, **114**(14), 143106.
- [17] Bahvalov N.S. *Numerical methods* (analysis, algebra, ordinary differential equations) [in Russian]. Nauka, Moscow, 1975.
- [18] Belonenko M.B., Dvuzhilov I.S., Tuzalina O.Yu. Two-dimensional Few-circle Optical Pulses in the Inhomogeneous Environment of Carbon Nanotubes. *J. Nano-Electron. Phys.*, 2015, **7**(4), 04013.
- [19] Belonenko M.B., Dvuzhilov I.S., Galkina E.N., Nevzorova Y.V. Three-dimensional few cycle optical pulses in nonlinear medium with carbon nanotubes. *Mod. Phys. Lett. B.*, 2016, **30**(28), 1650345.
- [20] Dvuzhilova Y.V., Dvuzhilov I.S., Ten A.V. et al. Three-dimensional few-cycle optical pulses of Gaussian and super-Gaussian cross-section inside the Bragg medium based on carbon nanotubes with dissipation. *Mod. Phys. Lett. B.*, 2019, **33**(23), 1950275.

Submitted 1 February 2022; revised 18 April 2022; accepted 19 April 2022

Information about the authors:

Yu. V. Dvuzhilova – Volgograd State University, Universitetsky, 100, Volgograd, 400062, Russia; dvuzhilov.ilya@volsu.ru

N. G. Glazkova – Volgograd State University, Universitetsky, 100, Volgograd, 400062, Russia;

I. S. Dvuzhilov – Volgograd State University, Universitetsky, 100, Volgograd, 400062, Russia;

I. V. Zaporotskova – Volgograd State University, Universitetsky, 100, Volgograd, 400062, Russia;

M. B. Belonenko – Volgograd State University, Universitetsky, 100, Volgograd, 400062, Russia; mbelonenko@yandex.ru

Conflict of interest: the authors declare no conflict of interest.

Impact of the channel shape, back oxide and gate oxide layers on self-heating in nanoscale JL FINFET

A. E. Atamuratov^{1,a}, B. O. Jabbarova^{1,b}, M. M. Khalilloev^{1,c}, A. Yusupov^{2,d}, K. Sivasankaran^{3,e}, J. C. Chedjou^{4,f}

¹Urgech State University, Urgench, 220100, Uzbekistan

²Tashkent University of Information Technologies, Tashkent, 100200, Uzbekistan

³Vellore Institute of Technology, Vellore, Tamilnadu, India

⁴University of Klagenfurt, Klagenfurt, 9020, Austria

^aatabek.atamuratov@yahoo.com, ^bbahorbahor1989@mail.ru, ^cx-mahkam@mail.ru,

^dayus@mail.ru, ^eksivasankaran@vit.ac.in, ^fjean.chedjou@aau.at

Corresponding author: A. E. Atamuratov, atabek.atamuratov@yahoo.com

PACS 85.30.Tv

ABSTRACT We study the impact of channel shape, back oxide, and gate oxide on the self-heating performance in nanoscale junctionless Fin Field Effect Transistor through numerical simulation. The role of back oxide and gate oxide layers in setting the channel temperature is compared. Simulation results show that in the case of hafnium oxide (HfO₂) as the gate oxide and silicon dioxide (SiO₂) as the back oxide, the main role in setting the channel temperature corresponds to the base width of the channel that is in contact with the back oxide layer.

KEYWORDS self-heating effect, junctionless FinFET, channel shape, channel temperature.

ACKNOWLEDGEMENTS This research was funded by the Ministry of Innovative Development of the Republic of Uzbekistan in the frame of joint Uzbek-Indian project Uzb-Ind-2021-80.

FOR CITATION Atamuratov A.E., Jabbarova B.O., Khalilloev M.M., Yusupov A., Sivasankaran K., Chedjou J.C. Impact of the channel shape, back oxide and gate oxide layers on self-heating in nanoscale JL FINFET. *Nanosystems: Phys. Chem. Math.*, 2022, **13** (2), 148–155.

1. Introduction

Over the last few decades, the capabilities of metal-oxide-semiconductor field effect transistor (MOSFET) characteristics have adapted to a variety of CMOS integrated circuit (IC) applications [1–4] and have led to various new requirements for MOSFET characteristics and parameters. One of these requirements is the increasing degree of the integration and the reduction in IC power consumption. This requirement is mainly related to the reduction in size of the transistors included in the IC as a component. MOSFET, especially junctionless (JL) MOSFET [5], is one of the widely used transistor ICs. Currently, most transistor structures are based on JL transistors such as bulk planar BPJLT, double gate JL transistors, multi-gate JL transistors, silicon on insulator (SOI) JL transistors, and gate all around JL transistors. When the MOSFET sizes are reduced, the various types of degradation effects, for example short channel effects and random telegraph noise, are increased [6, 7]. In order to reduce the short-channel effects, the triple-gate Fin Field Effect Transistor (FinFET) [8] and then the JL-FinFET [9] based on SOI technology were proposed. In these transistors, the back oxide is in contact with the channel and it has considerably low thermal conductivity relative to the silicon substrate, which is generally used in bulk MOSFETs. This leads to an accumulation of heating in the transistor channel (self-heating effect (SHE)) [10]. The SHE influences the drain current and changes the characteristics of the transistor. For the SHE in FinFETs, various methods and the structures of transistors able to reduce this effect were considered in many works [11–15]. In [11], the charge plasma (CP) based JL MOSFET on a selective buried oxide (SELBOX-CPJLT) is proposed. This approach is used to reduce the SHE presented in SOI-based devices. The proposed device shows better thermal efficiency compared to SELBOX-JLT, which has not charge plasma. The impact of the Gaussian channel doping profile (GCD) in enhancing the double gate (DG) JL MOSFET reliability against SHE is presented in [12]. It is found that the amended channel doping has a profound implication in improving both the device's electrical performance and the reliability against the undesired SHE. The role of the gate oxide layer in the SHE was considered in [13]. The SHE for a vacuum gate dielectric (VGD) tri-gate FinFET versus a high-k (HK) tri-gate dielectric FinFET were investigated. Simulation results show that the VGD device has fiercer SHEs than the HK device, resulting in greater saturation current degradation. This is due to the low thermal conductivity of the gas around the channel, which impedes the heat diffusion to the sinks and increases the peak temperature in the hot spot region. The influence of the material of the back oxide layer

on the SHE was considered in [14]. In this work, aluminum nitride is used as the back oxide in a Si MOSFET (SOAN MOSFET) and a strained Si/SiGe layer is formed on a SOAN substrate called SGSOAN nMOSFET. Further, the thermal properties of SGSOAN nMOSFET and SGOI nMOSFET with different channel expansions/dimensions are compared.

In Ref. [15], a device structure called an undoped buried region MOSFET (UBR-MOSFET) by introducing a region that acts as an undoped region under the channel and an oxide buried only under the source and drain regions was simulated to examine the current of drain and temperature distribution due to SHE. The higher thermal conductivity of the UBR region is shown to lead to more efficient heat dissipation.

Other interesting works have also considered the influence of channel shape on the performance of FinFET and JL FinFET [16–19]. In [16], it is shown that the transistor threshold voltage dependence on the channel doping concentration is different for different JL FinFET channel shapes. This is attributed to stronger gate coupling, since the gate plane is closer to the bottom of the channel with the non-vertical sidewalls of the triangular fin device compared to the rectangular fin device. The effect of fin shape on the thermal resistance of the proposed irregular SOI FinFET is analyzed in [17]. It is shown that the SHE can be controlled by regulating the corner effect by using the rounded shape of edges.

Overall, analysis of the literature related to SHE in FinFET and particularly in JL FinFET shows that the influence of the shape of the channel on SHE has not been taken into account, whereas in the nanoscale JL FinFETs, the variability of the shape of the channel can take place. To investigate this very important issue, which is not covered in the literature, this work uses a 3D simulation to compare the role of the gate oxide and back oxide layers in SHE in nanometer size JLFinFETs with different channel shapes.

This paper is organized as follows: Section 2 analyzes the different shapes of the JL FinFETs and provides a clear definition of the parameter settings that are used for the simulation. Section 3 focuses on both the presentation and discussion of the simulation results. Finally, in Section 4, important concluding remarks are formulated.

2. Device structure and simulation setup

In order to compare the influence of the back oxide and gate oxide layers on the SHE in nanoscale JL FinFETs, the devices with different channel shapes and constant cross-sectional areas are considered for the study. Two groups of junctionless FinFETs are considered for the study. In the first group, the transistors with a rectangular cross-section, different thickness T_{Si} and width, but with a constant cross-sectional area were considered, as shown in Fig. 1.

In the second group, the channel base width W_{Si} and cross-section area are constant, while the shape of the channel cross-section is changed from a rectangle to a trapezoid shape, as shown in Fig. 2. The ratio of channel thickness to the channel base width (T_{Si}/W_{Si}) is used as a parameter that reflects the channel shape. The structures shown in Fig. 1 and Fig. 2 are designed and simulated using Sentaurus TCAD 3D device simulator [20]. Along with the default model, the models for mobility degradation were included in order to take into account the mobility dependency on the doping concentration.

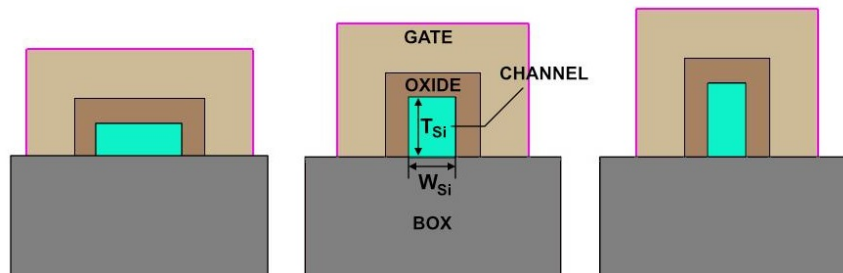


FIG. 1. Schematic of JL FinFETs with rectangle channel cross-section shape, the different ratio between width and thickness of the channel, and constant area of the cross-section

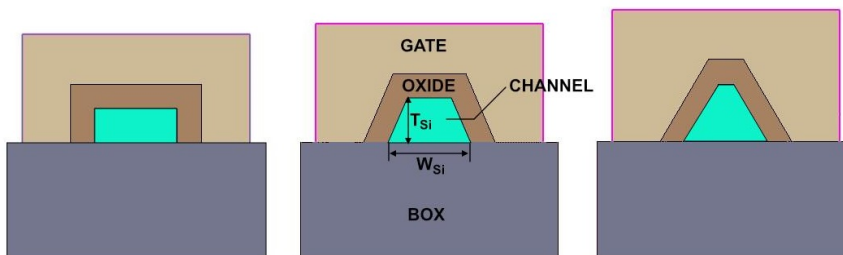


FIG. 2. Structures of simulated JL FinFETs with rectangle and trapezoid channel cross-section shape, constant area of the channel cross-section and base width, while the different thickness of the channel

For the simulation, scattering due to impurities and the effect of high fields to take into account the velocity saturation of charge carriers as well as the effect of the normal component of the field to take into account the effect of the interface on the drain current are considered. To account for the SHE, the thermodynamic transport model and the Shockley–Reed–Hall recombination model were used. Since we used a dielectric with high dielectric permittivity as the gate dielectric, the relevant mobility degradation model, the Lombardi model was used, which includes empirical degradation terms accounting for remote Coulomb scattering and remote phonon scattering. A quantum correction with regard to the density gradient is used in both drift-diffusion and thermodynamic models [21]. The device and the model used were calibrated based on the experimental results reported in [22]. The parameters considered for the simulation are shown in Table 1 and the transfer characteristics are depicted in Fig. 3. This device's parameters mainly correspond to the CMOS technology node of 10 nm.

TABLE 1. Parameters considered for Device Simulation

Parameters	Designation	Values
Si channel doping level	N_{sub}	$5 \cdot 10^{18} \text{ cm}^{-3}$ (n-type)
Thickness of HfO_2 gate oxide layer	t_{ox}	6.7 nm ($t_{eqv} = 1.2$ nm)
Channel thickness	T_{si}	9–22 nm
Width of the channel base	W_b	22–5 nm
The thickness of the SiO_2 back oxide layer	T_{box}	145 nm
Width of the SiO_2 back oxide layer	W_{box}	69.4 nm
TiN Gate length	L_{gate}	10 nm

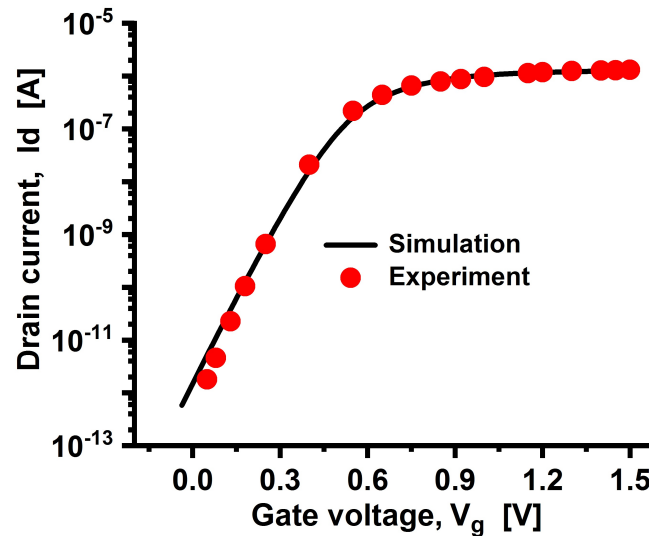


FIG. 3. Transfer characteristics of simulated and experimental transistors taken from [22], with the same geometries and parameters

3. Results and discussion

The main source of heat dissipation in the channel is Joule heat, which depends on the current in the channel. The main components of the channel are the drift current J_{dr} , the diffusion current J_{dif} , and the thermic current J_t . To understand the impact of geometrical and physical parameters on SHE, we consider nanoscale JLFinFETs of both transistor groups.

3.1. Performance analysis of nanoscale JL FinFET with rectangular channel

The resulting current density in the middle of the channel for different T_{Si}/W_{Si} is shown in Fig. 4a. Fig. 4b shows the simulation result of the electric field dependence on T_{Si}/W_{Si} , concentration, and temperature gradient for the different ratios of T_{Si}/W_{Si} shown in Fig. 4c.

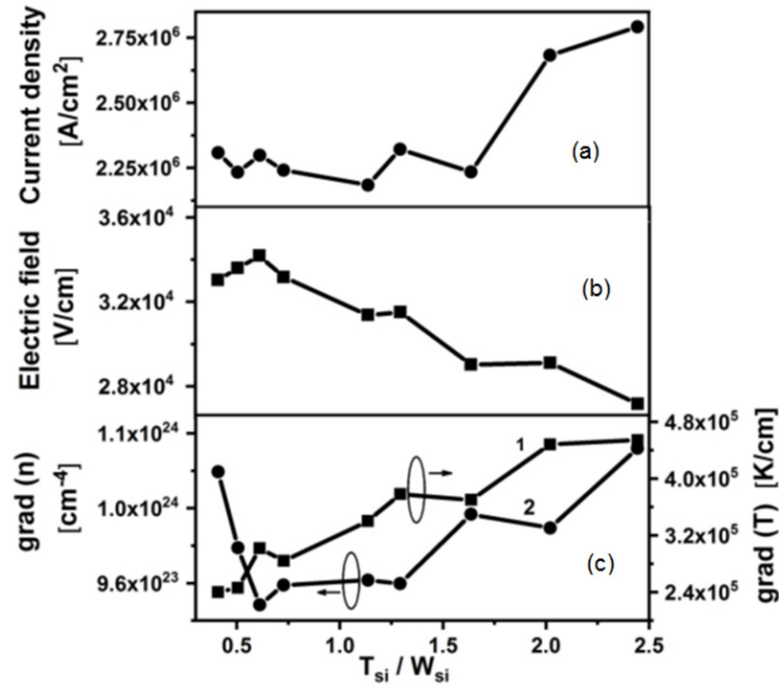


FIG. 4. (a) current density, (b) electric field, (c) concentration gradient (curve 1), and temperature gradient (curve 2) as a function of T_{Si}/W_{Si} in the center of the channel

The dependences shown in Fig. 4 were carried out from the distribution of the field, concentration, and temperature along the center of the channel. Typical distributions, for example for $T_{Si}/W_{Si} = 0.4$ are shown in Fig. 5. Based on the dependences shown in Fig. 4 all types of density currents were estimated. For example, for $T_{Si}/W_{Si} = 1.3$, the densities of drift current (j_E), diffusion current ($j_{\Delta n}$), and thermal current ($j_{\Delta T}$) are calculated from equations (1)–(3):

$$j_E = en\mu E, \quad (1)$$

$$j_{\Delta n} = eD \frac{\Delta n}{\Delta x}, \quad (2)$$

$$j_{\Delta T} = \sigma S \frac{\Delta T}{\Delta x}. \quad (3)$$

In equations (1)–(3), e is the elementary charge, n stands for the carrier concentration, μ represents the electron mobility, D is the diffusion coefficient of electrons in silicon, σ the conductivity of silicon, and S stands for the Seebeck coefficient for silicon.

The calculation has led to the values $j_E = 6.98 \cdot 10^6$ A/cm², $j_{\Delta n} = 4.83 \cdot 10^6$ A/cm², and $j_{\Delta T} = 3.78 \cdot 10^2$ A/cm². It is observed that the thermal current density is several orders of magnitude lower than the other two types of current density. It can therefore be taken into account that the main contribution to the resulting current density has a drift current (lower inset in Fig. 5) and a diffusion current (upper inset in Fig. 5), which have the same order of values.

In Fig. 5, it can be seen that the concentration gradient has two components with opposite directions and different values. This is related to the different influences of the normal (vertical) gate field at the source and drain end on the drain current. In fact, one component is directed along (J_{n+}) and the second one is directed opposite (J_{n-}) to the field between source and drain (upper insertion in Fig. 5). The estimations show that the resulting diffusion current ($J_n = J_{n+} - J_{n-}$) is directed opposite to the drift current. The resulting channel current is therefore defined as the difference between the drift and the resulting diffusion current.

A comparison of the dependencies in Fig. 4 shows that the increase in the current density at a high T_{Si}/W_{Si} is due to an increase in the diffusion current. It can be seen that the current density is increased for transistors with T_{Si}/W_{Si} greater than 1.75, while the lattice temperature in the middle of the channel increases monotonically in all ranges with increasing T_{Si}/W_{Si} (Fig. 6), which is not appropriate to the current density dependence on T_{Si}/W_{Si} .

Our findings allow the conclusion that the resulting current density in the channel is not only the main factor for the dependence of the lattice temperature on the channel shape. It is mainly related to the structure's capability/ability to dissipate heat and not just to the power of the heat source. The main routes for heat dissipation from the center of the channel are through the back oxide layer and the gate oxide layer. These heat dissipation capabilities can be expressed by the formula (see Eq. (4)) of the dependence of the temperature change in a channel on the thickness of the back oxide

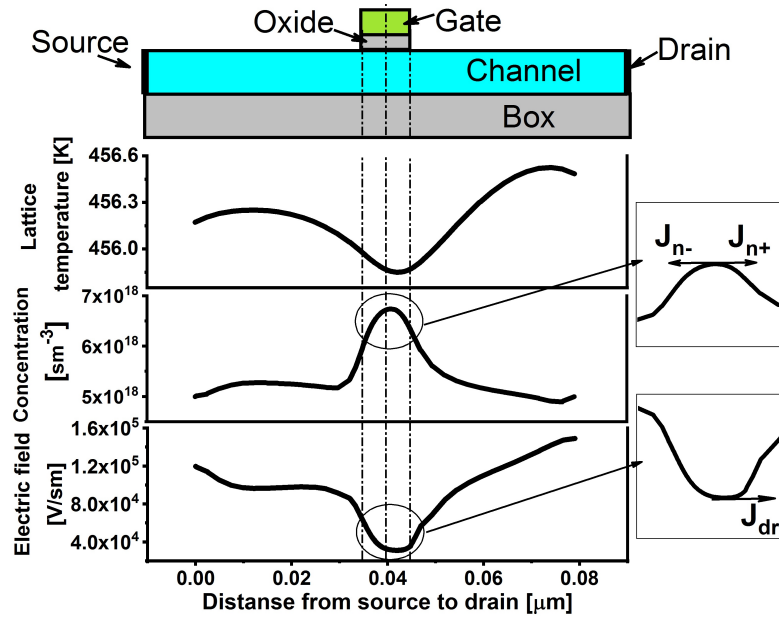


FIG. 5. Typical distribution of the temperature, electron concentration, and the field along the middle of the channel. $T_{Si}/W_{Si} = 0.4$

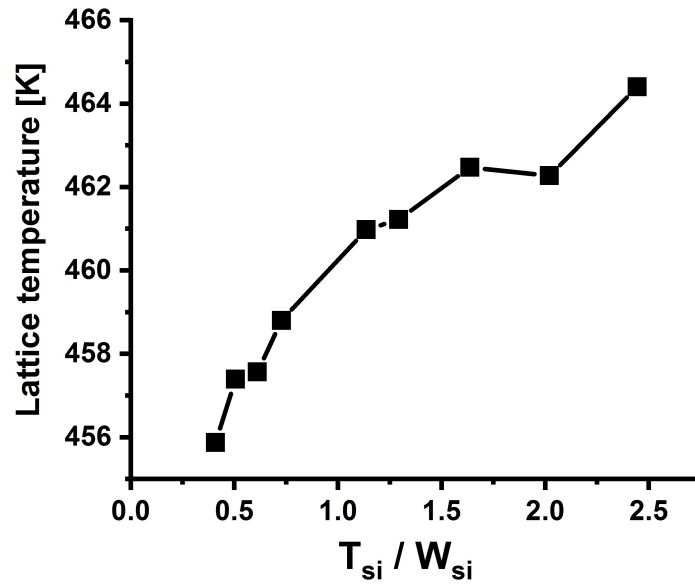


FIG. 6. Dependence of the temperature in the middle of the channel on the ratio T_{Si}/W_{Si} for transistors of the first group

layer, proposed in [23]:

$$\Delta T = \frac{(P_t \cdot T_{ox})}{K_b \cdot A}, \quad (4)$$

where P_t stands for the heat power generated by current in the channel, K_b is the heat conductance of the oxide layer, and A represents the area of the contact surface between the oxide layer and the channel. To compare the heat dissipation through back oxide and gate oxide layers, we used equation (4) for both gate oxide and back oxide layers. From equation (4), the gate oxide is justified, because the physical mechanism of heat dissipation through the back oxide and gate oxide are the same. For the back oxide layer $A = W_{Si} \cdot L$ and gate oxide layer $A = (2T_{Si} + W_{Si}) \cdot L$, where L stands for the channel length. Therefore, when using the independent heat dissipation through the oxide layers, the temperature changes associated with the heat dissipation through the back oxide layer and gate oxide layer, normalized to the heat power, can be written from (4) using the following formulas:

$$\frac{\Delta T}{P_t} = \frac{T_{box}}{K_{box} \cdot W_{Si} \cdot L}, \quad (5)$$

$$\frac{\Delta T}{P_t} = \frac{T_{gox}}{K_{gox} \cdot (2 \cdot T_{Si} + W_{Si}) \cdot L}, \quad (6)$$

where, T_{box} is the thickness of the back oxide layer, T_{gox} represents the thickness of the gate oxide layer, K_{box} and K_{gox} are the heat conductivity of the back and gate oxide layers, respectively. For these two heat dissipation mechanisms, the $\Delta T/P_t$ dependence on T_{Si}/W_{Si} (channel shape) is presented in Fig. 7. For simulation, we considered SiO_2 as the back oxide layer and HfO_2 as a gate oxide. The heat conductance of the hafnium oxide layer is in the range from 0.49–0.95 W/(m·K) in the temperature range from 300–500 K, and the heat conductance of SiO_2 is in the range from 1.2–2 W/(m·K) in the temperature range from 200–1500 K. In the simulation we used the value of the heat conductance 0.6 for HfO_2 and 1.5 for SiO_2 . As it appears from Fig. 7, a big gap in the values of heat conductances results in a higher heat dissipation through the back oxide layer. The curve of the $\Delta T/P_t$ dependence on T_{Si}/W_{Si} for the back oxide layer (Fig. 7, curve 1 (SiO_2)) grows monotonically like the T dependence on T_{Si}/W_{Si} depicted in Fig. 6. At the same time, during the heat dissipation through the gate oxide, the $\Delta T/P_t$ slowly decreases with increasing T_{Si}/W_{Si} (insertion in Fig. 7). This testifies to the main role played by the back oxide layer in heat dissipation and temperature setting in the center of the channel.

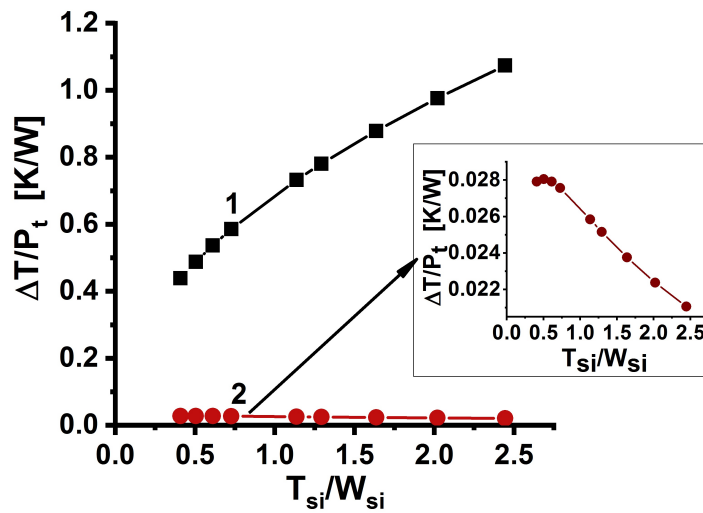


FIG. 7. $\Delta T/P_t$ dependence on T_{Si}/W_{Si} in cases of the heat dissipation through back oxide (curve 1) and gate oxide (curve 2) layers for the transistors of the first group

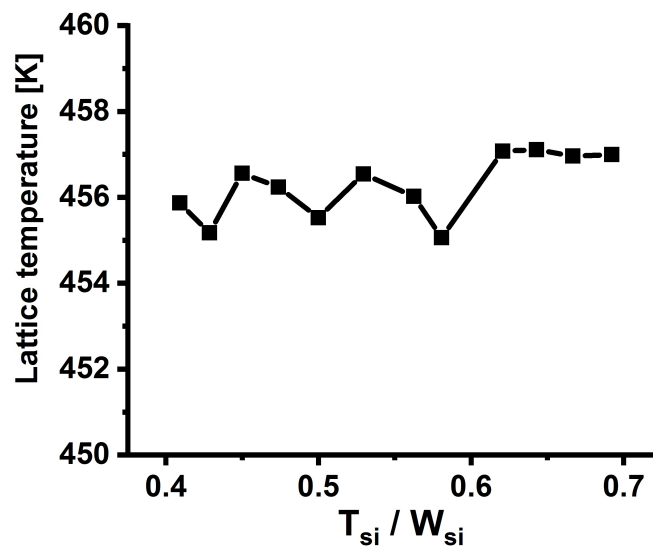


FIG. 8. Dependence of the temperature in the middle of the channel on the ratio T_{Si}/W_{Si} for transistors of the second group

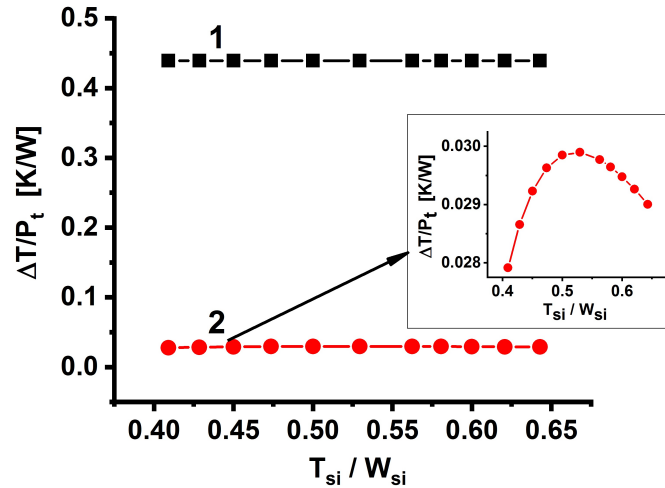


FIG. 9. $\Delta T/P_t$ dependence on T_{Si}/W_{Si} in cases of the heat dissipation through the back oxide (curve 1) and gate oxide (curve 2, inset) layers for the transistors of the second group

3.2. Performance Analysis of nanoscale JL FinFET with different channel shapes

In order to define the role of back and gate oxide layers in SHE in transistors with different channel cross-sections, the temperature dependence (in the channel center) on T_{Si}/W_{Si} was simulated for transistors of the second group. With transistors of this group, the channel width and the channel cross-sectional area are constant, while the cross-sectional shape changes from rectangular to trapezoidal shape (Fig. 2). In this case, the values of T_{Si}/W_{Si} can be changed only in the range from 0.4 up to 0.7. The results of the simulation are shown in Fig. 8. It can be seen that the temperature in the center of the channel is practically unchanged. This is associated with a constant channel base width while the cross-sectional shape is changed. In the case of heat dissipation through the back oxide layer, $\Delta T/P_t$ practically does not change with the increase in T_{Si}/W_{Si} , as shown in Fig. 9. In the case of heat dissipation through the gate oxide layer, the $\Delta T/P_t$ dependence on T_{Si}/W_{Si} does not have a monotonic character (inset in Fig. 9). The underlined dependence does not correspond to the temperature dependency in the center of the channel on the channel cross-sectional shape. Therefore, in this case too, a back oxide layer plays the main role in heat dissipation.

4. Conclusions

The above results revealed that for nanoscale JL FinFET with the different channel cross section shapes and with a defined thickness of back and gate oxide layers, the main factors that define the temperature at the center of the channel are the thermal conductivity of the oxide materials and the contact surface area between the channel and the oxide layers. In the case of transistors with SiO_2 as the back oxide layer and HfO_2 as the gate oxide layer, the temperature in the channel center is mainly defined by the width of the channel base in contact with the back oxide layer. Considering an increase in the T_{Si}/W_{Si} ratio with a constant channel cross-sectional area, the channel temperature rises, which is associated with a reduction in the channel base width of a transistor with a rectangular cross-section. Therefore, when considering the channel shape for nanoscale JL FinFETs, in order to reduce the SHE and obtain a more reliable nanoscale device, the main focus should be given to the contact surface between the channel and the oxide layers.

References

- [1] Srivastava N.A., Priya A., Mishra R.A. Analog and radio-frequency performance of nanoscale SOI MOSFET for RFIC based communication systems. *Microelectronics Journal*, 2020, 10473198.
- [2] Shahroury F.R., Mohamad A.A. Design of a passive CMOS implantable continuous monitoring biosensors transponder front-end. *Microelectronics Journal*, 2019, S0026-2692(18)30866-8.
- [3] Babadzhyanov R.D., Palvanov S.R., Razhabov O. Equipment for intrachamber irradiation of samples by betatron Bremsstrahlung. *Instruments and Experimental Techniques*, 1997, **40**(2), P. 154–155.
- [4] Lackner E., Krainer J., Wimmer-Teubenbacher R., Sosada F., Christian Gspan, Rohrer K., Ewald Wachmann, Köck A. CMOS Integrated Nanocrystalline SnO_2 Gas Sensors for CO Detection. *Procedia Engineering*, 2016, **168**, P. 297–300.
- [5] Colinge J., Chi-Woo Lee, Afzalain A., Akhavan N.D., Ran Yan, Ferain I., Razavi P., O'Neill B., Blake A., White M., Kelleher A., McCarthy B., Murphy R. *Nature Nanotechnology*, 2010, **5**, P. 225–229.
- [6] Abdikarimov A.E., Yusupov A., Atamuratov A.E. The Effect of the Fin Shape and Thickness of the Buried Oxide on the DIBL Effect in an SOI FinFET. *Technical Physics Letters*, 2018, **44**(11), P. 962–964.
- [7] Atamuratov A.E., Khalilloev M.M., Yusupov A., García-Loureiro J., Chedjou J., Kyandoghore K. Contribution to the Physical Modelling of Single Charged Defects Causing the Random Telegraph Noise in Junctionless FinFET. *Applied Sciences*, 2020, **10**(15), 5327.
- [8] Fossum J.G., Zhou Z., Mathew L., Nguyen B. SOI versus bulk-silicon nanoscale FinFETs. *Solid-State Electronics*, 2010, **54**, P. 86–89.

- [9] Han M.H., Chang C.Y., Chen H.B., Wu J., Cheng Y., Wu Y. Performance Comparison Between Bulk and SOI Junctionless Transistors. *IEEE Electron. Device Lett.*, 2013, **34**, P. 169–171.
- [10] Ahn W., Shin S. H., Jiang C., Jiang H., Wahab M.A. Integrated modeling of Self-heating of confined geometry (FinFET, NWFET, and NSHFET) transistors and its implications for the reliability of sub-20 nm modern integrated circuits. *Microelectron. Reliability*. 2018, **81**, P. 262–273.
- [11] Kumar A., Gupta A., Rai S., Reduction of self-heating effect using selective buried oxide (SELBOX) charge plasma based junctionless transistor. *International Journal of Electronics and Communications*, 2018, **95**, P. 162–169.
- [12] Ferhati H., Douak F., Djeflal F. Role of non-uniform channel doping in improving the nanoscale JL DG MOSFET reliability against the self-heating effects. *Superlattices and Microstructures*, 2017, **109**, P. 869–879.
- [13] Zhang G., Lai J., Zhu Sh., Wei S., Liang F., Chen Ch. Numerical study on the self-heating effects for vacuum/high-k gate dielectric tri-gate FinFETs. *Microelectronics Reliability*, 2019, **95**, P. 52–57.
- [14] Liu H., Li B., Li J., Yuan B. A comparative study of self-heating effect of nMOSFETs fabricated on SGOI and SGSOAN substrates. *Microelectronics Reliability*, 2010, **50**, P. 1942–1950.
- [15] Rahimian M., Ali A. A novel nanoscale MOSFET with modified buried layer for improving of AC performance and self-heating effect. *Materials Science in Semiconductor Processing*, 2012, **15**, P. 445–454.
- [16] Park S.J., Jeon D.Y., Kim G.T. Impact of fin shapes and channel doping concentrations on the operation of junctionless transistors. *Microelectronic Engineering*, 2019, **15**, P. 50–54.
- [17] Karimi F., Ali A. Electro-thermal analysis of non-rectangular FinFET and modeling of fin shape effect on thermal resistance. *Physica E: Low-dimensional Systems and Nanostructures*, 2017, **90**, P. 218–227.
- [18] Atamuratov A.E., Abdikarimov A., Khalilloev M., Atamuratova Z.A., Rahmanov R., Garcia-Loureiro A., Yusupov A. Simulation of DIBL effect in 25 nm SOI-FinFET with the different body shapes. *Nanosystems: Physics, Chemistry, Mathematics*, 2017, **8**(1). P. 71–74.
- [19] Atamuratov A.E., Xalilloev M.M., Abdikarimov A., Atamuratova Z.A., Kittler M., Granzner R., Schwierz F. Simulation of DIBL effect in junctionless SOI MOSFETs with extended gate. *Nanosystems: Physics, Chemistry, Mathematics*, 2017, **8**(1), P. 75–78.
- [20] <http://www.synopsys.com>
- [21] Loureiro A., Seoane N., Aldegunde M.R., Valin R., Asenov A., Martinez A., Kalna K. Implementation of the Density Gradient Quantum Corrections for 3-D Simulations of Multigate Nanoscaled Transistors *IEEE Trans. Comput.-Aided Des. Integr. Circuits Syst*, 2011, 30(6), P. 841–851.
- [22] Barraud S., Berthome M., Coquand R., Casse M., Ernst T., Samson M.-P., Perreau P., Bourdelle K. K., Faynot O., Poiroux T. Scaling of Trigate Junctionless Nanowire MOSFET With Gate Length Down to 13 nm. *IEEE Electron Device Letters*, 2012, **33**(9), P. 1225–1227.
- [23] McDavid L.J., Hall S., Mellor P.H., Eccleston W., Alderman J.C. Physical origin of negative differential resistance in SOI transistors. *Electron Letters*, 1989, **25**(13), P. 827–828.

Submitted 3 February 2022; revised 14 February 2022; accepted 15 February 2022

Information about the authors:

A. E. Atamuratov – Physics department, Urgech State University, Urgench, Kh.Olimjan,14, 220100, Uzbekistan; atabek.atamuratov@yahoo.com

B. O. Jabbarova – Physics department, Urgech State University, Urgench, Kh.Olimjan,14, 220100, Uzbekistan; bahorbahor1989@mail.ru

M. M. Khalilloev – Physics department, Urgech State University, Urgench, Kh.Olimjan,14, 220100, Uzbekistan; x-mahkam@mail.ru

A. Yusupov – Department of Electronics and Electrical Engineering, Tashkent University of Information Technologies, Tashkent, A.Temur,108, 100200, Uzbekistan; ayus@mail.ru

K. Sivasankaran – School of Electronics Engineering, Vellore Institute of Technology, Vellore, Tamilnadu, India; ksisivasankaran@vit.ac.in

J. C. Chedjou – University of Klagenfurt, Klagenfurt, 9020, Austria; jean.chedjou@aau.at

Conflict of interest: the authors declare no conflict of interest.

On the discrete spectrum of a quantum waveguide with Neumann windows in presence of exterior field

A. S. Bagmutov^{1,a}, H. Najar^{2,b}, I. F. Melikhov^{1,c}, I. Y. Popov^{1,d}¹ITMO University, St. Petersburg, 197101, Russia²Département de Mathématiques, Faculté des Sciences de Moanstir. Avenue de l'environnement 5019 Monastir, Tunisie^abagmutov94@mail.ru; ^bhatemnajar@ipeim.rnu.tn; ^civan.melikhov@gmail.com; ^dpopov1955@gmail.com

Corresponding author: A. S. Bagmutov, bagmutov94@mail.ru

ABSTRACT The discrete spectrum of the Hamiltonian describing a quantum particle living in three dimensional straight layer of width d in the presence of a constant electric field of strength F is studied. The Neumann boundary conditions are imposed on a finite set of bounded domains (windows) posed at one of the boundary planes and the Dirichlet boundary conditions on the remaining part of the boundary (it is a reduced problem for two identical coupled layers with symmetric electric field). It is proved that such system has eigenvalues below the lower bound of the essential spectrum for any $F \geq 0$. Then we closer examine a dependence of bound state energies on F and window's parameters, using numerical methods.

KEYWORDS quantum waveguide, Schrödinger operator, discrete spectrum.

ACKNOWLEDGEMENTS The work was partially supported by grant 20-31-90050 of Russian Foundation for Basic Research.

FOR CITATION Bagmutov A.S., Najar H., Melikhov I.F., Popov I.Y. On the discrete spectrum of a quantum waveguide with Neumann windows in presence of exterior field. *Nanosystems: Phys. Chem. Math.*, 2022, **13** (2), 156–163.

1. Introduction

The study of quantum waveguides is an active field of research since 1990th, when replication of nanoelectronic devices on the scale of nanometres became possible. On these scales, wave nature of an electron becomes vital and modelling the system by one-particle Schrödinger equation with various boundary conditions, becomes acceptable. In this context, boundary conditions are imposed on various surfaces in 2D and 3D, restricting the waveguide, such as infinite planar layers, strips or cylinders, usually, with introducing of a perturbation, which affects the spectrum. There are results for a number of different types of perturbations, including deformations of geometry [1–8], addition of a potential [5] or magnetic field [9, 10]. The Laplace operator can be perturbed by differential operator [11], or, for more general case of operator perturbation, see [12]. A multi-particle problem for such systems was also considered in a number of works ([13–16]).

In the present work, the perturbation by changing the type of the boundary condition on a part of the boundary is considered. Let E_j and $f_j(\mathbf{r})$, $j = 1, 2, \dots$ be eigenvalues and the corresponding eigenfunctions of the Laplacian with the following conditions: a 3D layer, confined between two planes, with the Dirichlet boundary conditions imposed on them:

$$f_j(\mathbf{r})|_{\partial\Omega_D} = 0. \quad (1)$$

One of the planes contains a finite domain, there are a finite number of regions, on which the boundary condition is replaced by the Neumann one:

$$\mathbf{n}\nabla f_j(\mathbf{r})|_{\partial\Omega_N} = 0, \quad (2)$$

where \mathbf{n} is a unit vector normal to the surface. The Neumann part of the boundary is referred to as "window(s)". The problems of this type are called Zaremba problems [17].

In this context, we refer to the main results in [12, 18–25] and references therein. For the case of 2D strip, where there is a Neumann condition on a part of boundary, representing a window, existence of bound states was proven in [26, 27], and in [21], it was shown that with the increase of window width, the number of bound states rises and their energies fall. For the case of 3D straight strip with circular Neumann windows, see [28, 29], where the existence of bound states is proven and asymptotics of energies for large window radii were given.

An additional magnetic field in a waveguide with the Neumann window is considered in [9, 30]. In [30], for a 3D waveguide with the Aharonov-Bohm magnetic field, the authors proved existence of threshold window length $a_0 > 0$, such that for $a < a_0$, the discrete spectrum is empty, and obtained a condition for bound state existence.

For systems of a type studied in this paper, but with uniform electric field in both layers, there are results in [31], where dependence on window's parameters was calculated numerically. Analogous numerical results for similar system is in [32]. Further results, concerning existence of bound states and their classification, extended to the multi-particle case were received in [13].

In general, the investigations of the quantum waveguides mostly cover the case of external magnetic field [9, 10, 30, 33], while there are many unanswered questions concerning waveguides in electric field alone. In [34], the case of bent tubes with non-linear electrostatic potential was investigated. In this case it was shown that Stark effect is non-trivial due to perturbations. Generally, mixed boundary conditions or curvature, affect propagation of waves, creating a situation analogous to the shock wave picture.

The paper is organized as follows. In section 2, we define the model of the quantum waveguide, give properly the functional domain, and study the self-adjointness of the operator. Then we show the stability of the essential spectrum when we consider perturbation by varying boundary condition from Dirichlet to Neumann. Section 3 is devoted to the main result and its proof. It deals with the effect of the electric field on our system. Precisely, we prove that such system exhibits discrete eigenvalues below the essential spectrum for any $F \geq 0$. The last section is devoted to numerical results for specifying the dependence of eigenvalues on system parameters.

2. The model

2.1. Geometry of the system

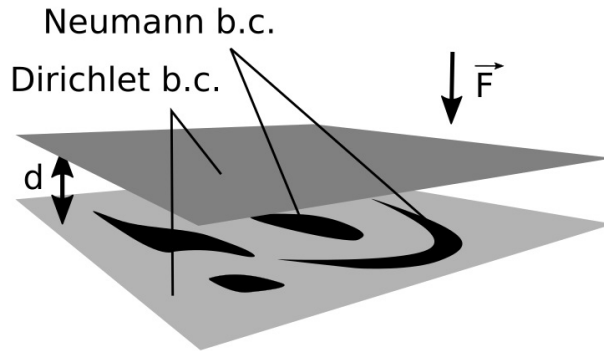


FIG. 1. The waveguide with a family of windows and two different boundary conditions with orthogonal electric field

The system we are going to study is given in Fig. 1. We consider a quantum particle confined inside two parallel layers coupled through a system of windows. We assume the Dirichlet condition at the layer boundaries. We simulate windows as regions at the boundary where the Neumann boundary conditions are imposed. This model is appropriate if the layers have identical widths and the electric field is symmetric in respect to the plane separating the layers. In this case, it is sufficient to deal with the Hamiltonian $H(F)$ for one layer between the planes $z = 0$ and $z = d$. We shall denote this configuration space by Ω ,

$$\Omega = \mathbb{R}^2 \times [0, d].$$

We assume that the considered particle is under the influence of a homogeneous electric field of intensity E orthogonal to the layers. We denote $F := Eq$, where q is the particle charge. We assume that $F \geq 0$. Let $(\gamma_i)_{1 \leq i \leq p}$ be a finite family of bounded and open sets lying on the boundary of Ω at $z = 0$.

We set $\Gamma = \partial\Omega \setminus (\cup_{i=1}^p \gamma_i)$. We consider the Dirichlet boundary conditions on Γ and the Neumann boundary conditions on $\cup_{i=1}^p \gamma_i$. The black surface in Fig. 1 corresponds to the Neumann boundary condition, while the grey surfaces correspond to the Dirichlet condition.

2.2. The Hamiltonian

Let us define the self-adjoint operator on $L^2(\Omega)$ corresponding to the particle Hamiltonian $H(F)$. For this purpose we use quadratic forms. Precisely, let $q(F)$ be the quadratic form

$$q(F)[u, v] = \int_{\Omega} (\nabla u \nabla \bar{v} + F z u \bar{v}) dx dy dz, \quad u, v \in \mathcal{D}(q(F)), \quad (3)$$

where $\mathcal{D}(q(F)) := \{u \in H^1(\Omega), u|_{\Gamma} = 0\}$, $H^1(\Omega)$ is the standard Sobolev space and $u|_{\Gamma}$ is the trace of the function u on Γ . It follows that $q(F)$ is a densely defined, symmetric, positive and closed quadratic form [35]. We denote the unique self-adjoint operator associated with $q(F)$ by $H(F)$ and its domain by \mathcal{D} . It is the Hamiltonian describing our system (we

will use the atomic units $2m = h = q = 1$ to simplify the equation). From [36] (page 276) and [35](page 263), one infers that the domain \mathcal{D} of $H(F)$ is as follows

$$\mathcal{D} = \{u \in H^1(\Omega); -\Delta u \in L^2(\Omega), u|_{\Gamma} = 0, \frac{\partial u}{\partial z}[\cup_{i=1}^p \gamma_i = 0]\} \tag{4}$$

and

$$H(F)u = (-\Delta + Fz)u, \quad \forall u \in \mathcal{D}. \tag{5}$$

2.3. Preliminary: Cylindrical coordinates

As γ_i are open sets, they contain a small disc of radius a , $a > 0$. Let us mark this disc on the plane $z = 0$ as $\gamma(a)$. Without loss of generality, we assume that the center of $\gamma(a)$ is the point $(0, 0, 0)$ and $\gamma(a) \subset \gamma_{i_0}$ for some $1 \leq i_0 \leq p$;

$$\gamma(a) = \{(x, y, 0) \in \mathbb{R}^3; x^2 + y^2 \leq a^2\}. \tag{6}$$

There exists b , $0 < a < b$ such that for all i , $1 \leq i \leq p$, one has $\gamma_i \subset \gamma(b)$. We denote, respectively, by $H_b(F)$ and $H_a(F)$ the operator (5) with unique disc window with radius b and a , respectively. For $i \in \{a, b\}$, we denote the domain of $H_i(F)$ by

$$\mathcal{D}(i) = \{u \in H^1(\Omega); -\Delta u \in L^2(\Omega), u|_{\Gamma} = 0, \frac{\partial u}{\partial z}[\gamma(i) = 0]\}.$$

Using the inclusion for the domains;

$$\mathcal{D}(b) \subseteq \mathcal{D} \subseteq \mathcal{D}(a),$$

one obtains the following bracketing [35]

$$H_b(F) \leq H(F) \leq H_a(F). \tag{7}$$

Let us notice that the new domains $\mathcal{D}(a)$ and $\mathcal{D}(b)$ have a cylindrical symmetry. Therefore, it is natural to consider the cylindrical coordinates system (r, θ, z) . Indeed, we have that

$$L^2(\Omega, dx dy dz) = L^2((0, +\infty) \times [0, 2\pi] \times [0, d], r dr d\theta dz).$$

We denote by $\langle \cdot, \cdot \rangle_r$, the scalar product in $L^2(\Omega, dx dy dz) = L^2((0, +\infty) \times [0, 2\pi] \times [0, d], r dr d\theta dz)$ given by the formula

$$\langle f, g \rangle_r = \int_{(0, +\infty) \times [0, 2\pi] \times [0, d]} f g r dr d\theta dz.$$

We denote the gradient in cylindrical coordinates by ∇_r . The Laplace operator in cylindrical coordinates is given by the following expression

$$\Delta_{r, \theta, z} = \frac{1}{r} \frac{\partial}{\partial r} \left(r \frac{\partial}{\partial r} \right) + \frac{1}{r^2} \frac{\partial^2}{\partial \theta^2} + \frac{d^2}{dz^2}. \tag{8}$$

2.4. A few known facts

Let us start this subsection by recalling that in the particular case when $a = 0$, one has $H_0(F)$, the Dirichlet Stark operator, and $b = +\infty$ one has $H_\infty(F)$, the Dirichlet-Neumann Stark operator. For $\bullet \in \{0, \infty\}$, let

$$H_\bullet(F) = (-\Delta_{\mathbb{R}^2}) \otimes I_d \oplus I_d \otimes (h_\bullet(F)), \text{ on } L^2(\mathbb{R}^2) \otimes L^2([0, d]),$$

where the transverse operator $h_\bullet(F) := -\Delta_{[0, d]} + Fz$ defined on $L^2([0, d])$ with the Dirichlet boundary conditions at d and 0 for $\bullet = 0$ and Neumann boundary at 0 for $\bullet = \infty$. The operator $h_\bullet(F)$ has purely discrete spectrum. We denote by λ_\bullet^1 the lowest transverse mode. Using Dirichlet Neumann bracketing, (see [35]), one obtains that

$$[\lambda_0^1, +\infty) = \sigma(H_0(F)) \subseteq \sigma(H_a(F)) \subseteq \sigma(H(F)) \subseteq \sigma(H_b(F)) \subseteq \sigma(H_\infty) = [\lambda_\infty^1, +\infty). \tag{9}$$

2.5. Stability of the essential spectrum

Using the property that the essential spectrum is preserved under compact perturbations, we are going to obtain its stability. We recall that the essential spectrum of an operator A which we denote by $\sigma_{ess}(A)$ consists of the point λ at which $\mathfrak{R}(\lambda I - A)$, the range of $\lambda I - A$ is not closed and of eigenvalues of infinite multiplicity. The discrete spectrum is the set of isolated eigenvalues with finite multiplicities. It is denoted by $\sigma_{dis}(A)$.

Theorem 2.1. *Let $H(F)$ be the operator given by (5). Then,*

$$\sigma_{ess}(H(F)) = [\lambda_0^1, +\infty[. \tag{10}$$

Proof.

First, let us note that an equation analogous to (9) also holds for the essential spectrum. Let $\Omega^{-,a}$ be the cylinder $\gamma(a) \times [0, d]$ and $\Omega^{+,a}$ the outside part of $\Omega^{-,a}$ in Ω . So

$$L^2(\Omega) = L^2(\Omega^{+,a}) \oplus L^2(\Omega^{-,a}). \tag{11}$$

Let H be, formally, the operator analogous to $H_a(F)$ but with imposing an extra Dirichlet condition on both sides of the lateral surface of the cylinder $\Omega^{-,a}$. The decomposition (11) yields that $H = H_1 \oplus H_2$. The operator H_2 defined on bounded domain $\Omega^{-,a}$ is known to have a discrete spectrum and $\sigma_{ess}(H_2)$ is empty. So $\sigma_{ess}(H) = \sigma_{ess}(H_1)$.

Using Wolf result [37] for operators of the form

$$A = -\sum_i \frac{\partial^2}{\partial x_i^2} + \sum_i a_i(x) \frac{\partial}{\partial x_i} + b(x), \tag{12}$$

one obtains that for $\lambda < 0$, the difference of resolvents,

$$(\lambda I - H_a(F))^{-1} - (\lambda I - H)^{-1}, \tag{13}$$

is a compact operator. It follows that $(\lambda I - H)^{-1}$ is a compact perturbation of $(\lambda I - H_a(F))^{-1}$. By Weyl Theorem, it immediately follows that the essential spectrum of $(\lambda I - H)^{-1}$ and $(\lambda I - H_a(F))^{-1}$ are the same and by the spectral mapping theorem one concludes that

$$\sigma_{ess}(H) = \sigma_{ess}(H_a(F)). \tag{14}$$

As the steps in the previous study are independent of a , we get

$$\sigma_{ess}(H) = \sigma_{ess}(H_1) = \sigma_{ess}(H_b(F)) = \sigma_{ess}(H(F)) = \sigma_{ess}(H_a(F)). \tag{15}$$

Using cylindrical symmetry once more, we consider H as acting on

$$L^2((a, +\infty) \times [0, 2\pi] \times [0, d], r dr d\theta dz).$$

One can write

$$H_1 = -\Delta_{(a, +\infty) \times [0, 2\pi]} \otimes I_{d_{[0, d]}} \oplus I_{d_{(a, +\infty) \times [0, 2\pi]}} \otimes h_0(F).$$

So

$$\sigma_{ess}(H_1) = [\lambda_0^1, +\infty).$$

By (15), one ends the proof. □

3. Existence of eigenvalues for one-particle Hamiltonian

In the last subsection, we have proved that

$$\sigma_{ess}(H(F)) = [\lambda_0^1, +\infty[. \tag{16}$$

So, by this and the min-max principle [35] we conclude that if the discrete spectrum exists, it lies below λ_0^1 . The main result of the paper is the following:

Theorem 3.1. *For any $F \geq 0$, the operator $H(F)$ has at least one isolated eigenvalue below λ_0^1 i.e*

$$\sigma_{dis}(H(F)) \neq \emptyset.$$

As it was already mentioned earlier, the result differs from one, corresponding to two-dimensional waveguides considered in [34], which shows that the existence of the discrete spectrum depends on the values of F . The absence of eigenvalues for some F in [34] is due to the fact that the field in the waveguide has a tilt, which gives one two parts of the operator with different essential spectra. In the present paper we deal with electric field symmetric in respect to the plane separating the layers.

It is important to notice that electric and magnetic fields have different effects on the spectrum of our system. Indeed, it was proved in [30] that in the case of magnetic field, there is some critical values of window radius to get existence of discrete spectrum.

The proof is based on the Goldstone and Jaffe trick [38], boosting the trial function by a deformation in the Neumann region. First we note that due to the fact that

$$\sigma(H(F)) \subseteq \sigma(H_a(F)); \quad \sigma_{ess}(H_a(F)) = \sigma_{ess}(H(F)),$$

one obtains

$$\sigma_{dis}(H_a(F)) \neq \emptyset \Rightarrow \sigma_{dis}(H(F)) \neq \emptyset. \tag{17}$$

Let us consider the quadratic form Q_r

$$Q_r[f, g] = \int_{(0, +\infty) \times [0, 2\pi] \times [0, d]} \nabla_r f \overline{\nabla_r g} + F z f \bar{g} r dr d\theta dz,$$

with the domain

$$\mathcal{D}_r = \{f \in L^2(\Omega, r dr d\theta dz); \nabla_r f \in L^2(\Omega, r dr d\theta dz); f|_{\Gamma} = 0\}.$$

Consider the quadratic function Q defined by

$$Q[\Phi] = Q_r[\Phi] - \lambda_0^1 \|\Phi\|_{L^2(\Omega, r dr d\theta dz)}^2. \quad (18)$$

Since the essential spectrum of $H_a(F)$ starts at λ_0^1 , if we construct a trial function $\Phi \in \mathcal{D}_r$ such that $Q[\Phi]$ has a negative value then the task is achieved. Using the quadratic form domain, Φ must be continuous inside, but not necessarily smooth. Let χ_1 be the positive eigenfunction associated to λ_0^1 of the operator $h_0(F)$ (ie. $-\chi_1'' = (\lambda_0^1 - Fz)\chi_1$), with $\|\chi_1\| = 1$ (see [36]).

For $\Phi(r, \theta, z) = \varphi(r)\chi_1(z)$, we compute

$$\begin{aligned} Q[\Phi] &= Q_r[\Phi] - \lambda_0^1 \|\Phi\|_{L^2(\Omega, r dr d\theta dz)}^2 \\ &= \int_{(0, +\infty) \times [0, 2\pi] \times [0, d]} \left(|\chi_1(z)|^2 |\varphi'(r)|^2 + |\chi_1'(z)|^2 |\varphi(r)|^2 \right. \\ &\quad \left. + Fz |\chi_1(z)|^2 |\varphi(r)|^2 \right) r dr d\theta dz - \lambda_0^1 \|\varphi \chi_1\|_{L^2(\Omega, r dr d\theta dz)}^2 \\ &= 2\pi \|\varphi'\|_{L^2((0, +\infty), r dr)}^2 \\ &\quad + \int_{(0, +\infty) \times [0, 2\pi] \times [0, d]} \left((\lambda_0^1 - Fz) |\chi_1(z)|^2 |\varphi(r)|^2 \right) r dr d\theta dz \\ &\quad + \int_{(0, +\infty) \times [0, 2\pi] \times [0, d]} Fz |\chi_1(z)|^2 |\varphi(r)|^2 r dr d\theta dz - \lambda_0^1 \|\varphi \chi_1\|_{L^2(\Omega, r dr d\theta dz)}^2 \\ &= 2\pi \|\varphi'\|_{L^2((0, +\infty), r dr)}^2. \end{aligned} \quad (19)$$

Now, let us consider an interval $I = [0, b]$ for a positive b , $b > a$, and a function $\varphi \in \mathcal{S}([0, +\infty[)$ such that $\varphi(r) = 1$ for $r \in I$. We also define a family $\{\varphi_\tau : \tau > 0\}$ by

$$\varphi_\tau(r) = \begin{cases} \varphi(r) & \text{if } r \in (0, b) \\ \varphi(b + \tau(\ln r - \ln b)) & \text{if } r \geq b. \end{cases} \quad (20)$$

We have,

$$\begin{aligned} \|\varphi'_\tau\|_{L^2([0, +\infty[, r dr)} &= \int_{(0, +\infty)} |\varphi'_\tau(r)|^2 r dr \\ &= \int_{[b, +\infty[} \frac{\tau^2}{r^2} |\varphi'(b + \tau(\ln r - \ln b))|^2 r dr \\ &= \tau \int_{[b, +\infty[} \frac{\tau}{r} |\varphi'(b + \tau(\ln r - \ln b))|^2 dr \\ &= \tau \int_{(0, +\infty)} |\varphi'(s)|^2 ds \\ &= \tau \|\varphi'\|_{L^2([0, +\infty[)}^2. \end{aligned} \quad (21)$$

We set

$$\begin{aligned} \Phi_{\tau, \varepsilon}(r, z) &= \varphi_\tau(r)[\chi_1(z) + \varepsilon \chi_1(z) \phi^2(r)] \\ &= \varphi_\tau(r)\chi_1(z) + \varepsilon \varphi_\tau(r)\chi_1(z)\phi^2(r) \\ &= \Phi_{1, \tau}(r, z) + \Phi_{2, \tau, \varepsilon}(r, z). \end{aligned} \quad (22)$$

Then,

$$\begin{aligned} Q[\Phi_{\tau, \varepsilon}] &= Q[\Phi_{1, \tau} + \Phi_{2, \tau, \varepsilon}] \\ &= Q_r[\Phi_{1, \tau} + \Phi_{2, \tau, \varepsilon}] - \lambda_0^1 \|\Phi_{1, \tau} + \Phi_{2, \tau, \varepsilon}\|_{L^2(\Omega, r dr d\theta dz)}^2 \\ &= Q_r[\Phi_{1, \tau}] - \lambda_0^1 \|\Phi_{1, \tau}\|_{L^2(\Omega, r dr d\theta dz)}^2 + Q_r[\Phi_{2, \tau, \varepsilon}] - \lambda_0^1 \|\Phi_{2, \tau, \varepsilon}\|_{L^2(\Omega, r dr d\theta dz)}^2 \\ &\quad + 2\langle \nabla_r \Phi_{1, \tau}, \nabla_r \Phi_{2, \tau, \varepsilon} \rangle_r + 2F\langle z \Phi_{1, \tau}, \Phi_{2, \tau, \varepsilon} \rangle_r - 2\lambda_0^1 \langle \Phi_{1, \tau}, \Phi_{2, \tau, \varepsilon} \rangle_r. \end{aligned}$$

Using the properties of χ_1 and taking into account (19) and (21), one obtains

$$\begin{aligned} Q_r[\Phi_{1, \tau}] - \lambda_0^1 \|\Phi_{1, \tau}\|_{L^2(\Omega, r dr d\theta dz)}^2 &= Q[\varphi_\tau \chi_1] \\ &= 2\pi \|\varphi'_\tau\|_{L^2((0, +\infty), r dr)}^2 \\ &= 2\pi \tau \|\varphi'\|_{L^2((0, +\infty))}^2. \end{aligned}$$

As the supports of φ and ϕ are disjoint, one gets

$$\begin{aligned}
 & Q_r[\Phi_{2,\tau,\varepsilon}] - \lambda_0^1 \|\Phi_{2,\tau,\varepsilon}\|^2 \\
 &= \int_{(0,+\infty) \times [0,2\pi] \times [0,d]} \left(\left| \nabla_r (\varepsilon \varphi_\tau(r) \chi_1(z) \phi(r)^2) \right|^2 \right. \\
 &+ \left. \varepsilon^2 Fz |\varphi_\tau(r)|^2 |\chi_1(z)|^2 |\phi^2(r)|^2 \right) r dr d\theta dz - \varepsilon^2 \lambda_0^1 \|\varphi_\tau \chi_1 \phi^2\|_{L^2(\Omega, r dr d\theta dz)}^2 \\
 &= \int_{(0,+\infty) \times [0,2\pi] \times [0,d]} 4\varepsilon^2 |\chi_1(z)|^2 |\phi'(r) \phi(r) \varphi(r)|^2 + \varepsilon^2 |\chi_1'(z)|^2 |\varphi_\tau(r) \phi^2(r)|^2 \\
 &+ \varepsilon^2 Fz |\varphi_\tau(r) \chi_1(z) \phi^2(r)|^2 r dr d\theta dz - \varepsilon^2 \lambda_0^1 \|\varphi_\tau \chi_1 \phi^2\|_{L^2(\Omega, r dr d\theta dz)}^2 \\
 &\leq \varepsilon^2 d 2\pi \left(4 \|\phi \phi' \varphi_\tau(r)\|_{L^2([0,+\infty[, r dr)}^2 + Fd \|\varphi_\tau(r) \phi^2\|_{L^2([0,+\infty[, r dr)}^2 \right. \\
 &+ \left. \|\chi_1'(z) \varphi_\tau(r) \phi^2(r)\|_{L^2([0,+\infty[\times [0,d], r dr dz)}^2 - \lambda_0^1 \|\phi^2\|_{L^2([0,+\infty[, r dr)}^2 \right).
 \end{aligned}$$

As the supports of φ_τ and ϕ are disjoint, one obtains

$$\langle \nabla_r \Phi_{1,\tau}, \nabla_r \Phi_{2,\tau,\varepsilon} \rangle_r = \langle \nabla_r (\varphi_\tau \chi_1), \nabla_r (\varepsilon \varphi_\tau \chi_1 \phi^2) \rangle_r = 0.$$

Using the fact that $-\chi_1'' = (\lambda_0^1 - Fz)\chi_1$ and properties of φ_τ and ϕ one gets to the following estimation:

$$\begin{aligned}
 \langle (Fz - \lambda_0^1) \Phi_{1,\tau}, \Phi_{2,\tau,\varepsilon} \rangle_r &= \langle (Fz - \lambda_0^1) \varphi_\tau \chi_1, \varepsilon \varphi_\tau \chi_1 \phi^2 \rangle_r \\
 &= \varepsilon \langle (Fz - \lambda_0^1) \chi_1, \chi_1 \phi^2 \rangle_r \\
 &= \varepsilon \langle \chi_1'', \chi_1 \phi^2 \rangle_r \\
 &= -\varepsilon \left(2\pi \|\phi\|_{L^2([0,+\infty[, r dr)}^2 \int_0^d |\chi_1'(z)|^2 dz \right) < 0.
 \end{aligned}$$

Therefore, one has

$$\begin{aligned}
 Q[\Phi_{\tau,\varepsilon}] &\leq 2\pi\tau \|\varphi'\|_{L^2([0,+\infty[)}^2 \\
 &+ \varepsilon^2 d 2\pi \left(4 \|\phi \phi'\|_{L^2([0,+\infty[, r dr)}^2 + Fd \|\varphi_\tau(r) \phi^2\|_{L^2([0,+\infty[, r dr)}^2 \right. \\
 &+ \left. \|\chi_1'(z) \varphi_\tau(r) \phi^2(r)\|_{L^2([0,+\infty[\times [0,d], r dr dz)}^2 - \lambda_0^1 \|\phi^2\|_{L^2([0,+\infty[, r dr)}^2 \right) \\
 &- \varepsilon \left(2\pi \|\phi\|_{L^2([0,+\infty[, r dr)}^2 \int_0^d |\chi_1'(z)|^2 dz \right). \tag{23}
 \end{aligned}$$

We notice that only the first term of the last equation depends on τ . The linear term in ε is negative and could be chosen sufficiently small so that it dominates over the quadratic one. Fixing this ε and then choosing τ sufficiently small, one makes the right hand side of (23) negative. So, $\sigma_{dis}(H_a(F)) \neq \emptyset$ by (17). This ends the proof of the Theorem. \square

4. Numerical results and conclusion

In this section, we study the dependence of the discrete spectrum on system's parameters, to build an intuition about a system and suggest directions for further research. We use a finite element method and consider a case of a single circular window, with varying area (and elliptical window for the last result). In all calculations, we use atomic system of units, with $\hbar = e = 1$, $m = 0.5$ (e, m are the electron charge and mass, correspondingly). The colors of energy levels are consistent between all plots. Across all plots, the black line represents a lowest boundary of the essential spectrum.

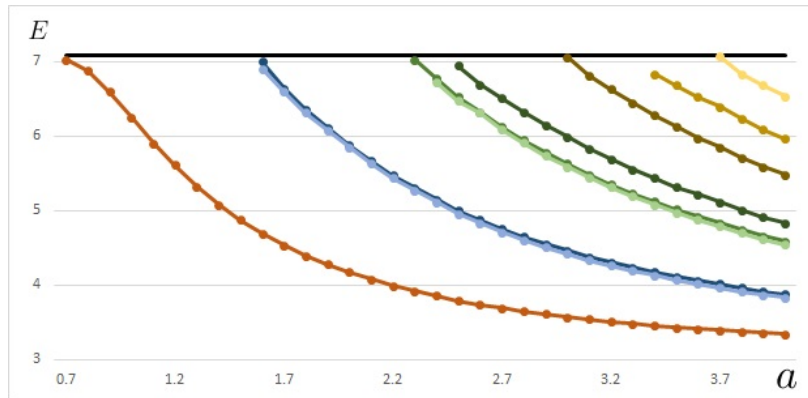


FIG. 2. Energies of bound states as functions of window radius a . Electric field intensity is fixed $F = 5$

First, we study dependence of the discrete spectrum on window's area, shown in Fig. 2. Here a field intensity is fixed, $F = 5$ (which corresponds to middle value from the second plot). The essential spectrum is independent of window's parameters (Th. 2.1). Each bound state as a function of window's area is monotonically decreasing and a number of bound states is increasing. In accordance with the main theorem, the first bound state is lower than the boundary for all positive radii, and merges with the essential spectrum boundary as radius goes to zero.

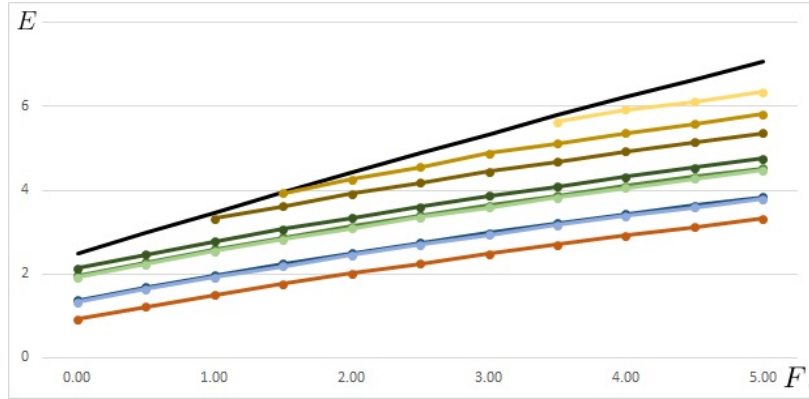


FIG. 3. Energies of bound states as functions of electric field intensity F . Window radius is fixed $a = 4$

Now we investigate the dependence of spectrum on the electric field intensity (Fig. 3). The window radius is fixed, $a = 4$ (which is the maximum radius from Fig. 2) An electric field isn't a local perturbation of a system, so it changes the essential spectrum, as well as discrete. Both spectra are increasing functions of F , but essential spectrum boundary grows faster, allowing more bound states to emerge, as field intensity increases.

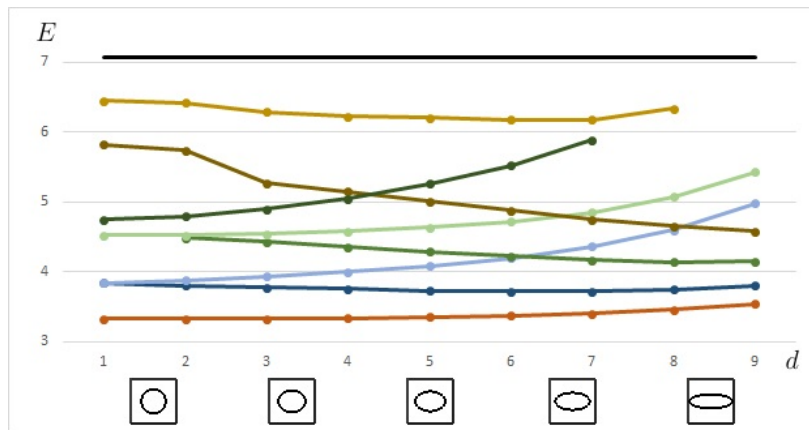


FIG. 4. Energies of bound states as functions of distance between foci of elliptical window. Window's area is constant (16π) and electric field intensity is fixed $F = 5$

Naturally, the question arises, about which parameters of the window are important. Particularly, how the discrete spectrum depends on window's area, perimeter and shape. These questions are considered in more detail for a similar system (same geometry, but homogeneous electrical field), in [13]. Here we consider influence of window's shape, particularly, we change an eccentricity of elliptical window, tracking different bound states, see Fig. 4. Area is fixed and corresponds to area of a circle with $a = 4$. Field intensity is fixed, $F = 5$. Here we can see different dynamics for different types of bound states (see [13] for more details of the classification).

To summarize, we considered a quantum system of parallel 3D layers of the same width, connected through a set of windows in a bounded region, with symmetrical external electrical field (Fig. 1). For such a system we have proven existence of at least one discrete eigenvalue below essential spectrum, for any size of windows. Then, numerically, we more closely examined a number of bound states, and their particular dependence on area of a window, different intensities of external field and shapes of a window. The results show a monotonic growth of bound states number with the increase of area or field intensity, for a circular opening. For the case of window shape's deformation, bound states form several distinct types, with consistent and predictable behaviour. The latter results suggest a number of directions for further research, such as getting bounds on number of bound states for certain types of windows and determining vital parameters of window's shape, when considering any particular bound state type.

References

- [1] Borisov D., Exner P. and Gadyl'shin R., Krejcirik D. Bound states in weakly deformed strips and layers. *Annales Henri Poincaré*, 2001, **2**(3), P. 553–572.
- [2] Briet Ph., Kovarik H., Raikov G. and Soccorsi E. Eigenvalue asymptotics in a twisted waveguide, *Comm. PDE*, 2009, **34**(8), P. 818–836.
- [3] Bulla W. and Renger W. Existence of bound states in quantum waveguides under weak conditions. *Lett. Math. Phys.*, 1995, **35**(1), 1–12.
- [4] Chenaud B., Duclos P., Freitas P. and Krejcirik D. Geometrically induced discrete spectrum in curved tubes. *Diff. Geom. Appl.*, 2005, **23**(2), P. 95–105.
- [5] Duclos P. and Exner P. Curvature-induced bound state in quantum waveguides in two and three dimensions. *Rev. Math. Phys.*, 1995, **7**(1), P. 73–102.
- [6] Duclos P., Exner P. and Stovicek P. Curvature-induced resonances in a two-dimensional Dirichlet tube. *Annales Henri Poincaré*, 1995, **62**(1), P. 81–101.
- [7] Ekholm T., Kovarik H. and Krejcirik D. A Hardy inequality in twisted waveguides. *Arch. Rat. Mech. Anal.*, 2008, **188**(2), P. 245–264.
- [8] Exner P. and Vugalter S.A. Bound States in a Locally Deformed Waveguide: The Critical Case. *Lett. Math. Phys.*, 1997, **39**(1), P. 59–68.
- [9] Borisov D., Ekholm T. and Kovarik H. Spectrum of the magnetic Schrodinger operator in a waveguide with combined boundary conditions. *Annales Henri Poincaré*, 2005, **6**(2), P. 327–342.
- [10] Ekholm T. and Kovarik H. Stability of the magnetic Schrodinger operator in a waveguide. *Comm. PDE*, 2005, **30**(4), P. 539–565.
- [11] Grushin V.V. On the eigenvalues of finitely perturbed laplace operators in infinite cylindrical domains. *Math. Notes*, 2004, **75**(3), P. 331–340.
- [12] Gadyl'shin R. On regular and singular perturbations of acoustic and quantum waveguides. *C.R. Mécanique*, 2004, **332**(8), P. 647–652.
- [13] Bagmutov A.S., Popov I.Y. Window-coupled nanolayers: window shape influence on one-particle and two-particle eigenstates. *Nanosystems: Phys. Chem. Math.*, 2020, **11**(6), P. 636–641.
- [14] Melikhov I.F. and Popov I.Yu. Hartree-Fock approximation for the problem of particle storage in deformed nanolayer. *Nanosystems: Physics, Chemistry, Mathematics*, 2013, **4**(4), P. 559–563.
- [15] Melikhov I.F. and Popov I.Yu. Multi-Particle Bound States in Window-Coupled 2D Quantum Waveguides. *Chin. J. Phys.*, 2015, **53**, 060802.
- [16] Popov S.I., Gavrilov M.I., and Popov I.Yu. Two interacting particles in deformed nanolayer: discrete spectrum and particle storage. *Phys. Scripta*, 2012, **86**(3), 035003.
- [17] Zaremba S. Sur un problème toujours possible comprenant, á titre de cas particulier, le problème de Dirichlet et celui de Neumann. *J. Math. Pure Appl.*, 1927, **6**, P. 127–163.
- [18] Borisov D. Discrete spectrum of a pair of asymmetric window-coupled waveguides. English transl. *Sb. Math.*, 2006, **197**(3-4), P. 475–504.
- [19] Borisov D. On the spectrum of two quantum layers coupled by a window. *J. Phys. A: Math. Theor.*, 2007, **40**(19), P. 5045–5066.
- [20] Borisov D. and Exner P. Exponential splitting of bound states in a waveguide with a pair of distant windows. *J. Phys A: Math and General*, 2004, **37**(10), P. 3411–3428.
- [21] Borisov D., Exner P. and Gadyl'shin R. Geometric coupling thresholds in a two-dimensional strip. *J. Math. Phys.*, 2002, **43**(12), P. 6265–6278.
- [22] Exner P. and Vugalter S.A. Bound state asymptotic estimate for window-coupled Dirichlet strips and layers. *J. Phys. A: Math. Gen.*, 1997, **30**(22), P. 7863–7878.
- [23] Exner P., Vugalter S.A. On the number of particles that a curved quantum waveguide can bind. *J. Math. Phys.*, 1999, **40**, P. 4630–4638
- [24] Popov I.Yu. Asymptotics of bound states and bands for laterally coupled three-dimensional waveguides. *Rep. on Math. Phys.*, 2001, **48**(3), P. 277–288.
- [25] Popov I.Yu. Asymptotics of bound state for laterally coupled waveguides. *Rep. on Math. Phys.*, 1999, **43**(3), P. 427–437.
- [26] Bulla W., Gesztesy F., Renger W. and Simon B. Weakly coupled bound states in quantum waveguides. *Proc. Amer. Math. Soc.*, 1997, **125**(5), P. 1487–1495.
- [27] Exner P., Šeba P., Tater M. and Vaněk D. Bound states and scattering in quantum waveguides coupled laterally through a boundary window. *J. Math. Phys.*, 1996, **37**(10), P. 4867–4887.
- [28] Najjar H., S. Ben Hariz and M. Ben Salah. On the Discrete Spectrum of a Spatial Quantum Waveguide with a Disc Window. *Math. Phys. Anal. Geom.*, 2010, **13**(1), P. 19–28.
- [29] Najjar H. and Olendski O. Spectral and localization properties of the Dirichlet wave guide with two concentric Neumann discs. *J. Phys. A: Math. Theor.*, 2011, **44**(30), 305304.
- [30] Najjar H. and Raissi M. A quantum waveguide with Aharonov-Bohm Magnetic Field. *Math. Meth. App. Sci.*, 2016, **39**(1), P. 92–103.
- [31] Popov I.Y., Bagmutov A.S., Melikhov I.F., Najjar H. Numerical analysis of multi-particle states in coupled nano-layers in electric field. *AIP Conf. Proc. Vol.*, 2020, **2293**, 360006.
- [32] Numerical results a quantum waveguide with Mixed boundary conditions M Raissi - arXiv preprint arXiv:1501.02073, 2015 - arxiv.org
- [33] Dunne G. and Jaffe R.L. Bound states in twisted Aharonov-Bohm tubes. *Ann. Phys.*, 1993, **233**(2), P. 180–196.
- [34] Exner P. A Quantum Pipette. *J. Phys A: Math and General*, 1995, **28**(18), P. 5323–5330.
- [35] Reed M. and Simon B. *Methods of Modern Mathematical Physics*, Vol. IV: Analysis of Operators. Academic Press, New York, 1978.
- [36] Reed M. and Simon B. *Methods of Modern Mathematical Physics*, Vol. I: Functionnal Analysis. Academic Press Inc; 2nd Revised edition, Academic Press, New York, 1981.
- [37] Wolf F. On the invariance of the essential spectrum under a change of boundary conditions of partial differential boundary operators. *Indag. Math.*, 1959, **21**, P. 142–147.
- [38] Goldstone J. and Jaffe R.L. Bound States in Twisting tubes. *Phys. Rev. B*, 1992, **45**, 14100

Submitted 3 October 2021; revised 28 December 2021; accepted 1 March 2022

Information about the authors:

A. S. Bagmutov – ITMO University, Kronverkskiy, 49, St. Petersburg, 197101, Russia; bagmutov94@mail.ru

H. Najjar – Département de Mathématiques, Faculté des Sciences de Moanstir. Avenue de l'environnement 5019 Monastir -Tunisie; hatemnajar@ipeim.rnu.tn

I. F. Melikhov – ITMO University, Kronverkskiy, 49, St. Petersburg, 197101, Russia; ivan.melikhov@gmail.com

I. Y. Popov – ITMO University, Kronverkskiy, 49, St. Petersburg, 197101, Russia; popov1955@gmail.com

Conflict of interest: the authors declare no conflict of interest.

Phase formation under conditions of self-organization of particle growth restrictions in the reaction system

Oksana V. Almjasheva^{1,a}, Vadim I. Popkov^{2,b}, Olga V. Proskurina^{2,3,c}, Victor V. Gusarov^{2,d}

¹St. Petersburg State Electrotechnical University "LETI", 197376 St. Petersburg, Russia

²Ioffe Institute, 194021 St. Petersburg, Russia

³St. Petersburg State Institute of Technology, 190013 St. Petersburg, Russia

^aalmjasheva@mail.ru, ^bvadim.i.popkov@mail.ioffe.ru, ^cproskurinaov@mail.ru, ^dvictor.v.gusarov@gmail.com

Corresponding author: Olga V. Proskurina, proskurinaov@mail.ru

ABSTRACT A systematic analysis of literature data concerning the influence of methods and conditions of synthesis on the possibility of self-organization of particle growth restrictions during chemical reactions of solid phase has been conducted. The prospects of using such methods to obtain nano-crystalline phases are shown. It is demonstrated that a disadvantage of such methods of synthesis is the risk of forming precursor phases instead of target products. To avoid such an outcome, several methods of synthesis are proposed. Based on the analysis of literature data, examples of the transformation of precursor nanoparticles into nanocrystals of target phases are classified and presented. A scheme that allows optimal combination of synthesis methods to obtain nano-crystalline particles of a given composition, structure, size, and shape is designed.

KEYWORDS nanocrystals, nanoparticles, self-organization, nanoreactors, particle growth restrictions

ACKNOWLEDGEMENTS The research was supported by the Russian Science Foundation Grant 21-13-00260.

FOR CITATION Almjasheva O. V., Popkov V. I., Proskurina O. V., Gusarov V. V. Phase formation under conditions of self-organization of particle growth restrictions in the reaction system. *Nanosystems: Phys. Chem. Math.*, 2022, **13** (2), 164–180.

1. Introduction

The production of crystalline particles with the smallest possible sizes can be achieved by two different mechanisms. First, it can result from thermodynamic processes related to the size of the critical phase embryo [1–4] and the crystal-chemical constraints determined by the minimum number of unit cell transformations for the formation of a stable crystalline structure of solid-phase particles [5]. Second, it can be caused by kinetic factors that condition the proportion of nucleation velocity to particle growth rate. In the latter case, it is possible to achieve minimum size particles by increasing the nucleation velocity and lowering the growth rate of new phase particles. Some aspects of increasing the rate of phase transformations were considered in [2, 6–13]. As examples of fast-flowing processes of formation of new phase crystalline particles, certain dehydration reactions under hydrothermal conditions [14–19], combustion reactions [20–30], as well as condensation of certain crystalline products from the gas phase [31–34], can be cited. It is crucial to highlight the processes whose high-speed results from the fact that the formation and growth of particles of a new phase is determined by the transfer of matter in the form of clusters with a large number of atoms [2, 35–42]. At the same time, in many cases obtaining nanoparticles in a fast-flowing process of phase formation is not possible. This is especially characteristic of the synthesis of crystalline phases of complex composition [43–56]. In these cases, it is possible to obtain nanoparticles of the synthesized phase with the smallest possible sizes by creating various kinds of restrictions for their growth. Particle growth restrictions may be thermodynamic (energetic) in nature, or they may be caused by kinetic factors. Conditions restricting the growth of particles of the new phase can be set before the start of the phase formation process or during the synthesis of a new phase. The first case involves physico-chemical processes in pre-created nanoreactors. The second case concerns self-organizing restrictions for the growth of nanoparticles during phase formation.

Different options for preliminary establishment of conditions under which mass transfer to particles of the forming phase would be restricted, that is, various types of nanoreactors were investigated in [57–68]. In these works, it was shown that the synthesis of nanoparticles in nanoreactors effectively restricts their growth and, in some cases, allows to control the morphology of the formed particles. As mentioned above, one of the options for restricting the growth of new phase particles is to conduct chemical processes in nanoreactors of diverse shapes, sizes, and compositions – such as dispersed, phase and chemical. Examples of such nanoreactors can be nanoscale and submicron pores in various materials [64, 65, 69–79], including channel pores in nanotubes [80–88], as well as various dispersed media such like microemulsions [89–91], and dispersions of nanoparticles in liquid media [92–95]. As an original nanoreactor, films

of nanoscale thickness applied, for example, by molecular layering (ML) [96–102], often called Atomic Layer Epitaxy (ALE) [103], or Atomic Layer Deposition (ALD) [104], to substrates of various compositions can be considered. Phase formation in such films or the interaction of their components with the substrate resulting in the formation of a new phase occurs with a natural restriction of the thickness of the obtained solid-phase product [105–111]. Interlayer spaces in compounds with a layered structure can also act as nanoreactors. An example of the use of interlayer spaces in hydrotalcites as nanoreactors is described in [57, 112–117]. Other heterogeneities in the structure of substances can also serve as nanoreactors – for example – cavities in polymers [118, 119]. A more complete description of various types of nanoreactors can be found in [57, 120–124], among other works.

A fundamentally different method for restricting particle growth rate is to increase the relaxation time of the process of mass transfer [6]:

$$\tau \sim D^{-1} \cdot (\Delta x)^2,$$

where D is the effective diffusion coefficient of the substance that determines the growth of particles, and Δx is the characteristic distance that the elementary components of the substance must overcome before they reach the growing particle. The latter value depends inversely on the concentration of the elementary components of the substance and the volume fraction of the particles formed in the reaction zone. Specific ways to reduce the rate of particle growth in this case may be to increase the viscosity of the reaction medium and to decrease the concentration of reagents.

Another principle of restricting the growth of particles of the synthesized phase is based on setting the conditions restricting their growth during the process of phase formation. To date, research in this area is fragmented. At the same time, the self-organization of growth restrictions of nanoparticles was observed during the formation of phases of different aggregate state, structure, chemical composition, and for nanocrystals with different morphology.

Recently, much attention has been paid to the study of the possibilities of obtaining oxide (including the production of oxyhydroxide and hydroxide) nanocrystals with a different range of variation in shape and size [11, 14, 16, 84, 125–137], including with the smallest possible crystal sizes [5]. Such interest is determined by the fact that their structure [20, 138–140] and functional properties [139, 141–147] may depend on the dimensional parameters of nanocrystals. In this regard, it is of interest to conduct a systematic analysis of the possibilities of self-organization of restrictions on the growth of particles of the forming crystalline phases. This work is devoted to this topic.

2. Nanoparticle growth restrictions occurring during the process of their formation

All types of restrictions on the growth of nanoparticles formed during their formation and presented in this paper can be conditionally divided into eight groups. The categorization depends on the physico-chemical reasons for the emergence of these restrictions as well as the methods of their formation.

The first group of restrictions on the growth of nanoparticles includes cases when the very structure of nanoparticles does not allow to increase its size continuously in certain or all directions by sequentially attaching atoms (molecules) to it. Usually, structures with a high degree of bond covalence act as such nanoparticles. The most well-known representatives of such nanostructures are carbon fullerenes, the sizes of which vary discretely depending on the number of carbon atoms in the structure from the smallest possible to the largest known to date [148–150]. It should be noted that there is a large group of similar nanostructures like buckyballs [151–153], with a very different chemical composition, including oxide buckyballs [154–160]. Analogically, the potential to increase the diameter of carbon nanotubes [161, 162] and nanotubes of other compounds [163–167] is restricted. Graphene particles, their derivatives, and morphological analogues with finite thickness are also close to the described group of nanoparticles. This variant of restricting the growth of nanoparticles can be referred to as restrictions resulting from their non-translational structure in one or more directions (Fig. 1).

The second group of restrictions on the growth of nanoparticles during their synthesis is characteristic, in particular, of nano-switches. This group is associated with the energy disadvantage of their folding following an increase in the diameter (decrease in curvature) of the nano-switch [168–173]. It is noteworthy that to date, there are only a small number of structures that differ in chemical composition and morphology (cylinders and cones) [174, 175]. The type of restrictions on the growth of nanoparticles in one or two directions that are similar in physico-chemical characteristics is associated with large differences in the values of the specific surface energy of the crystal faces. This leads to the redistribution of matter between the crystal faces during their growth and the formation of rod-shaped or lamellar morphology particles and, under certain conditions, to the formation of nanorods [19, 176–179] and nanoplates [180–183]. The described variants of self-organization of particle growth restrictions in certain directions during their formation can be classified as energy or, in generic terms, thermodynamic restrictions (Fig. 1).

Another type of nanoparticle growth restriction, which can occur during phase formation, is determined by the small magnitude of the driving force of the growth of nanoparticle size and is initiated by the high rate of nucleation [184–186]. In this case, the substance of the original composition is quickly exhausted for the almost simultaneous formation of the embryos of a new phase. The size of the forming particles in this case turns out to be close to the size of the critical embryo. Consequently, all the formed particles turn out to be similar in size. The transfer of matter from one particle to another in a system consisting of nanoparticles of almost the same size cannot be fast. This is because the driving force of the mass transfer process consists in the difference in the values of the specific surface energy, which in this specific case equals nearly zero. This type of restrictions on the growth of nanoparticles that occurred during the process of their

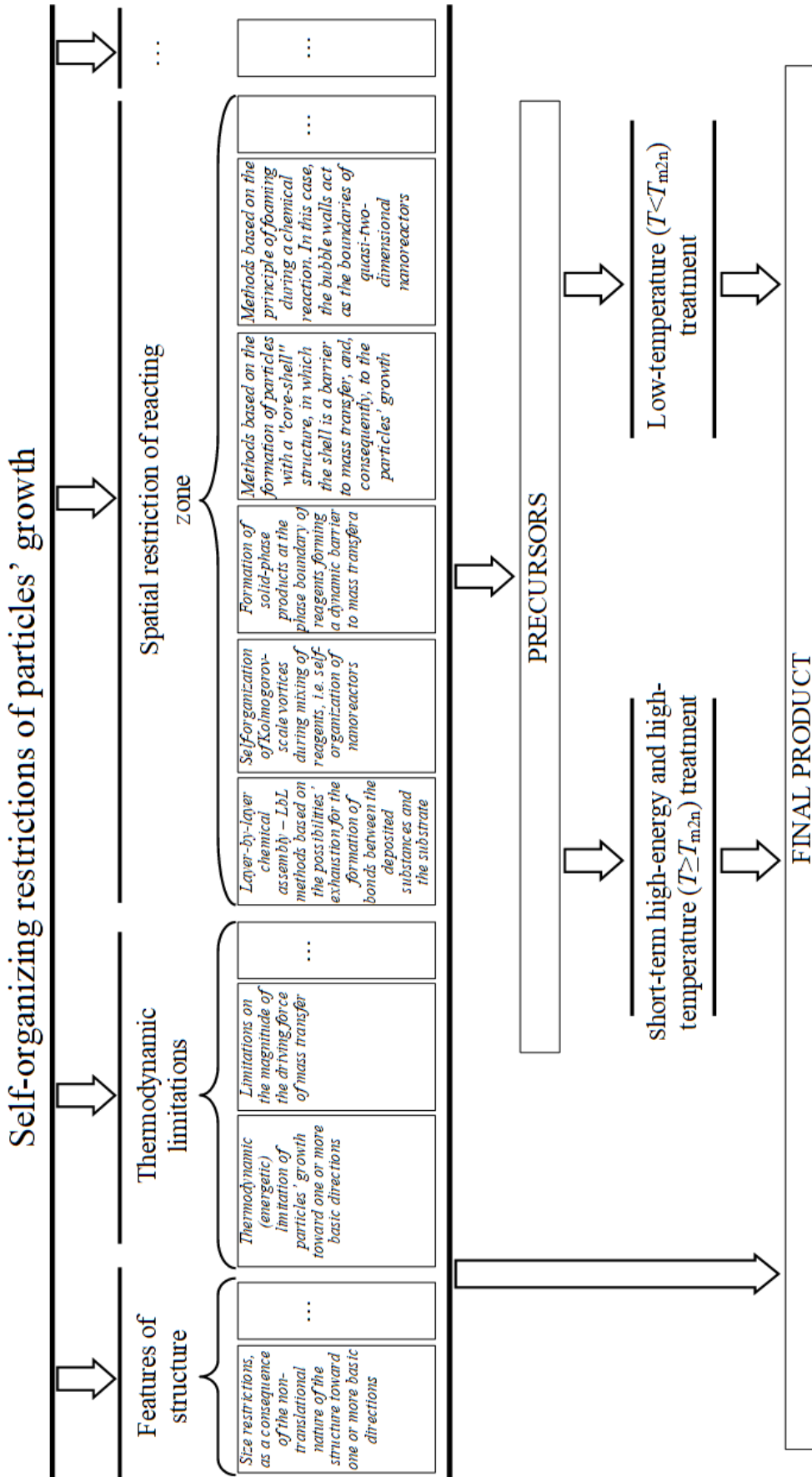


FIG. 1. Synthesis of solid phase particles over limited growth: principles and methods

formation can be classified as restrictions caused by minimizing the driving force of the mass transfer process. Some variant of this type of restriction of particle growth can be considered the case of the existence of very small particles whose specific surface energy decreases with a decrease in their size [187–193], as a result of which these particles may be in a state close to indifferent equilibrium with respect to each other. In particular, according to [194, 195], the specific surface energy of small particles is proportional to their diameter:

$$\sigma = \alpha \cdot d,$$

where $d < d_0$ is the diameter of small particles, and $\alpha = \sigma/d_0$ (Fig. 2a). In this case, in the particle size range $0 < d_i < d_0$ (Fig. 2) the expression for the value of the Gibbs energy of their formation, attributed to the unit volume, will have the following form:

$$\frac{\Delta G_i}{V_i} = \Delta g_V + \sigma_i \cdot \frac{S_i}{V_i},$$

ΔG_i is the Gibbs energy of the formation of the i -th particle, Δg_V is the volume specific Gibbs energy of the formation of the phase and, finally, S_i and V_i stand for the surface area and volume of the i -th particle. Consequently, taking into account the above dependence $\sigma(d)$, for an isometric particle, we obtain $\Delta G_i/V_i = \text{const}$ for all particles i whose size d_i lies in the interval $(0, d_0)$. In this case, none of these particles has a thermodynamic preference over other particles in the size range $(0, d_0)$.

The dependence of the Gibbs energy on the particle size can be represented as

$$\Delta G = \Delta g_V \cdot d^3 + k_f \cdot \sigma \cdot d^2 = \begin{cases} d < d_0 : & \Delta g_V \cdot d^3 + k_f \cdot \alpha \cdot d^3; \\ d \geq d_0 : & \Delta g_V \cdot d^3 + k_f \cdot \sigma_0 \cdot d^2, \end{cases}$$

where k_f is a coefficient depending on the shape of the particles.

For the case

$$k_f \cdot \alpha < |\Delta g_V|,$$

$$\sigma = \alpha \cdot d_0 : d_{cr} = \frac{2}{3} \left(\frac{k_f \cdot \alpha}{|\Delta g_V|} \right) \cdot d_0$$

the calculated value of the size of the critical nucleus is $d_{cr} < 2/3 d_0$ (Fig. 2b (I)), i.e. critical nucleus does not exist.

For the case

$$k_f \cdot \alpha > |\Delta g_V|,$$

$$\sigma = \alpha \cdot d_0 : d_{cr} = \frac{2}{3} \left(\frac{k_f \cdot \alpha}{|\Delta g_V|} \right) \cdot d_0$$

the calculated value of the size of the critical nucleus is $d_{cr} \geq d_0$ (Fig. 2b (II)).

Another type of restrictions on the growth of nanostructures is implemented within the framework of a group of methods that can be designated as methods of Layered Chemical Assembly [196]. To some extent, the term Layer-by-Layer (LbL) synthesis [196–200] is synonymous with the designation of this group of methods. Historically, the first method in this group of methods is the Molecular Layering (ML) method proposed by V.B. Aleskovsky and S.I. Koltsov [96, 99–102, 201]. In literature, this method is also referred to as Atomic Layer Epitaxy (ALE) [103] and Atomic Layer Deposition (ALD) [104]. Ideologically close to the ML is the ionic layer deposition method suggested by V.P. Tolstoy and co-authors [202]. Subsequently, this method was developed in the works of many authors [203–206]. In literature, this method is also found under terms such as Successive Ionic Layer Deposition (SILD) [207] and Successive Ionic Layer Adsorption (SILAR) [200]. The self-organization of restraining the growth of the thickness of nanolayers on the surface of a solid when using LbL methods is based on the exhaustion of the possibilities for the formation of chemical bonds between the active centers on the surface that self-organize during synthesis. These centers include landing pads and atoms (atomic groups), or ions deposited from mobile media either gaseous or liquid, with sequential (cyclic) introduction of reagents of different composition into the reaction system. The most precise synthesis of planar nanostructures by the ML method occurs in cases of formation of substances with a predominantly covalent nature of the bond. It should be noted that by changing the temperature of the ML process within a certain range, the composition, structure, and thickness of the film can be varied within this method by changing the number of active centers self-organizing in the ML process on the surface of the solid. As a consequence, the density of filling the surface layer with molecules deposited on the surface can be altered [105–108, 208]. In addition, the filling of the surface layer can also be influenced by the steric effect, which is more characteristic of organic compounds [209–211].

The described method of restricting the growth of film thickness, which is determined by the self-organization of the size of the reaction space in the direction perpendicular to the surface of the solid (Fig. 3), differs in its physico-chemical characteristics from those discussed above. The self-organization of restricting the growth of the film during its formation by LbL methods is not associated with a change in the magnitude of the driving force of the chemical interaction of reagents, as was the case in the cases described earlier. Instead, it is determined by the exhaustion of the possibility of interaction of components due to the corresponding self-organization of the reaction medium during the deposition of a substance on the surface of the solid. Thus, this type of restriction on the growth of particle sizes of the formed phases

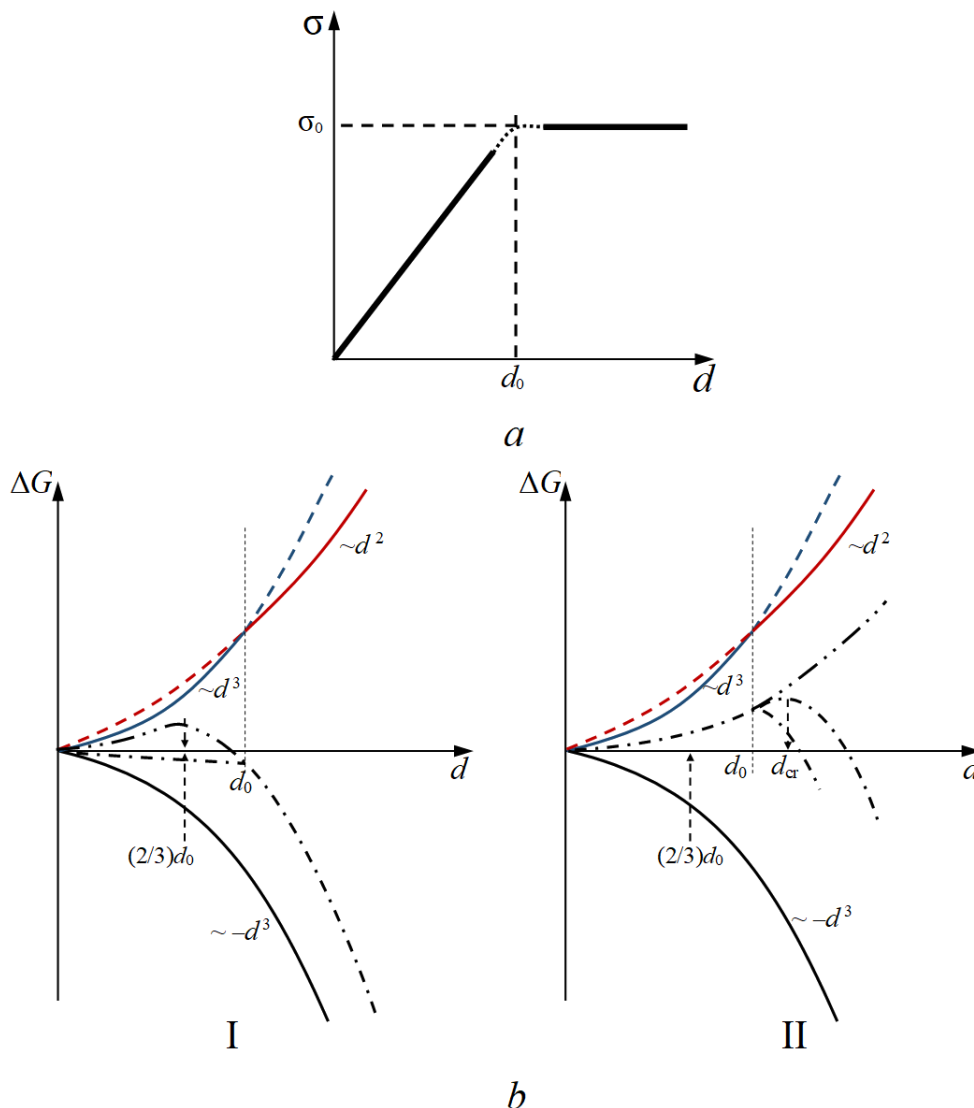
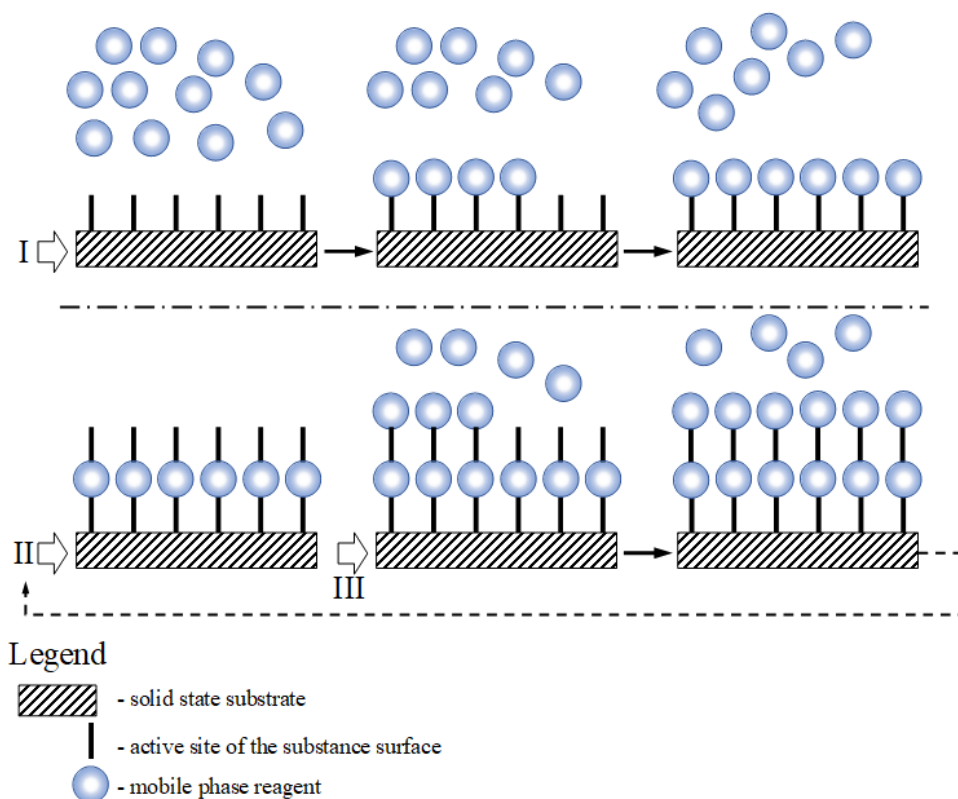


FIG. 2. Dependence of the surface energy (σ) on the particle size (d) (a); critical particle size (d_{cr}) of the formed phases (b)

introduces the next group of self-organizing constraints in the synthesis process. This class of self-organizing constraints will be based on a decrease in the possibilities for mass transfer of reagents into the reaction zone during the synthesis of nanostructures due to self-organization during the phase formation of spatially limited reaction zones (Fig. 1).

A promising direction in the organization of the synthesis of nanoparticles may be the use of intensive mixing of flows of liquid-phase reagents, in which vortices of the Kolmogorov scale are formed [212–214]. In this case, the synthesis takes place inside these vortices, and the mass transfer between the vortices is much less intense. This means that in this case, the vortices that self-organize during the mixing of reagents, in which phase formation occurs, can be considered as self-organizing nanoreactors (Fig. 1). In the works [176, 215–219] it was shown that such a method of mixing of reagents that exists, for instance, in microreactors with colliding jets [220–227], allows to synthesize nanoparticles with the smallest possible sizes under these conditions of chemical reactions. One disadvantage of the method based on the self-organization of spatial restrictions when mixing reagent solutions is, as a rule, the narrow temperature range at which solutions can be mixed. In some cases, these temperature values are not sufficient to form the final product. For example, when mixing aqueous solutions of reagents, intermediate hydroxides or amorphous forms of the substance are often created [20, 43, 142, 189, 228–232], and not the final product in the form of nanocrystalline oxide nanoparticles. That means that some nanoscale precursors are formed. In such cases, additional heat treatment is required, in which the particle size of the final product can significantly increase – as was observed during the formation of crystals of the phase with the structure of perovskite in the system $\text{Bi}_2\text{O}_3\text{--Fe}_2\text{O}_3$ [233–236].

Due to the need to achieve higher temperatures for the formation of oxide nanocrystals than is possible in the case of mixing aqueous solutions of components at atmospheric pressure, it is potentially possible to mix reagents dissolved in liquids that have higher boiling points. Another way to achieve higher temperatures is to increase the pressure in the



I – The cycle of mobile phase reagents' interaction with active centers on the surface of a solid-phase base;

II – Cycle of active centers' formation on the precipitated reagent;

III – Repeat of I-st cycle.

FIG. 3. Formation scheme of films with adjustable thickness by LbL methods

reactor to move into the field of hydrothermal synthesis. Naturally, the hydrodynamic conditions for the formation of vortices of the Kolmogorov scale change. Their boundaries acted as self-organizing spatial restrictions for mass transfer of reagents in the process of phase formation. At the same time, the transition to other reaction media in terms of chemical composition and other conditions of synthesis in terms of temperature and pressure, although it complicates in many cases the hardware design of the process, may expand the possibilities for self-organization of spatial restrictions in the reaction system.

It should be noted that when mixing reagents in the form of liquid solutions, in addition to vortex formation, other alternatives for self-organization of spatial restrictions for mass transfer of components to the particles of the resulting phase are possible. In particular, such a limitation may be the solid-phase product itself, which is formed at the contact boundary of reagent solutions (Fig. 1). The effectiveness of such a barrier for mass transfer of reagents in some cases leads to a situation where even with the usual form of introduction of one of the reagents – drops of a solution – nanocrystalline products can be obtained if two conditions are met. First, rapid nucleation is ensured at the interface of the reagents. Second, the particles formed during the new phase are quickly removed from the reaction zone, thereby ensuring the possibility of further nucleation process on the contact boundary of liquid-phase reagents [230, 234, 235, 237–240]. In the case described above, the layer of solid-phase reaction products itself acts as a self-organizing spatial restriction for the mass transfer of components from the liquid phase to the reaction zone. For the synthesis of nanoparticles with the smallest possible sizes under conditions of these spatial constraints being formed, it is important to organize a large contact surface of reagents and the rapid removal of interaction products from the reaction zone. It was shown in [241] that one of such possibilities is to carry out synthesis in apparatuses with swirling flows of reagent solutions.

A self-organizing barrier for mass transfer and, consequently, for particle growth can be surface layers that differ in their composition and structure from the volume of particles during the formation of “core-shell” structures (Fig. 1). Similar self-organizing structures during the formation of nanoparticles based on phases of variable composition were described in [242–245]. It should be noted that in these works, a noticeable decrease in the size of particles was experimentally shown precisely in the case of their formation as a “core-shell”. This is due to the difficulty of transferring matter

from one particle to another through a self-organized barrier that emerges during their formation as a surface layer of a different composition and structure – or a shell.

Another variant of self-organization of particle growth restriction is associated with the formation of foam during a chemical reaction. In cases where the layer of foam bubble walls in which phase formation occurs is thin, it can be considered as a quasi-two-dimensional microreactor or, at least, a nanoreactor. An example of such phase formation can be the synthesis of oxide nanoparticles obtained by the method of “solution combustion” [23, 25, 28, 29, 246–254] under a certain regime of this process [255, 256]. Such a “solution combustion” mode can be considered as an independent method of obtaining nanoparticles or as the method of “foam combustion” schematically depicted in Fig. 4. The effect of the self-organization of quasi-two-dimensional thin layers as quasi-two-dimensional nanoreactors upon the production of nanoparticles by the “foam combustion” method of the reduction of particle growth rate is associated with the walls (boundaries) of the layers blocking of the transfer of matter to the formed particles (Fig. 4).

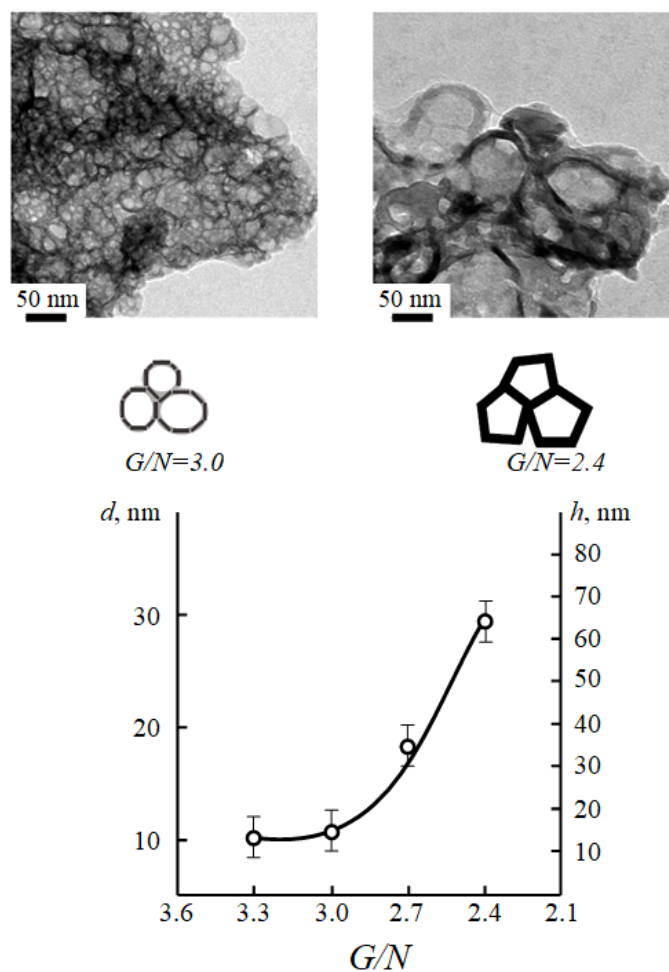


FIG. 4. Scheme of the particles growth restriction during their formation by the method of “foam combustion”. Dependence of the YFeO_3 crystallite size (d) on the thickness of the bubbles’ walls (h) formed during “foam combustion” (fuel-glycine, oxidizer-yttrium and iron (III) nitrates) at different glycine-nitrate ratios (G/N)

It should be emphasized that the effect of foaming on the course of chemical reactions was noted in different phase formation processes [20, 257–260]. Indicative in this regard is the self-oscillating process of foaming liquid during the decomposition of formic acid described in [260]. The self-oscillation of foaming is caused by an increase in the rate and reaction of decomposition of formic acid at the interface of the liquid and gaseous phases. This leads to an increase in the rate of foaming until it reaches exhaustion in the reaction zone of the reagent. Subsequently, the foam disappears, and the process starts from the initial state. Summarizing the considered cases of the influence of foaming on chemical reactions, it can be concluded that by conducting the synthesis process in a thin layer self-organizing during the chemical interaction of components at the interface of bulk phases, one can expect both an increase in the rate of chemical reactions and a decrease in the size of the particles formed due to the restricting of the mass transfer process by the boundaries of this layer (quasi-two-dimensional nanoreactor). As it was shown in [105, 106], the effects described above are also characteristic of some solid-phase reactions.

3. Multistage phase formation processes and combination of crystal growth restrictions

In some cases, one or more high-temperature operations are required to form the final product [43, 230, 234, 235, 261–263]. This is the case for example when the goal of synthesis is to obtain oxide nanoparticles and at the initial stage soft chemistry methods are used to form hydroxide nanoparticles that are stable at temperatures of soft chemical synthesis. Another similar example may be the formation of oxide nanoparticles by the “foam combustion” method in cases where the temperature-time regime of the combustion of reagents leads to the formation of an amorphous phase instead of the target product, like oxide nanocrystals of a given composition and structure, and additional processing of the precursor material is required [8, 20, 255, 264–266]. A common feature of these and other similar situations is that the conditions of synthesis with self-organizing restrictions for particle growth, primarily its temperature-time regime, do not allow the formation of the target product in one stage. Since to obtain small particles, it is necessary to reduce the influence of the mass transfer process as well as the temperature and duration of synthesis (Fig. 1), situations when additional higher temperature and longer stages are required for the formation of the target product are frequent.

An increase in the temperature of synthesis always leads to an increase in the diffusion rate, which means that it increases the growth rate of particles of the reaction product. The effect of increasing the mass transfer rate on particle growth can be reduced either by shortening the duration of heat treatment, or by spatial separation of precursor particles, or by both. Reducing the duration of heat treatment without reducing the effectiveness of obtaining the target product – nanoparticles of a given composition and structure – is possible by means of radiation and laser heating [267–273]. An example of a technology that combines short duration of heat treatment with spatial separation of precursor particles, is spray pyrolysis [274–280]. Other approaches that implement short-term high-intensity energy effects on materials are also being developed and those include processing in electron flows, radiation stimulation of processes in solid phases [281–284], processing in low-temperature plasma [285–287], and more.

The methods listed above can also be used as independent ways for obtaining nanoparticles, but their significant disadvantage is, as a rule, that they cannot be used for synthesizing nanoparticles of compounds of complex composition. Soft chemistry methods are devoid of this disadvantage. Therefore, it is promising to combine methods of soft chemistry, including in conditions of self-organization of particle growth restrictions in the reaction zone, with methods of short-term high-energy processing of precursors obtained at the first stage.

It should be noted that the high-energy effect on precursors is not the only method of transformation into the final product and, in particular, into nanocrystalline oxides from hydroxide nanoparticles. For example, methods for obtaining oxides from the corresponding hydroxides by varying the partial pressure of water in the reaction space appear to be promising in this area. The selection of the pressure (P) and temperature (T) values necessary for the dehydration of hydroxides can be carried out either according to experimental data on the stability diagrams of hydroxide phases [288, 289], or according to thermodynamic calculations [290]. When selecting (P, T)-conditions for the production of oxides within the framework of these methods, it should be taken into account that the temperature should not exceed some critical values to not critically activate mass transfer processes in the reaction system. As it was shown in [6], the melting point of non-autonomous phases (T_{m2n}) can act as such a temperature limitation [291–293]. At $T < T_{m2n}$ mass transfer cannot ensure rapid particle growth and, consequently, there are no firm restrictions on the duration of precursor treatment. In this regard, the value of T_{m2n} is a boundary that divides all phases into high-temperature $T > T_{m2n}$, processes that proceed with a high rate of transfer of matter between grains and low-temperature processes $T < T_{m2n}$ [6, 291, 294–299].

Precursors formed at the first stage of synthesis are not limited to hydroxides and, consequently, the choice of conditions for the formation of nanoparticles of the target product should be based on the analysis of the chemical stability of the corresponding precursor phases. As for hydroxides, such an analysis can be conducted on the basis of appropriate experimental data or by thermodynamic calculations.

The described approaches to the transformation of precursor nanoparticles into nanocrystalline target products can be supplemented by other methods based for example on mechanochemical effects [300–306]. However, since the systematic consideration of such methods is not the purpose of this work, it only provides a schematic representation of the possibility of combining various methods of restricting crystal growth using multistage processes of synthesis of nanocrystalline phases (Fig. 1).

4. Conclusion

Analysis of literature data has shown the prospects of synthesis methods in which particle growth restrictions are formed during the synthesis process itself. The disadvantage of many of such methods consisting in the fact that nanoparticles of precursor phases are formed instead of target products can be compensated by combining several different methods of synthesis. Based on the analysis of literature data, examples of the transformation of precursor nanoparticles into nanocrystals of target phases are classified and presented. A scheme that allows optimal combination of synthesis methods to obtain nano-crystalline particles of a given composition, structure, size, shape, is designed.

References

- [1] Kuni F.M., Rusanov A.I. The homogeneous nucleation theory and the fluctuation of the center of mass of a drop. *Physics Letters A*, 1969, **29** (6), P. 337–338.
- [2] Almjasheva O.V., Gusarov V.V. Metastable clusters and aggregative nucleation mechanism. *Nanosystems: Physics, Chemistry, Mathematics*, 2014, **5** (3), P. 405–417.
- [3] Shi R., Heo T.W., Wood B.C., Wang Y. Critical nuclei at hetero-phase interfaces. *Acta Materialia*, 2020, **200** (6201), P. 510–525.
- [4] Keesee R.G. Nucleation and Particle Formation in the Upper Atmosphere. *J. of Geophysical Research*, 1989, **94** (D12), P. 14683–14692.
- [5] Almyasheva O.V., Lomanova N.A., et al. The minimal size of oxide nanocrystals: phenomenological thermodynamic vs crystal-chemical approaches. *Nanosystems: Physics, Chemistry, Mathematics*, 2019, **10** (4), P. 428–437.
- [6] Gusarov V.V. Fast Solid-Phase Chemical Reactions. *Russian J. of General Chemistry*, 1997, **67** (12), P. 1846–1851.
- [7] Popkov V.I., Almjasheva O.V., Gusarov V.V. The investigation of the structure control possibility of nanocrystalline yttrium orthoferrite in its synthesis from amorphous powders. *Russian J. of Applied Chemistry*, 2014, **87**, P. 1417–1421.
- [8] Popkov V.I., Almjasheva O.V., et al. The role of pre-nucleus states in formation of nanocrystalline yttrium orthoferrite. *Doklady Chemistry*, 2016, **471**, P. 356–359.
- [9] Gusarov V.V., Almjasheva O.V. The role of non-autonomous state of matter in the formation of structure and properties of nanomaterials. Chapter 13 in the book *Nanomaterials: properties and promising applications*. Ed. A.B. Yaroslavtsev. Scientific World Publishing House, Moscow, 2014, P. 378–403. (in Russian)
- [10] Kotov Yu.A., Azarkevich E.I., et al. Iron oxide nanopowders prepared by the electroexplosion of wire. *Inorganic Materials*, 2007, **43** (6), P. 633–637.
- [11] Kotov Y.A. The electrical explosion of wire: A method for the synthesis of weakly aggregated nanopowders. *Nanotechnologies in Russia*, 2009, **4** (7–8), P. 415–424.
- [12] Kotov Y.A., Samatov O.M., et al. Production and Characteristics of Composite Nanopowders Using a Fiber Ytterbium Laser. *Technical Physics*, 2011, **56** (5), P. 652–655.
- [13] Ilyin A.P. Development of electroexplosive technology for obtaining nanopowders at the High Voltage Research Institute at Tomsk Polytechnic University. *Bulletin of the Tomsk Polytechnic University*, 2003, **306** (1), P. 133–139.
- [14] Pozhidaeva O.V., Korytkova E.N., Romanov D.P., Gusarov V.V. Formation of ZrO₂ nanocrystals in hydrothermal media of various chemical compositions. *Russian J. of General Chemistry*, 2002, **72** (6), P. 849–853.
- [15] Popkov V.I., Bachina A.K., et al. Synthesis, morphology and electrochemical properties of spherulite titania nanocrystals. *Ceramics International*, 2020, **56** (15), P. 24483–24487.
- [16] Ivanov V.K., Polezhaeva O.S. Synthesis of ultrathin ceria nanoplates. *Russian J. of Inorganic Chemistry*, 2009, **54** (10), P. 1528–1530.
- [17] Tyrsted C., Becker J., et al. In-Situ Synchrotron Radiation Study of Formation and Growth of Crystalline Ce_xZr_{1-x}O₂ Nanoparticles Synthesized in Supercritical Water. *Chemistry of Materials*, 2010, **22** (5), P. 1814–1820.
- [18] Ivanov V.K., Kopitsa G.P., et al. Hydrothermal growth of ceria nanoparticles. *Russian J. of Inorganic Chemistry*, 2009, **54** (12), P. 1857–1861.
- [19] Enikeeva M.O., Danilovich D.P., Proskurina O.V., Gusarov V.V. Formation of nanocrystals based on equimolar mixture of lanthanum and yttrium orthophosphates under microwave-assisted hydrothermal synthesis. *Nanosystems: Physics, Chemistry, Mathematics*, 2020, **11** (6), P. 705–715.
- [20] Popkov V.I., Almjasheva O.V., et al. Effect of spatial constraints on the phase evolution of YFeO₃-based nanopowders under heat treatment of glycine-nitrate combustion products. *Ceramics International*, 2018, **44** (17), P. 20906–20912.
- [21] Zaboeva E.A., Izotova S.G., Popkov V.I. Glycine-nitrate combustion synthesis of CeFeO₃-based nanocrystalline powders. *Russian J. of Applied Chemistry*, 2016, **89**, P. 1228–1236.
- [22] Simagina V.I., Komova O.V., et al. Study of Copper-Iron Mixed Oxide with Cubic Spinel Structure, Synthesized by the Combustion Method. *Russian J. of Applied Chemistry*, 2019, **92**, P. 20–30.
- [23] Ostroushko A.A., Russkikh O.V. Oxide material synthesis by combustion of organicinorganic Compositions. *Nanosystems: Physics, Chemistry, Mathematics*, 2017, **8** (4), P. 476–502.
- [24] Khaliullin Sh.M., Zhuravlev V.D., et al. Thermal characteristics, gassing in solution combustion synthesis and conductivity of CaZrO₃. *Int. J. of Self-Propagating High-Temperature Synthesis*, 2015, **24** (2), P. 83–88.
- [25] Varma A., Mukasyan A.S., Rogachev A.S., Manukyan K.V. Solution Combustion Synthesis of Nanoscale Materials. *Chemical Reviews*, 2016, **116**, P. 14493–14586.
- [26] Manukyan K.V., Cross A., et al. Solution Combustion Synthesis of Nano-Crystalline Metallic Materials: Mechanistic Studies. *J. of Physical Chemistry C*, 2013, **117**, P. 24417–24427.
- [27] Trusov G.V., Tarasov A.B., et al. Spray Solution Combustion Synthesis of Metallic Hollow Microspheres. *J. of Physical Chemistry C*, 2016, **120**, P. 7165–7171.
- [28] Khaliullin S.M., Zhuravlev V.D., Bamburov V.G. Solution-combustion synthesis of oxide nanoparticles from nitrate solutions containing glycine and urea: Thermodynamic aspects. *Int. J. of Self-Propagating High-Temperature Synthesis*, 2016, **25** (3), P. 139–148.
- [29] Li F.T., Ran J., Jaroniec M., Qiao S.Z. Solution combustion synthesis of metal oxide nanomaterials for energy storage and conversion. *Nanoscale*, 2015, **7** (42), P. 17590–17610.
- [30] Saukhimov A.A., Hobosyan M.A., et al. Solution-combustion synthesis and magnetodielectric properties of nanostructured rare earth ferrites. *Int. J. of Self-Propagating High-Temperature Synthesis*, 2015, **24** (2), P. 63–71.
- [31] Sun L., Yuan G., Gao L., Yang J., Chhowalla M., Gharahcheshmeh M.H., Gleason K.K., Choi Y.S., Hong B.H., Liu Z. Chemical vapour deposition. *Nature Reviews Methods Primers*, 2021, **1** (1), P. 5.
- [32] Cai Z., Liu B., Zou X., Cheng H.M. Chemical vapor deposition growth and applications of two-dimensional materials and their heterostructures. *Chemical Reviews*, 2018, **118**, P. 6091–6133.
- [33] Martínez L., Mayoral A., et al. Core@shell, Au@TiO_x nanoparticles by gas phase synthesis. *Nanoscale*, 2017, **9**, P. 6463–6470.
- [34] Deepak N., Carolan P., et al. Tunable nanoscale structural disorder in Aurivillius phase, $n = 3$ Bi₄Ti₃O₁₂ thin films and their role in the transformation to $n = 4$, Bi₅Ti₃FeO₁₅ phase. *J. of Materials Chemistry C*, 2015, **3** (22), P. 5727–5732.
- [35] Yau S.-T., Vekilov P.G. Quasi-planar nucleus structure in apoferritin crystallization. *Nature*, 2000, **406** (6795), P. 494–497.
- [36] Ivanov V.K., Fedorov P.P., Baranchikov A.Ye., Osiko V.V. Oriented attachment of particles: 100 years of investigations of non-classical crystal growth. *Russian Chemical Reviews*, 2014, **83** (12), P. 1204–1222.
- [37] Fedorov P., Mayakova M., et al. Preparation of "NaREF₄" phases from the sodium nitrate melt. *J. of Fluorine Chemistry*, 2019, **218**, P. 69–75.
- [38] Fedorov P.P., Ivanov V.K., Osiko V.V. Basic features and crystal-growth scenarios based on the mechanism of oriented attachment growth of nanoparticles. *Doklady Physics*, 2015, **60** (11), P. 483–485.

- [39] Penn R.L., Banfield J.F. Oriented attachment and growth, twinning, polytypism, and formation of metastable phases: Insights from nanocrystalline TiO_2 . *American Mineralogist*, 1998, **83** (9–10), P. 1077–1082.
- [40] Penn R.L., Banfield J.F. Imperfect oriented attachment: Dislocation generation in defect-free nanocrystals. *Science*, 1998, **281**, P. 969–971.
- [41] Fedorov P.P., Maslov V.A., et al. Flintstone as a nanocomposite material for photonics. *Nanosystems: Physics, Chemistry, Mathematics*, 2018, **9** (5), P. 603–608.
- [42] Lin Q., Wang X., Li J., Han Y. Oriented aggregation of silver particles in gel solutions. *Colloids and Surfaces A*, 2018, **555**, P. 161–169.
- [43] Lomanova N.A., Tomkovich M.V., et al. Formation of $\text{Bi}_{m+1}\text{Fe}_{m-3}\text{Ti}_3\text{O}_{3m+3}$ ($m = 4-9$) nanocrystals upon thermal decomposition of coprecipitated hydroxides. *Russian J. of Inorganic Chemistry*, 2021, **66** (5), P. 755–764.
- [44] Lomakin M.S., Proskurina O.V., et al. Hydrothermal Synthesis, Phase Formation and Crystal Chemistry of the Pyrochlore/ Bi_2WO_6 and Pyrochlore/ $\alpha\text{-Fe}_2\text{O}_3$ Composites in the $\text{Bi}_2\text{O}_3\text{-Fe}_2\text{O}_3\text{-WO}_3$ System. *J. of Solid State Chemistry*, 2020, **282**, P. 121064.
- [45] Lomakin M.S., Proskurina O.V., Gusarov V.V. Influence of hydrothermal synthesis conditions on the composition of the pyrochlore phase in the $\text{Bi}_2\text{O}_3\text{-Fe}_2\text{O}_3\text{-WO}_3$ system. *Nanosystems: Physics, Chemistry, Mathematics*, 2020, **11** (2), P. 246–251.
- [46] Kostyukhina E.M., Kustova A.L., Kustov L.M. One-step hydrothermal microwave-assisted synthesis of LaFeO_3 nanoparticles. *Ceramics International*, 2019, **45** (11), P. 14384–14388.
- [47] Denisova L.T., Molokeev M.S., et al. Synthesis, Crystal Structure, and Thermal Properties of Substituted Titanates $\text{Bi}_2\text{Pr}_2\text{Ti}_3\text{O}_{12}$ and $\text{Bi}_2\text{Nd}_2\text{Ti}_3\text{O}_{12}$. *Physics of the Solid State*, 2021, **63** (8), P. 1159–1164.
- [48] Zhuk N.A., Sekushin N.A., et al. Dielectric properties, Mössbauer study, ESR spectra of $\text{Bi}_2\text{FeTa}_2\text{O}_{9.5}$ with pyrochlore structure. *J. of Alloys and Compounds*, 2022, **903**, P. 163928.
- [49] Matsukevich I., Kulak A., et al. Comparison of different methods for $\text{Li}_2\text{MTi}_3\text{O}_8$ ($M = \text{Co}, \text{Cu}, \text{Zn}$) synthesis. *J. of Chemical Technology & Biotechnology*, 2021, **97** (4), P. 1021–1026.
- [50] Tugova E.A. A comparative analysis of the formation processes of Ruddlesden-Popper phases in the $\text{La}_2\text{O}_3\text{-SrO-M}_2\text{O}_3$ ($M = \text{Al}, \text{Fe}$) systems. *Glass Physics and Chemistry*, 2009, **35** (4), P. 416–422.
- [51] Klyndyuk A.I., Tugova E.A., et al. Formation of solid solutions of multiferroics in the $\text{Bi}_2\text{O}_3\text{-Nd}_2\text{O}_3\text{-Fe}_2\text{O}_3$ system. *Russian J. of General Chemistry*, 2016, **86** (10), P. 2282–2287.
- [52] Karami M., Masoudpanah S.M., Rezaie H.R. Solution combustion synthesis of hierarchical porous LiFePO_4 powders as cathode materials for lithium-ion batteries. *Advanced Powder Technology*, 2021, **32** (6), P. 1935–1942.
- [53] Alhaji A., Taherian M.H., Ghorbani S., Sharifnia S.A. Development of synthesis and granulation process of MgAl_2O_4 powder for the fabrication of transparent ceramic. *Optical Materials*, 2019, **98**, P. 109440.
- [54] Zhang Y., Bu A., et al. Rapid synthesis of $\text{Y}_3\text{Al}_5\text{O}_{12}$ powders via plasma electrolysis. *Ceramics International*, 2021, **47** (21), P. 30147–30155.
- [55] Opuchovic O., Beganskiene A., Kareiva A. Sol-gel derived $\text{Tb}_3\text{Fe}_5\text{O}_{12}$ and $\text{Y}_3\text{Fe}_5\text{O}_{12}$ garnets: Synthesis, phase purity, micro-structure and improved design of morphology. *J. of Alloys and Compounds*, 2015, **647**, P. 189–197.
- [56] Klyndyuk A.I., Chizhova E.A., et al. Thermoelectric Multiphase Ceramics Based on Layered Calcium Cobaltite, as Synthesized Using Two-Stage Sintering. *Glass Physics and Chemistry*, 2020, **46**, P. 562–569.
- [57] Tretyakov Yu.D., Lukashin A.V., Eliseev A.A. Synthesis of functional nanocomposites based on solid-phase nanoreactors. *Russian Chemical Reviews*, 2004, **73** (9), P. 899–921.
- [58] Petrosko S. H., Johnson R., White H., Mirkin C.A. Nanoreactors: small spaces, big implications in chemistry. *J. of the American Chemical Society*, 2016, **138**, P. 7443–7445.
- [59] Swisher J.H., Jibril L., Petrosko S.H., Mirkin C.A. Nanoreactors for particle synthesis. *Nature Reviews Materials*, 2022, **7**.
- [60] Eliseev A.A., Falaleev N.S., et al. Size-dependent structure relations between nanotube and encapsulated nanocrystal. *Nano Letters*, 2017, **17**, P. 805–810.
- [61] Eliseev A.A., Kharlamova M.V., et al. Preparation and properties of single-walled nanotubes filled with inorganic compounds. *Russian Chemical Reviews*, 2009, **78** (9), P. 833–854.
- [62] Yashina L.V., Eliseev A.A., et al. Growth and Characterization of One-Dimensional SnTe Crystals within the Single-Walled Carbon Nanotube Channels. *The J. of Physical Chemistry C*, 2011, **115** (9), P. 3578–3586.
- [63] Naberezhnov A.A., Stukova E.V., et al. Effects Associated with Confined Geometry in Nanocomposites Based on Mesoporous 2D-SBA-15 and 3D-SBA-15 Matrices Containing Sodium Nitrite Nanoparticles. *Technical Physics*, 2019, **64** (12), P. 1866–1871.
- [64] Alekseeva O.A., Naberezhnov A.A., et al. Temperature range broadening of the ferroelectric phase in KNO_3 nanoparticles embedded in the pores of the nanoporous Al_2O_3 matrix. *Ferroelectrics*, 2021, **574** (1), P. 8–15.
- [65] Bronstein L.M., Sidorov S.N., Valetsky P.M. Nanostructured polymeric systems as nanoreactors for nanoparticle formation. *Russian Chemical Reviews*, 2004, **73** (5), P. 501–515.
- [66] Maslennikova T.P., Korytkova E.N., Kuznetsova O.M., Pivovarova L.N. Thermochemical modification of $\text{Mg}_3\text{Si}_2\text{O}_5(\text{OH})_4$ hydrosilicate nanotubes by silver nitrate solutions. *Glass Physics and Chemistry*, 2016, **42** (3), P. 288–294.
- [67] Maslennikova, T.P., Korytkova, E.N. Influence of synthesis of physicochemical parameters on growth of $\text{Ni}_3\text{Si}_2\text{O}_5(\text{OH})_4$ nanotubes and their filling with solutions of hydroxides and chlorides of alkaline metals. *Glass Physics and Chemistry*, 2013, **39**, P. 67–72.
- [68] Maslennikova T.P., Gatina E.N. Modification of $\text{Mg}_3\text{Si}_2\text{O}_5(\text{OH})_4$ nanotubes by magnetite nanoparticles. *Glass Physics and Chemistry*, 2017, **43** (3), P. 257–262.
- [69] Molz E., Wong Apollo P.Y., Chan M.H.W., Beamish J.R. Freezing and melting of fluids in porous glasses. *Physical Review B*, 1993, **48** (9), P. 5741–5750.
- [70] Saridakis E., Chayen N.E., Sear R.P. Experiment and theory for heterogeneous nucleation of protein crystals in a porous medium. *Proceedings of the National Academy of Sciences of the United States of America*, 2006, **103** (3), P. 597–601.
- [71] Page A.J., Sear R.P. Heterogeneous Nucleation in and out of Pores. *Physical Review Letters*, 2006, **97**, 065701.
- [72] Nanev C., Govada L., Chayen N.E. Theoretical and experimental investigation of protein crystal nucleation in pores and crevices. *International Union of Crystallography*, 2021, **8** (2), P. 270–280.
- [73] Zalinaeva A., Serov A., et al. Self-supported PdxBi catalysts for the electrooxidation of glycerol in alkaline media. *J. of the American Chemical Society*, 2014, **136** (10), P. 3937–3945.
- [74] Kharlamova M.V., Sapoletova N.A., Eliseev A.A., Lukashin A.V. Magnetic properties of γ -iron oxide nanoparticles in a mesoporous silica matrix. *J. of Experimental and Theoretical Physics Letters*, 2007, **85** (9), P. 439–443.
- [75] Gorozhankin D.F., Eliseev A.A., et al. Synthesis and Properties of Iron Oxide Nanoparticles in the Matrix of Mesoporous Silica. *Doklady Chemistry*, 2004, **396** (4–6), P. 132–135.
- [76] Eliseev A.A., Gorozhankin D.F., et al. Preparation of strontium hexaferrite nanowires in the mesoporous silica matrix MCM-41. *J. of Magnetism and Magnetic Materials*, 2005, **290** (1), P. 106–109.

- [77] Burova L.I., Petukhov D.I., et al. Preparation and properties of ZnO nanoparticles in the mesoporous silica matrix. *Superlattices and Microstructures*, 2006, **39** (1–4), P. 257–266.
- [78] Sokolov M.R., Enakieva Y.Yu., et al. Intercalation of Porphyrin-Based SURMOF in Layered Eu(III) Hydroxide: An Approach Toward Sym-bimetic Hybrid Materials. *Advanced Functional Materials*, 2020, **30** (27), 2000681.
- [79] Yapryntsev A.D., Baranchikov A.E., Ivanov V.K. Layered rare-earth hydroxides: a new family of anion-exchangeable layered inorganic materials. *Russian Chemical Reviews*, 2020, **89** (6), P. 629–666.
- [80] Takaiwa D., Hatano I., Koga K., Tanakathe H. Phase diagram of water in carbon nanotubes. *Proceeding of the National Academy Sciences of the United States of America*, 2008, **105** (1), P. 39–43.
- [81] Findenege G.H., Jähner S., Akcakayiran D., Schreiber A. Freezing and melting of water confined in silica nanopores. *Chem. Phys. Chem.*, 2008, **9** (18), P. 2651–2659.
- [82] Ghernysheva M.V., Kiseleva E.A., et al. Synthesis and investigation of nanocrystals inside channels of single-walled carbon nanotubes. *Int. Sci. J. for Alternative Energy and Ecology*, 2008, **57** (1), P. 22–29. (In Russian)
- [83] Kharlamova M.V., Kramberger C. Applications of Filled Single-Walled Carbon Nanotubes: Progress, Challenges, and Perspectives. *Nanomaterials*, 2021, **11** (11), 2863.
- [84] Rempel A.A., Valeeva A.A., Vokhmintsev A.S., Weinstein I.A. Titanium dioxide nanotubes: synthesis, structure, properties and applications. *Russian Chemical Reviews*, 2021, **90** (11), P. 1397–1414.
- [85] Latysheva E.N., Pirozerskii A.L., et al. Polymorphism of Ga–In Alloys in Nanoconfinement Conditions. *Physics of the Solid State*, 2015, **57**, P. 131–135.
- [86] Riboni F., Nguyen N.T., So S., Schmuki P. Aligned metal oxide nanotube arrays: key-aspects of anodic TiO₂ nanotube formation and properties. *Nanoscale Horizons*, 2016, **1** (6), P. 445–466.
- [87] Li G., Fu C., et al. Giant Raman Response to the Encapsulation of Sulfur in Narrow Diameter Single-Walled Carbon Nanotubes. *J. of the American Chemical Society*, 2016, **138** (1), P. 40–43.
- [88] Monet G., Paineau E., et al. Solid wetting-layers in inorganic nano-reactors: the water in imogolite nanotube case. *Nanoscale Advances*, 2020, **2** (5), P. 1869–1877.
- [89] Vafakish B., Wilson, L.D. A Review on Recent Progress of Glycan-Based Surfactant Micelles as Nanoreactor Systems for Chemical Synthesis Applications. *Polysaccharides*, 2021, **2** (1), P. 168–186.
- [90] Porras M., Martínez A., et al. Ceramic particles obtained using W/O nano-emulsions as reaction media. *Colloids and Surfaces A: Physicochemical and Engineering Aspects*, 2005, **270–271**, P. 189–194.
- [91] Hada R. A Novel Synthesis Process for Making Nickel Oxide Nanoparticles. *Int. Research J. of Pure and Applied Chemistry*, 2013, **3**, P. 111–117.
- [92] Al'myasheva O.V., Gusarov V.V. Nucleation in media in which nanoparticles of another phase are distributed. *Doklady Physical Chemistry*, 2009, **424**, P. 43–45.
- [93] He Z., Alexandridis P. Nanoparticles in ionic liquids: interactions and organization. *Physical Chemistry Chemical Physics*, 2015, **17**, P. 18238–18261.
- [94] Hammond O., Mudring A.-V. Ionic Liquids and Deep Eutectics as a Transformative Platform for the Synthesis of Nanomaterials. *Chemical Communications*, 2022, **58**, P. 3865–3892.
- [95] Sergievskaya A., Chauvin A., Konstantinidis S. Sputtering onto liquids: a critical review. *Beilstein J. of Nanotechnology*, 2022, **13**, P. 10–53.
- [96] Kol'tsov S.I., Aleskovskii V.B. Effect of degree of dehydration of silica gel on mechanism of hydrolysis of adsorbed titanium tetrachloride. *Russian J. of Physical Chemistry*, 1968, **42** (5), P. 630–632.
- [97] Aleskovskii V.B. Chemistry and technology of solids. *J. of Applied Chemistry of the USSR*, 1974, **47** (10), P. 2207–2217.
- [98] Malygin A.A. Molecular Layering Nanotechnology. *Nanotechnologies in Russia (Rossiiskie Nanotekhnologii)*, 2007, **2** (3–4), P. 87–100. (In Russian)
- [99] Malygin A.A., Drozd V.E., et al. Aleskovskii's "Framework" Hypothesis to the Method of Molecular Layering/Atomic Layer Deposition. *Chemical Vapor Deposition*, 2015, **21**, P. 216–240.
- [100] Sosnov E.A., Malkov A.A., Malygin A.A. Nanotechnology of Molecular Layering in Production of Inorganic and Hybrid Materials for Various Functional Purposes (a Review): I. History of the Development of the Molecular Layering Method. *Russian J. of Applied Chemistry*, 2021, **94** (8), P. 1022–1037.
- [101] Sosnov E.A., Malkov A.A., Malygin A.A. Nanotechnology of Molecular Layering in Production of Inorganic and Hybrid Materials for Various Functional Purposes: II. Molecular Layering Technology and Prospects for Its Commercialization and Development in the XXI Century. *Russian J. of Applied Chemistry*, 2021, **94** (9), P. 1189–1215.
- [102] Malygin A.A. Molecular Layering Technology and Some of its Applications. *Russian J. of Applied Chemistry*, 1996, **69** (10) P. 1419–1426.
- [103] Goodman C.H.L., Pessa M.V. Atomic layer epitaxy. *J. of Applied Physics*, 1986, **60**, R65.
- [104] George S.M. Atomic layer deposition: An overview. *Chemical Review*, 2010, **110** (1), P. 111–131.
- [105] Gusarov V.V., Malkov A.A., Ishutina Zh.N., Malygin A.A. Phase formation in a nanosize silicon oxide film on the surface of aluminum oxide. *Technical Physics Letters*, 1998, **24** (1), P. 1–3.
- [106] Gusarov V.V., Ishutina Z.N., Malkov A.A., Malygin A.A. Peculiarities of the solid-phase chemical reaction in formation of mullite in the nanosize film composition. *Doklady Akademii Nauk*, 1997, **357** (2), P. 203–205. (In Russian)
- [107] Gusarov V.V., Malkov A.A., Malygin A.A., Suvorov S.A. Generation of aluminum titanate in compositions with high-level of space and structural conjugation of components. *Zhurnal Obshchei Khimii*, 1994, **64** (4), P. 554–557. (In Russian)
- [108] Smirnova Zh.N., Gusarov V.V., et al. High-Speed Synthesis of Mullite. *Zhurnal Obshchei Khimii*, 1995, **65** (2), P. 199–204. (In Russian)
- [109] Ramazanov S., Sobola D.S., et al. Surface Modification and Enhancement of Ferromagnetism in BiFeO₃ Nanofilms Deposited on HOPG. *Nanomaterials*, 2020, **10** (10), P. 1990.
- [110] Orudzhiev F., Ramazanov S., et al. Atomic Layer Deposition of Mixed-Layered Aurivillius Phase on TiO₂ Nanotubes: Synthesis, Characterization and Photoelectrocatalytic Properties. *Nanomaterials*, 2020, **10** (11), P. 2183.
- [111] Koshtyal Y., Nazarov D., et al. Atomic Layer Deposition of NiO to Produce Active Material for Thin-Film Lithium-Ion Batteries. *Coatings*, 2019, **9** (5), P. 301.
- [112] Lukashin A.V., Eliseev A.A., et al. Synthesis of PbS/S Nanostructures through. *Doklady Chemistry*, 2002, **383** (4–6), P. 93–96.
- [113] Lukashin A.V., Vertegel A.A., et al. Chemical Design of Magnetic Nanocomposites Based on Layered Double Hydroxides. *J. of Nanoparticle Research*, 2003, **5**, P. 455–464.
- [114] Nikiforov M.P., Chernysheva M.V., et al. Synthesis of Iron-Containing Oxide Nanocomposites from LDH Precursors. *Doklady Chemistry*, 2003, **391** (1–3), P. 173–176.

- [115] Lukashin A.V., Vyacheslavov A.S., Vertegel A.A., Tret'yakov Yu.D. Synthesis of PbS/LDH Nanocomposites with the Use of the Method of Reversible Delamination of LDHs. *Doklady Chemistry*, 2002, **385** (1–3), P. 178–181.
- [116] Parida K., Satpathy M., Mohapatra L. Incorporation of Fe³⁺ into Mg/Al layered double hydroxide framework: Effects on textural properties and photocatalytic activity for H₂ generation. *J. of Materials Chemistry*, 2012, **22**, P. 7350–7357.
- [117] Boumeriame H., Da Silva E.S., et al. Layered double hydroxide (LDH)-based materials: A mini-review on strategies to improve the performance for photocatalytic water splitting. *J. of Energy Chemistry*, 2022, **64**, P. 406–431.
- [118] Voropaeva D.Yu., Novikova S.A., Yaroslavtsev A.B. Polymer electrolytes for metal-ion batteries. *Russian Chemical Reviews*, 2020, **89** (10), P. 1132–1155.
- [119] Ushakov N.M., Yurkov G.Yu., et al. Nanocomposites based on the cerium oxide nanoparticles and polyethylene matrix: Syntheses and properties. *Acta Materialia*, 2008, **56** (10), P. 2336–2343.
- [120] De Martino M.T., Abdelmohsen L.K.E.A., Rutjes F.P.J.T., van Hest J.C.M. Nanoreactors for green catalysis. *Beilstein J. of Organic Chemistry*, 2018, **14**, P. 716–733.
- [121] Vriezema D.M., Aragonès M.C., et al. Self-Assembled Nanoreactors. *Chemical Reviews*, 2005, **105**, P. 1445–1489.
- [122] Syah R., Zahar M., Kianfar E. Nanoreactors: properties, applications and characterization. *Int. J. of Chemical Reactor Engineering*, 2021, **19** (10), P. 981–1007.
- [123] Kaur M., Singh B. A Brief Review of Construction, Working and Applications of Nanoreactors. *Chemical Sciences J.*, 2018, **09** (03), 1000192.
- [124] Volodin A.M., Bedilo A.F., Vedyagin A.A., Stoyanovskii V.O. Synthesis of Nanocrystalline Oxide Ceramic Materials: a Carbon Nanoreactor Concept. *JOJ Material Science*, 2017, **3** (4), P. 555617.
- [125] Ryabochkina P.A., Egorysheva A.V., et al. Synthesis and photoluminescence properties of novel LaGa_{0.5}Sb_{1.5}O₆: Eu³⁺, Dy³⁺, Tb³⁺ and BiGeSbO₆: Eu³⁺, Dy³⁺, Tb³⁺ phosphors. *J. of Alloys and Compounds*, 2021, **886**, P. 161175.
- [126] Proskurina O.V., Tomkovich M.V., et al. Formation of Nanocrystalline BiFeO₃ under Hydrothermal Conditions. *Russian J. of General Chemistry*, 2017, **87** (11), P. 2507–2515.
- [127] Wang C., Cui Z., et al. Theoretical and experimental studies on the size- and morphology-dependent thermodynamics of nanoparticle electrodes. *Thermochimica Acta*, 2022, **708**, P. 179140.
- [128] Bugrov A.N., Almjasheva O.V. Effect of hydrothermal synthesis conditions on the morphology of ZrO₂ nanoparticles. *Nanosystems: Physics, Chemistry, Mathematics*, 2013, **4** (6), P. 810–815.
- [129] Gopinath S., Mayakannan M., Vetrivel S. Structural, optical, morphological properties of silver doped cobalt oxide nanoparticles by microwave irradiation method. *Ceramics International*, 2022, **48** (5), P. 6103–6115.
- [130] Svinolupova A.S., Lomakin M.S., Kirillova S.A., Almjasheva O.V. Formation of Bi₂WO₆ nanocrystals under conditions of hydrothermal treatment. *Nanosystems: Physics, Chemistry, Mathematics*, 2020, **11** (3), P. 338–344.
- [131] Sukhdev A., Challa M., et al. Synthesis, phase transformation, and morphology of hausmannite Mn₃O₄ nanoparticles: photocatalytic and antibacterial investigations. *Heliyon*, 2020, **6** (1), P. e03245.
- [132] Rozenberg B.A., Tenne R. Polymer-assisted fabrication of nanoparticles and nanocomposites. *Progress in Polymer Science*, 2008, **33** (1), P. 40–112.
- [133] Kostyukhin E.M., Kustov L.M. Microwave-assisted synthesis of magnetite nanoparticles possessing superior magnetic properties. *Mendeleev Communications*, 2018, **28** (5), P. 559–561.
- [134] Golyeva E.V., Kolesnikov I.E., et al. Effect of synthesis conditions on structural, morphological and luminescence properties of MgAl₂O₄:Eu³⁺ nanopowders. *J. of Luminescence*, 2018, **194**, P. 387–393.
- [135] Lomanova N.A., Tomkovich M.V., Osipov A.V., Ugol'kov V.L. Synthesis of Nanocrystalline Materials Based on the Bi₂O₃–TiO₂ System. *Russian J. of General Chemistry*, 2019, **89**, P. 2075–2081.
- [136] Bugrov A.N., Smyslov R.Yu., et al. Phosphors with different morphology, formed under hydrothermal conditions on the basis of ZrO₂:Eu³⁺ nanocrystallites. *Nanosystems: Physics, Chemistry, Mathematics*, 2019, **10** (6), P. 654–665.
- [137] Kurdyukov D.A., Feoktistov N.A., et al. Template Synthesis of Monodisperse Submicrometer Spherical Nanoporous Silicon Particles. *Semiconductors*, 2019, **53**, P. 1048–1053.
- [138] Almjasheva O.V. Formation and structural transformations of nanoparticles in the TiO₂–H₂O system. *Nanosystems: Physics, Chemistry, Mathematics*, 2016, **7** (6), P. 1031–1049.
- [139] Popkov V.I., Almjasheva O.V., et al. Crystallization Behavior and Morphological Features of YFeO₃ Nanocrystallites Obtained by Glycine-Nitrate Combustion. *Nanosystems: Physics, Chemistry, Mathematics*, 2015, **6** (6), P. 866–874.
- [140] Tajiri T., Terashita N., et al. Size dependences of crystal structure and magnetic properties of DyMnO₃ nanoparticles. *J. of Magnetism and Magnetic Materials*, 2013, **345**, P. 288–293.
- [141] Lomanova N.A., Panchuk V.V., et al. Bismuth orthoferrite nanocrystals: magnetic characteristics and size effects. *Ferroelectrics*, 2020, **569** (1), P. 240–250.
- [142] Popkov V.I., Almjasheva O.V., et al. Magnetic properties of YFeO₃ nanocrystals obtained by different soft-chemical methods. *J. of Materials Science: Materials in Electronics*, 2017, **28** (10), P. 7163–7170.
- [143] Manukyan A., Elsukova A., et al. Structure and size dependence of the magnetic properties of Ni@C nanocomposites. *J. of Magnetism and Magnetic Materials*, 2018, **467**, P. 150–159.
- [144] Tian Z., Zhu C., et al. Size dependence of structure and magnetic properties of CoCr₂O₄ nanoparticles synthesized by hydrothermal technique. *J. of Magnetism and Magnetic Materials*, 2015, **377**, P. 176–182.
- [145] Farbod M., Dehbidi V.K., Shoushtari M.Z. Size dependence of optical and magnetic properties of nickel oxide nanoparticles fabricated by electric arc discharge method. *Ceramics International*, 2017, **43** (16), P. 13670–13676.
- [146] Murakami N., Kawakami S., Tsubota T., Ohno T. Dependence of photocatalytic activity on particle size of a shape-controlled anatase titanium(IV) oxide nanocrystal. *J. of Molecular Catalysis A: Chemical*, 2012, **358**, P. 106–111.
- [147] Li L., Gao H., et al. Comparative investigation on synthesis, morphological tailoring and photocatalytic activities of Bi₂O₂CO₃ nanostructures. *Colloids and Surfaces A Physicochemical and Engineering Aspects*, 2022, **644**, P. 128758.
- [148] Kroto H.W., Heath J.R., O'Brien S.C., Curl R.F. C₆₀: Buckminsterfullerene. *Nature*, 1985, **318**, P. 162–163.
- [149] Kratschmer W., Lamb L.D., Fostiropoulos K., Huffman D.R. Solid C₆₀: a new form of carbon. *Nature*, 1990, **347** (6291), P. 354–358.
- [150] Dunk P., Niwa H., et al. Large fullerenes in mass spectra. *Molecular Physics*, 2015, **113** (15), P. 1–3.
- [151] Müller A., Shah S.Q.N., et al. Archimedean Synthesis and Magic Numbers: "Sizing" Giant Molybdenum-Oxide-Based Molecular Spheres of the Keplerate Type. *Angewandte Chemie International Edition*, 1999, **38** (21), P. 3238–3241.
- [152] Müller A., Krickemeyer E., et al. Organizational Forms of Matter: An Inorganic Super Fullerene and Keplerate Based on Molybdenum Oxide. *Angewandte Chemie International Edition*, 1998, **37** (24), P. 3359–3363.

- [153] Ostroushko A.A., Gagarin I.D., Danilova I.G., Gette I.F. The use of nanocluster polyoxometalates in the bioactive substance delivery systems. *Nanosystems: Physics, Chemistry, Mathematics*, 2019, **10** (3), P. 318–349.
- [154] Müller A., Gouzerh P. From linking of metal-oxide building blocks in a dynamic library to giant clusters with unique properties and towards adaptive chemistry. *Chemical Society Reviews*, 2012, **41** (22), P. 7431–7463.
- [155] Awada M., Floquet S., et al. Synthesis and Characterizations of Keplerate Nanocapsules Incorporating L- and D-Tartrate Ligands. *J. of Cluster Science*, 2017, **28** (2), P. 799–812.
- [156] Ostroushko A.A., Tonkushina M.O., et al. Stability of the $\text{Mo}_{72}\text{Fe}_{30}$ polyoxometalate buckyball in solution. *Russian J. of Inorganic Chemistry*, 2012, **57** (9), P. 1210–1213.
- [157] Qiao Z.-A., Zhang P., et al. Lab-in-a-Shell: Encapsulating Metal Clusters for Size Sieving Catalysis. *J. of the American Chemical Society*, 2014, **136** (32), P. 11260–11263.
- [158] Hervieu M., Mellène B., et al. The route to fullerene oxides. *Nature Materials*, 2004, **3**, P. 269–273.
- [159] Lebedev O.I., Bals S., et al. Mixed $(\text{Sr}_{1-x}\text{Ca}_x)_3\text{Bi}_{24}\text{Al}_{48}\text{O}_{141}$ fullerenoids: the defect structure analysed by (S)TEM techniques. *Int. J. of Materials Research*, 2006, **97** (7), P. 978–984.
- [160] Boudin S., Mellenne B., et al. New Aluminate with a Tetrahedral Structure Closely Related to the C84 Fullerene. *Inorganic Chemistry*, 2004, **43** (19), P. 5954–5960.
- [161] Iijima S. Helical microtubules of graphitic carbon. *Nature*, 1991, **354**, P. 56–58.
- [162] Venkatesan S., Visvalingam B., et al. Effect of chemical vapor deposition parameters on the diameter of multi-walled carbon nanotubes. *International Nano Letters*, 2018, **8** (4), P. 297–308.
- [163] Serra M., Arenal R., Tenne R. An overview of the recent advances in inorganic nanotubes. *Nanoscale*, 2019, **11** (17), P. 8073–8090.
- [164] Zhang Y.J., Ideue T., et al. Enhanced intrinsic photovoltaic effect in tungsten disulfide nanotubes. *Nature*, 2019, **570** (7761), P. 349–353.
- [165] Qin F., Shi W., et al. Superconductivity in a chiral nanotube. *Nature Communications*, 2017, **8** (1), P. 14465.
- [166] Panchakarla L.S., Radovsky G., et al. Nanotubes from Misfit Layered Compounds: A New Family of Materials with Low Dimensionality. *J. of Physical Chemistry Letters*, 2014, **5** (21), P. 3724–3736.
- [167] Polyakov A.Yu., Zak A., et al. Nanocomposites based on tubular and onion nanostructures of molybdenum and tungsten disulfides: inorganic design, functional properties and application. *Russian Chemical Reviews*, 2018, **87**, P. 251–271.
- [168] Lourenco M.P., de Oliveira C., et al. Structural, Electronic, and Mechanical Properties of Single-Walled Chrysotile Nanotube Models. *J. of Physical Chemistry C*, 2012, **116**, P. 9405–9411.
- [169] Guimarães L., Enyashin, A.N., Seifert G., Duarte H.A. Structural, Electronic, and Mechanical Properties of Single-Walled Halloysite Nanotube Models. *J. of Physical Chemistry C*, 2010, **114**, P. 11358–11363.
- [170] Krasilin A.A., Gusarov V.V. Energy Model of Bilayer Nanoplate Scrolling: Formation of Chrysotile Nanoscroll. *Russian J. of General Chemistry*, 2015, **85**, P. 2238–2241.
- [171] Demichelis R., De La Pierre M., et al. Serpentine Polymorphism: A Quantitative Insight from First-Principles Calculations. *Cryst. Eng. Comm.*, 2016, **18**, P. 4412–4419.
- [172] Krasilin A.A., Gusarov V.V. Energy model of radial growth of a nanotubular crystal. *Technical Physics Letters*, 2016, **42** (1), P. 55–58.
- [173] Krasilin A.A., Nevedomsky V.N., Gusarov V.V. Comparative Energy Modeling of Multi-Walled $\text{Mg}_3\text{Si}_2\text{O}_5(\text{OH})_4$ and $\text{Ni}_3\text{Si}_2\text{O}_5(\text{OH})_4$ Nanoscrolls Growth. *J. of Physical Chemistry C*, 2017, **121** (22), P. 12495–12502.
- [174] Krasilin A.A., Suprun A.M., Nevedomsky V.N., Gusarov V.V. Formation of conical $(\text{Mg,Ni})_3\text{Si}_2\text{O}_5(\text{OH})_4$ nanoscrolls. *Doklady Physical Chemistry*, 2015, **460** (2), P. 42–44.
- [175] Krasilin A.A., Gusarov V.V. Redistribution of Mg and Ni cations in crystal lattice of conical nanotube with chrysotile structure. *Nanosystems: Physics, Chemistry, Mathematics*, 2017, **8** (5), P. 620–627.
- [176] Proskurina O.V., Sivtsov E.V., et al. Formation of rhabdophane-structured lanthanum orthophosphate nanoparticles in an impinging-jets microreactor and rheological properties of sols based on them. *Nanosystems: Physics, Chemistry, Mathematics*, 2019, **10** (2), P. 206–214.
- [177] Avdeeva A.V., Zang X., Muradova A.G., Yurtov E.V. Formation of Zinc-Oxide Nanorods by the Precipitation Method. *Semiconductors*, 2017, **51** (13), P. 1724–1727.
- [178] Zaïen M., Ahmed N.M., Hassan Z. Growth of cadmium oxide nanorods by vapor transport. *Chalcogenide Letters*, 2012, **9** (3), P. 115–119.
- [179] Tokunaga T., Kawamoto T., et al. Growth and structure analysis of tungsten oxide nanorods using environmental TEM. *Nanoscale Research Letters*, 2012, **7** (1), P. 85.
- [180] Ma M., Zhang Y., Guo Z., Gu N. Facile synthesis of ultrathin magnetic iron oxide nanoplates by Schikorr reaction. *Nanoscale Research Letters*, 2013, **8** (1), P. 16.
- [181] Nguyen V.T., Nguyen H.S., et al. Tungsten Oxide Nanoplates: Facile Synthesis, Controllable Oxygen Deficiency and Photocatalytic Activity. *Communications in Physics*, 2020, **30** (4), P. 319.
- [182] Krasilin A.A. Energy modeling of competition between tubular and platy morphologies of chrysotile and halloysite layers. *Clays and Clay Minerals*, 2020, **68**, P. 436–445.
- [183] Krasilin A.A. The influence of edge specific surface energy on the direction of hydrosilicate layers scrolling. *Nanosystems: Physics, Chemistry, Mathematics*, 2021, **12** (5), P. 623–629.
- [184] Antonov N.M., Popov I.Y., Gusarov V.V. Model of spinodal decomposition of phases under hyperbolic diffusion. *Physics of the Solid State*, 1999, **41** (5), P. 824–826.
- [185] Jáger C., Tomán J.J., Erdélyi Z. Nanoparticle formation by spinodal decomposition in ion implanted samples. *J. of Alloys and Compounds*, 2022, P. 164781.
- [186] Ahmadi R., Masoudi A., Hamid Reza Madaah Hosseini, Gu N. Kinetics of magnetite nanoparticles formation in a one step low temperature hydrothermal process. *Ceramics International*, 2013, **39** (5), P. 4999–5005.
- [187] Tyrsted C., Becker J., et al. In-situ synchrotron radiation study of formation and growth of crystalline $\text{Ce}_x\text{Zr}_{1-x}\text{O}_2$ nanoparticles synthesized in supercritical water. *Chemistry of Materials*, 2010, **22** (5), P. 1814–1820.
- [188] Ivanov V.K., Polezhaeva O.S., et al. Microwave-hydrothermal synthesis of stable nanocrystalline ceria sols for biomedical uses. *Russian J. of Inorganic Chemistry*, 2010, **55** (1), P. 1–5.
- [189] Kuznetsova V.A., Almjashaeva O.V., Gusarov V.V. Influence of microwave and ultrasonic treatment on the formation of CoFe_2O_4 under hydrothermal conditions. *Glass Physics and Chemistry*, 2009, **35** (2), P. 205–209.
- [190] Liu L., Wang S., et al. Supercritical hydrothermal synthesis of nano- ZrO_2 : Influence of technological parameters and mechanism. *J. of Alloys and Compounds*, 2022, **898**, P. 162878.
- [191] Bachina A.K., Almjashaeva O.V., et al. Heat-stimulated crystallization and phase transformation of titania nanoparticles. *J. of Crystal Growth*, 2021, **576**, P. 126371.

- [192] Escobedo-Morales A., Téllez-Flores D., et al. Green method for producing hierarchically assembled pristine porous ZnO nanoparticles with narrow particle size distribution. *Materials Chemistry and Physics*, 2015, **151**, P. 282–287.
- [193] Ngoi K.H., Wong J.C., et al. Morphological structure details, size distributions and magnetic properties of iron oxide nanoparticles. *J. of Industrial and Engineering Chemistry*, 2021, **95**, P. 37–50.
- [194] Rusanov A.I. *Fazovyie ravnovesiya i poverkhnostnyye yavleniya (Phase Equilibria and Surface Phenomena)*, Leningrad: Khimiya, 1967, 388 p. (In Russian)
- [195] Rusanov A.I. *Phasengleichgewichte und Grenzflächenscheinungen*. Berlin: Akademie Verlag, 1978, 465 p.
- [196] Tolstoy V.P. *Fundamentals of Ion Layering Nanotechnology. Tutorial*. SPbU, SPb, 2020, 142 p. (In Russian)
- [197] Ermakov S.S., Nikolaev K.G., Tolstoy V.P. Novel electrochemical sensors with electrodes based on multilayers fabricated by layer-by-layer synthesis and their analytical potential. *Russian Chemical Reviews*, 2016, **85** (8), P. 880–900.
- [198] Tolstoy V.P. New routes for the synthesis of nanocomposite layers of inorganic compounds by the layer-by-layer scheme. *Russian J. of General Chemistry*, 2009, **79** (12), P. 2578–2583.
- [199] Mateos-Maroto A., Abelenda-Núñez I., et al. Polyelectrolyte Multilayers on Soft Colloidal Nanosurfaces: A New Life for the Layer-By-Layer Method. *Polymers (Basel)*, 2021, **13** (8), P. 1221.
- [200] Richardson J.J., Björnalm M., Caruso F. Technology-driven layer-by-layer assembly of nanofilms. *Science*, 2015, **348** (6233), P. 411.
- [201] Ahvenniemi E., Akbashev A.R., et al. Review Article: Recommended reading list of early publications on atomic layer deposition—Outcome of the “Virtual Project on the History of ALD”. *J. of Vacuum Science and Technology A*, 2017, **35** (1), P. 010801.
- [202] Method of manganese dioxide synthesis, Patent. 1396600, Russia: 4 C 03 17/25 Tolstoy V.P., Bogdanova L.B., Mitykova G.V. N 4010248/31-33, Prior. 01.06.1986. Issue N 3, p. 114, 1988.
- [203] Popkov V.I., Tolstoy V.P., Nevodomskiy V.N. Peroxide route to the synthesis of ultrafine CeO₂–Fe₂O₃ nanocomposite via successive ionic layer deposition. *Heliyon*, 2019, **5** (3), P. e01443.
- [204] Tolstoy V.P. Synthesis of thin-layer structures by the ionic layer deposition method. *Russian Chemical Reviews*, 1993, **62** (3), P. 237–242.
- [205] Tolstoy V.P., Altangerel B. A new “fluoride” synthesis route for successive ionic layer deposition of the Zn_xZr(OH)_yF_z · nH₂O nanolayers. *Materials Letters*, 2007, **53** (1), P. 123–125.
- [206] Li Z., Xiong S., et al. Role of Ag₂S coupling on enhancing the visible-light-induced catalytic property of TiO₂ nanorod arrays. *Scientific Reports*, 2016, P. 19754.
- [207] Popkov V.I., Tolstoy V.P. Controllable wettability tuning of the stainless steel surface through successive ionic layer deposition of Zn–Fe layered double hydroxysulfate. *Surface and Coatings Technology*, 2021, **409**, P. 126914.
- [208] Li X., Chen F., et al. Layer-by-layer synthesis of hollow spherical CeO₂ templated by carbon spheres. *J. of Porous Materials*, 2010, **17**, P. 297–303.
- [209] Shekhah O. Layer-by-Layer Method for the Synthesis and Growth of Surface Mounted Metal–Organic Frameworks (SURMOFs). *Materials*, 2010, **3**, P. 1302–1315.
- [210] Khajavian R., Ghani K. Fabrication of [Cu₂(bdc)₂(bpy)]_n thin films using coordination modulation-assisted layer-by-layer growth. *Cryst. Eng. Comm.*, 2018, **20**, P. 1546–1552.
- [211] Galkin V.I., Sayakhov R.D., Cherkasov R.A. Steric effects: the problem of their quantitative assessment and manifestation in the reactivity of organoelement compounds. *Russian Chemical Reviews*, 1991, **60** (8), P. 815–829.
- [212] Teychené S., Rodríguez-Ruiz I., Ramamoorthy R.K. Reactive crystallization: From mixing to control of kinetics by additives. *Current Opinion in Colloid & Interface Science*, 2020, **46**, P. 1–19.
- [213] Johnson B.K., Prud’homme R.K. Chemical Processing and Micromixing in Confined Impinging Jets. *AIChE J.*, 2003, **49** (9), P. 2264–2282.
- [214] Erkoç E., Fonte C.P., et al. Numerical and experimental modeling of mixing of impinging jets radially injected into crossflow. *Chemical Engineering Research and Design*, 2016, **106**, P. 74–91.
- [215] Abiev R.Sh., Almjashveva O.V., Popkov V.I., Proskurina O.V. Microreactor Synthesis of Nanosized Particles: The Role of Micromixing, Aggregation, and Separation Processes in Heterogeneous Nucleation. *Chemical Engineering Research and Design*, 2022, **178**, P. 73–94.
- [216] Abiev R.S., Almyasheva O.V., Izotova S.G., Gusarov V.V. Synthesis of cobalt ferrite nanoparticles by means of confined impinging-jets reactors. *J. of Chemical Technology and Applications*, 2017, **1** (1), P. 7.
- [217] Maki T., Takeda S., Muranaka Y., Mae K. Silver Nanoparticle Synthesis Using an Inkjet Mixing System. *Frontiers in Chemical Engineering*, 2021, **3**, P. 742322.
- [218] Wu Y., Lu J., Yang Q. A Control System Design for Nanoparticle Manufacturing by Using Impinging-jet Micromixers. *Advanced Materials Research*, 2012, **528**, P. 3–9.
- [219] Rivallin M., Benmami M., Kanaev A., Gaunand A. Sol–Gel reactor with rapid micromixing: modelling and measurements of titanium oxide nano-particle growth. *Chemical Engineering Research and Design*, 2005, **83**, P. 67–74.
- [220] Abiev R.S. Impinging-Jets Micromixers and Microreactors: State of the Art and Prospects for Use in the Chemical Technology of Nanomaterials (Review). *Theoretical Foundations of Chemical Engineering*, 2020, **54** (6), P. 1131–1147.
- [221] Abiev R.S., Proskurina O.V., Enikeeva M.O., Gusarov V.V. Effect of Hydrodynamic Conditions in an Impinging-Jet Microreactor on the Formation of Nanoparticles Based on Complex Oxides. *Theoretical Foundations of Chemical Engineering*, 2021, **55** (1), P. 12–29.
- [222] Zhao C.-X., He L., Qiao S.Z., Middelberg A.P.J. Nanoparticle synthesis in microreactors. *Chemical Engineering Science*, 2011, **66** (7), P. 1463–1479.
- [223] Barashok K.I., Panchuk V.V., et al. Formation of cobalt ferrite nanopowders in an impinging-jets microreactor. *Nanosystems: Physics, Chemistry, Mathematics*, 2021, **12** (3), P. 303–310.
- [224] Zdravkov A.V., Kudryashova Y.S., Abiev R.S. Synthesis of Titanium Oxide Doped with Neodymium Oxide in a Confined Impinging-Jets Reactor. *Russian J. of General Chemistry*, 2020, **90** (9), P. 1677–1680.
- [225] Kudryashova Y.S., Zdravkov A.V., Ugolkov V.L., Abiev R.S. Preparation of Photocatalyzers Based on Titanium Dioxide Synthesized Using a Microreactor with Colliding Jets. *Glass Physics and Chemistry*, 2020, **46** (4), P. 335–340.
- [226] Abiev R.Sh., Sirotkin A.A. Influence of Hydrodynamic Conditions on Micromixing in Microreactors with Free Impinging Jets. *Fluids*, 2020, **5** (4), P. 179.
- [227] Ravi Kumar D.V., Prasad B.L.V., Kulkarni A.A. Impinging Jet Micromixer for Flow Synthesis of Nanocrystalline MgO: Role of Mixing/Impingement Zone. *J. of Industrial and Engineering Chemistry*, 2013, **52**, P. 17376.
- [228] Proskurina O.V., Nogovitsin I.V., et al. Formation of BiFeO₃ Nanoparticles Using Impinging Jets Microreactor. *Russian J. of General Chemistry*, 2018, **88** (10), P. 2139–2143.
- [229] Kudryashova Y.S., Zdravkov A.V., Abiev R.S. Synthesis of Yttrium–Aluminum Garnet Using a Microreactor with Impinging Jets. *Glass Physics and Chemistry*, 2021, **47** (3), P. 260–264.

- [230] Sokolova A.N., Proskurina O.V., Danilovich D.P., Gusarov V.V. Photocatalytic properties of composites based on $Y_{1-x}Bi_xFeO_3$ ($0 \leq x \leq 0.15$) nanocrystalline solid solutions with a hexagonal structure. *Nanosystems: Physics, Chemistry, Mathematics*, 2022, **13** (1), P. 87–95.
- [231] Lomakin M.S., Proskurina O.V., et al. Crystal structure and optical properties of the Bi-Fe-W-O pyrochlore phase synthesized via a hydrothermal method. *J. of Alloys and Compounds*, 2022, **889** (5), P. 161598.
- [232] Vo Q.M., Mittova V.O., et al. Strontium doping as a means of influencing the characteristics of neodymium orthoferrite nanocrystals synthesized by co-precipitation method. *J. of Materials Science: Materials in Electronics*, 2021, **32**, P. 26944–26954.
- [233] Gao T., Chen Z., et al. A review: Preparation of bismuth ferrite nanoparticles and its applications in visible-light induced photocatalyses. *Reviews on Advanced Materials Science*, 2012, **40** (2), P. 97–109.
- [234] Proskurina O.V., Abiev R.S., et al. Formation of nanocrystalline $BiFeO_3$ during heat treatment of hydroxides co-precipitated in an impinging-jets microreactor. *Chemical Engineering and Processing – Process Intensification*, 2019, **143**, P. 107598.
- [235] Proskurina O.V., Sokolova A.N., et al. Role of Hydroxide Precipitation Conditions in the Formation of Nanocrystalline $BiFeO_3$. *Russian J. of Inorganic Chemistry*, 2021, **66** (2), P. 163–169.
- [236] Chang Chien S.-W., Ng D.-Q., et al. Investigating the effects of various synthesis routes on morphological, optical, photoelectrochemical and photocatalytic properties of single-phase perovskite $BiFeO_3$. *J. of Physics and Chemistry of Solids*, 2022, **160**, P. 110342.
- [237] Che D., Zhu X., et al. A facile aqueous strategy for the synthesis of high-brightness $LaPO_4$: Eu nanocrystals via controlling the nucleation and growth process. *J. of Luminescence*, 2014, **153**, P. 369–374.
- [238] Nightingale A.M., de Mello J.C. Segmented Flow Reactors for Nanocrystal Synthesis. *Advanced Materials*, 2013, **25**, P. 1813–1821.
- [239] Kawase M., Suzuki T., Miura K. Growth mechanism of lanthanum phosphate particles by continuous precipitation. *Chemical Engineering Science*, 2007, **62**, P. 4875–4879.
- [240] Kawase M., Miura K. Fine particle synthesis by continuous precipitation using a tubular reactor. *Advanced Powder Technology*, 2007, **18** (6), P. 725–738.
- [241] Abiev R.Sh., Zdravkov A.V., et al. Synthesis of Calcium Fluoride Nanoparticles in a Microreactor with Intensely Swirling Flows. *Russian J. of Inorganic Chemistry*, 2021, **66** (7), P. 1047–1052.
- [242] Almjasheva O.V., Krasilin A.A., Gusarov V.V. Formation mechanism of core-shell nanocrystals obtained via dehydration of coprecipitated hydroxides at hydrothermal conditions. *Nanosystems: Physics, Chemistry, Mathematics*, 2018, **9** (4), P. 568–572.
- [243] Smirnov A.V., Fedorov B.A., et al. Core-shell nanoparticles forming in the ZrO_2 – Gd_2O_3 – H_2O system under hydrothermal conditions. *Doklady Physical Chemistry*, 2014, **456** (1), P. 71–73.
- [244] Almjasheva O.V., Smirnov A.V., et al. Structural features of ZrO_2 – Y_2O_3 and ZrO_2 – Gd_2O_3 nanoparticles formed under hydrothermal conditions. *Russian J. of General Chemistry*, 2014, **84** (5), P. 804–809.
- [245] Malygin A.A., Malkov A.A., Sosnov A.A. Structural-dimensional effects and their application in the “core-nanoshell” systems synthesized by the molecular layering. *Russian Chemical Bulletin*, 2017, **66**, P. 1939–1962.
- [246] Patil K.C., Aruna S.T., Mimani T. Combustion synthesis: an update. *Current Opinion in Solid State and Materials Science*, 2002, **6** (6), P. 507–512.
- [247] Merzhanov A.G. Combustion and explosion processes in physical chemistry and technology of inorganic materials. *Russian Chemical Reviews*, 2003, **72** (4), P. 323–345.
- [248] Sytshev A.E., Merzhanov A.G. Self-propagating high-temperature synthesis of nanomaterials. *Russian Chemical Reviews*, 2004, **73** (2), P. 157–170.
- [249] Deshpande K., Mukasyan A., Varma A. Direct synthesis of iron oxide nanopowders by the combustion approach: Reaction mechanism and properties. *Chemistry of Materials*, 2004, **16** (24), P. 4896–4904.
- [250] Mukasyan A.S., Epstein P., Dinka P. Solution combustion synthesis of nanomaterials. *Proceedings of the Combustion Institute*, 2007, **31**, P. 1789–1795.
- [251] Aruna S.T., Mukasyan A.S. Combustion synthesis and nanomaterials. *Current Opinion in Solid State and Materials Science*, 2008, **12** (3–4), P. 44–50.
- [252] Martinson K.D., Kondrashkova I.S., Popkov V.I. Synthesis of $EuFeO_3$ nanocrystals by glycine-nitrate combustion method. *Russian J. of Applied Chemistry*, 2017, **90**, P. 1214–1218.
- [253] Lomanova N.A., Tomkovich M.V., et al. Formation of $Bi_{1-x}Ca_xFeO_{3-\delta}$ Nanocrystals via Glycine-Nitrate Combustion. *Russian J. of General Chemistry*, 2019, **89**, P. 1843–1850.
- [254] Tugova E.A., Karpov O.N. Glycine-nitrate combustion engineering of neodymium cobaltite nanocrystals. *Rare Metals*, 2021, **40**, P. 1778–1784.
- [255] Martinson K.D., Ivanov V.A., et al. Facile combustion synthesis of $TbFeO_3$ nanocrystals with hexagonal and orthorhombic structure. *Nanosystems: Physics, Chemistry, Mathematics*, 2019, **10** (6), P. 694–700.
- [256] Martinson K.D., Pantelev I.B., Shevchik A.P., Popkov V.I. Effect of the Red/Ox ratio on the structure and magnetic behavior of $Li_{0.5}Fe_{2.5}O_4$ nanocrystals synthesized by solution combustion approach. *Letters on Materials*, 2019, **9** (4), P. 475–479.
- [257] Tretyakov Y.D., Oleinikov N.N., et al. Self-organization in physicochemical systems: On the path to creating novel materials. *Inorganic Materials*, 1994, **30** (3), P. 277–290.
- [258] Noyes R.M. Gas-Evolution Oscillators. 4. Characteristics of the Steady State for Gas Evolution. *J. of Physical Chemistry*, 1984, **88**, P. 2827–2833.
- [259] Yang J., Sasaki T. Synthesis of $CoOOH$ Hierarchically Hollow Spheres by Nanorod Self-Assembly through Bubble Templating. *Chemistry of Materials*, 2008, **20** (5), P. 2049–2056.
- [260] Morgan J.S. The Periodic Evolution of Carbon Monoxide. *J. of the Chemical Society, Transaction*, 1916, **109**, P. 274–283.
- [261] Duyen P.T.H., Nguyen A.T. Optical and magnetic properties of orthoferrite $NdFeO_3$ nanomaterials synthesized by simple co-precipitation method. *Condensed Matter and Interphases*, 2021, **23** (4), P. 600–606.
- [262] Rotermel M.V., Samigullina R.F., Ivanova I.V., Krasnenko T.I. Synthesis of the $Zn_{1.9}Cu_{0.1}SiO_4$ pigment via the sol-gel and coprecipitation methods. *J. of Sol-Gel Science and Technology*, 2021, **100**, P. 404–413.
- [263] Kiseleva T.Yu., Uyangaa E., et al. Structure, magnetic, and magnetocaloric properties of submicronic yttrium iron garnet particles. *J. of Structural Chemistry*, 2022, **63**, P. 26–36.
- [264] Matrosova A.S., Kuz'menko N.K., et al. Synthesis of Nanosized Luminophores $Gd_2O_3:Nd^{3+}$ by Polymer-Salt Method and Study of Their Main Characteristics. *Optics and Spectroscopy*, 2021, **129**, P. 662–669.
- [265] Zhuravlev V.D., Dmitriev A.V., et al. Parameters of Glycine-Nitrate Synthesis of $NiCo_2O_4$ Spinel. *Russian J. of Inorganic Chemistry*, 2021, **66**, P. 1895–1903.
- [266] Kondrat'eva O.N., Nikiforova G.E., Smirnova M.N., Pechkovskaya K.I. Synthesis and Thermophysical Properties of Ceramics Based on Magnesium Gallate. *Russian J. of Inorganic Chemistry*, 2021, **66**, P. 957–962.

- [267] Sheindlin M.A., Kirillin A.V., Heyfetz L.M., Khodakov K.A. Fast automated-system for high-temperature (2500–6000-degrees-K) measurements of samples heated by laser-radiation. *High Temperature*, 1981, **19** (4), P. 620–627.
- [268] Kirillin A.V., Kovalenko M.D., et al. Apparatus and methods for examining the properties of refractory substances at high-temperatures and pressures by stationary laser-heating. *High Temperature*, 1986, **24** (2), P. 286–290.
- [269] Sheindlin M.A., Son E.E. Lasers in high-temperature energy materials. *Izvestiya RAS. Energy*, 2011, **5**, P. 88–103. (In Russian)
- [270] Rivera-Chaverra M.J., Restrepo-Parra E., et al. Synthesis of Oxide Iron Nanoparticles Using Laser Ablation for Possible Hyperthermia Applications. *Nanomaterials*, 2020, **10** (11), P. 2099.
- [271] Kim M., Ozone S., et al. Synthesis of Nanoparticles by Laser Ablation: A Review. *Powder and Particle J.*, 2017, **34**, P. 80–90.
- [272] Amendola V., Amans D., et al. Room-temperature laser synthesis in liquid of oxide, metal-oxide core-shells and doped oxide nanoparticles. *Chemistry – A European J.*, 2020, **26**, P. 9206–9242.
- [273] Popova-Kuznetsova E., Tikhonowski G., et al. Laser-Ablative Synthesis of Isotope-Enriched Samarium Oxide Nanoparticles for Nuclear Nanomedicine. *Nanomaterials*, 2020, **10** (1), P. 69.
- [274] Liu S., Moein Mohammadi M., Swihart M.T. Fundamentals and Recent Applications of Catalyst Synthesis Using Flame Aerosol Technology. *Chemical Engineering J.*, 2021, **405**, P. 126958.
- [275] Nemade K.R., Waghuley S.A. Synthesis of MgO Nanoparticles by Solvent Mixed Spray Pyrolysis Technique for Optical Investigation. *Int. J. of Metals*, 2014, **5**, P. 389416.
- [276] Santiago A.A.G., Tranquilin R.L., et al. Effect of temperature on ultrasonic spray pyrolysis method in zinc tungstate: The relationship between structural and optical properties. *Materials Chemistry and Physics*, 2021, **258**, P. 123991.
- [277] Matsukevich I., Krutko N.P., et al. Effect of preparation method on physicochemical properties of nanostructured MgO powder. *Proceedings of the National Academy of Sciences of Belarus, Chemical Series*, 2018, **54** (3), P. 281–288.
- [278] Ivanovskaya M.I., Tolstik A.I., Pan'kov V.V. Synthesis of $Zn_{0.5}Mn_{0.5}Fe_2O_4$ by low-temperature spray pyrolysis. *Inorganic Materials*, 2009, **45** (11), P. 1309–1313.
- [279] Puzyrev I.S., Andreikov E.I., et al. Adsorption properties of mesoporous carbon synthesized by pyrolysis of zinc glycerolate. *Russian Chemical Bulletin*, 2021, **70** (5), P. 805–810.
- [280] Melkozerova M.A., Ishchenko A.V., et al. Intrinsic Defects and their Influence on Optical Properties of $ALa_9(GeO_4)_6O_2$ (A = Li, Na, K, Rb, Cs) Oxyapatites prepared by Spray Pyrolysis. *J. of Alloys and Compounds*, 2020, **839**, P. 155609.
- [281] Boldyrev V.V., Voronin A.P., et al. Radiation-Thermal Synthesis. Current Achievement and Outlook. *Solid State Ionics*, 1989, **36**, P. 1–6.
- [282] Lyakhov N.Z., Boldyrev V.V., et al. Electron beam stimulated chemical reactions in solids. *Thermal Analysis*, 1995, **43**, P. 21–31.
- [283] Ancharova U.V., Mikhailenko M.A., et al. Effect of irradiation with relativistic electrons on the synthesis kinetics of $Ni_{0.75}Zn_{0.25}Fe_2O_4$. *Vestnik NSU. Series: Physics*, 2013, **8** (4), P. 41–48. (In Russian)
- [284] Stepanov V.A. Radiation-stimulated diffusion in solids. *Technical Physics*, 1998, **43** (8), P. 938–942.
- [285] Kretusheva I.V., Mishin M.V., Aleksandrov S.E. Synthesis of silicon dioxide nanoparticles in low temperature atmospheric pressure plasma. *Russian J. of Applied Chemistry*, 2014, **87** (11), P. 1581–1586.
- [286] Kim K.S., Kim T.H. Nanofabrication by thermal plasma jets: From nanoparticles to low-dimensional nanomaterials. *J. of Applied Physics*, 2019, **125** (7), P. 070901.
- [287] Uschakov A.V., Karpov I.V., Lepeshev A.A., Petrov M.I. Plasma-chemical synthesis of copper oxide nanoparticles in a low-pressure arc discharge. *Vacuum*, 2016, **133**, P. 25–30.
- [288] Toropov N.A., Barzakovskii V.P., Lapin V.V., Kurtseva N.N. *Handbook of Phase Diagrams of Silicate Systems. I. Binary Systems*. Second Revised Edition (Diagrammy Sostoyaniya Silikatnykh Sistem - Spravochnik), Nauka, Leningrad, 1969, 822 p. (In Russian)
- [289] *Minerals: Phase Equilibrium Diagrams: Handbook*. Resp. ed. F.V. Chukhrov, Moscow, Nauka, 1974. Issue 1: Phase equilibria important for natural mineral formation. Resp. ed. F.V. Chukhrov, I.A. Ostrovsky, V.V. Lapin., 1974, 514 p. (In Russian)
- [290] Belov G.V., Iorish V.S., Yungman V.S. Simulation of equilibrium states of thermodynamic systems using IVTANTERMO for Windows. *High Temperature*, 2000, **38**, P. 191–196.
- [291] Gusarov V.V., Suvorov S.A. Melting-point of locally equilibrium surface phases in polycrystalline systems based on a single volume phase. *J. of Applied Chemistry of the USSR*, 1990, **63** (8), P. 1560–1565.
- [292] Gusarov V.V. The thermal effect of melting in polycrystalline systems. *Thermochimica Acta*, 1995, **256** (2), P. 467–472.
- [293] Dash J.G. History of the search for continuous melting. *Reviews of Modern Physics*, 1999, **71** (5), P. 1737–1743.
- [294] Gusarov V.V., Suvorov S.A. Transformation of Nonautonomous Phases and Densification of Polycrystalline Systems. *J. of Applied Chemistry of the USSR*, 1992, **65** (7), P. 1227–1235.
- [295] Gusarov V.V., Suvorov S.A. Transformation and transport processes in polycrystalline systems and creep of materials. *J. of Applied Chemistry of the USSR*, 1992, **65** (10), P. 1961–1964.
- [296] Gusarov V.V., Popov I.Yu. Flows in two-dimensional nonautonomous phases in polycrystalline systems. *Nuovo Cimento*, 1996, **18D** (7), P. 1834–1840.
- [297] Gusarov V.V., Malkov A.A., Malygin A.A., Suvorov S.A. Thermally Activated Transformations of 2D Nonautonomous Phases and Contraction of Polycrystalline Oxide Materials. *Inorganic Materials*, 1995, **31** (3), P.320–323.
- [298] Ishutina Zh.N., Gusarov V.V., et al. Phase Transformations in Nanosized $\gamma\text{-Al}_2\text{O}_3\text{-SiO}_2\text{-TiO}_2$ Compositions. *Russian J. of Inorganic Chemistry*, 1999, **44** (1), P. 12–14.
- [299] Neiman A.Ya., Uvarov N.F., Pestereva N.N. Solid state surface and interface spreading: An experimental study. *Solid State Ionics*, 2007, **177** (39–40), P. 3361–3369.
- [300] Boldyrev V.V. Mechanochemistry and mechanical activation of solids. *Russian Chemical Reviews*, 2006, **75** (3), P. 177–189.
- [301] Grigorjeva T., Korzhagin M., Lyakhov N. Combinations of SHS and mechanochemical synthesis for nanopowder technologies. *Powder and Particle*, 2002, **20**, P. 144–158.
- [302] Isupov V.P., Borodulina I.A., Gerasimov K.B., Bulina N.V. Effect of Mechanical Activation on Reaction between Boehmite and Lithium Carbonate. *Inorganic Materials*, 2020, **56**, P. 56–61.
- [303] Eremina N.V., Isupov V.P. Mechanochemical synthesis of lithium pentaaluminate from lithium carbonate and boehmite. *Inorganic Materials*, 2020, **56** (5), P. 466–472.
- [304] Avvakumov E., Senna M., Kosova N. *Soft Mechanochemical Synthesis: a Basis for New Chemical Technologies*. Boston/Dodrecht/ London: Kluwer Academic Publishers, 2001, 201 p.
- [305] Avvakumov E.G., Pushnyakova V.A. Mechanochemical synthesis of complex oxides. *Khimicheskaya Tekhnologiya*, 2002, **5**, P. 6–17. (In Russian)
- [306] Kolbanev I.V., Shlyakhtina A.V., et al. Room-temperature mechanochemical synthesis of RE molybdates: Impact of structural similarity and basicity of oxides. *J. of the American Ceramic Society*, 2021, **104**, P. 5698–5710.

Submitted 12 November 2021; revised 21 November 2021; accepted 15 November 2021

Information about the authors:

Oksana V. Almjasheva – St. Petersburg State Electrotechnical University “LETI”, 197376 St. Petersburg, Russia; ORCID 0000-0002-6132-4178; almjasheva@mail.ru

Vadim I. Popkov – Ioffe Institute, 194021 St. Petersburg, Russia; ORCID 0000-0002-8450-4278; vadim.i.popkov@mail.ioffe.ru

Olga V. Proskurina – Ioffe Institute, 194021 St. Petersburg, Russia; St. Petersburg State Institute of Technology, 190013 St. Petersburg, Russia; ORCID 0000-0002-2807-375X; proskurinaov@mail.ru

Victor V. Gusarov – Ioffe Institute, 194021 St. Petersburg, Russia; ORCID 0000-0003-4375-6388; victor.v.gusarov@gmail.com

Conflict of interest: the authors declare no conflict of interest.

Synthesis, characterization and electrical properties of the nanosized perovskite LaFeO₃

Muhammad Irfan Asghar^{1,a}, Muhammad Kashif Shahid^{2,b}, Muhammad Haq Nawaz^{3,c},
Muhammad Idrees^{1,d}, Muhammad Asif^{4,e}, Ahsan Ali^{5,f}

¹Department of Physics, COMSATS University Islamabad, Lahore Campus, Pakistan

²Research Institute of Environment & Biosystem, Chungnam National University, Daejeon, Republic of Korea

³Department of Physics, University of Gujrat, Hafiz Hayat Campus, Gujrat, Pakistan

⁴Department of Physics, University of Engineering and Technology Lahore, Pakistan

⁵School of Mechanical Engineering, University of Leeds, Leeds LS2 9JT, UK

^airfanmeo1@gmail.com, ^bmkbutt2000@gmail.com, ^chaqn5656@gmail.com,

^dmidrees@cuilahore.edu.pk, ^easif81292@yahoo.com, ^fahsanali23654@gmail.com

Corresponding author: Muhammad Idrees, midrees@cuilahore.edu.pk

ABSTRACT Single-phase highly crystalline LaFeO₃ is synthesized by autocombustion of the gel complex obtained from citrate and metal nitrate precursors. The XRD analysis exhibited the transformation of amorphous phases of La₂O₃ and Fe₂O₃ into highly crystalline LaFeO₃ at 1000 °C. The agglomerated semi spherical morphology is observed. The average particle size of sintered pellets at 1000 °C for 4 h, 8, 12, and 16 h heating time is found 105, 130, 160 and 200 nm, respectively. TGA analysis revealed 27% weight lost due to the decomposition of La(OH)₃ and Fe(OH)₃ into La₂O₃, Fe₂O₃, and LaFeO₃. Electrical properties of LaFeO₃ were found to be dependent on micro-structural heterogeneities i.e., grain and grain boundaries. Two probe DC resistivity exhibited decrease in resistance with increasing heat treatment and time. The outcomes of this study confirmed the potential applications of perovskite-type LaFeO₃ in energy and environmental sectors.

KEYWORDS Impedance spectroscopy, LaFeO₃, perovskite, sintering, TGA

ACKNOWLEDGEMENTS Authors thank to the National Centre for Physics, Islamabad for assistance in instrumental analysis.

FOR CITATION Muhammad Irfan Asghar, Muhammad Kashif Shahid, Muhammad Haq Nawaz, Muhammad Idrees, Muhammad Asif, Ahsan Ali Synthesis, characterization and electrical properties of the nanosized perovskite LaFeO₃. *Nanosystems: Phys. Chem. Math.*, 2022, **13** (2), 181–191.

1. Introduction

While industrial development has improved the quality of life with the remarkable inventions and revolutions, it has also created several issues and challenges related to the environment and energy [1]. The need for solutions to environmental issues and alternative energy sources has increased the interest in synthesis and application of new materials [2–4]. In recent years, much attention is given to the perovskite materials for their substantial optical and electrical characteristics [5,6]. Recently, novel materials having perovskite structures, including HoFeO₃ [7], GdFeO₃ [8] CaMnO₃ [9] Nd_{1-x}Sr_xFeO₃ [10], YbFeO₃ [11] SmFeO₃ [12] etc. have been thoroughly studied Lanthanum orthoferrite (LaFeO₃), is one of the recognized perovskite-type oxides. It has an orthorhombic perovskite structure with space group Pbnm [13] LaFeO₃ constitutes FeO₆ units with La³⁺ ions inserted between these units [14]. Considering Neel temperature (T_N) of 740 K bulk LaFeO₃ is known to be antiferromagnetic [15]. The prominent mixed conductivity properties of LaFeO₃ encourage its electro-ceramic applications. It is chemically stable in both reducing and oxidizing environments With atomic doping of LaFeO₃, several improved properties can be achieved including higher electrical conductivity, greater dielectric constant and low dielectric loss susceptibility, polarizability and average type of permittivity [16, 17] Several methods have been introduced for the synthesis of LaFeO₃ [18]. These methods include the thermal decomposition of the coprecipitated precursor [La(OH)₃ and Fe(OH)₃], calcination of a mixture of La₂O₃ and Fe₂O₃, and the thermal decomposition of heteronuclear complex i.e., La[Fe(CN)₆] [19] LaFeO₃ is found to be synthesized at 600, 800 and 1000 °C from La-Fe-(CN), La-Fe-OH and La-Fe-O respectively. The uniform atomic level structure of LaFeO₃ is obtained during thermal decomposition of the La[Fe(CN)₆].5H₂O heteronuclear complex. Hence, the low temperature condition favored the synthesis of pure LaFeO₃ nanoparticles.

Another study used La₂(CO₃)₃ and Fe(CO)₅ as a starting material for the synthesis of nanocrystalline perovskite-type LaFeO₃ via sonochemical method [20]. The highly crystalline and homogenized product is obtained and the particles were found to have 30 nm size, as confirmed by transmission electron microscopy (TEM). The coercivity and saturation magnetization of the particles were found 250 H_c and 40 memu g⁻¹, respectively. The shorter annealing time and lower

processing temperature increase the significance of this method than that of other chemical techniques that involve the longer soaking and very high calcination temperature. It is noteworthy that longer soaking and higher temperature result in high porosity and poor uniformity that may affect the properties of the powder [20].

A study reported the synthesis of nanosized (30 nm) LaFeO_3 powder via sol-gel auto-combustion method [21]. The process involved the homogeneous sol formation followed by dried gel formation and combustion of dried gel. The citrate-based sol-gel pathway is also introduced for the synthesis of uniform LaFeO_3 nanowires [22]. Other methods for synthesis of LaFeO_3 include glycine combustion method [23], SBA-16 template method [24], microwave-assisted method [25], glucose sol-gel method [26], solid-state reaction method [27], starch assisted soft-chemistry method [28], high energy milling [29], floating zone method [30], and auto-combustion of the gel complex acquired from metal nitrate and citrate precursor [31].

The main objective of this study is to synthesize the single-phase highly crystalline perovskite-like LaFeO_3 for practical application in the field of energy and environment. The influence of sintering conditions on the phase transformation is determined via advanced characterization techniques and the results are discussed concisely. The electrical properties of perovskite-like LaFeO_3 are also determined. Based on findings of this study, perovskite-like LaFeO_3 is proposed for practical application in the field.

2. Materials and methods

2.1. Chemicals and reagents

All the chemicals and reagents used in this study were of analytical grade and used as received. Lanthanum nitrate hexahydrate and iron nitrate nonahydrate were purchased from Sigma-Aldrich.

2.2. Synthesis of LaFeO_3

The appropriate amount of lanthanum nitrate hexahydrate [$\text{La}(\text{NO}_3)_3 \cdot 6\text{H}_2\text{O}$], citric acid monohydrate [$\text{C}_6\text{H}_8\text{O}_7 \cdot \text{H}_2\text{O}$] and iron (III) nitrate nonahydrate [$\text{Fe}(\text{NO}_3)_3 \cdot 9\text{H}_2\text{O}$] were dissolved (separately) in deionized water to achieve 0.1 M concentration (Fig. 1). Both nitrate solutions were mixed in glass beaker and stirred for 45 min. The prepared solution was dropwise added into the 500 mL solution of citric acid monohydrate. The mixture was heated to 70–75 °C. Followed by evaporation of solvent, wet yellow gel is obtained that was further dried in electric furnace (100 °C). The dried gel is ground and kept in the glass beaker. The top of beaker is covered with aluminum foil and small holes were made in the foil. The beaker was placed in furnace and the temperature is increased to 150 °C with the increasing rate of 5 °C/min. The brown color precipitate is collected at bottom that was ground to the fine particles. The obtained particles were sintered at different temperatures (450, 600, 800 and 1000 °C) for 4 h. The obtained products were named as described in Table 1.



FIG. 1. Scheme of LaFeO_3 synthesis

TABLE 1. List of samples prepared with different sintering conditions

Sample identity	Sintering conditions
LFO-COP-Precipitates	precipitated powder
LFO-COP-450 °C	sample treated at 450 °C for 4 h
LFO-COP-600 °C	sample treated at 600 °C for 4 h
LFO-COP-800 °C	sample treated at 800 °C for 4 h
LFO-COP-1000 °C	sample treated at 1000 °C for 4 h

2.3. Instrumentation

Different characterization techniques are applied to identify the elemental and morphological properties of the synthesized products. Temperature of electric furnaces is internally controlled. The crystallization progression was examined by differential thermal analysis (DTA) and thermogravimetric analysis (TGA). The surface morphology and crystalline structure of LaFeO_3 is examined by scanning electron microscope (SEM) and X-ray diffraction (XRD), respectively. The resistance and capacitance characteristics of LaFeO_3 are measured via impedance spectroscopy.

3. Results and discussion

3.1. Thermal analysis

Fig. 2 shows the thermal decomposition progression of LaFeO_3 . A small endothermic peak was appeared at 330 °C and the sharp change in phase is started after 600 °C. The weight loss is proceeded up to 800 °C in several steps. About 27% weight loss is observed due to the decomposition of $\text{La}(\text{OH})_3$ and $\text{Fe}(\text{OH})_3$ present in the total mass of the sample. The decomposition of hydroxides resulted in the La_2O_3 , Fe_2O_3 and LaFeO_3 phases. This weight loss was found in consistent with reported value of 27.5% [20]. About 90% decomposition of hydroxides is achieved at 650 °C. A negligible weight loss is observed when the temperature is increased from 800 to 1200 °C. The heat absorption at 800 °C is intensely reduced when compared to 600 °C, however, a minor heat absorption was observed up to 1200 °C. Although LFO450 and LFO600 contributed to initiate the transformation of amorphous phases, these conditions are not enough to achieve the higher crystalline form of LaFeO_3 . The single crystalline phase of LaFeO_3 is started at 800 °C. The slight loss in weight from 800 to 1200 °C is attributed to the loss of minute quantity of oxygen [32].

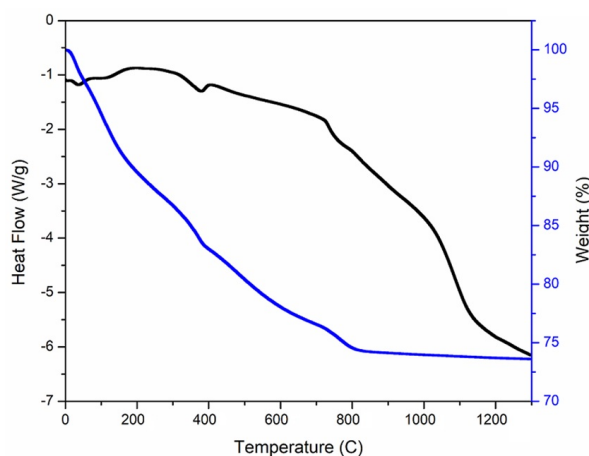


FIG. 2. TGA results of the precipitated powder

3.2. XRD analysis

The XRD analysis of the precipitate and the sintered samples is conducted to determine the phase transformation and crystallinity of the material. Fig. 3 shows the XRD pattern of the precipitate. The diffraction peaks observed at the 2θ of 27.5° , 28.1° , 39.8° , 48.8° , 55.7° and 64.8° represented the crystalline planes of $\text{La}(\text{OH})_3$ (110), (101), (201), (211), (112) and (311), respectively. The corresponding planes were compared with the standard XRD pattern of $\text{La}(\text{OH})_3$ (JCPDS card No. 36-1481) and found in fine agreement with earlier studies [33, 34]. In addition, the diffraction peaks at the 2θ of 22.1° , 26.0° , 38.5° , 42.6° , 43.9° , 61.4° and 70.0° indicated a phase of $\text{Fe}(\text{OH})_3$. The major peaks of amorphous

phase of $\text{Fe}(\text{OH})_3$ found at 2θ of 38.5° , 42.6° and 43.9° assigned to the corresponding (031), (222) and (213) planes, respectively [35]. The characteristic peaks of $\text{Fe}(\text{OH})_3$ were also found in good agreement with standard pattern (JCPDS card 38-0032).

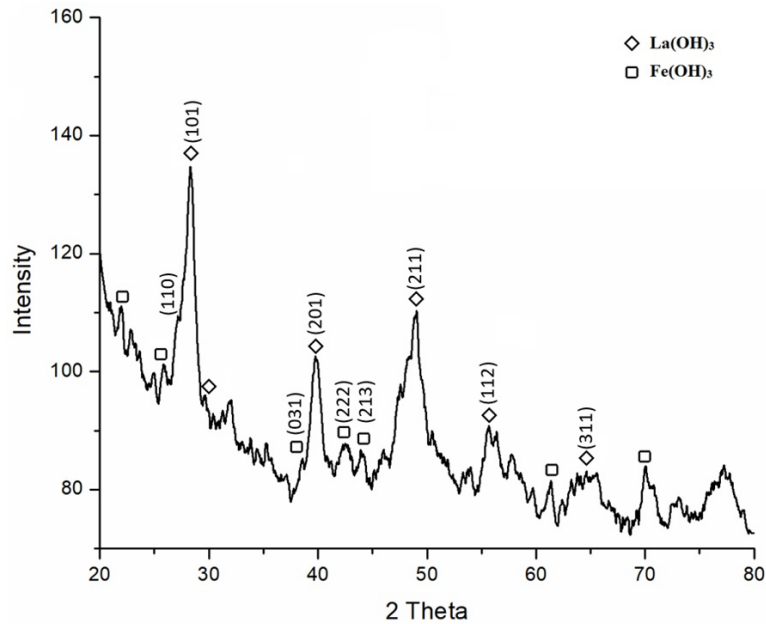


FIG. 3. XRD pattern of LFO-COP-Precipitate

Followed by 4 h sintering at 450°C , a peak appeared at 2θ of 31.6° indicated the presence of LaFeO_3 due to the onset of the reaction between $\text{Fe}(\text{OH})_3$ and $\text{La}(\text{OH})_3$ (Fig. 4). However, the existence of LaFeO_3 is not highly marked due to the incomplete transformation of $\text{La}(\text{OH})_3$ and $\text{Fe}(\text{OH})_3$ into LaFeO_3 . Another study found that the diffraction peaks of LaFeO_3 remains uncertain when the sample is calcined below 500°C [24]. The major reason behind this phenomenon is the low crystallinity and higher amorphous phase of LaFeO_3 . In addition, differential peaks corresponding to Fe_2O_3 and La_2O_3 were also found, as compared with the reported spectra of Fe_2O_3 [36] and La_2O_3 [37]. It is noteworthy that the amorphous phases of hydroxides started transformation into crystalline form due to heat treatment.

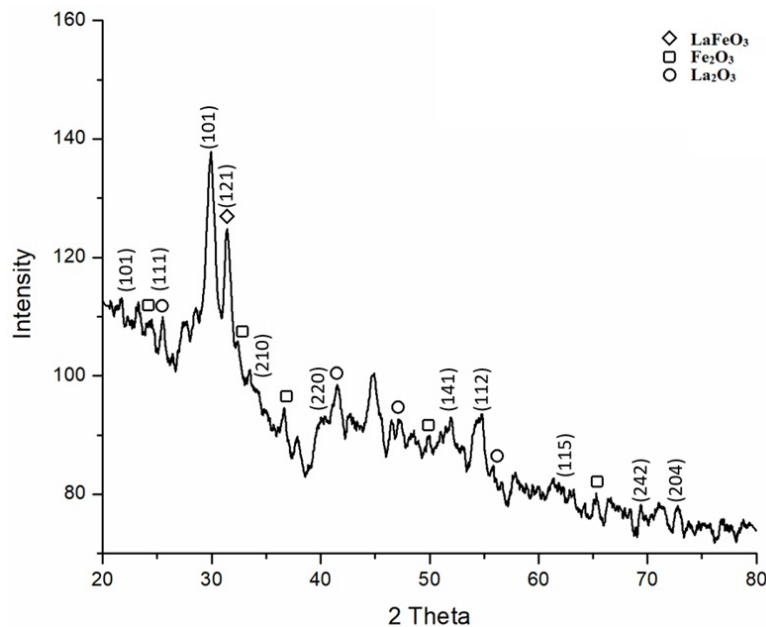


FIG. 4. XRD pattern of LFO-COP- 450°C

The samples obtained after 4 h sintering at 600°C also displayed the amorphous phase of LaFeO_3 , Fe_2O_3 and La_2O_3 as shown in Fig. 5. XRD pattern of LFO 600 revealed the higher crystallinity than that of LFO 450. This is found in

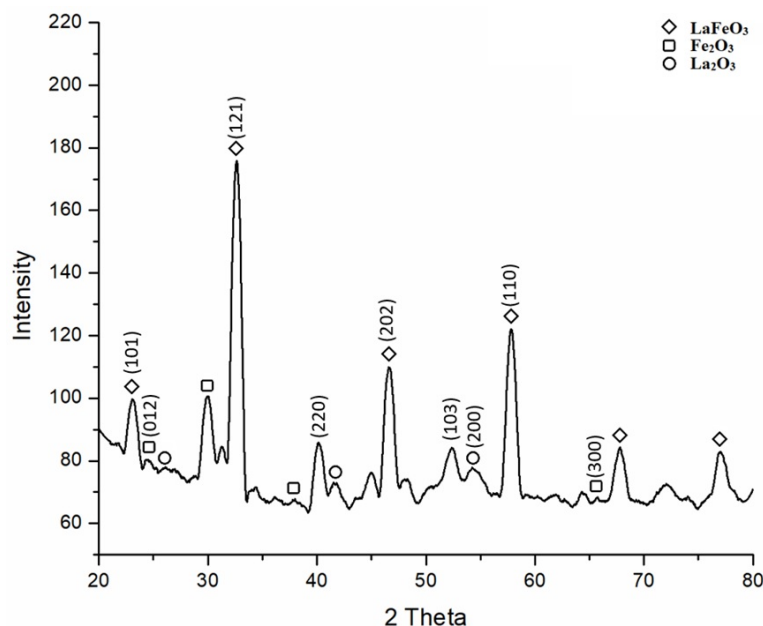


FIG. 5. XRD pattern of LFO-COP-600 °C

consistence with TGA results, where, 90% of hydroxides were decomposed when 600 °C is applied. Fig. 6 shows the XRD pattern of particles sintered for 4 h at 800 °C. The diffraction peaks observed at the 2θ of 23.1°, 32.5°, 40.1°, 46.8°, 57.9°, 67.0° and 77.5° represented the crystalline planes of LaFeO₃ (101), (121), (22), (202), (123), (004) and (204), respectively. The obtained data was appeared in fine agreement with a reported XRD pattern of LaFeO₃ that is calcined at 850 °C [38]. Although the higher level of crystallization is evident from the XRD pattern of LFO 800, some impurities such as La₂O₃ and Fe₂O₃ are also observed.

Although, the XRD pattern of the as-burnt powder is attributable to a mixture of amorphous and crystalline phases, heat treatment progressively improved the crystallinity of the powder to a well crystalline phase at 800 °C. All the XRD peaks are well indexed by an orthorhombic unit cell of LaFeO₃ with space group of Pbnm (JCPDS 37-1493). Substantial variations in the peak intensity and full width at half maximum (FWHM) of orthoferrite peak were identified during heat treatment. It is found that FWHM of the orthoferrite peak decreased as we increased the temperature of heat treatment. This infers an increase in crystallite size at higher temperatures. The average crystallite sizes determined by Scherer's formula were 12, 23 and 43 nm for LFO450, LFO600 and LFO800, respectively. LaFeO₃ phase formation during ignition and increase in crystallinity with increase in heat treatment temperature were appeared in fine agreement with the reported studies [39].

Further sintering at 1000 °C resulted in the formation of the crystalline phase of LaFeO₃, as identified via XRD analysis (Fig. 7). All the diffraction peaks were attributed to the single crystalline phase of LaFeO₃ without any impurity. The obtained pattern was found in consistence with the standard pattern of orthorhombic LaFeO₃ (JCPDS card 37-1493). The calculated cell parameters of LaFeO₃ were $a = 5.563$, $b = 5.562$ and $c = 7.868$. The diffraction peaks and corresponding crystalline planes were also found in fine agreement with earlier studies [16, 40]. The effect of sintering time on the crystalline structure of synthesized LaFeO₃ is also assessed. LaFeO₃ pellets were prepared under 40 bar hydraulic pressure and sintered at 1000 °C by keeping in a ceramic boat for 4, 8, 12 and 16 h. The XRD pattern of all the samples is presented in Fig. 8. All the spectra indicated the single crystalline phase of LaFeO₃. However, an increase in the time of heat treatment resulted a slight shift in diffraction peaks towards higher or lower angle from their actual position. This phenomenon indicates the compressive strain and decrease in the length of the cell parameters. As shown in Fig. 8, at 4 h we can see that there is a non uniform strain in which broadening of the peak is visible whereas, the peak position is shifted toward the higher angle due to the uniform strain in case of 8 h sample. The XRD pattern after 12 h did not indicate any strain and peak was found at its original position. In case of 16 h treatment, the peak is again shifted to the higher angle from their original position that is an indication of uniform strain.

3.3. SEM Analysis

Fig. 9 shows the SEM images of the LaFeO₃ sintered at different conditions. The microstructure shows that particles have sharp grain boundaries and well defined geometric shapes. The agglomerated semi spherical particles were found similar to the reported nano scale structure of LaFeO₃ [41]. A prominent difference is observed in size of the particles sintered for the different time duration. It is found that the particle size is expanded with increasing the duration of heat treatment. Another study also found the similar expansion in particle size, when the LaFeO₃ is sintered at higher

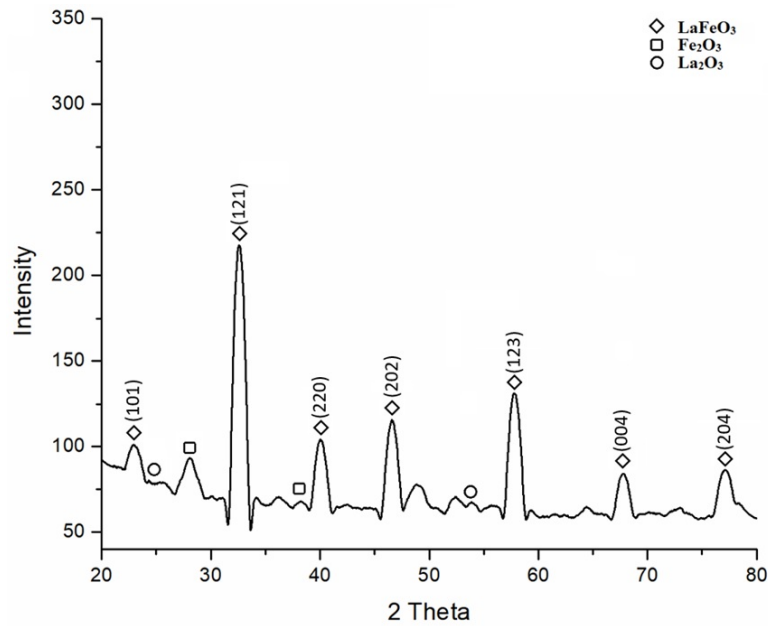


FIG. 6. XRD pattern of LFO-COP-800 °C

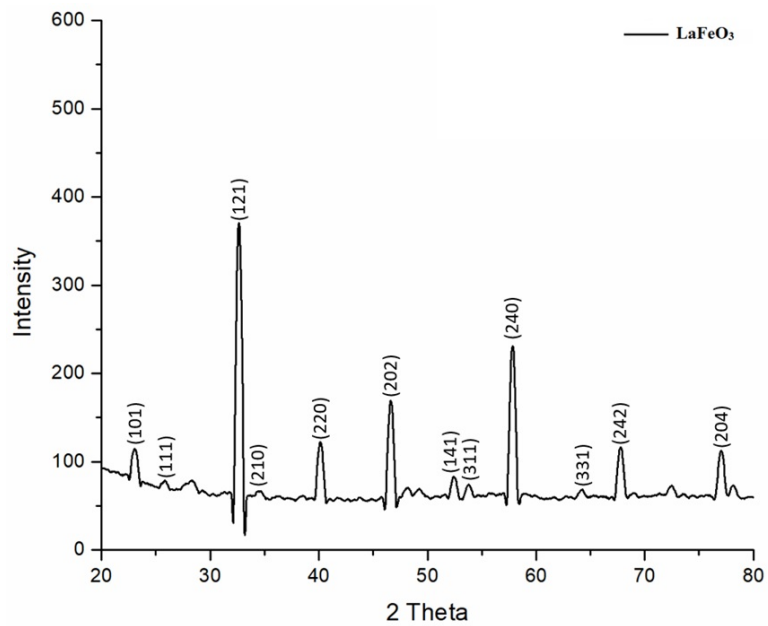


FIG. 7. XRD pattern of LFO-COP-1000 °C

temperature [42]. The average particle size is found 105, 130, 160 and 200 nm for the samples sintered at 1000 °C for 4, 8, 12 and 16 h, respectively. It depends on the diffusion rate of ions and the concentration of oxygen vacancies that cause the increase in grain boundaries.

3.4. DC resistivity

The DC electrical resistance is measured by two-probe method. This method involves two electrical contacts, and each contact plays both roles of voltage measurement and current application [43]. The resistance can be determined by measuring the voltage drop across the sample when passing a constant known current across the samples. The results obtained from the resistance measurement are summarized in Fig. 10 and Table 2. As the heating time is increased, a slight decrease in resistance is observed. At the extended heating time, the excessive oxygen vacancies and the defects resulted in the low resistivity.

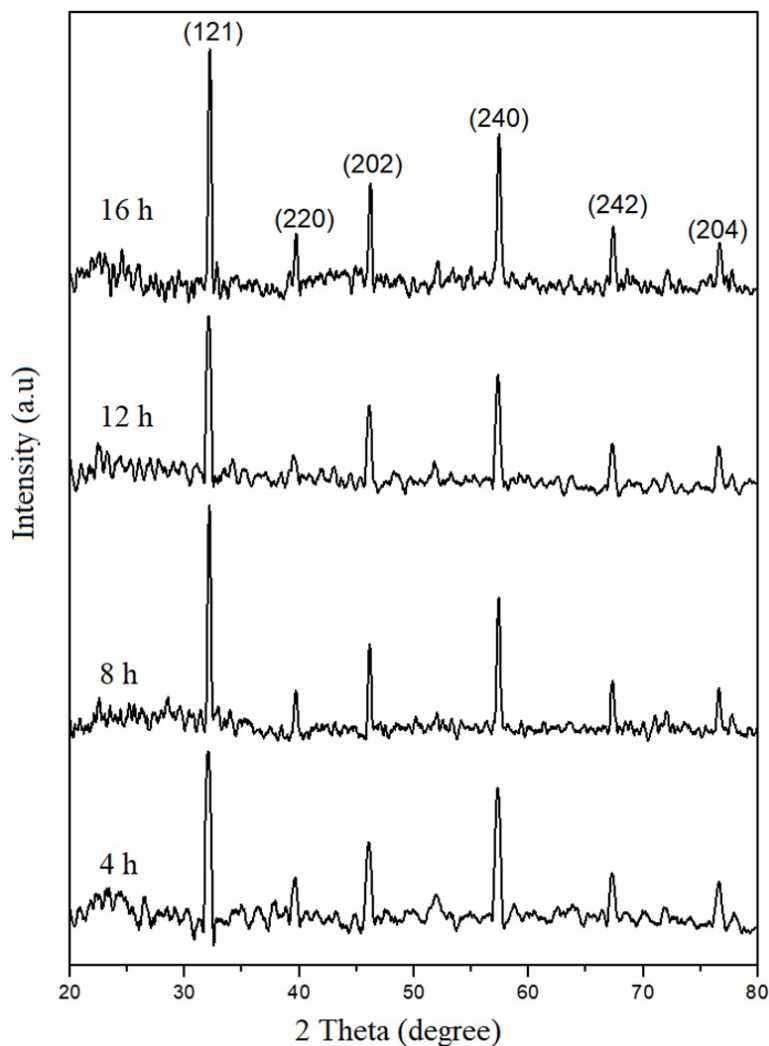


FIG. 8. XRD patterns of pellets sintered at 1000 °C for different time

TABLE 2. The resistance of sintered sample at 1000 °C

Samples	Resistance (Ω)
LFO-COP-1000 °C 4 h	$16.1 \cdot 10^7$
LFO-COP-1000 °C 8 h	$15.4 \cdot 10^7$
LFO-COP-1000 °C 12 h	$12.6 \cdot 10^7$
LFO-COP-1000 °C 16 h	$10.7 \cdot 10^7$

3.5. Impedance spectroscopy

The impedance spectroscopy is applied to determine the electrical properties of LaFeO_3 . At room temperature the frequency range 0 Hz to 10 MHz shows the frequency dependence of the dielectric constant (Fig. 11). The results exhibited that the high dielectric constant is due to grain-grain boundaries that changes with particle size, as the increase in heat treatment time resulted in higher grain size. The sample sintered at 1000 °C for 4 h displayed the lowest value at low frequency as compared to the sample at 16 h. This is the normal behavior of the dielectrics and the grain size distribution is narrow. Generally, four types of electric polarization processes (electronic, ionic, dipolar and space charge polarization) contribute to the dielectric properties [44]. At low frequency all of these polarizations are significant. At higher frequency space charge polarization gradually decreases. Therefore, the value of dielectric constant is constant at high frequency (10 MHz).

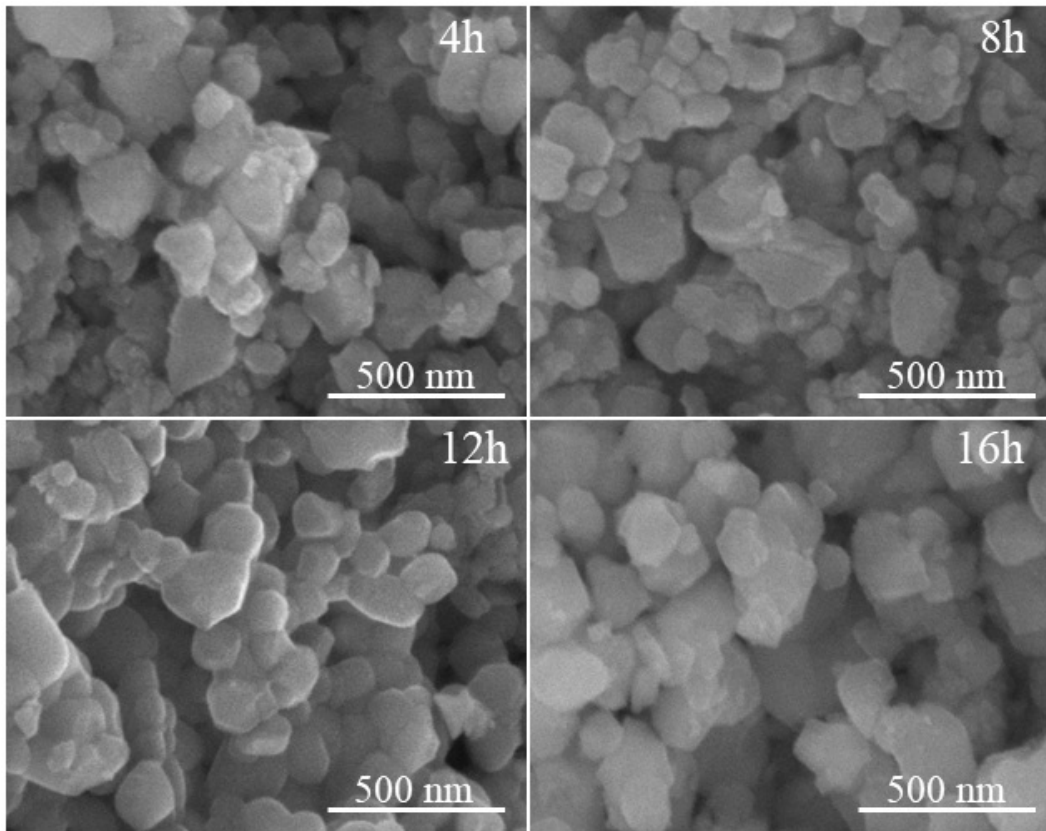


FIG. 9. SEM images of pellets sintered at 1000 °C for different time

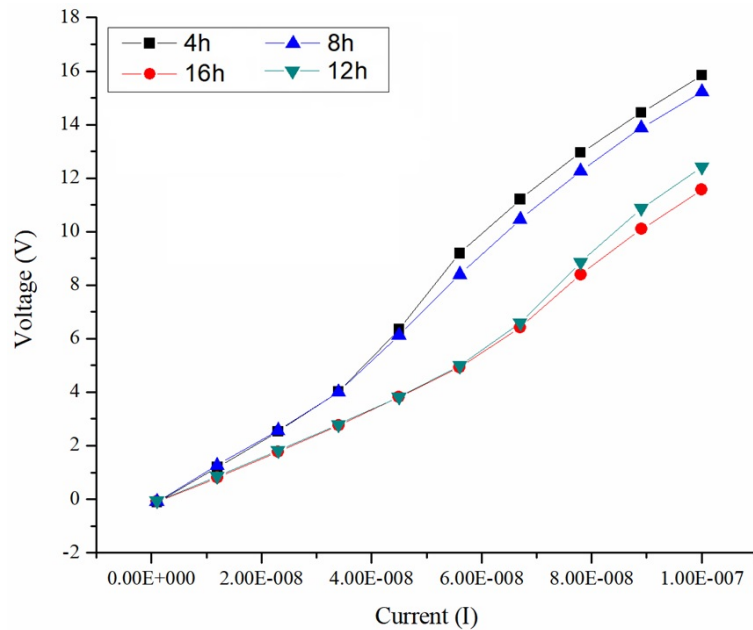


FIG. 10. The IV curve of the pellets sintered at 1000 C for 4, 8, 12 and 16 h

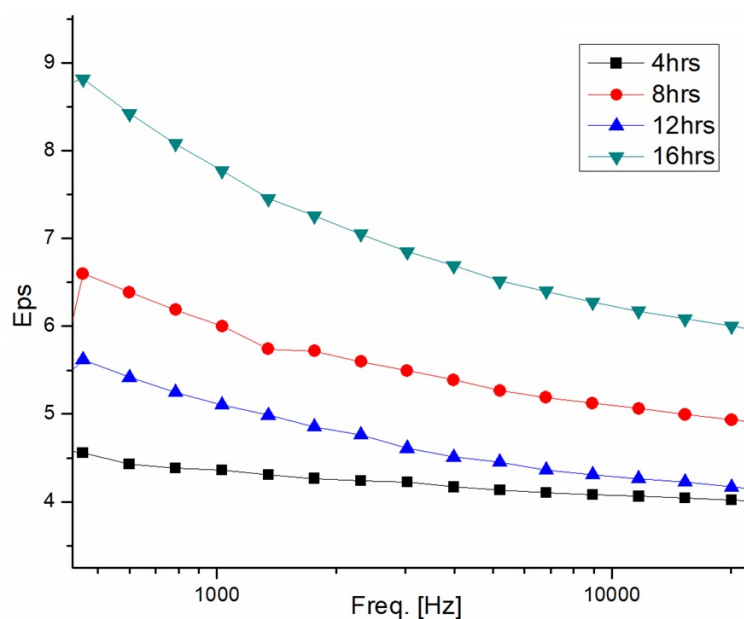


FIG. 11. The frequency dependence of dielectric constant

4. Conclusion

This study details the synthesis and characterization of perovskite-type LaFeO_3 . The synthesized particles were characterized by XRD and the effect of sintering conditions on crystal symmetry and geometric structure is examined. It was found that an increase in temperature resulted in the transformation of amorphous hydroxide phases to the crystalline LaFeO_3 phase. It is also confirmed from XRD results that the synthesized perovskite-like LaFeO_3 has an orthorhombic unit cell with space group of pbnm . The unit cell parameters of LaFeO_3 were calculated as; $a = 5.563$, $b = 5.562$ and $c = 7.868$. The SEM results exhibited the semi-spherical particles with sharp grain boundaries. The particles were found in aggregation and expanded in size when sintered at high temperature. The average particle size of sintered pellets at 1000°C for 4, 8, 12 and 16 h is determined 105, 130, 160 and 200 nm respectively. TGA analysis indicates that up to 800°C of the hydroxides were strongly decomposed. However, after 800°C weight loss is remarkably decreased. At 650°C , 90% of the hydroxides were decomposed attributed to 27% weight loss. Two probe DC resistivity shows that resistance decreases with the increase in heat treatment and time due to excessive oxygen vacancies and an increase in particle size. Impedance spectroscopy displayed the high dielectric constant due to the grain-grain boundaries which change with particle size. Based on the results, perovskite-type LaFeO_3 material is proposed for practical application in energy and environmental fields.

References

- [1] Shahid M.K., Batool A., Kashif A., Nawaz M.H., et al. Biofuels and biorefineries: Development, application and future perspectives emphasizing the environmental and economic aspects. *J. Environ. Manage.*, 2021, **297**, 113268.
- [2] Khan S.A., Arshad Z., Shahid S., Arshad I., et al. Synthesis of TiO_2 /Graphene oxide nanocomposites for their enhanced photocatalytic activity against methylene blue dye and ciprofloxacin. *Compos. Part B Eng.*, 2019, **175**, 107120.
- [3] Wang H., Zheng H., Jiang Z., Dai Y., et al. Efficacies of biochar and biochar-based amendment on vegetable yield and nitrogen utilization in four consecutive planting seasons. *Sci. Total Environ.* 2017, **593–594**, P. 124–133.
- [4] Shahid M.K., Kashif A., Fuwad A., Choi, Y. Current advances in treatment technologies for removal of emerging contaminants from water – A critical review. *Coord. Chem. Rev.*, 2021, **442**, 213993.
- [5] Hasan S.A.U., Lee D.S., Im S.H., Hong K.H. Present Status and Research Prospects of Tin-based Perovskite Solar Cells. *Sol. RRL*, 2020, **4**, 1–30.
- [6] Sri Gyan D., Dwivedi A., Roy P., Maiti T. Synthesis and thermoelectric properties of $\text{Ba}_2\text{TiFeO}_6$ double perovskite with insight into the crystal structure. *Ferroelectrics*, 2018, **536**, P. 146–155.
- [7] Nguyen A.T., Phung V.D., Mittova V.O., Ngo H.D., et al. Fabricating nanostructured HoFeO_3 perovskite for lithium-ion battery anodes via co-precipitation. *Scr. Mater.*, 2022, **207**, 114259.
- [8] Albadi Y., Martinson K.D., Shvidchenko A.V., Buryanenko I.V., et al. Synthesis of GdFeO_3 nanoparticles via low-temperature reverse co-precipitation: the effect of strong agglomeration on the magnetic behavior. *Nanosyst. Physics, Chem. Math.*, 2020, **11**, P. 252–259.
- [9] Chang L., Li J., Le Z., Nie P., et al. Perovskite-type CaMnO_3 anode material for highly efficient and stable lithium ion storage. *J. Colloid Interface Sci.*, 2021, **584**, P. 698–705.
- [10] Vo Q.M., Mittova V.O., Nguyen V.H., Mittova I.Y., et al. Strontium doping as a means of influencing the characteristics of neodymium orthoferrite nanocrystals synthesized by co-precipitation method. *J. Mater. Sci. Mater. Electron.*, 2021, **32**, P. 26944–26954.
- [11] Tikhanova S.M., Lebedev L.A., Martinson K.D., Chebanenko M.I., et al. The synthesis of novel heterojunction $\text{h-YbFeO}_3/\text{o-YbFeO}_3$ photocatalyst with enhanced Fenton-like activity under visible-light. *New J. Chem.*, 2021, **45**, P. 1541–1550.

- [12] Liu J., Sheha E., El-Dek S.I., Goonetilleke D., et al. SmFeO₃ and Bi-doped SmFeO₃ perovskites as an alternative class of electrodes in lithium-ion batteries. *CrystEngComm*, 2018, **20**, P. 6165–6172.
- [13] Fossdal A., Menon M., Wiik K., Einarsrud M., et al. Crystal Structure and Thermal Expansion of La_{1-x}Sr_xFeO₃ materials. *J. Am. Ceram. Soc.*, 2004, **87**, P. 1952–1958.
- [14] Scrimshire A., Lobera A., Bell A.M.T., Jones A.H., et al. Determination of Debye temperatures and Lamb-Mössbauer factors for LnFeO₃ orthoferrite perovskites (Ln = La, Nd, Sm, Eu, Gd). *J. Phys. Condens. Matter*, 2018, **30**, 105704.
- [15] Seo J.W., Fullerton E.E., Nolting F., Scholl A., et al. Antiferromagnetic LaFeO₃ thin films and their effect on exchange bias. *J. Phys. Condens. Matter*, 2008, **20**, 264014.
- [16] Wheeler G.P., Baltazar V.U., Smart T.J., Radmilovic A., et al. Combined Theoretical and Experimental Investigations of Atomic Doping to Enhance Photon Absorption and Carrier Transport of LaFeO₃ Photocathodes. *Chem. Mater.*, 2019, **31**, P. 5890–5899.
- [17] Abdallah F.B., Benali A., Triki M., Dhahri E., et al. Effect of annealing temperature on structural, morphology and dielectric properties of La_{0.75}Ba_{0.25}FeO₃ perovskite. *Superlattices Microstruct.*, 2018, **117**, P. 260–270.
- [18] Gosavi P.V., Biniwale R.B. Pure phase LaFeO₃ perovskite with improved surface area synthesized using different routes and its characterization. *Mater. Chem. Phys.*, 2010, **119**, P. 324–329.
- [19] Nakayama S., LaFeO₃ perovskite-type oxide prepared by oxide-mixing, co-precipitation and complex synthesis methods. *J. Mater. Sci.*, 2001, **36**, P. 5643–5648.
- [20] Sivakumar M., Gedanken A., Zhong W., Jiang Y.H., et al. Sonochemical synthesis of nanocrystalline LaFeO₃. *J. Mater. Chem.*, 2004, **14**, P. 764–769.
- [21] Qi X., Zhou J., Yue Z., Gui Z., et al. A simple way to prepare nanosized LaFeO₃ powders at room temperature. *Ceram. Int.*, 2003, **29**, P. 347–349.
- [22] Yang Z., Huang Y., Dong B., Li H.L. Controlled synthesis of highly ordered LaFeO₃ nanowires using a citrate-based sol-gel route. *Mater. Res. Bull.*, 2006, **41**, P. 274–281.
- [23] Wang Y., Zhu J., Zhang L., Yang X., et al. Preparation and characterization of perovskite LaFeO₃ nanocrystals. *Mater. Lett.*, 2006, **60**, P. 1767–1770.
- [24] Su H., Jing L., Shi K., Yao C., et al. Synthesis of large surface area LaFeO₃ nanoparticles by SBA-16 template method as high active visible photocatalysts. *J. Nanoparticle Res.*, 2010, **12**, P. 967–974.
- [25] Tang P., Tong Y., Chen H., Cao F., et al. Microwave-assisted synthesis of nanoparticulate perovskite LaFeO₃ as a high active visible-light photocatalyst. *Curr. Appl. Phys.*, 2013, **13**, P. 340–343.
- [26] Liu T., Xu Y. Synthesis of nanocrystalline LaFeO₃ powders via glucose sol-gel route. *Mater. Chem. Phys.*, 2011, **129**, P. 1047–1050.
- [27] Idrees M., Nadeem M., Atif M., Siddique M., et al. Origin of colossal dielectric response in LaFeO₃. *Acta Mater.*, 2011, **59**, P. 1338–1345.
- [28] Köferstein R., Jäger L., Ebbinghaus, S.G., Magnetic and optical investigations on LaFeO₃ powders with different particle sizes and corresponding ceramics. *Solid State Ionics*, 2013, **249–250**, 1–5.
- [29] Thuy N.T., Minh D. Le, Size effect on the structural and magnetic properties of nanosized perovskite LaFeO₃ prepared by different methods. *Adv. Mater. Sci. Eng.*, 2012, 380306.
- [30] Liu W., Zeng X., Liu S., Zhu Y., et al. Growth and characterization of LaFeO₃ crystals. *Key Eng. Mater.*, 2014, **602–603**, P. 27–31.
- [31] Idrees M., Nadeem M., Siddiqi S.A., Ahmad R., et al. The organic residue and synthesis of LaFeO₃ by combustion of citrate and nitrate precursors. *Mater. Chem. Phys.*, 2015, **162**, P. 652–658.
- [32] Vijayaraghavan T., Bradha M., Babu P., Parida K.M., et al. Influence of secondary oxide phases in enhancing the photocatalytic properties of alkaline earth elements doped LaFeO₃ nanocomposites. *J. Phys. Chem. Solids*, 2020, **140**, 109377.
- [33] Zhao F., Bai Z., Fu Y., Zhao D., et al. Tribological properties of serpentine, La(OH)₃ and their composite particles as lubricant additives. *Wear*, 2012, **288**, P. 72–77.
- [34] Kang J.G., Kim Y. Il, Won Cho D., Sohn Y. Synthesis and physicochemical properties of La(OH)₃ and La₂O₃ nanostructures. *Mater. Sci. Semicond. Process.*, 2015, **40**, P. 737–743.
- [35] Lazarević Z.Ž., Jovalekić Č., Recnik A., Ivanovski V.N., et al. Study of manganese ferrite powders prepared by a soft mechanochemical route. *J. Alloys Compd.*, 2011, **509**, P. 9977–9985.
- [36] Shahid M.K., Choi Y. Characterization and application of magnetite Particles, synthesized by reverse coprecipitation method in open air from mill scale. *J. Magn. Magn. Mater.*, 2020, **495**, 165823.
- [37] Kabir H., Nandyala S.H., Rahman M.M., Kabir M.A., et al. Influence of calcination on the sol–gel synthesis of lanthanum oxide nanoparticles. *Appl. Phys. A Mater. Sci. Process.*, 2018, **124**, 1–11.
- [38] Boumaza S., Boudjellal L., Brahimi R., Belhadi A., et al. Synthesis by citrates sol-gel method and characterization of the perovskite LaFeO₃: application to oxygen photo-production. *J. Sol-Gel Sci. Technol.*, 2020, **94**, P. 486–492.
- [39] Al-Mamari R.T., Widatallah H.M., Elzain M.E., Gismelseed A.M., et al. Structural, Mössbauer, and Optical studies of mechano-synthesized Ru³⁺-doped LaFeO₃ nanoparticles. *Hyperfine Interact.*, 2021, **243**, 4.
- [40] Thirumalairajan S., Girija K., Ganesh I., Mangalaraj D., et al. Controlled synthesis of perovskite LaFeO₃ microsphere composed of nanoparticles via self-assembly process and their associated photocatalytic activity. *Chem. Eng. J.*, 2012, **209**, P. 420–428.
- [41] Thirumalairajan S., Girija K., Mastelaro V.R., Ponpandian N. Photocatalytic degradation of organic dyes under visible light irradiation by floral-like LaFeO₃ nanostructures comprised of nanosheet petals. *New J. Chem.*, 2014, **38**, P. 5480–5490.
- [42] Tho N.D., Huong D., Van Ngan P.Q., Thai G.H., et al. Effect of sintering temperature of mixed potential sensor Pt/YSZ/LaFeO₃ on gas sensing performance. *Sensors Actuators B Chem.*, 2016, **224**, P. 747–754.
- [43] Wang S., Wang D., Chung D.D.L., Chung J.H. Method of sensing impact damage in carbon fiber polymer-matrix composite by electrical resistance measurement. *J. Mater. Sci.*, 2006, **41**, P. 2281–2289.
- [44] Pirzada B.M., Sabir S. Polymer-based nanocomposites for significantly enhanced dielectric properties and energy storage capability, in: *Polymer-Based Nanocomposites for Energy and Environmental Applications*, Elsevier Ltd., 2018, P. 132–183.

Submitted 2 November 2021; revised 20 April 2022; accepted 22 April 2022

Information about the authors:

Muhammad Irfan Asghar – Department of Physics, COMSATS University Islamabad, Lahore Campus, Pakistan; irfanmeo1@gmail.com

Muhammad Kashif Shahid – Research Institute of Environment & Biosystem, Chungnam National University, Daejeon, Republic of Korea; mkbbutt2000@gmail.com

Muhammad Haq Nawaz – Department of Physics, University of Gujrat, Hafiz Hayat Campus, Gujrat, Pakistan; haqn5656@gmail.com

Muhammad Idrees – Department of Physics, COMSATS University Islamabad, Lahore Campus, Pakistan; midrees@cuilahore.edu.pk

Muhammad Asif – Department of Physics, University of Engineering and Technology Lahore, Pakistan; asif81292@yahoo.com

Ahsan Ali – School of Mechanical Engineering, University of Leeds, Leeds LS2 9JT, UK; ahsanali23654@gmail.com

Conflict of interest: the authors declare no conflict of interest.

The joint effect of doping with tin(IV) and heat treatment on the transparency and conductivity of films based on titanium dioxide as photoelectrodes of sensitized solar cells

Svetlana Kuznetsova^{1,a}, Olga Khalipova¹, Yu-Wen Chen², Vladimir Kozik¹

¹National Research Tomsk State University, Tomsk, 634050 Russia

²National Central University, Jhongli, 32001, Taiwan

^aonm@mail.tsu.ru

Corresponding author: Svetlana Kuznetsova, onm@mail.tsu.ru

ABSTRACT This study focuses on the preparation of transparent conducting TiO₂ films with the addition of Sn(IV) by sol-gel method from film-forming solutions based on n-C₄H₉OH-(C₄H₉O)₄Ti-SnCl₄·5H₂O at the temperature of 300–400 °C. Such films attract great attention because they can be used in flexible transparent photoanodes for the preparation of high effective sensitized solar cells. The morphology, phase composition, and optical properties of films were studied by X-ray diffraction, X-ray spectral microanalysis, scanning electron microscopy, spectrophotometry, and ellipsometry. The content of Sn(IV) influences the composition of films. The solid solution based on titanium dioxide with anatase structure is formed at a content of 5 mol.% Sn(IV); the films with a content of 10–30 mol.% Sn(IV) are the mixture of the TiO₂:Sn solid solution and SnO₂ with rutile structure. Regardless of the tin content, all films contain an amorphous TiO₂·nH₂O phase. The formation of oxide phases occurs through the stages of thermal destruction of Sn(OH)₃Cl, tin acid, and burnout of butoxy groups of butoxytitanium(IV). The as-synthesized oxide films are uniform and continuity regardless of the tin content. An increase in the content of Sn(IV) in the composition of the films leads to an increase in their thickness from 48 to 105 nm and a decrease in the refractive index from 1.89 to 1.66. The minimum resistance value is characteristic for films that are the solid solution with an anatase structure and with an admixture of the amorphous phase of titanous acid. The surface resistance of the glass decreases by 10⁸ times after deposition of the film based on TiO₂ with 5 mol.% Sn(IV). Films based on TiO₂ with 5 mol.% Sn(IV) are characterized by a higher transparency coefficient in the entire visible range of the spectrum (80–70%) and can be used in photoelectrode in dye-sensitized solar cells.

KEYWORDS film-forming solution, oxide composite film, tin oxide, titanium oxide, sol-gel method.

ACKNOWLEDGEMENTS This work was carried out within the framework of project No 18-29-11037 of Russian Foundation for Basic Research.

FOR CITATION Kuznetsova S., Khalipova O., Yu-Wen Chen, Kozik V. The joint effect of doping with tin(IV) and heat treatment on the transparency and conductivity of films based on titanium dioxide as photoelectrodes of sensitized solar cells. *Nanosystems: Phys. Chem. Math.*, 2022, **13** (2), 192–203.

1. Introduction

Driven by the growing threat of energy crisis, the use of solar energy is one of the most remarkable approaches for renewable natural resources utilization. It is inducing the scientific community to make great efforts towards the direction of improving solar energy conversion technologies. One of the main trends in modern solar energy is the creation of non-silicon photovoltaic devices. The great interested device of the last generation is the dye-sensitized solar cell (DSSC), being a low-cost and high-efficiency solar energy-to-electricity converter. The DSSCs may represent a cost-effective alternative to traditional silicon solar cells which have a number of disadvantages such as high cost, the need for a large area of the battery itself, as well as low efficiency in geographic areas with a large amount of precipitation [1–3]. The light absorption and the charge carrier transport are separated in DSSCs, which allow one to improve the performance of the device by optimizing each process separately. Moreover, the technology of DSSC allows creating the flexible solar cells. In such photovoltaic devices, wide-gap semiconductors are used as a photoanode.

A lot of research has been done on titanium dioxide electrodes [4, 5], but the efficiency of these dye-sensitized solar cells was only 12.3% which is much lower than that of solar cells produced by silicon technology [6, 7]. Thus, it is an urgent task to search for new approaches to the production of photoanodes based on thin oxide films for high-efficiency DSSCs. One of the ways is a modification of titanium dioxide by tin dioxide. Tin dioxide is one of the most studied metal oxide semiconductor, which has attracted a great deal of attention in the field of solar cells and photocatalysis due to its excellent optical properties, high stability of its photochemical properties, quick recombination of photo-generated

charge carriers, large band gap ($E_g = 3.6$ eV), high electron mobility ($125 \text{ cm}^2\text{V}^{-1}\text{s}^{-1}$) [8–14]. Moreover, the SnO_2 can act itself as a photoanode replacing titanium dioxide. Previous research showing the possibility of using tin dioxide as an electronically conductive transparent layer have appeared quite recently. Li et al. [15] were one of the first researchers who developed solar cells with such photoanodes. However, the highest power conversion efficiency of these devices was less than 3.8%. Later, Ke et al. [16] obtained the oxide film from a tin(II) chloride solution and prepared the photoanode with an average efficiency of 16.0%. In addition, according to the literature [17, 18], the use of a $\text{TiO}_2/\text{SnO}_2$ bilayer as an effective layer for extracting electrons makes it possible to increase power conversion efficiency of perovskite solar cell device up to 18.85% compared to the individual TiO_2 .

There are many previous reports available about the preparation of TiO_2 and SnO_2 films using not expensive, simple chemical methods such as sol-gel method. Most of the works performed earlier show that the synthesis temperature of conductive and transparent tin dioxide by the sol-gel method from film-forming solutions (FFSs) should be at least 500–600 °C, since at this temperature crystalline phase of tin oxide is formed [19, 20]. The production of crystalline titanium dioxide also requires high temperatures [21]. This is a serious obstacle to the use of TiO_2 and SnO_2 films on flexible transparent photoanodes that can withstand temperatures of 200–300 °C. Some research groups propose to obtain TiO_2 films with SnO_2 at temperatures of 400–500 °C from sols based on organic derivatives of titanium(IV), and tin(II) or tin(IV) chloride. For example, in work [22], films were obtained from sols based on titanium(IV) n-butoxide and tin(II) chloride in ethanol at 450 °C. The authors of this work claim the formation of a solid solution based on titanium dioxide up to 30 mol.% tin. The same composition was indicated by the authors of the work [23], in which films based on titanium dioxide and tin dioxide were obtained from isopropanol-based sols with titanium isopropoxide, and tin(II) chloride. However, very wide diffraction maxima and modes in the Raman spectra, which are presented in these works, indicate the presence of an amorphous phase in these samples, the composition of which is unknown. Moreover, there are no data in the literature that make it possible to evaluate the possibility of using the sol-gel method to obtain the transparent conducting films of titanium dioxide with the addition of tin(IV) at temperatures below 450 °C.

In this present study, the transparent conducting TiO_2 films with the addition of tin(IV) was obtained by sol-gel method from FFSs based on $n\text{-C}_4\text{H}_9\text{OH}-(\text{C}_4\text{H}_9\text{O})_4\text{Ti-SnCl}_4 \cdot 5\text{H}_2\text{O}$ at temperatures of 300–400 °C and the process of obtaining films was researched. As a consequence of this systematic study, we established that the composition of films obtained at temperatures of 300–400 °C differs depending on the content of tin(IV). A comparative study of optical properties of films with different compositions and preparing temperatures have also been made. It was found that it is possible to obtain transparent conducting films of titanium dioxide with the addition of tin(IV) at temperatures below 450 °C by sol-gel method, indicating the considerable potential for application in high-efficiency solar converter.

2. Experimental part

2.1. Preparation of TiO_2 with Sn(IV) composite films on glass substrates

Films based on titanium dioxide with Sn(IV) additive (1–30 mol.% Sn(IV)) were obtained by the sol-gel method from FFSs based on titanium(IV) n-butoxide (TBT) and tin(IV) chloride in butanol-1. The starting reagents were butanol-1 (AO "EKOS-1", Russia, reagent purity 99,9 wt. %), titanium(IV) n-butoxide (TBT) ("Acros Organic, USA, reagent purity 99,9 wt. %), $\text{SnCl}_4 \cdot 5\text{H}_2\text{O}$ (Neftegazkhimkoplect, Russia, reagent purity 99 wt. %). Laboratory glass slides 2.0 ± 0.2 mm (Russia) were used as the substrates.

The FFSs were obtained at room temperature by dissolving a crystalline hydrate of tin(IV) chloride and then TBT in butanol-1. The amounts of substances were such that the total molar concentration of tin(IV) chloride and TBT was 0.3 mol/L. The FFSs were applied to glass substrates by dip-coating at a rate of 3 mm/min. The device consisted of a clamp for the substrate, a speed controller for dip-coating, and a little table on which the cuvette with FFSs are placed. After the application of FFSs on glass substrates, the samples were dried in a SNOL58/350 LEN drying oven at a temperature of 60 °C (FFS 60 °C) for one hour and annealed in a PM-1.0-20 muffle furnace at 300, or 400 °C for 1 and 9 hours.

2.2. Methods for studying film-forming solutions and TiO_2 with Sn(IV) composite films

The composition of the FFSs and the processes occurring in them were investigated by IR spectroscopy and viscometry. The IR spectra of the samples were carried out on a Nicolet 6700 spectrophotometer (USA) in the frequency range from 400 to 4000 cm^{-1} . The viscosity of the FFSs was determined using a VPZh-2 (Russia) capillary viscometer with a capillary diameter of 0.73 mm^3 . The capillary viscometer consisted of one capillary with a funnel and a narrow tube. The assessment of the viscosity was carried out by measuring the time during which a certain volume of the investigated FFS flows out of the funnel. The kinematic viscosity was calculated using the following formula:

$$\eta = \left(\frac{g}{9.807} \right) \cdot \tau \cdot K \quad (1)$$

where η is kinematic viscosity of the liquid, mm^2/s ; τ is time of liquid flow, s; g is acceleration due to gravity, m/s^2 ; and K is viscometer constant, mm^2/s^2 . The average size of colloidal particles in the FFSs was determined by the "turbidity spectrum" method. The method is based on the use of the Rayleigh equation for colloidal systems with low concentration,

the dispersed phase of which doesn't absorb incident light and is optically isotropic [24]. The absorption spectra of FFSs in the visible and ultraviolet regions were recorded relative to air on a PE-5400 UV spectrophotometer (Russia).

The thermal decomposition of the butanol-1-TBT-SnCl₄·5H₂O film-forming solution containing 20 mol.% Sn(IV) was studied by thermal analysis and IR spectroscopy. Before analysis, solution was dried at 60 °C until the formation of dry residue. The obtained sample was denoted as FFS-60(20 mol.% Sn(IV)). For comparison, the thermal decomposition of the dry (drying at 60 °C) residue of butanol-1-TBT and butanol-1-SnCl₄·5H₂O solution was also investigated. Synchronous thermal analysis was conducted using an STA 449 F1 Jupiter thermoanalyzer (Netzsch-Gertebau GmbH, Germany).

The phase composition of the composites based on titanium dioxide with tin(IV) additive was determined by X-ray diffraction (XRD) using a Rigaku Miniflex 600 diffractometer (Rigaku, Japan) with CuK_α radiation in the 2θ range from 10 to 80°. The diffraction pattern was scanned by steps of 0.02 and a recording rate of 2 deg/min. The resulting diffractograms were interpreted using the JCPDS-ICDD diffraction database. The morphology of the composites was studied by scanning electron microscopy (SEM). The distribution of the elements on the surface was determined based on energy-dispersive X-ray spectroscopic (EDX) analysis. It was performed on a Hitachi TM-3000 scanning electron microscope with a ShiftED 3000 electron microprobe (Hitachi High-Technologies Corporation, Japan). The transmittance of the investigated composite films on the glass in the visible region of the spectrum was studied on a PE5400UF spectrophotometer in the wavelength range of 340–1000 nm. Pure glass was used as a reference sample. The thicknesses and refractive indexes of the composite materials were investigated by the ellipsometry method using SE400 (Germany) and LEF-3M (Russia) ellipsometers. Surface resistance was measured by the two-probe method. The surface resistance of the samples was measured from room temperature to 200 °C. The activation energy of charge carriers was calculated from the tangent of the angle of inclination of the tangent as follows:

$$\operatorname{tg} \alpha = \frac{\Delta \log(1/R)}{\Delta(1/T)}, \quad (2)$$

$$E_a = \frac{2 \tan \alpha R}{0.43}, \quad (3)$$

where $R = 8.314 \text{ J/mol}\cdot\text{K}$.

3. Results and discussion

3.1. Composition and properties of film-forming solutions based on Butanol-1-TBT-SnCl₄·5H₂O

The IR spectra of FFSs with different ratios of TBT and tin(IV) chloride (Fig. 1) have the same set of absorption frequencies for different bond vibrations, which slightly differ in the absorption coefficient.

The observed absorption bands were assigned based on the literature data [25,26]. An analysis of the obtained spectra showed that the FFSs contain hydroxyl groups (the broad peak with a maximum at a frequency of 3921 cm⁻¹), methyl and methylene groups (the stretching vibrations at 2958, 2931, and 2872 and bending vibrations at 1457 cm⁻¹) of butanol and butoxy groups of TBT. The absorption bands at frequencies of 1009, 951, and 512 cm⁻¹ correspond to the vibrations of Ti-OH, O-Ti-O, and Ti-O bonds. The band at a frequency of 822.4 cm⁻¹ corresponds to the vibration of the Sn-O bond. The results of IR spectroscopy indicate that hydrolysis of TBT and SnCl₄ occurs in butanol with the participation of crystallization water introduced into butanol together with SnCl₄·5H₂O.

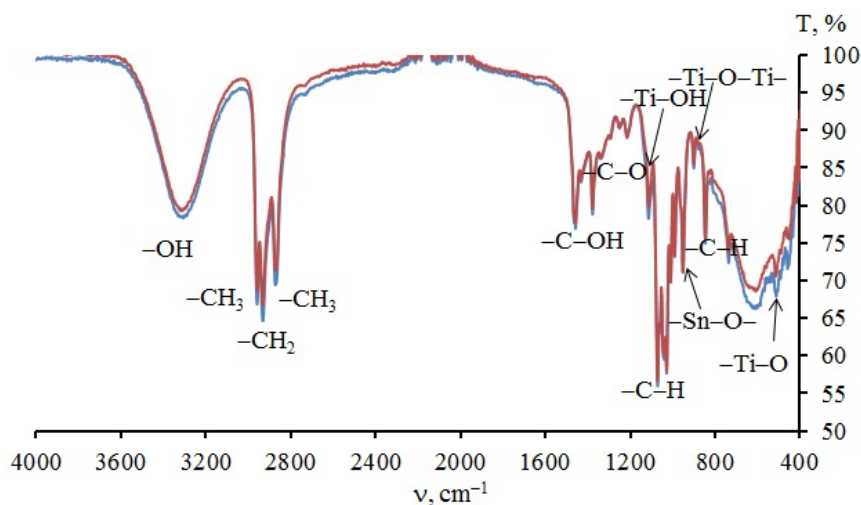
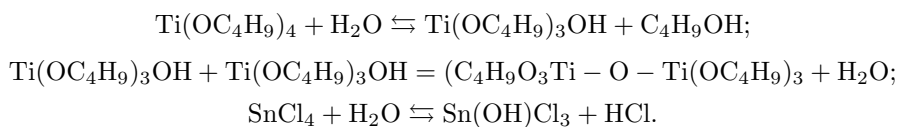


FIG. 1. IR spectra of FFSs based on Butanol-1-TBT-SnCl₄·5H₂O with the Sn(IV) content of 1 mol.% (red curve) and 5 mol.% (blue curve)

The presence in the IR transmission spectrum of absorption characteristic of the vibrations of the Ti–O–Ti bond indicates the interaction of the hydrolyzed $\text{Ti}(\text{OC}_4\text{H}_9)_3\text{OH}$ molecules with each other. The processes passing in FFSs based on Butanol-1–TBT– $\text{SnCl}_4 \cdot 5\text{H}_2\text{O}$ can be represented as follow:



The degree of hydrolysis of titanium(IV) and tin(IV) compounds is insignificant, as evidenced by the change in the kinematic viscosity of FFSs over time ($T = 20 \pm 2 \text{ }^\circ\text{C}$) and their comparison with the viscosity of butanol ($4.00 \pm 0.03 \text{ mm}^2/\text{s}$ at $T = 20 \text{ }^\circ\text{C}$). As can be seen from Fig. 2, the values the kinematic viscosity of FFSs in the equilibrium region (after 7 days) are close and are in the range from 4.50 (5 mol.% Sn(IV)) to $4.70 \pm 0.03 \text{ mm}^2/\text{s}$ (30 mol.% Sn(IV)).

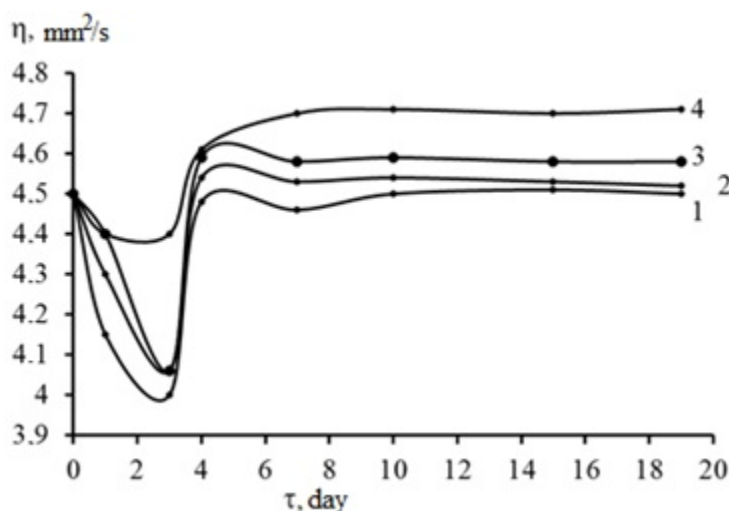


FIG. 2. The change of the kinematic viscosity of FFSs based on Butanol-1–TBT– $\text{SnCl}_4 \cdot 5\text{H}_2\text{O}$, with different content of Sn(IV) (mol.%): 1–5; 2–15; 3–25; 4–30

Presumably, a decrease of the viscosity of all FFSs in the first three days is associated with the processes of destruction of intermolecular bonds between *n*-butanol molecules [27]. An increase of the viscosity after the third day is explained by the formation of a new structure of the solutions, where bonds are formed between *n*-butanol molecules and hydrolyzed salts, as well as by the formation of $(\text{C}_4\text{H}_9\text{O})_3\text{Ti}-\text{O}-\text{Ti}(\text{OC}_4\text{H}_9)_3$. The state of equilibrium in FFSs, in which there is no change in viscosity, is observed after 7 days of keeping the solutions at a temperature of $20 \text{ }^\circ\text{C}$ and it lasts up to 20 days. At this period of time, FFSs are suitable for the preparation of oxide films with stable properties. An increase in the addition of $\text{SnCl}_4 \cdot 5\text{H}_2\text{O}$ does not affect the stability of the solution, but insignificantly increases the value of the kinematic viscosity. The increase of the viscosity can be associated with the amount of introduced water with crystalline hydrate, which is involved in the processes of salt hydrolysis and polycondensation. According to the results of the “Spectrum-turbidity” method, all FFSs belong to colloidal systems (sols) and contain colloidal particles with a size of 80–90 nm.

The results of thermal analysis of the dry residue of Butanol-1– $\text{SnCl}_4 \cdot 5\text{H}_2\text{O}$ solution (Fig. 3) indicate that the process of its thermal destruction is characterized by three stages of decomposition and ends at the temperature of about $350 \text{ }^\circ\text{C}$. According to the XRD results, the final decomposition product of the dry residue of Butanol-1– $\text{SnCl}_4 \cdot 5\text{H}_2\text{O}$ solution is tin dioxide with a rutile structure (Fig. 4).

As can be seen in Fig. 4, the degree of crystallinity of the sample obtained at a temperature of $400 \text{ }^\circ\text{C}$ (Fig. 4a) is small and increases with the increase of the annealing temperature up to $600 \text{ }^\circ\text{C}$ (Fig. 4b).

The results of the analysis of the change in mass on the TG curve of decomposition of the dry residue of Butanol-1– $\text{SnCl}_4 \cdot 5\text{H}_2\text{O}$ solution are presented in Table 1. The loss of mass according to the TG curve at the third stage is 2.79 wt.%. This corresponds to the removal of two water molecules from stannic acid, which is formed at the second stage in the temperature range between 225 and $285 \text{ }^\circ\text{C}$. The stannic acid is formed from tin(IV) hydroxychloride crystalline hydrate with an endothermic effect with a maximum of $244.1 \text{ }^\circ\text{C}$. It is not possible to determine the composition of the removed products and the initial composition of the dry residue of Butanol-1– $\text{SnCl}_4 \cdot 5\text{H}_2\text{O}$ solution using the TG curve, due to the superposition of the processes of its thermal destruction in the temperature range between 20 and $225 \text{ }^\circ\text{C}$. However, the IR spectrum of this sample indicates that it contains not only hydrolyzed tin(IV) salt, but also butanol (Fig. 5).

Therefore, four endothermic effects accompanying the first stage of the thermal decomposition of the dry residue of solution with temperature maxima of 46.8 , 76.0 , 163.3 , and $190.5 \text{ }^\circ\text{C}$, can be associated with the removal of molecules

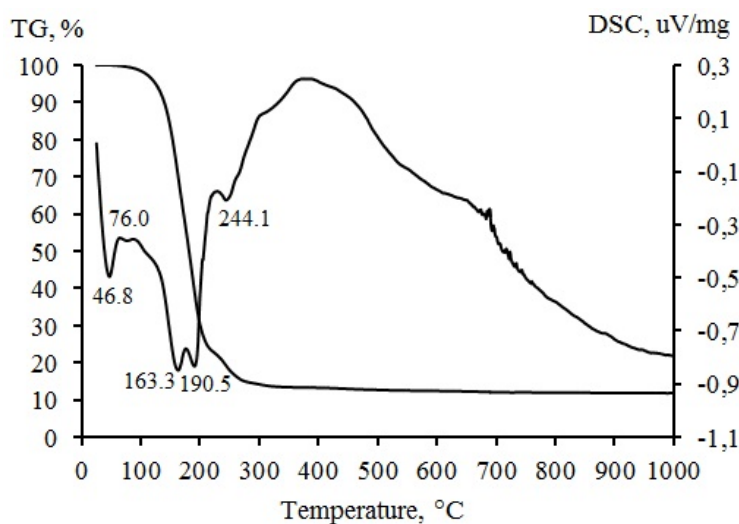


FIG. 3. The thermogram of the decomposition of the dry residue of Butanol-1–SnCl₄·5H₂O solution

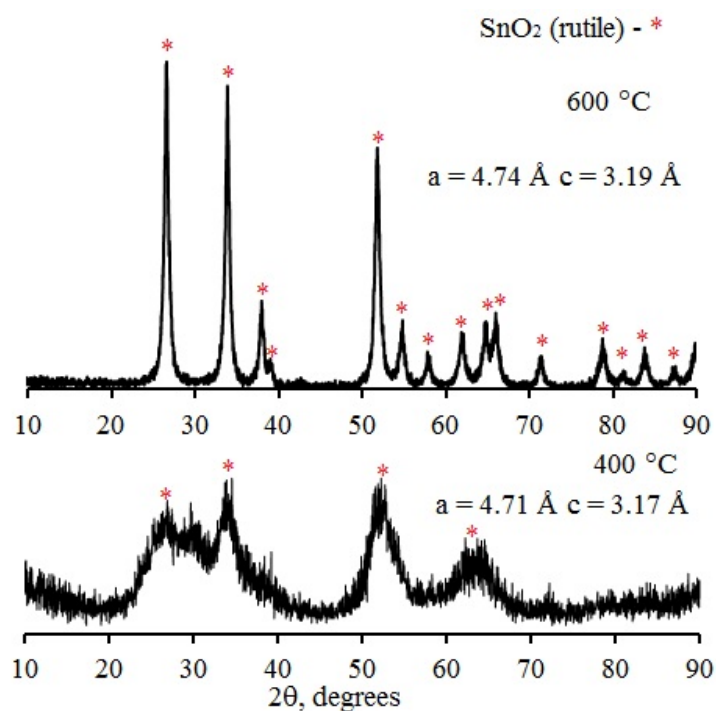
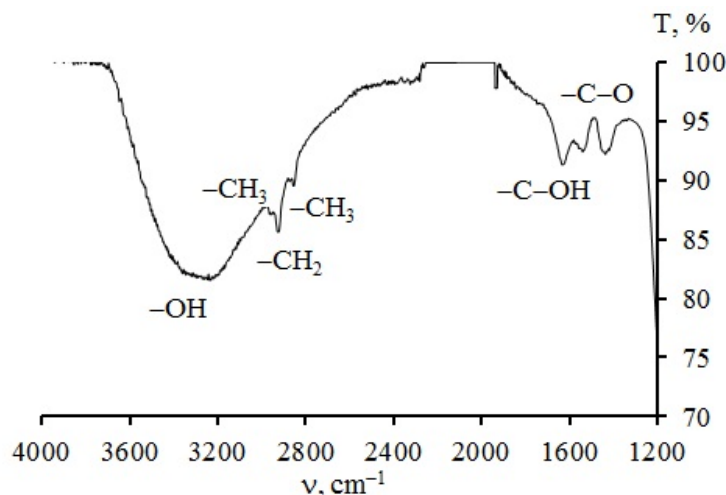


FIG. 4. The diffraction patterns of the dry residue of Butanol-1–SnCl₄·5H₂O solution annealed at 400 °C (1 hours) and 600 °C (1 hours)

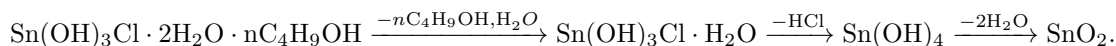
TABLE 1. The results of the analysis of the change in mass on the TG curve of the dry residue of Butanol-1–SnCl₄·5H₂O solution

Stage	T , °C	Loss of mass, wt. %	M , g/mol and composition of the removed material practice/theory	M , g/mol and the composition of the resulting material practice/theory
I	20–225	77.13	*	222.85 Sn(OH) ₃ Cl·H ₂ O/ 223.14 Sn(OH)₃Cl·H₂O
II	225–285	8.20	36.71 HCl/ 36.45 HCl	186.14 Sn(OH) ₄ / 186.69 Sn(OH)₄
III	285–350	2.79	17.73 H ₂ O/ 17.99 H₂O	151.13 SnO ₂ / 150.69 SnO₂

*The composition was not determined

FIG. 5. The IR spectrum of the dry residue of Butanol-1-SnCl₄·5H₂O solution

of adsorbed water, butanol, and hydrogen chloride, respectively. The scheme of thermal destruction of the dry residue of Butanol-1-SnCl₄·5H₂O solution can be represented as follows:



The thermal decomposition of the dry residue of Butanol-1-TBT solution proceeds stepwise with 3 stages (Fig. 6). The first stage proceeds at the temperature range between 25 and 330 °C and is characterized by the maximum change in the mass of the sample. The decomposition process in this temperature range is accompanied by two endothermic effects with maxima of 47.4 and 80.2 °C, as well as the exothermic effect at a temperature of 285.4 °C. The removal of adsorbed butanol and water molecules proceeds with the endothermic effects, and the exothermic effect indicates the burnout of butoxy-groups.

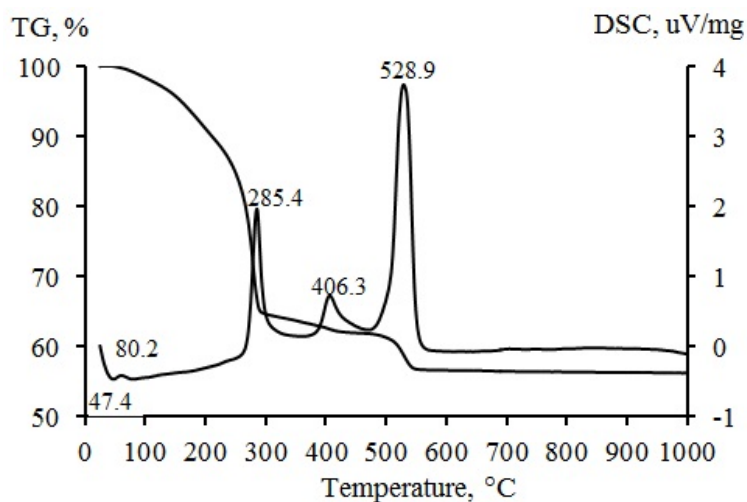


FIG. 6. The thermogram of the decomposition of the dry residue of Butanol-1-TBT solution

The next two stages (330–450 °C – stage II, 450–560 °C – stage III) are accompanied by exothermic effects with maxima at 406.3 and 528.9 °C, respectively. At these stages, further burnout of butoxy-groups occurs and, eventually, at a temperature of 550 °C, titanium dioxide is obtained:



The XRD results indicate that titanium oxide crystallizes in the anatase phase at a given temperature (Fig. 7).

Figure 8 shows the thermogram of decomposition of FFS-60(20 mol.% Sn(IV)) sample. The TG curve indicates four stages of thermal destruction of this sample. The comparison with the thermograms of dry residues of Butanol-1-SnCl₄·5H₂O and Butanol-1-TBT solutions indicates that with the combined presence of TBT and tin(IV) chloride in butanol, the temperature regimes of each stage shift to lower temperatures and the decomposition process ends at

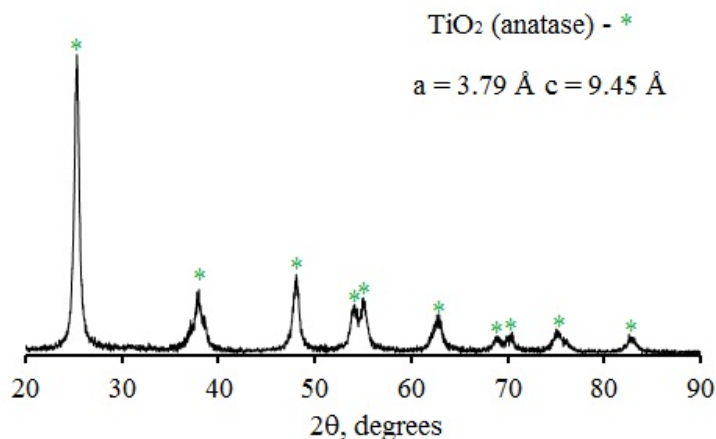


FIG. 7. The diffraction pattern of the dry residue of Butanol-1–TBT solution annealed at 550 °C

the temperature of 500 °C. This is 50 °C lower than the final decomposition temperature of dry residue of Butanol-1–TBT solution. The change in the intensity of the maxima on the DSC curve indicates the superposition of processes accompanied by the removal of hydrogen chloride, water (endothermic effects) with the process of burnout of butoxy-groups (exothermic effects).

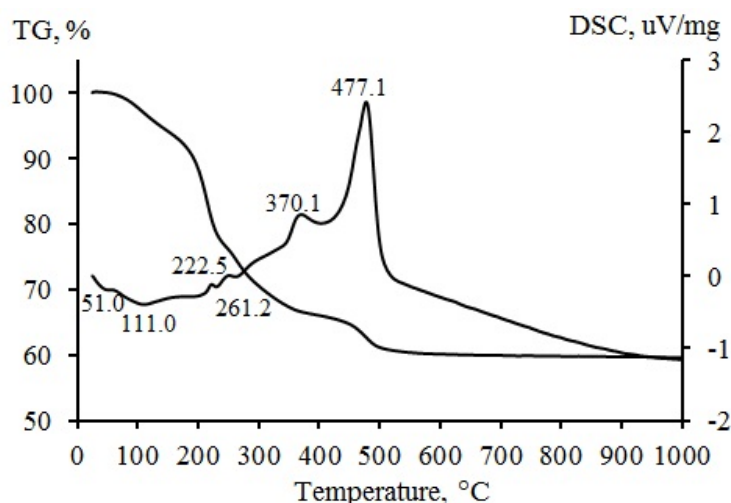


FIG. 8. The thermogram of the FFS-60(20 mol.% Sn(IV)) decomposition

The results of XRD analysis of the FFS-60(30 mol.% Sn(IV)) sample annealed at 500 °C indicate the formation of two substances: TiO₂:Sn solid solution with an anatase structure and SnO₂ with a rutile structure (Fig. 9). The broad diffraction peaks indicate a low crystallinity of the sample. A decrease in the content of SnO₂ in the composition of the samples from 30 mol.% to 5 mol.% makes it possible to obtain a solid solution of the anatase structure (Fig. 9) from the FFS based on Butanol-1–TBT–SnCl₄·5H₂O.

A decrease in the FFS annealing temperature to 300 °C even with increase time of calcination up to 9 hours leads to the formation of X-ray amorphous sample. The elemental composition of such samples was studied based on the results of EDX analysis. The results of analysis of the sample with a content of 10 mol. % Sn(IV) are shown in Fig. 10. As can be seen in Fig. 10, the sample contains the element chlorine, which distributes with the tin over the sample surface. In addition, the sample contains oxygen and titanium.

An increase in the annealing temperature of FFS-60 to 400 °C (9 hours) leads to the formation of TiO₂:Sn solid solution from FFS-60(5 mol.% Sn(IV)) and a mixture of TiO₂:Sn solid solution with SnO₂ from FFS-60(30 mol.% Sn(IV)) (Fig. 11).

The formation of TiO₂:Sn solid solution and a mixture of TiO₂:Sn solid solution with SnO₂ from FFS based on Butanol-1–TBT–SnCl₄·5H₂O is possible at a temperature of at least 400 °C. Titanium dioxide and possibly tin(IV) hydroxychlorides are present in the samples obtained from FFS at 300 °C.

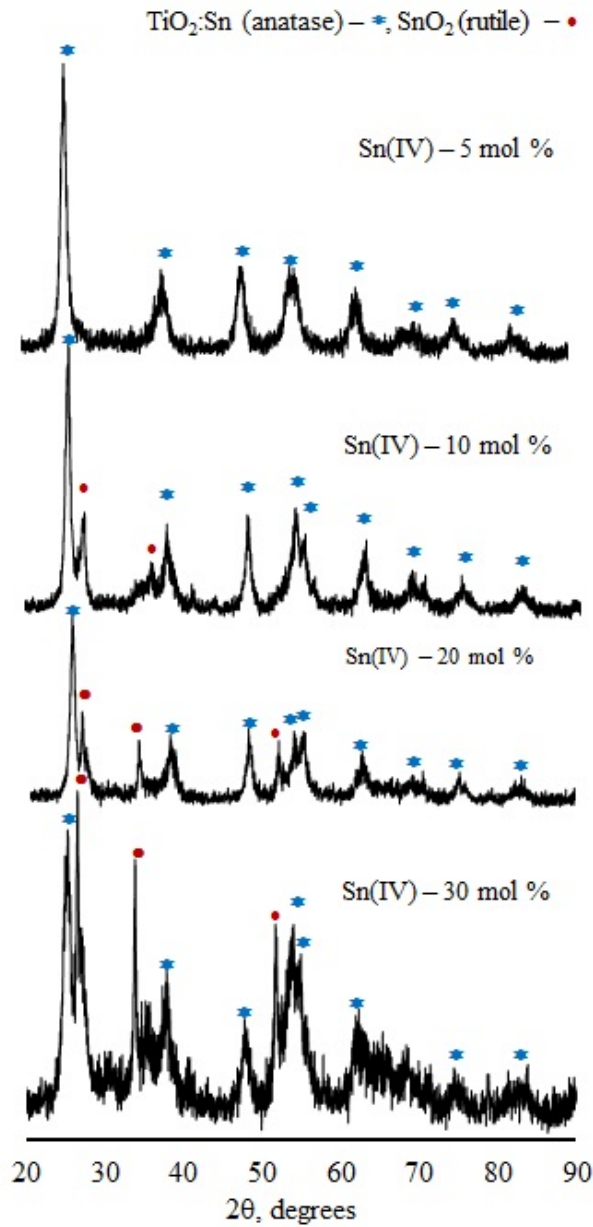


FIG. 9. The X-ray diffraction patterns of samples obtained from FFS-60(5–30 mol.% Sn(IV)) at 500 °C (1 hours)

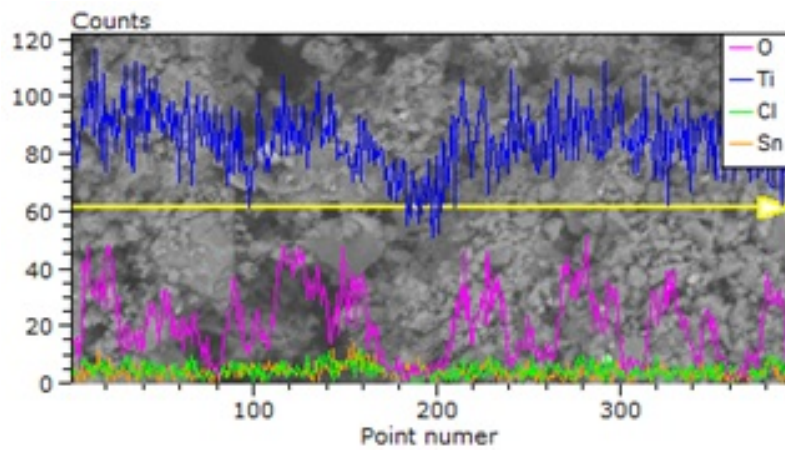


FIG. 10. The distribution of elements over the surface of the sample obtained from the FFS-60(10 mol.% Sn(IV)) at 300 °C (9 hours)

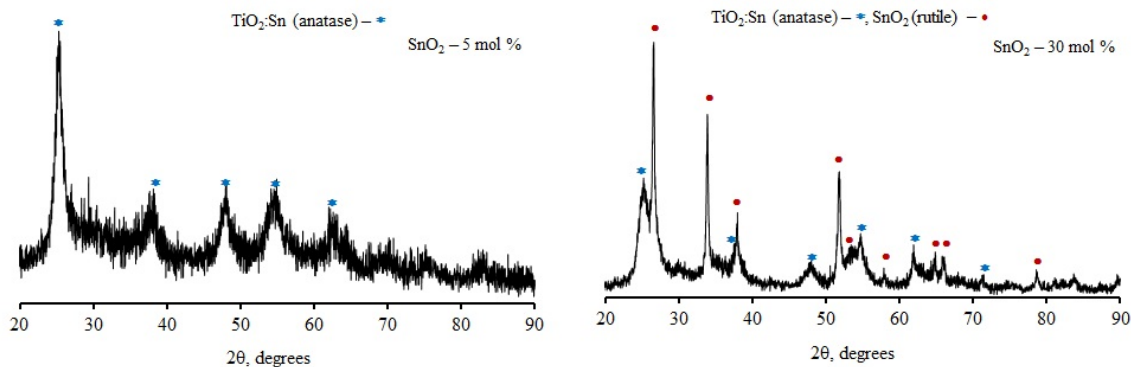


FIG. 11. The XRD patterns of samples obtained from the FFS-60 at 400 °C (9 hours)

3.2. Composition and properties of films obtained from FFS based on Butanol-1-TBT-SnCl₄·5H₂O

The films were prepared by the sol-gel method on glass substrates using FFSs at annealing temperatures of 60, 300, and 400 °C, respectively. The EDX analysis of films obtained on glass substrates at 400 °C (Fig. 12a) indicates the presence of the maximum emission of the Si, O, Ca, Mg, Na, Al elements of the substrate, as well as Ti, Sn, O elements of the films.

In addition to the emission maxima of the substrate elements, the EDX spectrum of the films annealed at a temperature of 300 °C for 9 hours contains the maxima emission of the Ti, Sn, O, and Cl elements. Consequently, both in the powder state and in the thin-film state, tin(IV) hydroxychlorides do not decompose completely at a temperature of 300 °C. The results of EDX analysis of the films annealed at 300 and 400 °C indicate that oxide phases are formed only at a temperature of 400 °C (Fig 10, 11). It has been shown by scanning electron spectroscopy that oxide films are uniform and continuous regardless of the tin content (Fig. 12b).

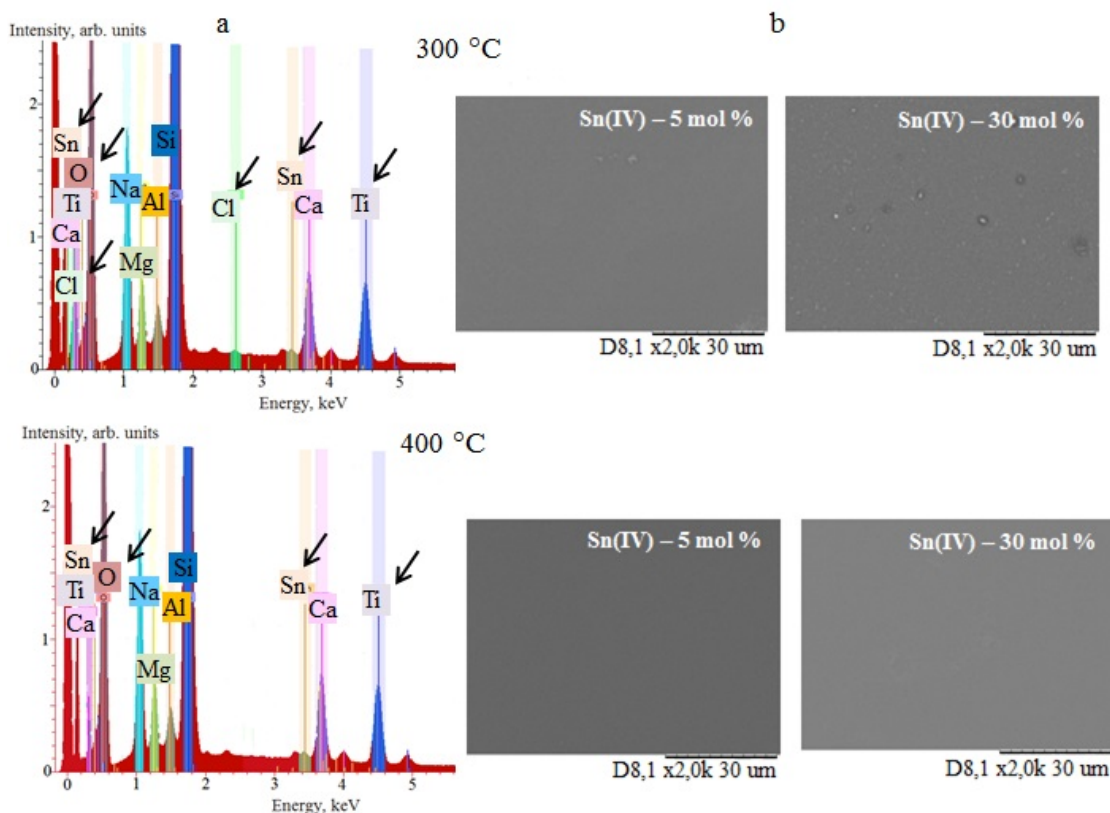


FIG. 12. EDX results (a) and SEM images (b) of the films obtained on glass substrates from FFSs at 300 and 400 °C (9 hours)

Taking into account the conditions and intermediate products of the preparation of TiO₂ with Sn(IV) films, one should expect the presence of amorphous titanic (TiO₂·nH₂O) and stannous (SnO₂·mH₂O) acids in their IR spectra. The

IR spectra of TiO_2 with 5 mol.% Sn(IV) films on glass substrates (Fig. 13) annealed at temperatures of 300 and 400 °C confirm the presence of water and hydroxyl groups in the samples. There are broad absorption bands with maxima at $3270\text{--}3360\text{ cm}^{-1}$, caused by the vibrations of --OH groups. The IR spectra of the films annealed at 600 °C do not contain vibrations of the --OH groups. If one take into account the results of XRD analysis of powders obtained at 400 °C (Fig. 11) where the crystalline phase of tin dioxide is recorded, and the diffraction maxima related to the anatase phase are wide enough, it can be assumed that the amorphous titanic acid is present in the films obtained at 300 and 400 °C.

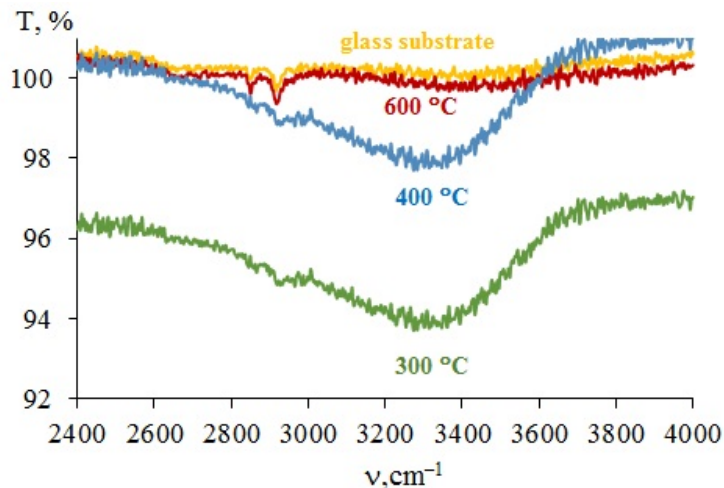


FIG. 13. IR spectrum of pure glass and TiO_2 with 5 mol.% Sn (IV) films on glass substrates annealed at different temperatures (9 hours)

Table 2 shows the compositions as well as the thickness (d), refractive index (n), surface resistance (R) and the value of the energy level of charge carriers (ΔE_a) of films obtained from FFSs at 400 and 300 °C.

TABLE 2. Compositions and properties of the films

Sn(IV), mol.%/ Properties	0	5	10	20	30
	after annealing at 300 °C				
composition of film	$\text{TiO}_2 \cdot n\text{H}_2\text{O}$	$\text{TiO}_2 \cdot n\text{H}_2\text{O}$ $\text{Sn}(\text{OH})_3\text{Cl}$	$\text{TiO}_2 \cdot n\text{H}_2\text{O}$ $\text{Sn}(\text{OH})_3\text{Cl}$	$\text{TiO}_2 \cdot n\text{H}_2\text{O}$ $\text{Sn}(\text{OH})_3\text{Cl}$	$\text{TiO}_2 \cdot n\text{H}_2\text{O}$ $\text{Sn}(\text{OH})_3\text{Cl}$
$d \pm 0.02$, nm	48.13	90.21	100.05	105.34	107.86
$n \pm 0.01$	1.89	1.84	1.78	1.73	1.69
R , Ω	$> 10^{10}$	10^9	10^9	10^9	10^9
	after annealing at 400 °C				
composition of film	TiO_2 anatase $\text{TiO}_2 \cdot n\text{H}_2\text{O}$	TiO_2 :Sn anatase $\text{TiO}_2 \cdot n\text{H}_2\text{O}$	TiO_2 :Sn anatase SnO_2 rutile $\text{TiO}_2 \cdot n\text{H}_2\text{O}$	TiO_2 :Sn anatase SnO_2 rutile $\text{TiO}_2 \cdot n\text{H}_2\text{O}$	TiO_2 :Sn anatase SnO_2 rutile $\text{TiO}_2 \cdot n\text{H}_2\text{O}$
$d \pm 0.02$, nm	48.01	88.14	99.18	102.87	104.15
$n \pm 0.01$	1.89	1.84	1.76	1.72	1.66
R , Ω	10^{10}	10^8	$10^8\text{--}10^9$	10^9	10^9
ΔE_a , eV	–	0.5	0.5	0.9	1.3

As can be seen in Table 2, the increase of the Sn(IV) content in the composition of the films leads to an increase in their thickness and a decrease in the refractive index. The thickness of the films obtained from FFS depends on the value

of the FFSs viscosity. The viscosity of FFSs increases with an increase of Sn(IV) content and, consequently, the thickness of the films increases with an increase of tin dioxide content in the composition. The decrease in the refractive index is due to the increase in the thickness of the coatings.

The change in the composition of the films with an increase in the temperature of their preparation from 300 to 400 °C practically does not affect the value of the refractive index, but affects the conductivity. All films are highly resistive and electronically conductive. However, the minimum resistance value is characteristic for films that are a solid solution with an anatase structure and with an admixture of the amorphous phase of titanate acid.

The transmittance spectra of TiO₂, SnO₂ and TiO₂ with Sn(IV) films annealed at 400 °C on glass substrate and spectrum of pure glass are shown in Fig. 14.

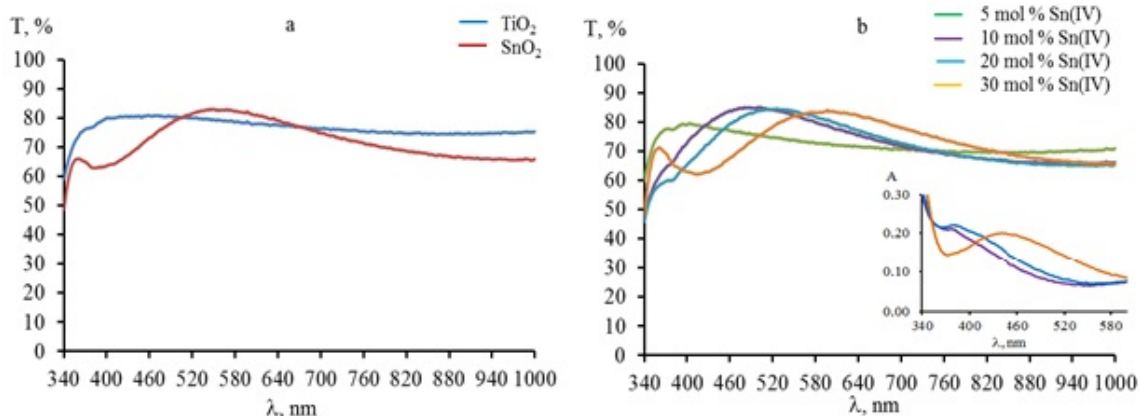


FIG. 14. The transmittance spectra of (a) TiO₂, SnO₂ films and (b) TiO₂ with Sn(IV) films prepared on the glass substrate at 400 °C

A wide absorption band with a maximum of about 380 nm is present in the spectra of tin dioxide film (Fig. 14a). The appearance of this absorption band is due to the charge transfer Sn(II) → Sn(IV) and the destruction of these centers as a result of the migration of bulk oxygen to the surface. It is assumed that Sn(II) is always present on the surface of SnO₂ [28]. The absorption at 580–600 nm is caused by the presence of oxygen vacancies (single- and double-charged) in SnO₂ [29]. The transmission spectrum of the titanium dioxide film (Fig. 14a) has no maxima or minima and is characterized by a transmission coefficient of 75–80% in the visible light range. The transmission spectrum of films based on a solid solution without tin dioxide (Fig. 14b, 5 mol.% Sn(IV)) impurities is the same as the transmission spectrum for films based on titanium dioxide, which once again confirms the formation of a solid solution in the film samples. The transmittance of these films in the visible light regime of the spectrum is 78–70%. A decrease in the transmittance of films based on a solid solution compared to titanium dioxide films is caused by their greater thickness. A general view of the transmission spectra of films containing 10–30 mol.% Sn(IV) (Fig. 14b) is similar to the transmission spectrum of the SnO₂ film (Fig. 14a). A decrease in the tin(IV) contents (30–10%) in the composition of oxide films leads to a hypsochromic shift of the absorption maximum corresponding to the transition of Sn(II) → Sn(IV) electrons.

4. Conclusion

In this study, the formation of transparent conductive films on glass substrates based on titanium dioxide with 5–30 mol.% Sn(IV) additives by sol-gel method from FFSs based on Butanol-1-TBT-SnCl₄·5H₂O and annealed at temperature 300–400 °C (9 hours) has been demonstrated. The content of Sn(IV) influences the composition of films. The solid solution based on titanium dioxide with anatase structure is formed at a content of 5 mol.% Sn(IV); the films with a content of 10–30 mol.% Sn(IV) are the mixture of the TiO₂:Sn solid solution and SnO₂ with rutile structure. Regardless of the tin content, all films contain an amorphous TiO₂·nH₂O phase. The formation of oxide phases occurs through the stages of thermal destruction of Sn(OH)₃Cl, tin acid, and burnout of butoxy groups of butoxytitanium(IV). In addition to titanate acid, the films obtained at 300 °C contain a tin salt of presumptive of the composition Sn(OH)₃Cl. The surface resistance of glass decreases by 10⁸ times after deposition of the film based on TiO₂ with 5 mol.% Sn(IV) and by 10⁷ times after deposition of the film based on TiO₂ with 10–30 mol.% Sn(IV). The transparency coefficient of films based on TiO₂ with 5 mol.% Sn(IV) in the entire visible light range of the spectrum is 80–70%, the maximum transmittance of 78–85% of the films based on TiO₂ with 10, 20 and 30 mol.% Sn(IV) are at wavelengths of 423–745 nm, 452–734 nm and 505–830 nm, respectively. The Sn(IV) additive up to 5 mol. % in the TiO₂: Sn solid solution is the key to successfully obtaining a transparent conductive coating that can be used as a photoelectrode in dye-sensitized solar cells.

References

- [1] Abudayyeh O.K., Chavez A., Han S.M., Rounsaville B., Upadhyaya V. and Rohatgi A. Silver-carbon-nanotube composite metallization for increased durability of silicon solar cells against cell cracks. *Sol. Energy Mater. Sol. Cells.*, 2021, **225**, 111017.
- [2] Ramprabhu R., Sanjay K., Saran Kumar V., Santhosh A.C., Saravanan M. and Ajayan J. An overview of recent developments in silicon solar cells. *ICACCS*, 2019, P. 1120–1122.
- [3] R.H.E. Hassanien, M. Li and F. Yin. The integration of semi-transparent photovoltaic on greenhouse roof for energy and plant production. *Renew. Energ.*, 2018, **121**, P. 377–388.
- [4] Das P., Sengupta D., Kasinadhuni U., Mondal B. and Mukherjee K. Nano-crystalline thin and nano-particulate thick TiO₂ layer: Cost effective sequential deposition and study on dye sensitized solar cell characteristics. *Mater. Res. Bull.*, 2015, **66**, P. 32–38.
- [5] Fitra M., Daut I., Irwanto M., Gomesh N. and Irwan Y.M. Effect of TiO₂ thickness Dye Solar Cell on charge generation, *Energy Procedia, Energy Procedia*, 2013, **36**, P. 278–286.
- [6] Winkless L. Could dye-sensitized solar cells work in the dark. *Mater. Today*, 2017, **20**, 289.
- [7] Blakers A., Zin N., McIntosh K.R. and Fong K. High efficiency silicon solar cells. *Energy Procedia*, 2013, **33**, 1–10.
- [8] Wang W.W., Zhu Y.J. and Yang L.X. ZnO-SnO₂ Hollow Spheres and Hierarchical Nanosheets: Hydrothermal Preparation, Formation Mechanism, and Photocatalytic Properties. *Adv. Funct. Mater.*, 2007, **17**, P. 59–64.
- [9] Li N., Du K., Liu G., Xie Y., Zhou G., Zhu J., Li F. and Cheng H.-M. Effects of oxygen vacancies on the electrochemical performance of tin oxide. *J. Mater. Chem. A*, 2013, **1**, P. 1536–1539.
- [10] Yang L., Yang Y., Liu T., Ma X., Lee S.W. and Wang Y. Oxygen vacancies confined in SnO₂ nanoparticles for glorious photocatalytic activities from the UV, visible to near-infrared region. *New J. Chem.*, 2018, **42**, P. 15253–1526.
- [11] Domashevskaya E.P., Ryabtsev S.V., Tutov E.A., Yurakov, Chuvenkova O.A.Y.A., Lukin A.N. Optical properties of SnO_{2-x} nanolayers. *Tech. Phys. Lett.*, 2006, **32**, P. 782–784.
- [12] Senevirathna M.K.I., Pitigala P.K.D.P., Premalal E.V.A., Tennakone K., Kumara G.R.A. and Konno A. Stability of the SnO₂/MgO dye-sensitized photoelectrochemical solar cell. *Sol. Energy Mater. Sol. Cells*, 2007, **91**, P. 544–547.
- [13] C. Kılıç and Zunger A. Origins of Coexistence of Conductivity and Transparency in SnO₂. *Phys. Rev. Lett.*, 2002, **88**(9), 95501.
- [14] Snaith H.J. and Ducati C. SnO₂-based dye-sensitized hybrid solar cells exhibiting near unity absorbed photon-to-electron conversion efficiency. *Nano Lett.*, 2010, **10**(4), P. 1259–1265.
- [15] Li Y., Zhu J., Huang Y., Liu F., Lu M., Chen S., Hu L., Tang J., Yao J., Dai S. Mesoporous SnO₂ nanoparticle films as electron-transporting material in perovskite solar cells. *RSC Adv.*, 2015, **5**, 28424–28429.
- [16] Ke W., Fang G., Liu Q., Xiong L., Qin P., Tao H., Wang J., Lei H., Li B., Wan J., Yang G., Yan Y. Low-temperature solution processed tin oxide as an alternative electron transporting layer for efficient perovskite solar cells. *J. Am. Chem. Soc.*, 2015, **137**, P. 6730–6733.
- [17] Xie H., Yin X., Liu J., Guo Y., Chen P., Que W., Wang G. and Gao B. Low temperature solution-derived TiO₂-SnO₂ bilayered electron transport layer for high performance perovskite solar cells. *Appl. Surf. Sci.*, 2019, **464**, P. 700–707.
- [18] Pitchaiy S., Eswaramoorthy N., Natarajan M., Santhanam A., Ramakrishnan V.M., Asokan V., Palanichamy P., Palanisamy B., Kalimuthua A. and Velauthapillaib D. Interfacing green synthesized flake like-ZnO with TiO₂ for bilayer electron extraction in perovskite solar cells. *New J. Chem.*, 2020, **44**, P. 8422–8433.
- [19] Gambhire A.B., Lande M.K., Kalokhe S.B., Shirsat M.D., Patil K.R., Gholap R.S. and Arbad B.R. Synthesis and characterization of high surface area CeO₂-doped SnO₂ nanomaterial. *Mater. Chem. Phys.*, 2008, **112**, P. 719–722.
- [20] Bose A.C., Kalpana D., Thangadurai P. and Ramasamy S. Synthesis and characterization of nanocrystalline SnO₂ and fabrication of lithium cell using nano-SnO₂. *J. Power Sources.*, 2002, **107**, P. 138–141.
- [21] Yang Y., Zhang Q., Zhang B., Mi W.B., Chen L., Li L., Zhao C., Diallo K.E.M. and Zhang X.X. The influence of metal interlayers on the structural and optical properties of nano-crystalline TiO₂ films. *Appl. Surf. Sci.*, 2012, **258**, P. 4532–4537.
- [22] Kaleji B.K. and Sarraf-Mamoory R. Nanocrystalline sol-gel TiO₂-SnO₂ coatings: preparation, characterization and photo-catalytic performance. *Mater. Res. Bull.*, 2012, **47**, P. 362–369.
- [23] Medjaldi F., Bouabellou A., Bouachiba Y., Taabouche A., Bouatia K. and Serrar H. Study of TiO₂, SnO₂ and nanocomposites TiO₂:SnO₂ thin films prepared by sol-gel method: Successful elaboration of variable-refractive index systems. *Mater. Res. Express.*, 2020, **7**, 016439.
- [24] Jalava J., Taavitsaine V., Haario H. and Lamberg L. Determination of particle and crystal size distribution from turbidity spectrum of TiO₂ pigments by means of t-matrix. *J. Quant. Spectrosc. Radiat. Transfer*, 1998, **60**, P. 399–409.
- [25] Zhrebtsov D.A., Kuznetsov G.F., Kleshchev D.G., Syutkin S.A., Pervushin V.Y., German V.A., Viktorov V.V., Kolmogortsev A.M. and Serikov A.S. Characteristics of the hydrous titanium dioxide-anatase phase transformation during hydrothermal treatment in aqueous solutions. *Russ. J. Inorg. Chem.*, 2010, **55**, P. 1197–1201.
- [26] Jackson P. and Parfitt G.D. Infra-red study of the surface properties of rutile adsorption of ethanol, n-butanol and n-hexanol. *J. Chem. Soc. Faraday Trans. I.*, 1972, 1443.
- [27] Erdei-Gruz T. *Transfer Phenomena in Water Solutions*. John Wiley & Sons, New York, 1974, 512 p.
- [28] Batzill M. and Diebold U. The surface and materials science of tin oxide. *Progress in Surface Science*, 2005, **79**, P. 47–154.
- [29] Popescu D.A., Herrmann J., Ensuque A. and Bozon-Verduraz F., Nanosized tin dioxide: Spectroscopic (UV-VIS, NIR, EPR) and electrical conductivity studies. *Phys. Chem. Chem. Phys.*, 2001, **3**, P. 2522–2530.

Submitted 1 February 2022; revised 18 April 2022; accepted 19 April 2022

Information about the authors:

S. Kuznetsova – National Research Tomsk State University, Lenin, 36, Tomsk, 634050, Russia; onm@mail.tsu.ru

O. Khalipova – National Research Tomsk State University, Lenin, 36, Tomsk, 634050, Russia;

Yu-Wen Chen – Department of Chemical Engineering, National Central University, Jhongli 32001, Taiwan;

V. Kozik – National Research Tomsk State University, Lenin, 36, Tomsk, 634050, Russia;

Conflict of interest: the authors declare that they have no known competing financial interests or personal relationships that have influenced the work reported in this paper.

Synthesis and analysis of cerium-containing carbon quantum dots for bioimaging *in vitro*

A. L. Popov^{1,a}, I. V. Savintseva^{1,b}, A. M. Ermakov^{1,c}, N. R. Popova^{1,d}, D. D. Kolmanovich^{1,e},
N. N. Chukavin^{1,2,f}, A. F. Stolyarov^{1,g}, A. B. Shcherbakov^{3,h}, O. S. Ivanova^{4,j}, V. K. Ivanov^{4,k}

¹Institute of Theoretical and Experimental Biophysics of the Russian Academy of Sciences, 142290, Russia

²Moscow Region State University, 141014, Moscow, Russia

³Zabolotny Institute of Microbiology and Virology, National Academy of Sciences of Ukraine, Kyiv D0368, Ukraine

⁴Kurnakov Institute of General and Inorganic Chemistry of the Russian Academy of Sciences, Moscow, 119991, Russia

^aantonpopovleonid@gmail.com, ^bsavintseva_irina@mail.ru, ^cao_ermakovy@rambler.ru,

^dnellipopovaran@gmail.com, ^ekdd100996@mail.ru, ^fchukavinnik@gmail.com,

^ga.f.stolyaroff@gmail.com, ^hceroform@gmail.com, ^jrunetta05@mail.ru, ^kvan@igic.ras.ru

Corresponding author: A. L. Popov, antonpopovleonid@gmail.com

PACS 68.65.-k, 81.20.-n, 82.70. Dd, 87.80.-y

ABSTRACT The latest biomedical approaches based on the use of nanomaterials possessing luminescent properties make it possible to effectively visualize cancer cells or tissues, thus expanding diagnostic capabilities of the current bioimaging techniques. In this paper, a new scheme is proposed for the synthesis of cerium-containing carbon quantum dots (Ce-Qdots) of ultra-small size, promising for biomaging. Ce-Qdots have a high degree of biocompatibility, as well as remarkable redox activity. Cytotoxicity analysis performed using 4 human cell cultures confirmed the high degree of Ce-Qdots biocompatibility. It was shown that Ce-Qdots in concentrations up to 200 $\mu\text{g/ml}$ do not have a negative effect on the metabolic, proliferative, migration and clonogenic activity of cell cultures after 24, 48 and 72 hours of co-incubation. Ce-Qdots can be considered as the basis of a new theranostic agent for bioimaging and targeted delivery of biologically active substances.

KEYWORDS carbon dots, quantum dots, ceria, bioimaging, cell uptake, viability, luminescence.

ACKNOWLEDGEMENTS The work was supported by the Russian Science Foundation (project 20-74-00086).

FOR CITATION Popov A.L., Savintseva I.V., Ermakov A.M., Popova N.R., Kolmanovich D.D., Chukavin N.N., Stolyarov A.F., Shcherbakov A.B., Ivanova O.S., Ivanov V.K. Synthesis and analysis of cerium-containing carbon quantum dots for bioimaging *in vitro*. *Nanosystems: Phys. Chem. Math.*, 2022, **13** (2), 204–211.

1. Introduction

Bioimaging is one of the most promising and actively developing tools for socially significant diseases diagnosis. The development of this technology is associated with a significant breakthrough in the design and functionalization of carbon quantum dots (Qdots), which characteristics can be tuned at the synthesis stage and additionally modified with chemical agents in order to impart the necessary biological activity [1–3]. Carbon quantum dots possess unique luminescent characteristics: multi-color emission, customizable optical properties, high quantum yield, excellent photostability and solubility in water, as well as good biocompatibility, which allows them to be used in various biomedical applications [4, 5]. It is also worth noting that carbon quantum dots can be synthesized through simple schemes and methods, such as hydrothermal or microwave, using inexpensive chemical reagents [6, 7].

Today, methods are being developed for obtaining carbon quantum dots for selective visualization of various types of cells (cancer, stem or neuronal) with the possibility of tracking them *in vivo*, providing selective accumulation in given cell types [8]. There are also techniques for obtaining functionalized quantum dots for precise visualization of individual cell organoids [9]. Quantum dots are widely used for early cancer diagnosis by functionalizing their surface with cancer cell-specific molecules or antibodies. For example, an effective accumulation was shown of PEG-labeled quantum dots modified with the peptide angioprep-2, which provided selective accumulation in human glioblastoma cells and effectively visualized the tumor [10]. Earlier, pH-sensitive carbon quantum dots were synthesized for HeLa cells visualization [11]. Thus, the design of carbon quantum dots capable of not only effectively visualising tumor cells, but also providing a therapeutic effect, is a frontier area of nanomedicine.

One of the most promising agents for nanomedicine, which has pronounced therapeutic activity and the ability to provide a synergistic effect with the other medicinal substances, is cerium oxide. We have previously shown that a nanocomposite based on cerium oxide and curcumin is capable of protecting normal cells under H₂O₂-induced oxidative stress, and inhibit metabolic activity of tumour cells in a time-increasing manner [12]. We also demonstrated the synergistic effect of cerium oxide nanoparticles with tumor necrosis factor, increasing cytotoxicity for A-549 and HEp-2 cancer cells [13]. The functionalization of cerium oxide nanoparticles with D-panthenol provides an increased antioxidant and UV-protective effect better than individually panthenol or CeO₂ nanoparticles [14].

Here, we proposed a new synthesis scheme of organic carbon quantum dots, modified with cerium for additional biological activity, and carried out a comprehensive analysis of their cytotoxicity using cancer and normal cells.

2. Materials and methods

2.1. Synthesis and characterization of Ce-Qdots

Ce-Qdots were synthesized by the hydrothermal method using a teflon autoclave. At the first stage, 0.8 g of Ce(NO₃)₆·6H₂O, 1 g of citric acid and 1 g of carbamide were dissolved in 20 ml of deionized water on a magnetic stirrer. After dissolution, 1.1 ml of polyethylenepolyamine (PEPA) was added and stirring was continued for 20 minutes at a temperature of 25°C. Next, the resulting suspension was transferred to an autoclave and heated at a temperature of 240°C for 4 hours. After cooling to room temperature, the resulting Q-dots colloid solution was separated from the precipitate by centrifugation at 3000 rpm and further purified by dialysis (1 kDa bag) for 48 hours against distilled water. The resulting solution was dried at 50°C.

2.2. Cell cultures

We used 4 types of cell cultures from Cell&Tissue biobank of the Institute of Theoretical and Experimental Biophysics of the Russian Academy of Sciences: MNNG/Hos human osteosarcoma, NCI-ADR human ovarian adenocarcinoma, MCF-7 human breast adenocarcinoma and human mesenchymal stem cells (MSCc) isolated from dental pulp. Cells were cultured in DMEM/F12 medium containing with 10% fetal calf serum and 200 units of penicillin/streptomycin at 37°C under 5% CO₂ atmosphere. Cells were removed from culture flasks using 0.25% trypsin-EDTA solution after washing them three times with Hanks' buffer.

2.3. MTT assay

Analysis of cell viability after 24 or 72 hours incubation with Ce-Qdots was performed using the MTT assay. Cells were seeded in 96 well plates at a density of 2.5·10⁴/cm² in a DMEM/F12 culture medium containing 10% fetal calf serum. After 8 hours, Ce-Qdots (1-200 µg/ml) were added by changing the culture medium. Then, after 24 and 72 hours, the medium was replaced with a medium with a solution of the MTT reagent (0.5 mg/mL) and further analysis was carried out according to the standard method [15].

2.4. Fluorescent microscopy

Intracellular visualization using Ce-Qdots was performed using an inverted fluorescence microscope Zeiss Axiovert 200. Cells were seeded in 35 mm Petri dishes with a central hole (Ibidi, Germany) at a density of 2.5·10⁴/cm² in a DMEM/F12 culture medium containing 10% fetal calf serum. Afterwards, Ce-Qdots were added to the cells at a concentration of 100 µg/mL. After 24 hours, microphotography of cell cultures was carried out after washing three times with a Hanks buffer. The luminescence of CeO₂-Qdots localized on the cell surface was inhibited by treating the cells with trypan blue.

2.5. Clonogenic assay

Clonogenic analysis was performed after 24 hours of incubation with Ce-Qdots. Cells were seeded in 6 well plates (SPL, Korea) at a density of 1.5·10³ cells per well. After 8-11 days (depending on the type of cell culture), the formed colonies were fixed using 4% paraformaldehyde and stained with 0.1% methylene blue solution. Cell aggregates containing more than 50 units were considered as a formed colony.

2.6. Migration assay

Analysis of cell migration after incubation with Ce-Qdots was performed within 48 hours after artificial scratch formation. 2-well silicone inserts (Ibidi, Germany) were used to form the scratch. The cells were seeded in the inserts at a density of 2.5·10⁴ cm⁻² after the formation of a monolayer. Further, various concentrations of Ce-Qdots (50, 100, and 200 µg/mL) were added to the cells for 3 hours, and then the insert was removed. The process of healing of the model wound was monitored by microphotography for 48 hours every 6 hours.

2.7. Statistical analysis

Data are presented as standard deviation from the mean value. The significance of differences between experimental groups was assessed by the Mann-Whitney U-test.

3. Results

The synthesis of Ce-Qdots was carried out according to the scheme shown in Fig. 1a. According to TEM data, the particle size of the Ce-Qdots was 2–3 nm (Fig. 1b). According to UV–visible spectroscopy the position of the absorption peak of the Ce-Qdots was at 390 nm. The peak of the emission of the Ce-Qdots was at 450 nm (Fig. 1c). The hydrodynamic radius of the Ce-Qdots upon dilution in water was about 40–50 nm (Fig. 1d). Zeta potential of the particles when diluted in distilled water was -32 ± 1.1 mV. The synthesized Ce-Qdots demonstrated good colloidal stability and can be stored for at least 90 days without any signs of precipitation.

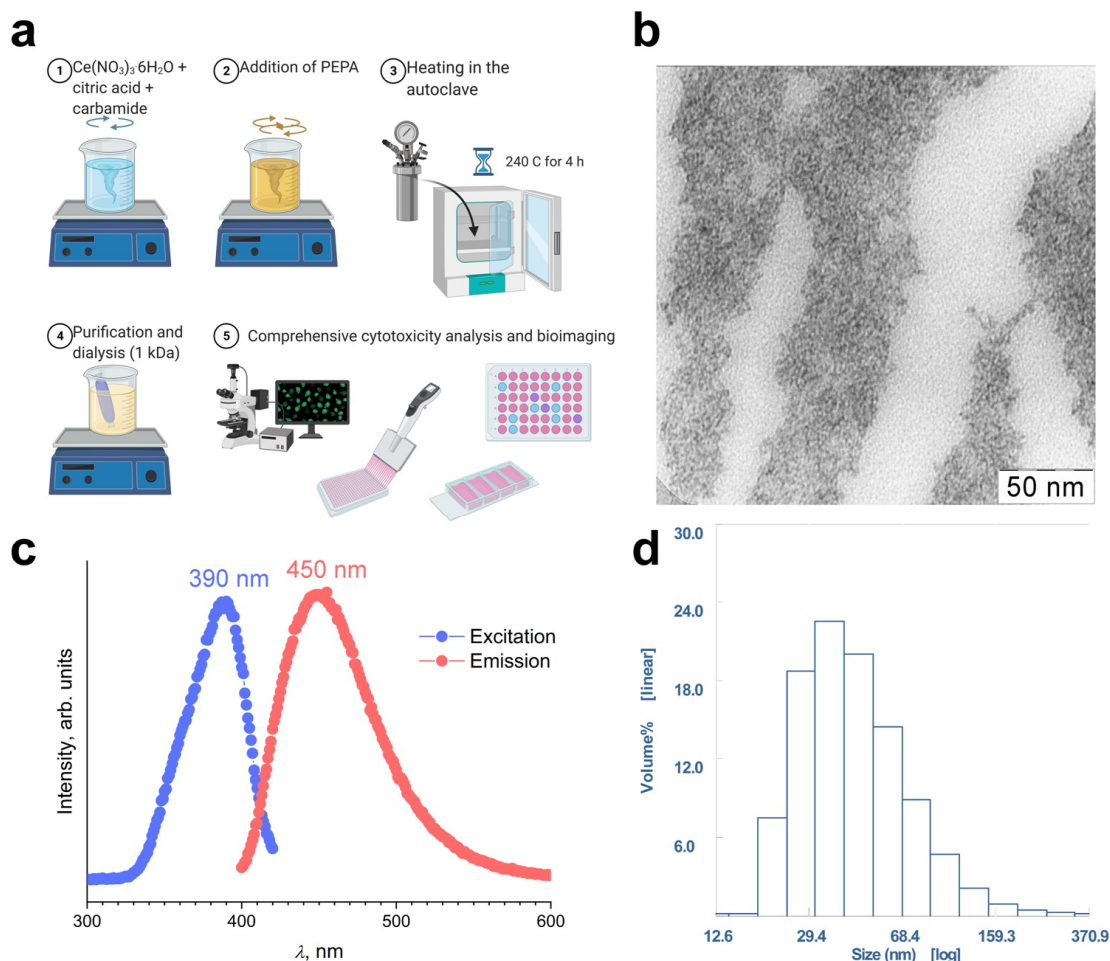


FIG. 1. Synthesis scheme of the Ce-Qdots (a), transmission electron microscopy (b), emission and excitation spectra(c), dynamic light scattering in MQ water (d)

The MTT assay was used to study the metabolic activity of cell cultures after 24, 48 and 72 hours incubation with Ce-Qdots (Fig. 2). It was shown that Ce-Qdots do not affect the metabolic activity of human MSCs at concentrations up to 200 $\mu\text{g}/\text{mL}$, which confirms a high level of biocompatibility (Fig. 2a). It is well known that human MSCs are a rather sensitive culture and can react to toxic agents by spontaneous differentiation or by stopping proliferation [16]. It was previously shown that carbon dots obtained by pyrolysis of a hydrazine solution have a high quantum yield and do not exhibit cytotoxicity against human neuronal MSCs in concentrations up to 100 mg/mL , and are also very effective for their visualization [17]. Citric acid-based carbon dots did not have a toxic effect on rat bone marrow mesenchymal stem cells in concentrations below 50 $\mu\text{g}/\text{mL}$, did not affect their subsequent ability to differentiate and were visualized easily [18]. Ce-Qdots did not cause a decrease in metabolic activity (1–200 $\mu\text{g}/\text{mL}$) after 24 and 48 hours incubation of human osteosarcoma MNNG/Hos cell cultures and radioresistant ovarian carcinoma cells NCI/ADR (Fig. 2c,d). Meanwhile, after 72 hours of incubation, there was a significant decrease in the viability level of MNNG/Hos cells at a Ce-Qdots concentration of 20 $\mu\text{g}/\text{mL}$, and also a decrease in the viability level of NCI/ADR cells at a Ce-Qdots concentration of 50 $\mu\text{g}/\text{mL}$. Human adenocarcinoma cell culture MCF-7 did not decrease its viability level after 72 hours of incubation with Ce-Qdots in the whole concentration range (1–200 $\mu\text{g}/\text{mL}$) (Fig. 2b).

The appearance of the cell cultures after 24 hours of incubation with Ce-Qdots in a wide range of concentrations (1–200 $\mu\text{g}/\text{mL}$) is shown in Fig. 3. Micrographs confirm that synthesized Ce-Qdots, even at the highest concentrations

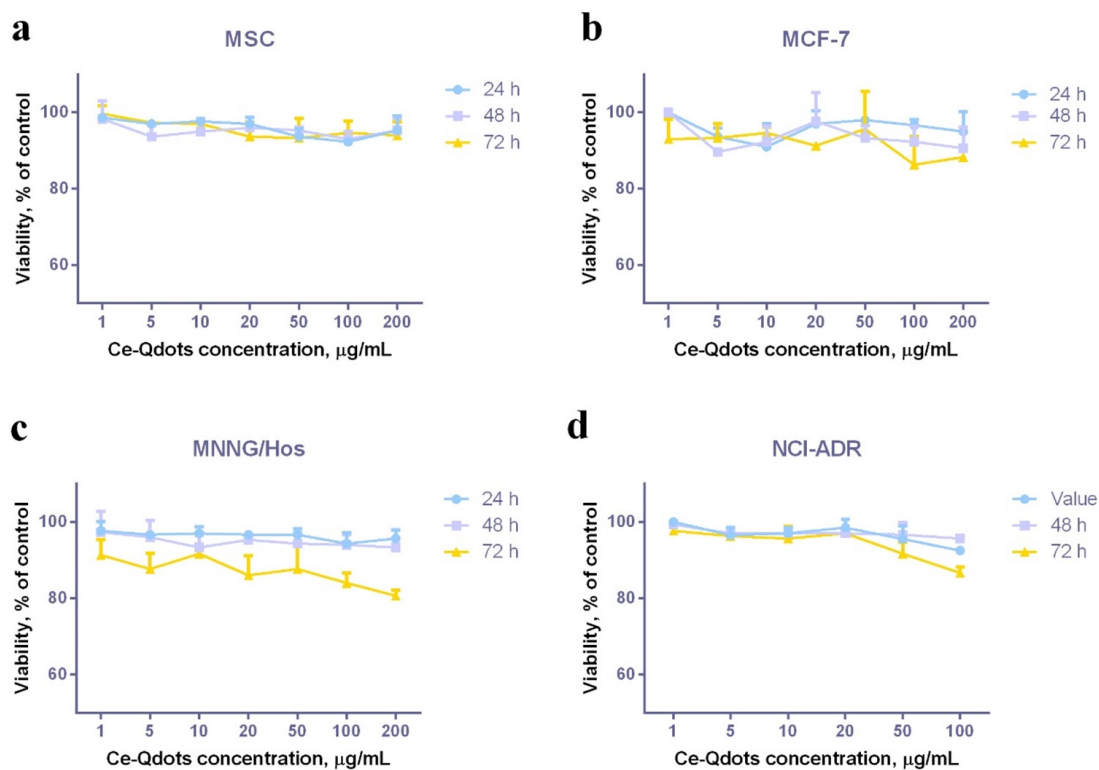


FIG. 2. Cytotoxicity analysis of Ce-Qdots (1–200 μg/mL) by the MTT assay using human MSC, MNNG/Hos, MCF-7 and NCI/ADR cell lines (24, 48 and 72 hours after incubation)

(100 and 200 μg/mL), do not have a negative effect on MSC, MNNG/Hos, MCF-7 and NCI/ADR cell lines cells. Morphological and phenotypic characteristics of cell cultures also do not change.

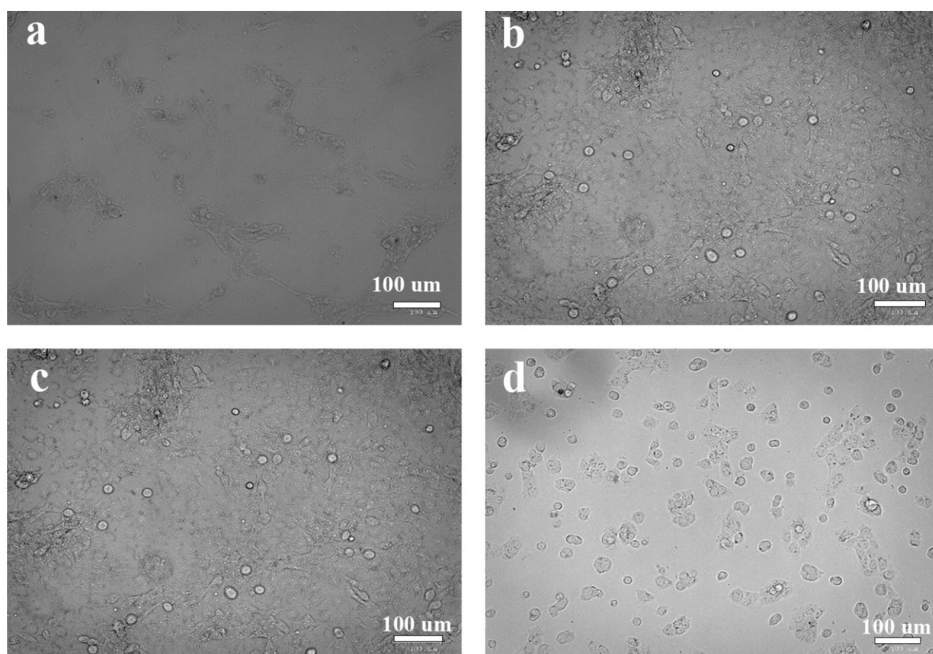


FIG. 3. The appearance of MSC (a), MNNG/Hos (b), MCF-7 (c), NCI/ADR (d) cell cultures after 16 hours incubation with Ce-Qdots (100 μg/mL)

Next, the clonogenic activity of cell cultures was evaluated after incubation with Ce-Qdots at a maximum concentration of 200 μg/mL. Cellular cooperation is one of the most important fundamental factors for their proliferation [19]. The action of paracrine factors stimulate the proliferative activity of neighboring cells, determining the rate of colony

formation [20]. We have shown the absence of the effect of Ce-Qdots on the clonogenic activity of 3 types of cell cultures - MCF-7, human MSCs NCI/ADR (Fig. 4). The MNNG/Hos human osteosarcoma cell culture showed a significant decrease in the number of formed colonies (up to 30% compared to the control), which confirms the MTT assay data. In a similar way, we have previously shown that cerium oxide nanoparticles can exhibit selective cytotoxic activity against certain types of cancer cells [21].

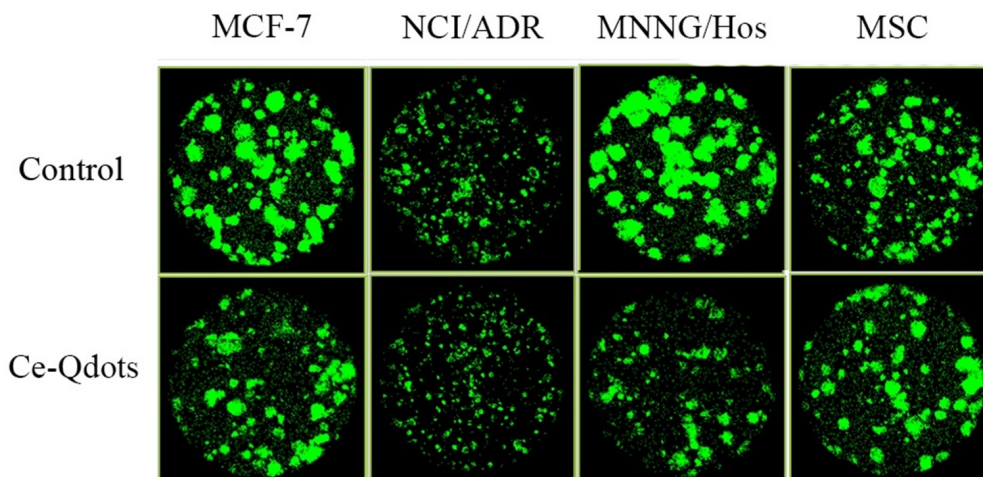


FIG. 4. Clonogenic analysis of Ce-Qdots (200 $\mu\text{g/mL}$) using human MSC, MNNG/Hos, MCF-7 and NCI/ADR cell lines (24 hours after incubation, cultivation for 264 hours)

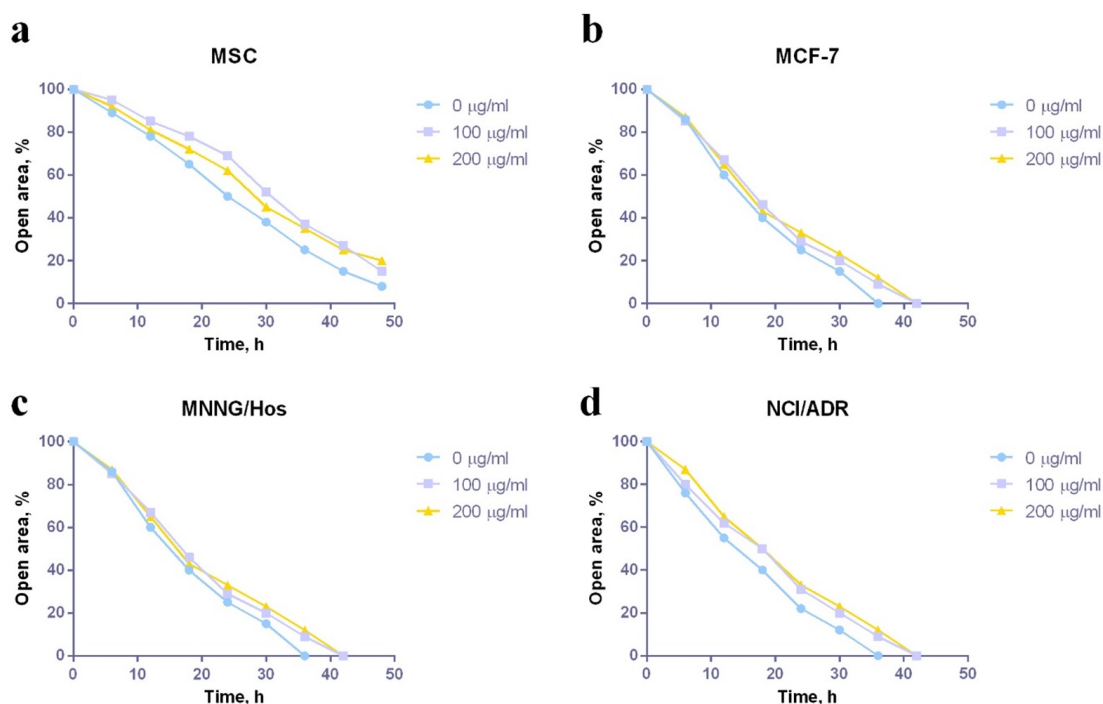


FIG. 5. Migration assay of Ce-Qdots (100 and 200 $\mu\text{g/mL}$) using human MSC, MNNG/Hos, MCF-7 and NCI/ADR cell lines (24 hours after incubation, cultivation for 48 hours). The analysis was carried out by assessing the open area of the model wound every 6 hours using a Clone Select Imager plate reader

Analysis of migration activity of cell cultures after incubation with carbon dots was performed by means of scratch test. The analysis of migration activity showed the absence of toxicity of Ce-Qdots for all studied concentrations (100 and 200 $\mu\text{g/mL}$) (Fig. 5). The migration activity of cells is one of the key indicators of the metabolic activity of cells [22]. Importantly, the migration activity of cells is associated not only with the metabolic activity of cells, but also with the efficiency of endocytosis of the nanoparticles [23]. For example, it was previously shown that ultra-small cerium oxide

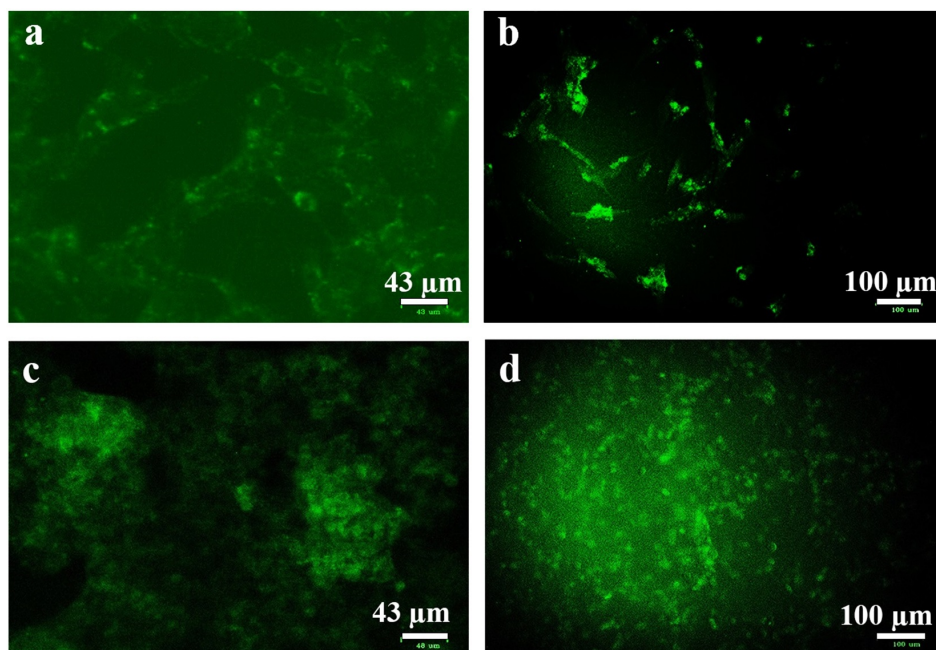


FIG. 6. Fluorescent inverted microscopy images of human MSC (a), MNNG/Hos (b), MCF-7 (c) and NCI/ADR cell lines labeled with 100 $\mu\text{g/ml}$ Ce-Qdots (100 $\mu\text{g/mL}$). Before the analysis, the cells were washed three times with a phosphate buffer

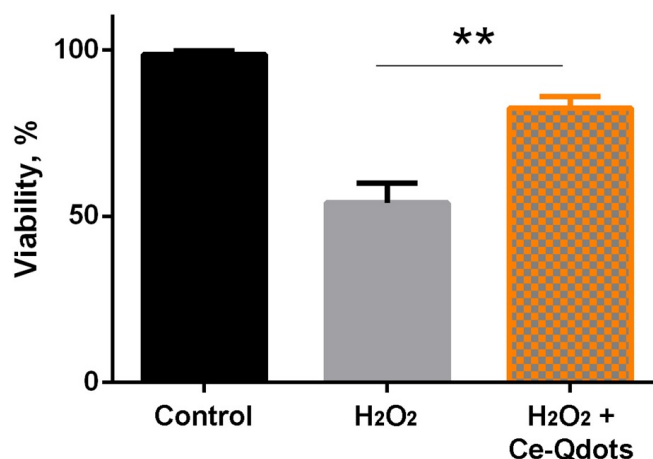


FIG. 7. Protective effect of Ce-Qdots (100 $\mu\text{g/ml}$) on MSCs under oxidative stress conditions induced by H₂O₂ treatment (as assessed using MTT assay). The cells were pretreated with Ce-Qdots (100 $\mu\text{g/ml}$) and then treated with hydrogen peroxide (500 μM for 30 min). Data are presented at mean \pm SD, * $p \leq 0.05\%$, ** $p \leq 0.001\%$

nanoparticles (3 nm) inhibit the migration and proliferation of gastric cancer by increasing DHX15 expression [24]. Chen et al. demonstrated that pristine carbon quantum dots/Cu₂O composite selectively inhibited ovarian cancer SKOV3 cells ($\text{IC}_{50} = 0.85 \mu\text{g/mL}$) by targeting cellular microenvironment, such as matrix metalloproteinases, angiogenic cytokines and cytoskeleton. In addition, CQDs/Cu₂O has a notable effect on transcriptional regulation of multiple genes in SKOV3 cells, where 495 genes were up-regulated and 756 genes were down-regulated [25].

The analysis of intracellular fluorescence of Ce-Qdots (100 $\mu\text{g/mL}$) showed their effective endocytosis into various cells (Fig. 4). The ultra-small size of nanoparticles allows for their effective penetration into the cytoplasm of cells [26]. The highest efficiency of uptake was typical of adenocarcinoma cells of the MCF-7 line and MNNG/Hos osteosarcoma cells (Fig. 4c,b). Mesenchymal stem cells also actively uptook Ce-Qdots, but less effectively than cancer cells (Fig. 4a). Such a difference in Ce-Qdots uptake efficiency may be associated not only with different metabolic activity of cells, but also with the efficiency of endocytosis, which is always higher in cancer cells than in primary cell culture like human MSC. Radioresistant NCI/ADR cells were also loaded with Ce-Qdots dots with high efficiency.

To confirm Ce-Qdots bioactivity, especially their antioxidant properties, we analyzed their protective activity in a H₂O₂-induced oxidative stress model. It was shown that a 30 minute exposure to hydrogen peroxide leads to a decrease in the viability of MSCs up to 57%. Pretreatment of the cell culture with carbon dots at a concentration of 100 µg/ml provided a pronounced protective effect, which was expressed in maintaining a high level of viability of the cell culture upon exposure to an oxidizer (Fig. 7). Hydrogen peroxide actively penetrates into the cell, causing lipid peroxidation, oxidation and crosslinking of proteins, DNA strand breaks, which generally leads to intracellular oxidative stress and ultimately to apoptosis [27]. It was previously shown that cerium dioxide nanoparticles effectively protect cells from hydrogen peroxide action [28]. It was also shown that various types of cells, including myoblasts, nerve cells, fibroblasts, can be effectively protected from the action of exogenous hydrogen peroxide by cerium-containing compounds including CeO₂ nanoparticles [29, 30]. It is worth noting that the catalase-like activity of cerium oxide nanoparticles is pH dependent, which is very promising for tumor therapy [31]. The same pH dependence could be anticipated for Ce-Qdots, too.

4. Conclusions

A two-stage scheme of synthesis of cerium-containing carbon dots is proposed. This scheme is very convenient, it involves the use of inexpensive reagents, that makes it possible to obtain the carbon capable of being effectively internalized by various types of cells. Obtained Ce-Qdots have high biocompatibility and antioxidant activity, providing good protection of living cells from oxidative stress.

References

- [1] Liu Q., Guo B.D., Rao Z.Y., Zhang B.H., Gong J.R. Strong two-photon-induced fluorescence from photostable, biocompatible nitrogen-doped graphene quantum dots for cellular and deep-tissue imaging. *Nano Lett.*, 2013, **13**, P. 2436–2441.
- [2] Ruan S.B., Qian J., Shen S., Zhu J.H., Jiang X.G., He Q., Gao H.L. A simple one-step method to prepare fluorescent carbon dots and their potential application in non-invasive glioma imaging. *Nanoscale*, 2014, **6**, P. 10040–10047.
- [3] Zholobak N.M., Popov A.L., Shcherbakov A.B., Popova N.R., Guzyk M.M., Antonovich V.P., Yegorova A.V., Scrypynets, Y.V. Leonenko I.I., Baranchikov A.Ye., Ivanov V.K. Facile fabrication of luminescent organic dots by thermolysis of citric acid in urea melt, and their use for cell staining and polyelectrolyte microcapsule labelling. *Beilstein Journal of Nanotechnology*, 2016, **7**, P. 1905–1917.
- [4] Zhang J., Yu S.H. Carbon dots: large-scale synthesis, sensing and bioimaging. *Mater. Today*, 2016, **19**, P. 382–393.
- [5] Xu Q., Li B., Ye Y., Cai W., Li W., Yang C., Chen Y., Xu M., Li N., Zheng X., Street J., Luo Y., Cai L. Synthesis, mechanical investigation, and application of nitrogen and phosphorus co-doped carbon dots with a high photoluminescent quantum yield. *Nano Res.*, 2018, **11**, P. 3691–3701.
- [6] Hamd-Ghadareh S., Salimi A., Fathi F., Bahrami S. An amplified comparative fluorescence resonance energy transfer immunosensing of CA125 tumor marker and ovarian cancer cells using green and economic carbon dots for bio-applications in labeling, imaging and sensing. *Biosensors and Bioelectronics*, 2017, **96**, P. 308–316.
- [7] Roy P., Chen P.C., Periasamy A.P., Chen Y.N., Chang H.T. Photoluminescent carbon nanodots: synthesis, physicochemical properties and analytical applications. *Mater. Today*, 2015, **18**(8), P. 447–458.
- [8] Zheng X.T., Ananthanarayanan A., Luo K.Q., Chen P. Glowing graphene quantum dots and carbon dots: properties, syntheses, and biological applications. *Small*, 2015, **11**(14), P. 1620–1636.
- [9] Shang W., Zhang X., Zhang M., Fan Z., Sun Y., Han M., Fan L. The uptake mechanism and biocompatibility of graphene quantum dots with human neural stem cell. *Nanoscale*, 2014, **6**, P. 5799–5806.
- [10] Mo L., Li J., Liu Q., Qiu L., Tan W. Nucleic acid-functionalized transition metal nanosheets for biosensing applications. *Biosensors and Bioelectronics*, 2017, **89**(1), P. 201–211.
- [11] Ruan S.B., Qian J., Shen S., Chen J.T., Zhu J.H., Jiang X.G., He Q., Yang W.L., Gao H.L. Fluorescent carbonaceous nanodots for noninvasive glioma imaging after angioprep-2 decoration. *Bioconjugate Chem.*, 2014, **25**, P. 2252–2259.
- [12] Wang N., Zheng A.Q., Liu X., Chen J.J., Yang T., Chen M., Wang J.H. Deep eutectic solvent-assisted preparation of nitrogen/chloride-doped carbon dots for intracellular biological sensing and live cell imaging. *ACS Appl. Mater. Interfaces*, 2018, **10**, P. 7901–7909.
- [13] Zholobak N.M., Shcherbakov A.B., Ivanova O.S., Reukov V., Baranchikov A.E., Ivanov V.K. Nanoceria-curcumin conjugate: synthesis and selective cytotoxicity against cancer cells under oxidative stress conditions. *J. Photochem. Photobiol. B.*, 2020, **209**, P. 111921.
- [14] Shydlovska O., Kharchenko E., Zholobak N., Shcherbakov A., Marynin A., Ivanova O., Baranchikov A., Ivanov V. Cerium oxide nanoparticles increase cytotoxicity of TNF-alpha *in vitro*. *Nanosyst. Phys. Chem. Math.*, 2018, **9**(4), P. 537–543.
- [15] Zholobak N.M., Shcherbakov A.B., Bogorad-Kobelska A.S., Ivanova O.S., Baranchikov A.Y., Spivak N.Y., Ivanov V.K. Panthenol-stabilized cerium dioxide nanoparticles for cosmeceutic formulations against ROS-induced and UV-induced damage. *J. Photochem. Photobiol. B.*, 2014, **130**, P. 102–108.
- [16] Popova N.R., Shekunova T.O., Popov A.L., Selezneva I.I., Ivanov V.K. Cerium oxide nanoparticles provide radioprotective effects upon X-ray irradiation by modulation of gene expression. *Nanosyst. Phys. Chem. Math.*, 2019, **10**(5), P. 564–572.
- [17] Fritsche E., Haarmann-Stemmann T., Kapr J., Galanjuk S., Hartmann J., Mertens P. R., Kämpfer A.A.M., Schins R.P.F., Tigges J., Koch K. Stem cells for next level toxicity testing in the 21st century. *Small*, 2021, **17**(15), P. 2006252.
- [18] Zhang M., Bai L., Shang W., Xie W., Ma H., Fu Y., Fang D., Sun H., Fan L., Han M., Liu C., Yang S. Facile synthesis of water-soluble, highly fluorescent graphene quantum dots as a robust biological label for stem cells. *J. Mater. Chem.*, 2012, **22**, P. 7461–7467.
- [19] Shao D., Lu M., Xu D., Zheng X., Pan Y., Song Y., Xu J., Li M., Zhang M., Li J., Chi G., Chen L., Yang B. Carbon dots for tracking and promoting the osteogenic differentiation of mesenchymal stem cells. *Biomater. Sci.*, 2017, **5**, P. 1820–1827.
- [20] Brix N., Samaga D., Hannel R., Gehr K., Zitzelsberger H., Lauber K. The clonogenic assay: robustness of plating efficiency-based analysis is strongly compromised by cellular cooperation. *Radiat. Oncol.*, 2020, **15**, P. 248.
- [21] Brix N., Samaga D., Belka C., Zitzelsberger H., Lauber K. Analysis of clonogenic growth *in vitro*. *Nature protocols*, 2021, **16**, P. 4963–4991.
- [22] Popov A., Abakumov M., Savintseva I., Ermakov A., Popova N., Ivanova O., Kolmanovich D., Baranchikov A., Ivanov V. Biocompatible dextran-coated gadolinium-doped cerium oxide nanoparticles as MRI contrast agents with high T1 relaxivity and selective cytotoxicity to cancer cells. *J. Mater. Chem. B.*, 2021, **9**, P. 6586–6599.
- [23] de Araújo Vieira L.F., Lins M.P., Nicácio Viana I.M.M., dos Santos J.E., Smaniotto S., dos Santos Reis M.D. Metallic nanoparticles reduce the migration of human fibroblasts *in vitro*. *Nanoscale res. lett.*, 2017, **12**(1), P. 200.

- [24] Ribeiro F.M., de Oliveira M.M., Singh S., Sakhivel T.S., Neal C.J., Seal S., Ueda-Nakamura T., Lautenschlager S.O.S., Nakamura C.V. Ceria nanoparticles decrease UVA-induced fibroblast death through cell redox regulation leading to cell survival, migration and proliferation. *Front. Bioeng. Biotechnol.*, 2020, P. 1133.
- [25] Xiao Y., Li J., Wang S., Yong X., Tang B., Jie M., Dong H., Yang X., Yang S. Cerium oxide nanoparticles inhibit the migration and proliferation of gastric cancer by increasing DHX15 expression. *Int J Nanomedicine*, 2016, **11**, P. 3023–3034.
- [26] Chen D., Li B., Lei T., Na D., Nie M., Yang Y., Xie C., He Z., Wang J. Selective mediation of ovarian cancer SKOV3 cells death by pristine carbon quantum dots/Cu₂O composite through targeting matrix metalloproteinases, angiogenic cytokines and cytoskeleton. *J Nanobiotechnol*, 2021, **19**, P. 68.
- [27] Manzanares D., Ceña V. Endocytosis: The nanoparticle and submicron nanocompounds gateway into the cell. *Pharmaceutics*, 2020, **12**, P. 371.
- [28] Clément M. V., Ponton A., Pervaiz S. Apoptosis induced by hydrogen peroxide is mediated by decreased superoxide anion concentration and reduction of intracellular milieu. *FEBS letters*, 1998, **440**(1-2), P. 13–18.
- [29] Clark A., Zhu A., Sun K., Petty H.R. Cerium oxide and platinum nanoparticles protect cells from oxidant-mediated apoptosis. *J Nanopart Res.*, 2011, **13**(10), P. 5547–5555.
- [30] Pagliari F., Mandoli C., Forte G., Magnani E., Pagliari S., Nardone G., Licoccia S., Minieri M., Di Nardo P., Traversa E. Cerium oxide nanoparticles protect cardiac progenitor cells from oxidative stress. *ACS Nano*, 2012, **6**(5), P. 3767–3775.
- [31] Weng Q., Sun H., Fang C., Xia F., Liao H., Lee H., Wang J., Xie A., Ren J., Guo X., Li F., Yang B., Ling D. Catalytic activity tunable ceria nanoparticles prevent chemotherapy-induced acute kidney injury without interference with chemotherapeutics. *Nat. Commun.*, 2021, **12**, P. 1436.

Submitted 8 February 2022; accepted 26 March 2022

Information about the authors:

A. L. Popov – Institute of Theoretical and Experimental Biophysics of the Russian Academy of Sciences, Institutskaya str., 3, Pushchino, 142290, Russia; antonpopovleonid@gmail.com

I. V. Savintseva – Institute of Theoretical and Experimental Biophysics of the Russian Academy of Sciences, Institutskaya str., 3, Pushchino, 142290, Russia; savintseva_irina@mail.ru

A. M. Ermakov – Institute of Theoretical and Experimental Biophysics of the Russian Academy of Sciences, Institutskaya str., 3, Pushchino, 142290, Russia; ao_ermakovy@rambler.ru

N. R. Popova – Institute of Theoretical and Experimental Biophysics of the Russian Academy of Sciences, Institutskaya str., 3, Pushchino, 142290, Russia; nellipopovaran@gmail.com

D. D. Kolmanovich – Institute of Theoretical and Experimental Biophysics of the Russian Academy of Sciences, Institutskaya str., 3, Pushchino, 142290, Russia; kdd100996@mail.ru

N. N. Chukavin – Institute of Theoretical and Experimental Biophysics of the Russian Academy of Sciences, Institutskaya str., 3, Pushchino, 142290, Russia; Moscow Region State University, 141014, Moscow, Russia; chukavinnik@gmail.com

A. F. Stolyarov – Institute of Theoretical and Experimental Biophysics of the Russian Academy of Sciences, Institutskaya str., 3, Pushchino, 142290, Russia; a.f.stolyaroff@gmail.com

A. B. Shcherbakov – Zabolotny Institute of Microbiology and Virology, National Academy of Sciences of Ukraine, Kyiv D0368, Ukraine; ceroform@gmail.com

O. S. Ivanova – Kurnakov Institute of General and Inorganic Chemistry of the Russian Academy of Sciences, Leninskiy prosp., 31, Moscow, 119991, Russia; runetta05@mail.ru

V. K. Ivanov – Kurnakov Institute of General and Inorganic Chemistry of the Russian Academy of Sciences, Leninskiy prosp., 31, Moscow, 119991, Russia; van@igic.ras.ru

Conflict of interest: the authors declare no conflict of interest.

Mechanism of formation of nanocrystalline particles with core-shell structure based on titanium oxynitrides with nickel in the process of plasma-chemical synthesis of TiNi in a low-temperature nitrogen plasma

Yuliya A. Avdeeva^a, Irina V. Luzhkova^b, Alexey N. Ermakov^c

Institute of Solid State Chemistry, Ural Branch, Russian Academy of Sciences, Ekaterinburg, 620990, Russia

^ay-avdeeva@list.ru, ^bkey703@yandex.ru, ^cermakovihim@yandex.ru

Corresponding author: Yu. A. Avdeeva, y-avdeeva@list.ru

PACS 61.46.+w, 61.46.-w, 61.66.Fn

ABSTRACT This paper presents the results of experiments, structural and morphological certification and modeling of ultrafine and nanocrystalline TiN-Ni “core-shell” structures obtained during plasma-chemical synthesis of industrially manufactured microcrystalline TiNi. Experiments on plasma-chemical synthesis were carried out by recondensation of ultrafine and nanocrystalline powders in a rotating cylinder of gaseous nitrogen. X-ray phase analysis and high-resolution transmission electron microscopy (HR TEM) showed the presence of refractory titanium compounds with nitrogen and metallic nickel, which are part of the core-shell structures, including the metastable, highly deformed complex nitride $Ti_{0.7}Ni_{0.3}N$ of hexagonal modification. HR TEM studies showed the localization of phases determined by X-ray diffraction and confirmed the “core-shell” structure on the example of nanocrystalline TiN-Ni fraction. Based on the experimental results, we have developed a model of crystallization of TiN-Ni “core-shell” structures under the conditions of a rotating cylinder of gaseous nitrogen, where the crystallization rate is 10^5 °C/s.

KEYWORDS titanium nickelide, nickel, plasma-chemical synthesis, low-temperature plasma, X-ray phase analysis, high-resolution transmission electron microscopy.

ACKNOWLEDGEMENTS The work was carried out in accordance with the state assignment for the Institute of Solid State Chemistry of the Ural Branch of the Russian Academy of Sciences (theme No 0397-2019-0003 “New functional materials for promising technologies: synthesis, properties, spectroscopy and computer simulation”).

FOR CITATION Avdeeva Yu.A., Luzhkova I.V., Ermakov A.N. Mechanism of formation of nanocrystalline particles with core-shell structure based on titanium oxynitrides with nickel in the process of plasma-chemical synthesis of TiNi in a low-temperature nitrogen plasma. *Nanosystems: Phys. Chem. Math.*, 2022, **13** (2), 212–219.

1. Introduction

Refractory compounds of titanium in the form of carbides and nitrides find wide application in different fields of technology. They are extensively used as tool and construction materials, as well as coatings for various purposes [1–5]. Another area of application of refractory compounds, including ultrafine and nanocrystalline compounds of all elements of subgroup IV-VIA of the Periodic system, is their use as modifying additives in foundry production, improving the final physical and mechanical properties of products [6, 7]. Various methods for the formation of ultrafine and nanocrystalline compounds of both titanium nitride and titanium carbide are amply covered in the literature [8–10]. It should be noted that all methods differ not only in the instrumentation involved in the preparation of dispersed refractory materials and compounds, but also in the productivity, which immediately affects the applicability of various synthesis methods, including their applicability under production conditions. Besides, an important aspect of the formation of refractory compounds can be the possibility of coating of particles, including ultra- or nanodispersed ones, with individual metals or their intermetallic compounds. The implementation of such ideas is considered in a number of publications [11–15], and the works of B. Chalmers (see, for example, [16]) provide a theoretical basis for heterogeneous nucleation, which makes it possible to form “core-shell” structures, where refractory compounds will act as a core, and the metal phases – as a shell of nanocrystalline particles.

The most convenient method for the formation of nanocrystalline particles based on refractory compounds with a “core-shell” structure, in which metal components participate, is extreme effect on microcrystalline materials, characterized by high rates of evaporation and crystallization. One of such methods is plasma-chemical synthesis in low-temperature nitrogen plasma with subsequent crystallization in a rotating cylinder of gaseous nitrogen. Methods of plasma-chemical synthesis suitable for the formation of a large number of ultra- and nanodispersed materials are quite

widely described in the literature [17, 18]. In particular, the final composition of synthesis products depends on the chemical composition of feedstock, processing conditions, gaseous media used for plasma formation processes, cooling, and transportation, as well as on the consideration of the issues of pyrophoricity reduction.

In this paper, to obtain ultrafine and nanocrystalline TiN-Ni powder materials, we proposed to use plasma-chemical synthesis in a low-temperature nitrogen plasma, which, in accordance with [19], makes it possible to obtain “core-shell” structures from microcrystalline powders of commercially produced titanium nickelide under “quasi-equilibrium” conditions. The main goal of the presented work is to form the scientific basis for obtaining ultrafine and nanocrystalline compositions in the form of TiN-Ni core-shell structures under the conditions of plasma-chemical synthesis in a low-temperature (4000–6000°C) nitrogen plasma.

2. Methods

In this work, to obtain ultra- and nanodispersed TiN-Ni “core-shell” structures, the method of plasma-chemical synthesis was used, followed by recondensation of titanium nickelide TiNi evaporated to the atomic state in a rotating cylinder of gaseous nitrogen. The crystallization rate under these conditions was 10^5 °C/s. Microcrystalline (~ 40 μm) titanium nickelide PN55T45 produced by OAO Polema (Tula) was used as the initial precursor raw material. After recondensation, the mixture of ultrafine and nanocrystalline synthesis products was transported to classifier 1, a vortex-type cyclone, and classifier 2, a bag-type fabric filter, where separation into ultrafine and nanocrystalline fractions of powder media was carried out. Each of the obtained fractions was encapsulated in a mixture of gasoline vapors and organic components to reduce the pyrophoricity of fine powders, which allows the resulting compositions to be stored under normal conditions. The technique of plasma-chemical synthesis according to the plasma recondensation scheme is best documented in [20].

The recondensed products of plasma-chemical synthesis were studied by X-ray phase analysis (SHIMADZU XRD – 7000 CuK α -cathode X-ray diffractometer) and high-resolution transmission electron microscopy (JEOL JEM 2100 transmission electron microscope). The results of instrumental studies were processed using modern software, so the X-ray data were processed in WinXPOW software packages (compatible with the ICDD database), and PowderCell 2.3 (refining of unit cell parameters). Electron microscopic images were processed in the DigitalMicrograph 7.0 software in order to analyze profilograms and fast Fourier transform, which confirms the radiography data.

The ultrafine fraction was studied by scanning tunneling microscopy on an SMM 2000 T tunneling microscope (Zelenograd, Moscow region).

3. Results and discussion

Refractory compounds of titanium with carbon and nitrogen crystallize, as a rule, in the form of cubic face-centered lattices of the NaCl type. In addition to individual carbides and nitrides, in the presence of both carbon and nitrogen simultaneously, refractory titanium compounds can be formed during synthesis, including those with the participation of oxygen, whose lattices are isomorphic to the NaCl structure.

The results of X-ray studies of the ultrafine fraction from the cyclone and the nanocrystalline fraction from the filter are shown in Fig. 1 and Table 1. So, the ultrafine fraction of the recondensed TiNi from the cyclone (Table 1, experiment 1) is represented by a mixture of refractory interstitial phases in the form of TiC $_x$ N $_y$ ($x + y \leq 1$) and cubic titanium nitride TiN (sp. gr. Fm-3m). Nickel, in its turn, is redistributed between the individual cubic modification (sp. gr. Fm-3m) [21] and the complex nitride Ti $_{0.7}$ Ni $_{0.3}$ N of the hexagonal modification (sp. gr. P-6m2) [22], being, in accordance with [23], in a highly deformed state along the (101) direction, which is expressed by the presence of a single reflection on the X-ray diffraction pattern. Additionally (Fig. 1, Table 1, experiment 1), there are reflections of cubic solid solutions of isomorphic TiN and intermetallic compounds of the Ti–Ni system: nickelide TiNi (sp. gr. Pm-3m) [24] and hexagonal TiNi $_3$ (sp. gr. P6 $_3$ /mmc) [25].

The nanocrystalline fraction of recondensed titanium nickelide extracted from the bag-type filter is represented by nonstoichiometric cubic titanium nitride TiN $_y$ (sp. gr. Fm-3m), cubic Ni (sp. gr. Fm-3m) [21] and complex nitride Ti $_{0.7}$ Ni $_{0.3}$ N of hexagonal modification (sp. gr. P-6m2) [22], which is also in a highly deformed state. The presence of a small amount of cubic carbonitride TiC $_x$ N $_y$ ($x + y \leq 1$) in the fraction from the vortex-type cyclone may be due to the fact that preliminary cleaning of the plasma-chemical installation before the experiment was carried out with powdered titanium carbide TiC.

Based on the data of X-ray phase analysis it should be noted that although the temperature of plasma-chemical synthesis (4000–6000°C) exceeds considerably the melting and boiling temperatures of Ti-Ni intermetallic phases, the TiNi and TiNi $_3$ intermetallics are present in the recondensed fraction from the vortex-type cyclone (Table 1, experiment 1). This can be justified by both the high flow rate of vortex plasma in the plasma-chemical reactor (~ 55 m/s) and the non-equilibrium of the plasma itself. As regards the disperse composition, it should be noted that the fraction from the cyclone is much larger and it contains inclusions of spherical shape. This is due to crystallization according to the “vapor-liquid-solid” scheme providing rounded surfaces of nanocrystalline particles.

Following the description of the X-ray data, special attention should be given to a considerable content of cubic nickel metal determined from the data of semi-quantitative analysis. In particular, it should be pointed out that nickel is a

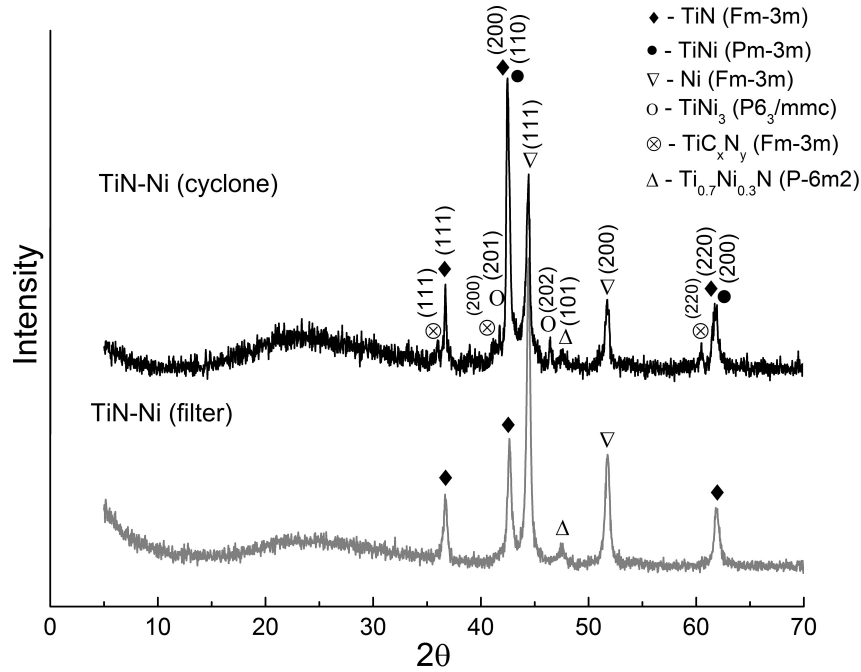


FIG. 1. X-ray patterns of TiN-Ni fractions after plasma-chemical synthesis

TABLE 1. Phase composition and lattice parameters of TiN-Ni fractions after plasma-chemical synthesis

Fraction	Phase composition (± 2 wt%), a, b, c (± 0.0001 Å)	$S_{sp}, m^2/g$	$\rho, g/cm^3$	d, μm
Cyclone	TiC _x N _y (Fm-3m), (24%), a = 4.3138	14.3	6.4	0.065
	TiN _y (Fm-3m), (2%), a = 4.2329			
	Ni (Fm-3m), (19%), a = 3.5234			
	TiNi (Pm-3m) (17%), a = 2.9986			
	TiNi ₃ (P6 ₃ /mmc) (38%), a = 5.0658, c = 8.4040			
	Ti _{0.7} Ni _{0.3} N (P-6m2) – not calculated			
Filter	TiN _y (Fm-3m), (53%), a = 4.2330	33.9	6.5	0.027
	Ni (Fm-3m), (43%), a = 3.5274			
	Ti _{0.7} Ni _{0.3} N (P-6m2), (3%), a = 2.9348, c = 2.8996			

material for selective filter of CuK α emission [26], which contributes to a decrease in the intensity of all determined phase components except for nickel itself. At the same time, when comparing the evaporation and crystallization temperatures of nickel and other X-ray fixed phase components, it can be assumed that the metal shell completely covers ultra- and nanodispersed particles based on refractory titanium compounds giving rise to a “core-shell” structure. However, if we are guided by the observance of the Arrhenius law and, accordingly, the “quasi-equilibrium” of processes [19] occurring under conditions of a hardening chamber, it must be stated that complete titanium nitrides are hardly wetted with nickel melts, and the wetting angle in this case is 120° [27]. In [27], it is reported that in the case of nonstoichiometric titanium nitride (\sim TiN_{0.7}), the angle of wetting with nickel melt decreases to 3°, which provides coating of ultra- and nanodispersed particles based on titanium nitride with nickel.

The visualization of the formed “core-shell” structures was demonstrated by HR TEM and scanning tunneling microscopy of recondensed titanium nickelide fractions from a cyclone (Fig. 2a) and a bag-type filter (Fig. 2b,c). Figures 2a,b present the total sets of particles, whose average size determined from direct measurements is, in accordance with the distribution histogram (Fig. 2d), 63 nm for the fraction from the cyclone and 20 nm for the fraction from the filter.

The magnification of individual particles from the filter shown in Fig. 3 allows one to see a multilayer structure of nanocrystalline particles, in which a layer of metallic nickel is presented as a high-contrast shell and the dark core is

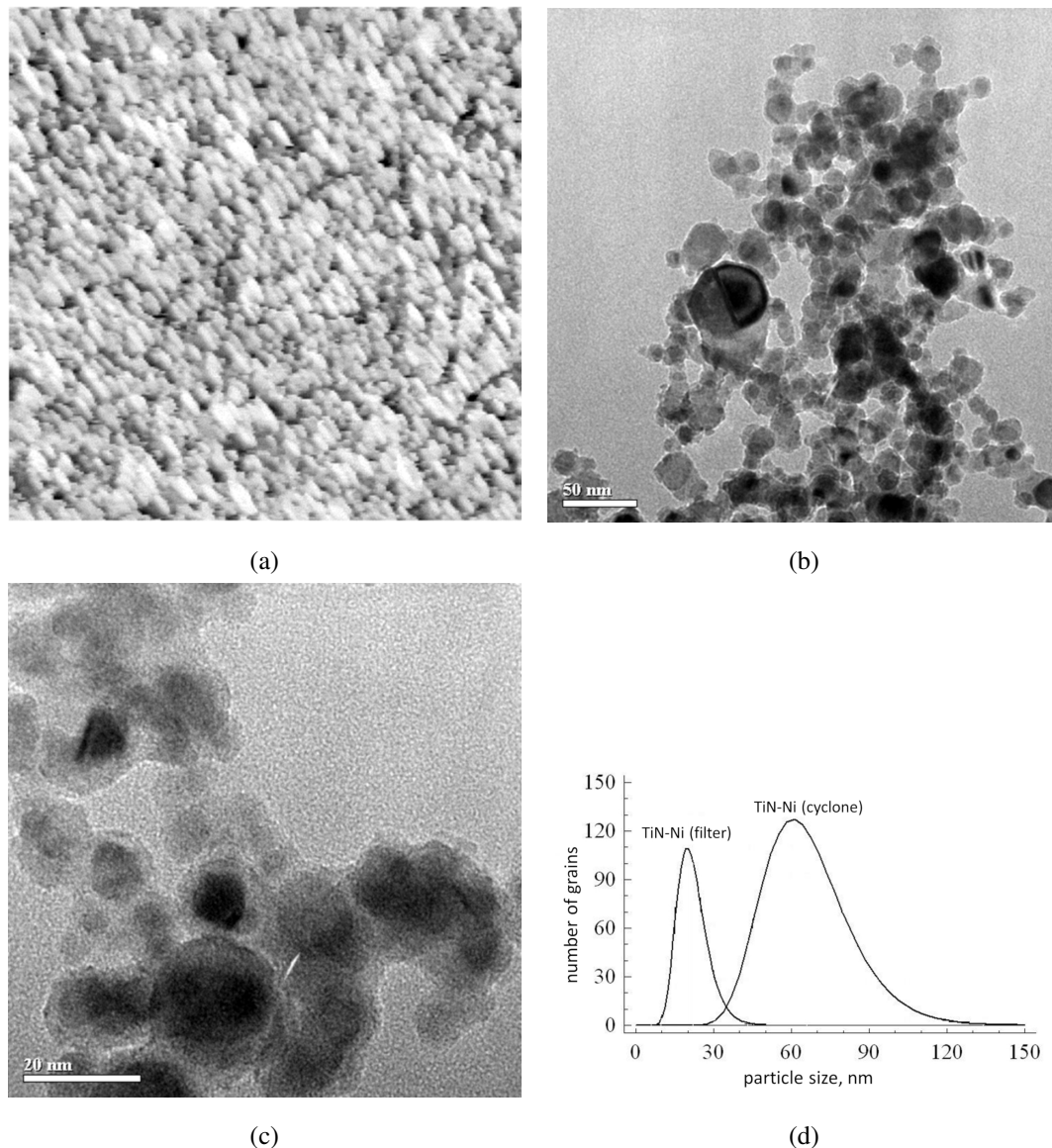


FIG. 2. Results of scanning tunneling and transmission microscopy of ultra- and nanodispersed TiN-Ni powders: a – STM fraction from the cyclone, scan size $2.8 \mu\text{m} \times 2.8 \mu\text{m} \times 87.07 \text{ nm}$, b, c – HR TEM fraction from the filter, d – particle size distribution histograms

composed of refractory interstitial phases recorded by X-ray diffraction. The maximum resolution images of individual sections (Fig. 3-6), containing nanocrystalline particles with a “core-shell” structure made it possible to interpret the individual phase components based on the measurement data of interplanar distances. In particular, in accordance with the measurements of interplanar distances (Fig. 3) and their comparison with the ICDD data, it was found that a layer of hexagonal Ni metal (sp. gr. $P6_3/mmc$) is formed on the surface of nanocrystalline particles [28]. Fig. 4a [29] shows a nanocrystalline particle, in which, according to the measurements of interplanar distances, a transition from metallic nickel to its oxide Ni_2O_3 is observed, which, in turn, is transformed into the complex nitride $\text{Ti}_{0.7}\text{Ni}_{0.3}\text{N}$. Fig. 4b shows monoclinic TiNi and tetragonal titanium nitride Ti_2N . Fig. 4c illustrates a nanoparticle whose shape is close to hexagonal, and the phase composition, according to the measurements of interplanar distances, is represented by the Ti_3Ni_4 intermetallic phase of rhombohedral modification.

In continuation of the description of electron microscopic studies, it should be noted that in the nanocrystalline fraction from the filter of recondensed titanium nickelide it was not possible to display and interpret the planes of refractory compounds based on titanium oxynitride $\text{TiN}_{0.84}\text{O}_{0.11}$ or other refractory phases. At the same time, considering that the X-ray phase analysis technique has a volumetric character compared to the capabilities of transmission electron microscopy characterized by high locality, the X-ray diffraction and HR TEM data complement each other. Thus, the refractory base in the form of $\text{TiN}_{0.84}\text{O}_{0.11}$ oxynitride can be considered as a refractory core of the “core-shell” structure,

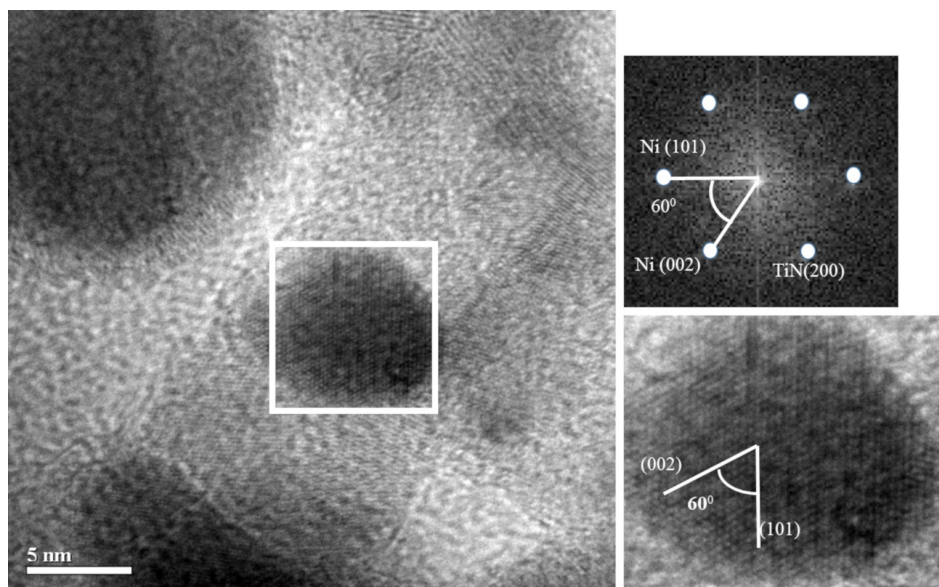


FIG. 3. HR TEM image of a segment of the fraction from TiN-Ni filter

where the peripheral layers can be represented by both locally positioned intermetallic compounds of the Ti-Ni system and bulk phases $\text{Ti}_{0.7}\text{Ni}_{0.3}\text{N}$ and Ni reflected by X-ray.

On the basis of the performed studies, it is possible to develop a model of phase formation of a “core-shell” structure in the process of crystallization of evaporated titanium nickelide in a rotating cylinder of gaseous nitrogen taking place in a quenching chamber.

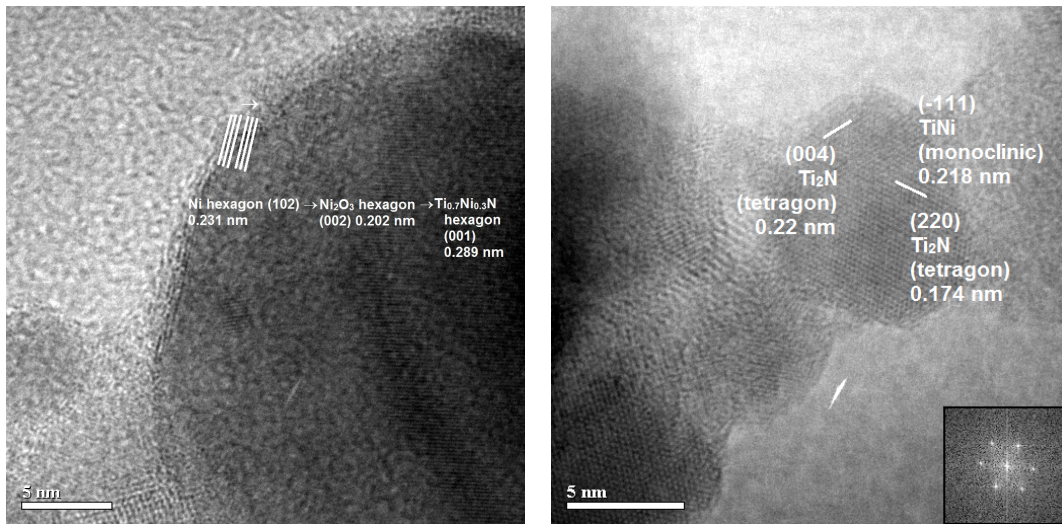
The model of TiN-Ni “core-shell” structure formation during plasma-chemical synthesis of TiNi can be substantiated in terms of physicochemistry by comparing the functions $\Delta G(T)$ (Fig. 5) [30] for all phase components (TiC, TiN, TiNi, TiNi_3) determined radiographically, except for $\text{Ti}_{0.7}\text{Ni}_{0.3}\text{N}$ and Ni, since for the former component there is no available information, while for individual metals $\Delta G(T) = 0$. It can be seen from the graphs that intermetallic phases of titanium with nickel exist at $\Delta G(T)$ values closer to 0 compared with refractory titanium-containing phase components at identical temperatures. At the same time, Ti-Ni intermetallic phases have relatively low melting points compared with refractory titanium carbide-nitride compounds.

In the process of modeling of the recondensed “core-shell” structures, the quenching chamber is separated by temperature barriers, for which the crystallization temperatures of the phase components recorded in the process of X-ray phase analysis are used, see Table 2. Note also that in the modeling process account is taken of the boiling points of both refractory components and individual metals, on the basis of which the individual components of ultra- and nanodispersed “core-shell” structures are formed.

TABLE 2. Melting and boiling points of phase components in the TiN-Ni system

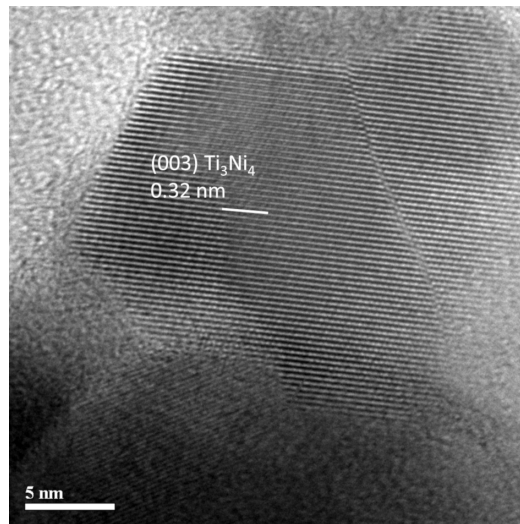
Component	$T_{melt}, ^\circ\text{C}$	$T_{boil}, ^\circ\text{C}$
TiN	2900	–
Ni	1453	2900
TiNi	1310	–

Considering that the low-temperature plasma in the performed experiments corresponded to the temperature range 4000–6000°C, the first temperature barrier can correspond to 4000°C as the lower threshold value of cold plasma. Since the melting temperature of the initial raw material, titanium nickelide, is equal to 1310°C [31], under low-temperature plasma conditions, it is in the state of two metals, Ti and Ni, evaporated to atomic level. It should be noted that the plasma-chemical installation was cleaned with titanium carbide TiC, the trace amounts of which could remain in the plasma-chemical reactor. At 3300°C, the TiC_{1-x} carbide phase and the highly defective TiN_{1-y} titanium nitride phase newly formed from atomic titanium and nitrogen crystallize from the vapor phase [32–35]. Thus, two types of particles crystallize under the conditions of the quenching chamber. Particles of the first type are formed on the basis of titanium carbonitride TiC_xN_y ($x + y \leq 1$) when passing the first temperature barrier under nitrogen atmosphere. Particles of the second type are formed at 2900°C, which corresponds to the crystallization of titanium nitride TiN [36]. The



(a)

(b)



(c)

FIG. 4. HR TEM of particles in the TiN-Ni fraction (a, b, c) from the filter

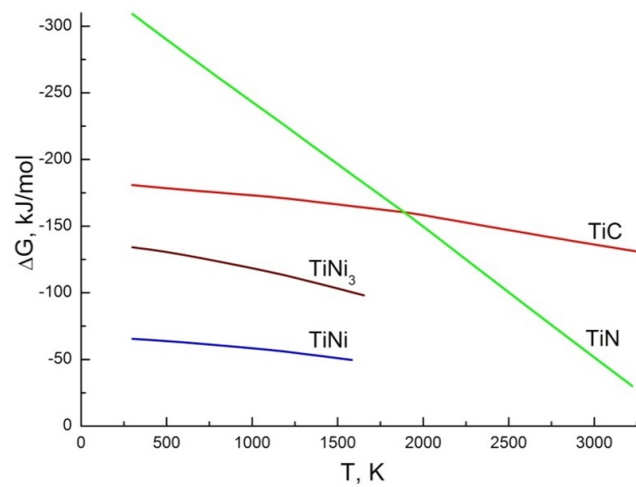


FIG. 5. Dependences $\Delta G(T)$ for compounds TiC, TiN, TiNi_3 , TiNi

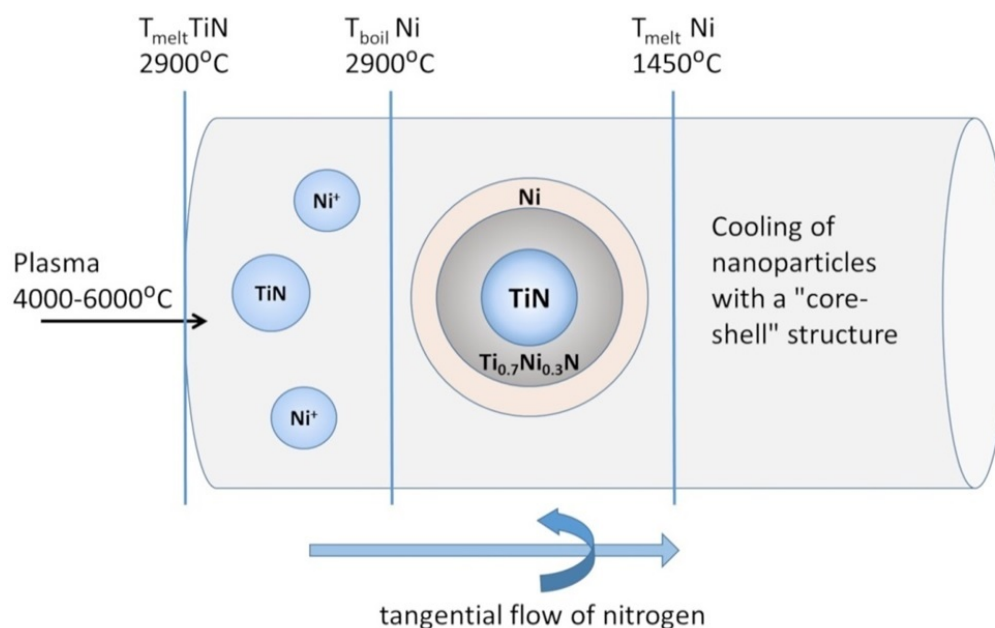


FIG. 6. Chemical mechanism of formation of TiN-Ni “core-shell” structures

nonstoichiometric state of refractory interstitial phases based on titanium, despite the presence of a sufficient amount of gaseous nitrogen, is governed by high crystallization rates under the conditions of the quenching chamber. Nickel metal at these stages is initially in the gaseous state and under these conditions does not react with gaseous nitrogen to form nickel nitrides. Nickel can partially react with gaseous titanium giving rise to Ti–Ni intermetallic compounds (Table 1, experiment 1). At 29–13°C (Table 2), gaseous Ni passes to a liquid phase, which allows intensive interaction with refractory titanium compounds. The fraction from the bag-type filter contains the complex titanium-nickel nitride $\text{Ti}_{0.7}\text{Ni}_{0.3}\text{N}$, which is supposed to be formed in the process of interaction between solid-phase titanium nitride $\text{TiN}_{0.7}$ and liquid Ni at a temperature of 1600°C [22] according to reaction.



A further decrease in temperature is responsible for the crystallization of metallic Ni on the surface of ultra- and nanodispersed particles and their cooling.

Pneumatic transport under the conditions of the plasma-chemical plant provides the transfer of all crystallized particles to the vortex-type cyclone, where the heavier, due to the presence of a larger number of phases (Table 1), ultrafine fraction is separated from the lighter nanocrystalline fraction. The nanocrystalline fraction is concentrated in the bag-type filter. The mechanism of formation of ultra- and nanodispersed “core-shell” structures is shown schematically in Fig. 6.

4. Conclusion

Based on the results of the research performed, it should be noted in conclusion that ultrafine and nanocrystalline TiN-Ni powder fractions with a “core-shell” structure were formed in the process of plasma-chemical synthesis of titanium nickelide in a low-temperature nitrogen plasma. The X-ray diffraction study revealed the phase composition of the powder compositions, in particular, it was shown that the nanocrystalline powder fraction contains the complex titanium-nickel nitride $\text{Ti}_{0.7}\text{Ni}_{0.3}\text{N}$ of hexagonal modification (sp. gr. P-6m2). High-resolution transmission electron microscopy was used to examine the TiN-Ni nanocrystalline fraction, in which the “core-shell” structure was visualized and the presence of all phase components determined by X-ray diffraction, including $\text{Ti}_{0.7}\text{Ni}_{0.3}\text{N}$, was confirmed.

Based on the experimental results obtained and their structural and morphological certification, we have developed a theoretical model of the formation of “core-shell” structures, which shows that the phase and structure formation in the TiN-Ni system depends on the crystallization rate and the presence of a cooling medium in the form of a rotating cylinder of gaseous nitrogen.

References

- [1] Liu F., Yang X., Dang D., Tian X. Engineering of hierarchical and three-dimensional architectures constructed by titanium nitride nanowire assemblies for efficient electrocatalysis. *ChemElectroChem*, 2019, **6**, P. 2208–2214.
- [2] Wang D., Xue C., Cao Y., Zhao J. Microstructure design and preparation of $\text{Al}_2\text{O}_3/\text{TiC}/\text{TiN}$ micro-nano-composite ceramic tool materials based on properties prediction with finite element method. *Ceram. Int.*, 2018, **44**, P. 5093–5101.
- [3] Cui X., Wang D., Guo J. Effects of material microstructure and surface microscopic geometry on the performance of ceramic cutting tools in intermittent turning. *Ceram. Int.*, 2018, **44**, P. 8201–8209.

- [4] Zhang J., Li S., Lu C., Sun C., Pu S., Xue Q., Lin Y., Huang M. Anti-wear titanium carbide coating on low-carbon steel by thermo-reactive diffusion. *Surf. Coat. Technol.*, 2019, **364**, P. 265–272.
- [5] Sarycheva A., Polemi A., Liu Y., Dandekar K., Anasori B., Gogotsi Y. 2D titanium carbide (MXene) for wireless communication. *Science Advances*, 2018, **4**(9).
- [6] Drozdov V.O., Cherepanov A.N., Chesnokov A.E., Smirnov A.V. Studying the production of modifying composite powders by plasma processing. *AIP Conference Proceedings*, 2018, **2053**, 030010.
- [7] Simonenko E.P., Simonenko N.P., Sevastyanov V.G., Kuznetsov N.T. ZrB₂/HfB₂-SiC ceramics modified by refractory carbides: an overview. *Russ. J. Inorg. Chem.*, 2019, **64**, P. 1697–1725.
- [8] Hammouti S., Holybee B., Zhu W., Allain J. P., Jurczyk B., Ruzic D.N. Titanium nitride formation by a dual-stage femtosecond laser process. *Appl. Phys. A*, 2018, **124**, 411.
- [9] Guo W.-P., Mishra R., Cheng C.-W., Wu B.-H., Chen L.-J., Lin M.-T., Gwo S. Titanium nitride epitaxial films as a plasmonic material platform: alternative to gold. *ACS Photonics*, 2019, **6**(8), P. 1848–1854.
- [10] Corradetti S., Carturana M., Maggionia G., Franchin G., Colombo P., Andrighetto A. Nanocrystalline titanium carbide/carbon composites as irradiation targets for isotopes production. *Ceram. Int.*, 2020, **46**(7), P. 9596–9605.
- [11] Huang H., Feng T., Gan Y., Fang M., Xia Y., Liang C., Tao X., Zhang W. TiC/NiO Core/Shell nanoarchitecture with battery-capacitive synchronous lithium storage for high-performance lithium-ion battery. *ACS Appl. Mater. Interfaces*, 2015, **7**(22), P. 11842–11848.
- [12] Zhang Y., Song R., Pei Y., Wen E., Zhao Z. The formation of TiC-NbC core-shell structure in hypereutectic high chromium cast iron leads to significant refinement of primary M7C₃. *J. Alloys Compd.*, 2020, **824**, 153806.
- [13] Dong S., Chen X., Gu L., Zhou X., Wang H., Liu Z., Han P., Yao J., Wang L., Cui G., Chen L. TiN/VN composites with core/shell structure for supercapacitors. *Mater. Res. Bull.*, 2011, **46**(6), P. 835–839.
- [14] Ding X.-Y., Luo L.-M., Huang L.-M., Luo G.-N., Zhu X.-Y., Cheng J.-G., Wu Y.-C. Preparation of TiC/W core-shell structured powders by one-step activation and chemical reduction process. *J. Alloys Compd.*, 2015, **619**(15), P. 704–708.
- [15] Xia M., Yan Q., Xu L., Zhu L., Guo H., Ge C. Synthesis of TiC/W core-shell nanoparticles by precipitate-coating process. *J. Nucl. Mater.*, 2012, **430**(1-3), P. 216–220.
- [16] Chalmers B. *Principles of solidification*. John Wiley and Sons, Springer, New York, Dordrecht, Heidelberg, London, 1964, 319 p.
- [17] Zalite I., Grabis J., Palcevskis E., Herrmann M. Plasma processed nanosized-powders of refractory compounds for obtaining fine-grained advanced ceramics. *IOP Conf. Ser.: Mater. Sci. Eng.*, 2011, **18**, 062024.
- [18] Filkov M., Kolesnikov A. Plasmachemical synthesis of nanopowders in the system Ti(O,C,N) for material structure modification. *Journal of Nanoscience*, 2016, **2016**, 1361436.
- [19] Polak L. Elementary chemical processes and kinetics in a non-equilibrium and quasi-equilibrium plasma. *Pure Appl. Chem.*, 1974, **39**(3), P. 307–342.
- [20] Storozhenko P.A., Guseinov Sh.L., Malashin S.I. Nanodispersed Powders: Synthesis Methods and Practical Applications. *Nanotech. in Russia*, 2009, **4**, P. 262–274.
- [21] Luo H.L., Duwez P.E. Solid solutions of rhodium with copper and nickel. *Journal of the Less-Common Metals*, 1964, **6**, P. 248–249.
- [22] Schönberg N. The tungsten carbide and nickel arsenide structures. *Acta Metall.*, 1954, **2**, P. 427–432.
- [23] Fultz B., Howe J.M. *Transmission electron microscopy and diffractometry of materials*, 3rd ed. Springer, Berlin, Heidelberg, 2008, 758 p.
- [24] Goryczka T., Morawiec H. Structure studies of the R-phase using X-ray diffraction methods. *J. Alloys Compd.*, 2004, **367**, P. 137–141.
- [25] Van Vucht J.H.N. Influence of radius ratio on the structure of intermetallic compounds of the AB₃ type. *Journal of the Less-Common Metals*, 1966, **11**, P. 308–322.
- [26] Kovba L.M., Trunov V.K. *X-ray phase analysis*. MGU, Moscow, 1976, 232 p. (in Russ.)
- [27] Kosolapova T.Ya. *Handbook of high temperature compounds: properties, production, applications*. CRC Press, New York, Washington, Philadelphia, London, 1990, 958 p.
- [28] Hemenger P., Weik H. On the existence of hexagonal nickel. *Acta Crystallogr.*, 1956, **19**, P. 690–691.
- [29] Ermakov A.N., Luzhkova I.V., Avdeeva Yu.A., Murzakaev A.M., Zainulin Yu.G., Dobrinsky E.K. Formation of complex titanium-nickel nitride Ti_{0.7}Ni_{0.3}N in the “core-shell” structure of TiN – Ni. *Int. J. Refract. Met. Hard Mater.*, 2019, **84**, 104996.
- [30] Barin I. *Thermochemical data of pure substances*. Third edition. VCH, Weinheim, New York, Base1, Cambridge, Tokyo, 1995, 2003 p.
- [31] Otsuka K., Shimizu K., Suzuki Yu. *Shape memory alloys*. Ed. Funakubo X. Metallurgiya, Moscow, 1990, 224 p. (In Russ.)
- [32] Gusev A.I. *Nonstoichiometry, disorder, short-range and long-range order in a solid*. FIZMATLIT, Moscow, 2007, 856 p. (In Russ.)
- [33] Samokhin A.V., Polyakov S.N., Alekseev N.V., Astashov A.G., Tsvetkov Yu.V. Simulation of the process of nanopowder synthesis in a jet-type plasma reactor. I. Statement of the problem and verification of the model. *Fizika i khimiya obrabotki materialov*, 2013, **6**, P. 40–46. (In Russ.)
- [34] Samokhin A.V., Polyakov S.N., Alekseev N.V., Astashov A.G., Tsvetkov Yu.V. Simulation of the process of nanopowder synthesis in a jet-type plasma reactor. II. Formation of nanoparticles. *Fizika i khimiya obrabotki materialov*, 2014, **3**, P. 2–17. (In Russ.)
- [35] Shiryayeva L.S., Gorbuzova A.K., Galevsky G.V. Production and application of titanium carbide (assessment, trends, forecasts). *Nauchno-tekhnicheskiye vedomosti Sankt-Peterburgskogo gosudarstvennogo politekhnicheskogo universiteta*, 2014, **2**(195), P. 100–107. (In Russ.)
- [36] Krzhizhanovskiy R.E., Stern Z.Yu. *Thermophysical properties of non-metallic materials (carbides)*. Handbook, Energiya, Leningrad, 1976, 120 p. (In Russ.)

Submitted 12 April 2022; accepted 14 April 2022

Information about the authors:

Yuliya A. Avdeeva – Institute of Solid State Chemistry, Ural Branch, Russian Academy of Sciences, Pervomaiskaya Street, 91, Ekaterinburg, 620990, Russia; y-avdeeva@list.ru

Irina V. Luzhkova – Institute of Solid State Chemistry, Ural Branch, Russian Academy of Sciences, Pervomaiskaya Street, 91, Ekaterinburg, 620990, Russia; key703@yandex.ru

Alexey N. Ermakov – Institute of Solid State Chemistry, Ural Branch, Russian Academy of Sciences, Pervomaiskaya Street, 91, Ekaterinburg, 620990, Russia; ermakovihim@yandex.ru

Conflict of interest: the authors declare no conflict of interest.

Impact of distributed Bragg's reflectors and nanogratings in thin film silicon solar cells

R. S. Dubey, S. Saravanan

Swarnandhra College of Engineering & Technology, Seetharampuram, Narsapur, 534280 West Godavari, Andhra Pradesh, India

Corresponding author: S. Saravanan, shasa86@gmail.com

ABSTRACT Photonic crystals possess periodic modulation of higher refractive index contrast which brings a unique photonic band gap. In this work, thin-film silicon solar cell optical performance was studied by the finite-difference time-domain (FDTD) method. The distributed Bragg reflector (DBR) and nanogratings are integrated as a backside reflector, which endorses the photonic modes in the silicon solar cell. The light trapping scheme plays a pivotal role in solar cells due to the limited absorption in the higher spectral region. For that, various silicon solar cell structures are investigated for better light absorption using photonic ray theories with numerical simulations. This result indicates the combination of DBR and nanogratings is capable and yielded a high relative enhancement of 59 % as compared with the reference cell which was endorsing the Fabry–Perot resonance and guided-modes in photovoltaic devices. These results show promise for designing thin film silicon solar cells with enhanced light absorption.

KEYWORDS DBR, nanogratings, silicon, thin-film, FDTD

FOR CITATION Dubey R.S., Saravanan S. Impact of distributed Bragg's reflectors and nanogratings in thin film silicon solar cells. *Nanosystems: Phys. Chem. Math.*, 2022, **13** (2), 220–226.

1. Introduction

Photonic crystals are attractive due to the unique optical performance in photovoltaic devices that convert optical power into electricity. As one-dimensional (1D) photonic crystals also known as distributed Bragg's reflector (DBRs), which is responsible for the desired optical reflectance from the shorter (300 – 700 nm) and longer spectral (> 700 nm) region by tuning different optical parameters such as refractive index contrast between the selected materials, incidence wavelength, angle of wavelength, thickness of the each layer etc [1]. The low-cost, easy fabrication and large scale manufacturing are the key factors, which are focused on by researchers. For that, thin-film crystalline silicon solar cells are the best candidate for future energy needs. In solar cells, one of the major challenges is the achievement of higher light absorption from thin film. In the photovoltaic (PV) market, the efficiency of thin film solar cells is very low due to their weak absorption in the longer (infrared) spectral region. Because of the light-trapping effects, thin film silicon solar cells have become a vital route to improve solar cell conversion efficiency. For that, the light trapping mechanism might be improved by various nanostructures integrated into thin-film solar cells such as nanoparticles (nanospheres), nanogratings, distributed Bragg reflectors, nanopillars, nanopyramids, nanodisks etc. [2–4]. The thin film solar cells are theoretically (simulation) studied by various methods, such as rigorous-coupled wave analysis (RCWA), finite-difference time-domain method (FDTD) and finite element method (FEM) [5, 6]. To date, light trapping mechanisms have been employed by incorporating various dielectric/metallic nanostructures including various shapes of nanostructures like nanoparticles and nanogratings [7–9]. This light trapping mechanism helps one to improve their omni-directional scattering and reflection. In the reported work, one describes different types of nanogratings used in thin film solar cells, such as triangular gratings [10], rectangular gratings [11], square gratings [12], dual gratings [13], double gratings, etc [14]. Tahmineh investigated the impact of one-dimensional photonic crystals as back reflectors on thin-film crystalline silicon (c-Si) solar cells using the two-dimensional (2D) FEM method. The obtained results showed an improved current density by integration of DBR (24.01 mA/cm²) and nanogratings (24.51 mA/cm²) in thin film c-Si solar cells [15]. Sanshui et al. demonstrated crystalline silicon (c-Si) solar cell performance by integrating the front and back-side of the metallic gratings. They have achieved the highest current density enhancement factor of 1.9 within a 200 nm thick c-Si absorber layer [16]. Dubey et al. studied the performance of SiO₂/Si₃N₄ multilayers and nanogratings for better amorphous silicon (a-Si) solar cell devices by using chemical vapor deposition and RCWA methods. With the effect of dielectric multilayers and nanogratings, 79 % relative enhancement was achieved as compared to the reference solar cell [17]. Saravanan and Dubey investigated the influence of 1D photonic (SiO₂) and plasmonic (Ag) nanostructure for the improvement of amorphous silicon solar cells using the RCWA method. The light harvesting enhanced in shorter and longer spectral regions and achieved the maximum current density of 33.54 mA/cm² [18]. Chen et al. experimentally prepared thin film amorphous silicon (a-Si) solar cells with a backside reflector of 6 pairs of ZnO/a-Si distributed Bragg reflectors using a magnetron sputtering method. The

fabricated 6 DBR pairs achieved a reflectance of 99 % and the stop-band (photonic band) from 686 to 1354 nm. They demonstrated the 50 % absorption enhancement noticed in the visible and near-infrared spectral region [19]. Heidarzadeh et al. presented the improved light trapping analysis in thin film silicon solar cells using RCWA, FEM and FDTD methods. They used rectangular and triangular gratings in the absorber region and the solar spectral range from 400 to 1100 nm. Under transverse electric (TE) polarization mode, the highest cell efficiencies of 20, 22.1 and 23.53 % were achieved with 2.5, 5 and 7.5 μm thick silicon solar cells [6]. The major goal of this work is reducing the cost (naturally abundant silicon) and improving the light absorption in thin-film silicon solar cells by integrating photonic nanostructures, which are easy to fabricate at device level.

In this paper, we focus on the optical performance of thin-film crystalline silicon solar cells using the finite-difference time-domain method. The designing parameters and simulation methods are discussed in Section 2. In Section 3, the optical properties (absorption, quantum efficiency) of the simulated solar cell are discussed. Finally, we conclude the work in Section 4.

2. Designing approach

Figure 1 shows the schematic diagram of a thin-film silicon solar cell with the integration of Si_3N_4 -anti-reflection coatings (ARCs) and back reflector of SiO_2 nanogratings and distributed Bragg's reflector (DBRs, a-Si/ SiO_2). The numerical investigation was carried out using the FDTD method (RSoft), which is useful to solve the issue between the matter (solid) and electromagnetic waves. The proposed solar cell anti-reflection coating (ARC) layer is made of silicon nitrate (Si_3N_4) with a thickness of 70 nm. Next, DBR or one-dimensional photonic crystals consist of five alternative layers (stacks) such as amorphous Si (a-Si) and silicon-di-oxide (SiO_2) thin films. The corresponding DBR refractive indices (n_i) are 3.6 ($n_{\text{a-Si}}$) and 1.45 (n_{SiO_2}), respectively, and the center wavelength (λ_C) for light is 800 nm. The thickness of each DBR layer is determined by the quarter-wave principle ($t = \lambda_C/4n$), where, n is the refractive index of the material, so we get the thickness of a-Si ($t_{\text{a-Si}}$) and SiO_2 (t_{SiO_2}) are 56 and 138 nm. The crystalline silicon ($t_{\text{Si}} = 1.5 \mu\text{m}$) acts as an absorber (intrinsically flat) and the photonic structures like periodic grating (or) photonic crystals should be directly imprinted on the c-Si layer. On top of the DBR (or bottom of the absorber), we further implement the integration of one-dimensional dielectric grating with a period ($G_p = 0.6 \mu\text{m}$). The SiO_2 nanogratings have a duty cycle (G_{dc}) of 0.5 and a thickness of 0.1 μm . The alternative periodic SiO_2 grating structure was embedded in between the c-Si layer and the DBR. It guides and enhances the light scattering and diffraction of light into the PV device. The total thickness of the thin film silicon solar cell is 2.54 μm .

The complete electric field distributions are simulated and investigated using the finite-difference time-domain method. It has periodic boundary conditions (PBC) on the X-axis to avoid boundary issues and a perfect matched layer (PML) applied on Y and Z-axis [5]. The PML is also known as the absorbing layer and is useful for absorbing (without any

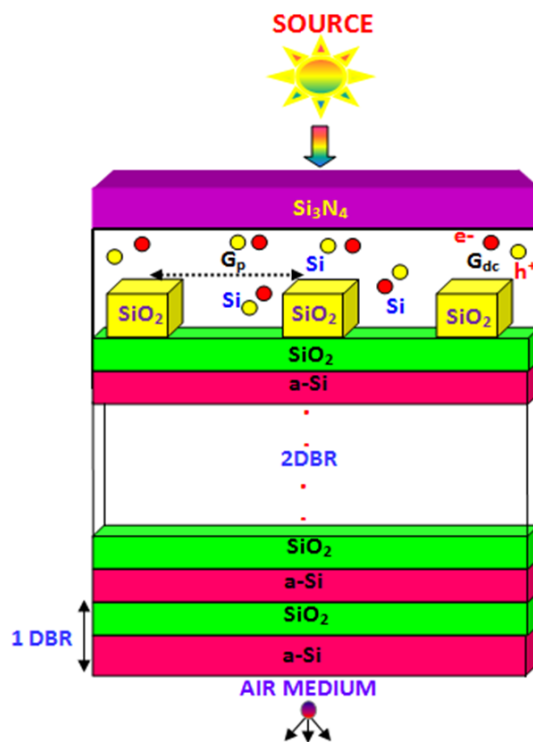


FIG. 1. The schematic diagram of the thin film silicon solar cell

reflection between the interfaces) the incident light that is travelling outward from the bounded domain [8,20]. This entire simulation process is carried out using RSoft synopsis tools. The incident spectrum is considered from the range of 300 to 1200 nm (λ) and beyond that the photons are unabsorbed.

3. Results and discussion

We have simulated thin film silicon solar cells using the FDTD method. This method is useful to solve the transverse electro (TE)/magnetic (TM) problems in Fourier space through Maxwell's equations.

3.1. Quantum efficiency

The quantum efficiency and light absorption spectra of different solar cell structures are measured and compared in Figs. 2 and 3. First, the quantum efficiency of various thin film solar cells is shown in Fig. 2. To get a clear understanding and the role or influence of backside reflector structures in solar cells, they are named as, 1) reference (ARC+Tc), 2) ARC+Tc+DBR, 3) ARC+Tc+GRA+DBR and 4) ARC+Tc+GRA+Metal BR. Here, 'Tc' is active (absorber) layer, 'ARC' is antireflection coatings, 'DBR' is distributed Bragg reflector (or one-dimensional photonic crystals) and 'Metal BR' is the aluminum metal back reflectors. Further, the incident light or photon energies are converted as charge carriers which are collected by the solar cell device. The quantum efficiency is the function of wavelength from 300 to 1200 nm. For instance, the conversion and collection of the carriers are enhanced (red dotted) with the assistance of back reflector of DBRs and nanogratings generated and increased quantum efficiency in the ultraviolet and infrared region. Tsai et al. reported that the DBRs integrated solar cells proved higher external quantum efficiency in the ultraviolet and visible spectral regions [19,21]. The quantum efficiency for the thin film silicon solar cell showed reducing in the near-infrared spectral region with the effect of recombination losses. The metal back reflector (ARC+Tc+GRA+Metal BR) showed the increased performance (green solid line). Next, the reference cell (ARC+Tc) generates less collection of the carriers (blue solid lines).

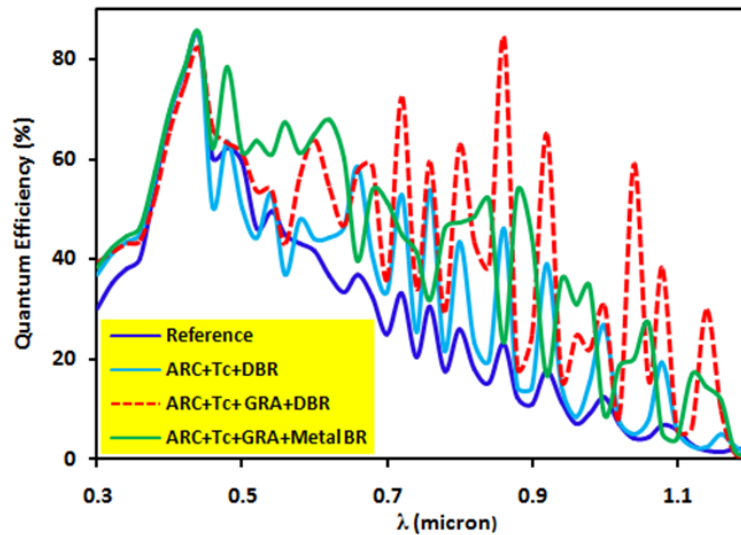


FIG. 2. The quantum efficiency as a function of wavelength (μm)

3.2. Absorption

The light absorption of different thin-film silicon solar cells is shown in Fig. 3 which demonstrates the influence of dielectric nanostructures of DBR and gratings in the silicon solar cell. The dielectric SiO_2 nanogratings help to extend the photon path length (or life time) in the silicon absorber region by maximizing the diffraction and larger scattering angle. However, the highest light absorption is achieved by 'ARC+Tc+GRA+Metal BR' structure in ultraviolet spectral region (green solid line). The diffraction of photons was calculated with the following equation:

$$n_x \sin \theta_m + n_y \sin \theta_i = \frac{N\lambda}{d}, \quad (1)$$

where, n_y is the refractive index of light incident material layer, n_x is the refractive index of the outgoing material layer, d is the constant, λ is the wavelength, N is the diffractive order ($N = 0, 1, -1, 2, -2, \dots$), θ_i the incident angle and θ_m is the diffractive angle [22, 23].

Furthermore, we have compared different types of silicon solar cells and studied the improved light absorption. In particular, DBR with nanogratings showed the highest light absorption due to the significant light scattering with the assistance of SiO_2 nanogratings and unusual (highest) reflection from five stacks of Si/a-Si DBR layers. The absorption

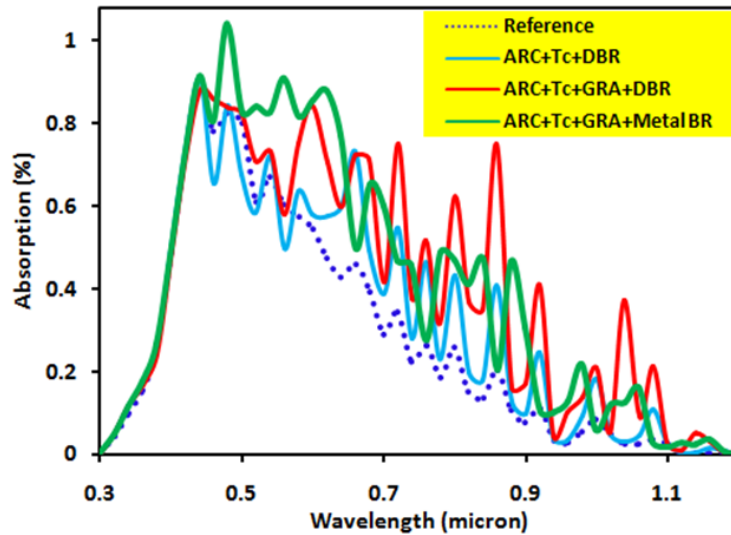


FIG. 3. The absorption (%) as a function of wavelength (λ) for various thin film silicon solar cell

result reached a value greater than 80 % and the highest absorption peaks were obtained for the spectral range from 450 to 1100 nm. In the silicon absorber region, the incident light absorption, $A(\lambda)$ can be calculated by the following equation:

$$A(\lambda) = 1 - R(\lambda) - T(\lambda). \quad (2)$$

Here, $R(\lambda)$ is the total reflection and $T(\lambda)$ is the total transmission from the proposed silicon solar cell. By placing monitors, the light reflectance (R) and transmittance (T) were calculated from the front surface and the rear surface (or backside) of the solar cell [11]. At longer spectral wavelengths, reduced optical performance is noticed, which is hampered by the various parameters like non-absorption of reduced photon energy, thermal losses from the absorption of high energy light photons, electrical losses, parasitic losses, extraction losses with the effect of unavoidable recombination losses from the charge-carriers etc [24]. This significant performance was achieved with the effect of Fabry–Perot resonance mode and surface guided modes (Fig. 4). With the addition of the distributed Bragg reflector (DBR) to the planar structure, the electric field evanescently decays into the DBR and it is reflected backwards (or) repetition in to the light path. The back reflector structures (or photonic crystals) are known as perfect mirrors (back reflecting). Since the light can be diffracted into oblique angles to enhance the absorption length. Compared to a smooth surface (reference cell) with the ‘ARC+Tc+GRA+DBR’ solar cell, the photon optical path length and lifetime increased as evidenced by their optical performance in Figs. 2 and 3. The solar cell power conversion was measured using numerically a sun simulator under AM1.5 conditions [20, 25].

The optical characteristics are changing with respect to the back reflectors or with the level of the irradiance (incidence) spectrum. In this section, the Maxwell’s equation is solved and the electric field distribution in the proposed silicon solar cell structure is at 860 nm (λ_C). Under the normal solar incident spectrum, the boundary conditions were applied for the achievement of TE field distribution. The transverse electric, TE (E_y) field is shown in Fig. 5 with an incidence wavelength (λ_C) of 860 nm. The incident light is reflected at each layer interface. The incident light (L_I) at a certain wavelength propagates into the DBR layers by considering a few factors (units) such as reflected light (L_R) and light (L_I) obtained from the interfaces. The electric field distribution shows a strong light trapping mechanism due to the Fabry–Perot resonance and surface guided modes (white region in the active region) [26–28]. The irradiating light is partially reflecting and diffracting into the 1.5 μm thick silicon active layer region and transmitting into the air. The diffraction from the bottom nanogratings constructively interferes with the absorber region. This higher absorption originates from the periodic diffraction gratings and DBR layers. The transverse electric field is highly confined in the absorber region. Further, the intensity bar confirmed the strong field (cyan and blue colors) noticed in the final cell structure due to the DBR plus periodically arranged nanogratings [6]. The open circuit voltage ($V_{OC} = 0.7 \text{ A/m}^2$) and fill factor ($FF = 84.5 \%$) were noticed.

3.3. Current density

The dielectric back reflectors show a significant performance in thin film silicon solar cells as evidenced by Figs. 4 and 6 and by calculation of the current density (J_{SC} , mA/cm^2) and relative enhancement (%). In Fig. 4, we summarize and compare the optical performance of various thin film silicon solar cells by changing the various backside reflectors or back reflector. The J–V relationship for the solar cell is calculated and it is dependent on the absorption of light photons under normal incidence angle (0°) and the AM1.5G spectrum. This photo-generated current (J_{SC}) is directly related to the collection of the photon absorption of the silicon absorber [12].

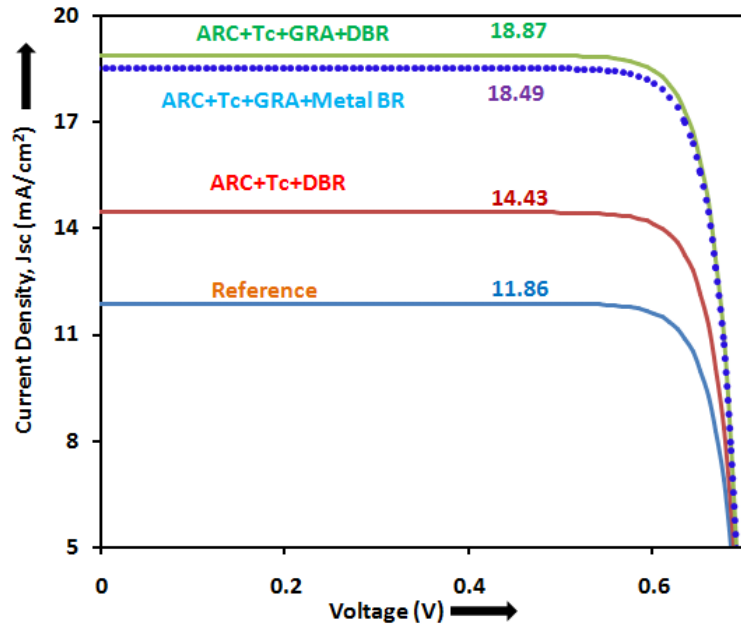


FIG. 4. The types of current density vs voltage

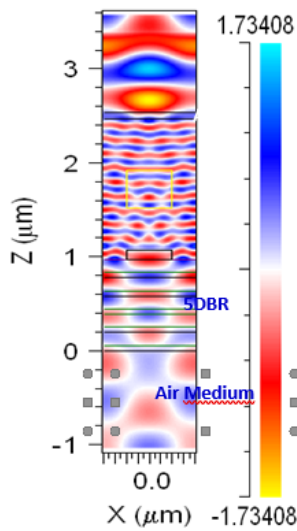


FIG. 5. The electric field (E_y , 860 nm) distribution of silicon thin film solar cell

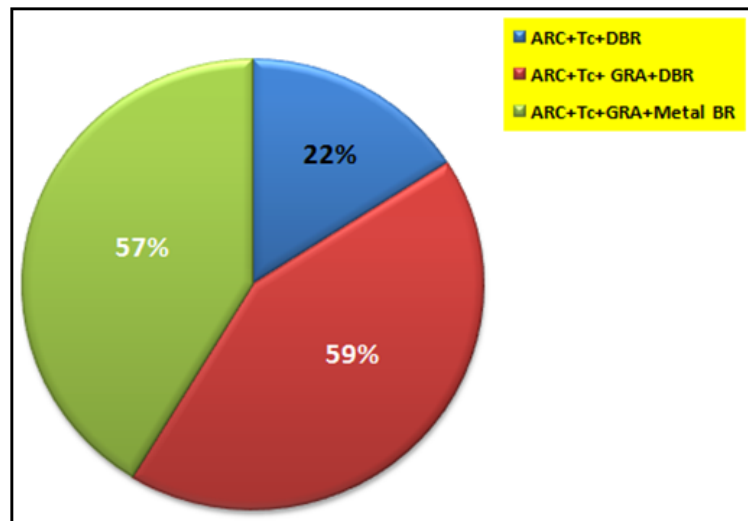


FIG. 6. The relative enhancement of various silicon solar cells

With the advantage of light trapping, the highest current density is received by absorbing the number of photons in the absorber region. The current density (J_{SC}) was calculated by using the following equation as,

$$J_{SC} = \frac{e}{hc} \int_{300}^{1200} \lambda A(\lambda) \frac{dI}{d\lambda} d\lambda, \tag{3}$$

where, e is the electron, h is the Planck's constant, c is the speed of light, λ is the wavelength, I is the incident solar spectrum, and A is the absorption [18]. The light trapping mechanism significantly improved and went back to the silicon absorber region. The DBR and nanogratings integrated cell '(ARC+Tc+GRA+DBR)' structures highly dominated for their improved current density compared to 18.87 mA/cm² as shown in Fig. 4. This optical performance is enhanced with the effect of photonic nanostructures. In the silicon absorber region, surface guided modes (white color) are noticed with the addition of effective photonic nanostructures including SiO₂ nanogratings and DBR layers. The metallic back reflector replaced by DBR showed improved current density as compared with the reference solar cell. Fig. 6 depicts the relative enhancement of various types of crystalline silicon thin film solar cell. The combination of periodic SiO₂ nanogratings with 5DBR showed improved performance as indicates 59 % enhancement as compared to the reference solar cell due

to the photonic effects such as Fabry–Perot resonance, surface guided modes. The plasmonic silicon solar cell integrated with a 200 nm thick aluminum back reflector yielded improved performance up to 57 %.

Overall, photovoltaic performance highly improved with respect to semiconductor materials due to the photonic effects. The designed multilayer based solar cell could be fabricated by using various techniques such as sol-gel spin coatings, magnetron sputtering, dip-coatings, electrochemical etching and plasma enhanced chemical vapour deposition (PECVD) techniques [29, 30].

4. Conclusions

In conclusion, we have theoretically investigated the light trapping mechanism of different thin film crystalline silicon solar cells by using FDTD numerical analysis. The combination of photonic nanostructures is capable for improving the current density due to their higher refractive index ratio. The DBR (a-Si/SiO₂) and nanogratings (SiO₂) were integrated as a backside reflector in a thin-film silicon solar cell and yielded the highest light absorption in the visible and near infrared region. The different solar cells are investigated in terms of quantum efficiency, absorption, and current density. Further, we have calculated the relative enhancement up to 59 % as compared to the reference cell due to the photonic modes of Fabry–Perot resonance and guided modes. This enhanced light trapping mechanism within the nanoscale will be greatly evident because of the better absorption in solar cells. Furthermore, the photo-current will be enhanced by considering optimization of each parameter.

References

- [1] Saravanan S., Dubey R.S. One-Dimensional Photonic Crystals (Si/SiO₂) for Ultrathin Film Crystalline Silicon Solar Cells. *Nanosystems: Physics, Chemistry, Mathematics*, 2020, **11**, P. 189–194.
- [2] Olaimat M.M., Yousefi L., Ramahi O.M. Using plasmonics and nanoparticles to enhance the efficiency of solar cells: review of latest technologies. *J. of the Optical Society of America B*, 2021, **38** (2), P. 638–651.
- [3] Shi Y., Wang X., et al. Nanopyramids and rear-located Ag nanoparticles for broad spectrum absorption enhancement in thin-film solar cells. *Optics Express*, 2014, **22**, P. 20473–20480.
- [4] Ankit V., Jephias G., et al. Multi-resonant silver nano-disk patterned thin film hydrogenated amorphous silicon solar cells for Staebler–Wronski effect compensation. *J. of Applied Physics*, 2014, **116**, 093103-1-10.
- [5] Singh G., Verma S.S. Enhanced efficiency of thin film GaAs solar cells with plasmonic metal nanoparticles. *Energy Sources, Part A: Recovery, Utilization, and Environmental Effects*, 2018, **40** (2), P. 155–162.
- [6] Heidarzadeh H., Rostami A., et al. Analysis of the light trapping effect on the performance of silicon-based solar cells: absorption enhancement. *Applied Optics*, 2015, **54** (12), P. 3591–3601.
- [7] Singh G., Sekhon J.S., Verma S.S. Cu nanoparticle plasmons to enhance GaAs solar cell efficiency, 13th Int. Conf. on Fiber Optics and Photonics, OSA Technical Digest, paper W3A.14, Kanpur (India), 4-8th December, 2016.
- [8] Shabani L., Mohammadi A., Jalali T. Numerical study of plasmonic effects of Ag nanoparticles embedded in the active layer on performance polymer organic solar cells. *Plasmonics*, 2022, **17** (5), P. 1–15.
- [9] Saravanan S., Dubey R.S., S. et al. Design and optimization of ultrathin crystalline silicon solar cells using an efficient back reflector. *AIP Advances*, 2015, **5**, 057160-1-9.
- [10] Saravanan S., Dubey R.S., Kalainathan S. Analytical study of plasmonic effect in ultrathin film silicon solar cells. *J. of Optoelectronics and Advanced Materials*, 2017, **19** (3–4), P. 173–177.
- [11] Sun C., Wang Z., Wang X., Liu J. A surface design for enhancement of light trapping efficiencies in thin film silicon solar cells. *Plasmonics*, 2016, **11** (4), P. 1–8.
- [12] Sheng X., Broderick L.Z., Kimerling L.C. Photonic crystal structures for light trapping in thin-film Si solar cells: Modeling, process and optimizations. *Optics Communications*, 2014, **314**, P. 41–47.
- [13] Zheng H., Yu Y., et al. Period-mismatched sine dual-interface grating for optical absorption in silicon thin-film solar cells. *Applied Optics*, 2020, **59** (33), P. 10330–10338.
- [14] Ming-Yi Lin, Kang Y.L., et al. Plasmonic ITO-free polymer solar cell. *Optics Express*, 2014, **22** (S2), P. A438–A445.
- [15] Tahmineh J. Impact of one-dimensional photonic crystal back reflector in thin-film c-Si solar cells on efficiency. *Applied Physics A*, 2018, **124**, 370-1-7.
- [16] Sanshui E. Stassen X., Mortensen N.A. Ultrathin silicon solar cells with enhanced photocurrents assisted by plasmonic nanostructures. *J. of Nanophotonics*, 2012, **6**, 061503-1-7.
- [17] Dubey R.S., Jhansirani K., Singh S. Investigation of solar cell performance using multilayer thin film structure (SiO₂/Si₃N₄) and grating. *Results in Physics*, 2017, **7**, P. 77–81.
- [18] Saravanan S., Dubey R.S. Study of ultrathin-film amorphous silicon solar cell performance using photonic and plasmonic nanostructure. *Int. J. of Energy Research*, 2022, **46** (3), P. 2558–2566.
- [19] Chen A., Yuan Q., Zhu K. ZnO/a-Si distributed Bragg reflectors for light trapping in thin film solar cells from visible to infrared range. *Applied Surface Science*, 2016, **360** (B), P. 693–697.
- [20] Zhao L., Zuo Y.H., et al. A highly efficient light trapping structure for thin film silicon solar cells. *Solar Energy*, 2010, **84**, P. 110–115.
- [21] Tsai Y.L., Lin C.C., et al. Improving efficiency of InGaN/GaN multiple quantum well solar cells using CdS quantum dots and distributed Bragg reflectors. *Solar Energy Materials & Solar Cells*, 2013, **117**, P. 531–536.
- [22] Raghvendra Sarvjeet Dubey, Sigamani S. Light trapping enhancement in thin film silicon solar cell with different back reflector. *Int. J. of Electrical Components and Energy Conversion*, 2017, **3** (5), P. 83–87.
- [23] Zheng G., Zhang W., et al. Absorbance enhancement of thin film solar cells with front double dielectric and back metallic grating. *Infrared Physics & Technology*, 2014, **67**, P. 52–57.
- [24] Day J., Senthilarasu S., Mallick T.K. Improving spectral modification for applications in solar cells: A review. *Renewable Energy*, 2019, **132**, P. 186–205.
- [25] Zeng L., Yi Y., et al. Efficiency enhancement in Si solar cells by textured photonic crystal back reflector. *Applied Physics Letters*, 2006, **89** (11), 111111-1-3.

- [26] Saravanan S., Dubey R.S. Optical absorption enhancement in 40 nm ultrathin film silicon solar cells assisted by photonic and plasmonic modes. *Optics Communications*, 2016, **377**, P. 65–69.
- [27] Sheng X., Johnson Steven G., et al. Integrated photonic structures for light trapping in thin film Si solar cells. *Applied Physics Letters*, 2012, **100**, 111110-1-3.
- [28] Olaimat M.M., Yousefi L., Ramahi O.M. Using plasmonic and nanoparticles to enhance the efficiency of solar cells: review of latest technologies. *J. of the Optical Society of America B*, 2021, **38** (2), P. 638–651.
- [29] Saravanan S., Dubey R.S. Ultraviolet and visible reflective TiO₂/SiO thin films on silicon using sol-gel spin coater. *Nanosystems: Physics, Chemistry, Mathematics*, 2021, **12** (3), P. 311–316.
- [30] Qingfei M., Li H., et al. Preparation and optical properties of angle-dependent photonic crystals based on multilayer films. *Optical Materials*, 2019, **88**, P. 488–491.

Submitted 11 November 2021; revised 28 December 2021; accepted 17 March 2022

Information about the authors:

Raghvendra Sarvjeet Dubey – Advanced Research Laboratory for Nanomaterials & Devices, Department of Nanotechnology, Swarnandhra College of Engineering & Technology, Seetharampuram, Narsapur, 534280 West Godavari, Andhra Pradesh, India; ORCID 0000-0003-1152-7257; rag_pcw@gmail.com

Sigamani Saravanan – Advanced Research Laboratory for Nanomaterials & Devices, Department of Nanotechnology, Swarnandhra College of Engineering & Technology, Seetharampuram, Narsapur, 534280 West Godavari, Andhra Pradesh, India; ORCID 0000-0003-3639-6214; shasa86@gmail.com

Conflict of interest: the authors declare no conflict of interest.



NANOSYSTEMS:

PHYSICS, CHEMISTRY, MATHEMATICS

INFORMATION FOR AUTHORS

The journal publishes research articles and reviews, and also short scientific papers (letters) which are unpublished and have not been accepted for publication in other magazines. Articles should be submitted in English. All articles are reviewed, then if necessary come back to the author to completion.

The journal is indexed in Web of Science Core Collection (Emerging Sources Citation Index), Chemical Abstract Service of the American Chemical Society, Zentralblatt MATH and in Russian Scientific Citation Index.

Author should submit the following materials:

1. Article file in English, containing article title, the initials and the surname of the authors, Institute (University), postal address, the electronic address, the summary, keywords, MSC or PACS index, article text, the list of references.
2. Files with illustrations, files with tables.
3. The covering letter in English containing the article information (article name, MSC or PACS index, keywords, the summary, the literature) and about all authors (the surname, names, the full name of places of work, the mailing address with the postal code, contact phone number with a city code, the electronic address).
4. The expert judgement on possibility of publication of the article in open press (for authors from Russia).

Authors can submit a paper and the corresponding files to the following addresses: nanojournal.ifmo@gmail.com, popov1955@gmail.com.

Text requirements

Articles should be prepared with using of text editors MS Word or LaTeX (preferable). It is necessary to submit source file (LaTeX) and a pdf copy. In the name of files the English alphabet is used. The recommended size of short communications (letters) is 4-6 pages, research articles– 6-15 pages, reviews – 30 pages.

Recommendations for text in MS Word:

Formulas should be written using Math Type. Figures and tables with captions should be inserted in the text. Additionally, authors present separate files for all figures and Word files of tables.

Recommendations for text in LaTeX:

Please, use standard LaTeX without macros and additional style files. The list of references should be included in the main LaTeX file. Source LaTeX file of the paper with the corresponding pdf file and files of figures should be submitted.

References in the article text are given in square brackets. The list of references should be prepared in accordance with the following samples:

- [1] Surname N. *Book Title*. Nauka Publishing House, Saint Petersburg, 2000, 281 pp.
- [2] Surname N., Surname N. Paper title. *Journal Name*, 2010, 1 (5), P. 17-23.
- [3] Surname N., Surname N. Lecture title. In: Abstracts/Proceedings of the Conference, Place and Date, 2000, P. 17-23.
- [4] Surname N., Surname N. Paper title, 2000, URL: <http://books.ifmo.ru/ntv>.
- [5] Surname N., Surname N. Patent Name. Patent No. 11111, 2010, Bul. No. 33, 5 pp.
- [6] Surname N., Surname N. Thesis Title. Thesis for full doctor degree in math. and physics, Saint Petersburg, 2000, 105 pp.

Requirements to illustrations

Illustrations should be submitted as separate black-and-white files. Formats of files – jpeg, eps, tiff.



NANOSYSTEMS:

PHYSICS, CHEMISTRY, MATHEMATICS

Журнал зарегистрирован

Федеральной службой по надзору в сфере связи, информационных технологий и массовых коммуникаций

(свидетельство ПИ № ФС 77 - 49048 от 22.03.2012 г.)

ISSN 2220-8054

Учредитель: федеральное государственное автономное образовательное учреждение высшего образования

«Санкт-Петербургский национальный исследовательский университет информационных технологий, механики и оптики»

Издатель: федеральное государственное автономное образовательное учреждение высшего образования

«Санкт-Петербургский национальный исследовательский университет информационных технологий, механики и оптики»

Отпечатано в Учреждении «Университетские телекоммуникации»

Адрес: 197101, Санкт-Петербург, Кронверкский пр., 49

Подписка на журнал НФХМ

На второе полугодие 2022 года подписка осуществляется через

ОАО «АРЗИ», подписной индекс Э57385